University of Alberta

An Experimental Study of Interfacial Waves and Instabilities in Exchange Flows over a Smooth Sill

by

Hesham Rabie Sayed Fouli ©

A thesis submitted to the Faculty of Graduate Studies and Research in partial

fulfillment of the requirements for the degree of Doctor of Philosophy

in

Water Resources Engineering

Department of Civil & Environmental Engineering,
Edmonton, Alberta
Spring 2006

Canada

To
Prophet Muhammad (peace be upon him),
the best person of human history
&
to my parents, my family, my wife, and my daughter
for all their love and kindness to me.

"My choice of Muhammad to lead the list of world's most influential persons may surprise some readers and may be questioned by others, but he was the only man in the history who was supremely successful on both the secular and religious level. It is this unparalleled combination of the secular and religious influence which I feel entitles Muhammad to be considered to be the most influential single figure in human history." -Michael Hart in his book: 'The 100 - A Ranking of the Most Influential Persons in the History.'

"I wanted to know the best of one who holds today's undisputed sway over the hearts of millions of mankind....I became more than convinced that it was not the sword that won a place for Islam in those days in the scheme of life. It was the rigid simplicity, the utter self-effacement of the Prophet, the scrupulous regard for his pledges, his intense devotion to this friends and followers, his intrepidity, his fearlessness, his absolute trust in God and in his own mission. These and not the sword carried everything before them and surmounted every obstacle. When I closed the 2nd volume (of the Prophet's biography), I was sorry there was not more for me to read of the great life." – Mahatma Gandhi in his book: 'Young India.'

"Muhammad was by far the most remarkable man that ever set foot on this earth. He preached a religion, founded a state, built a nation, laid down a moral code, initiated numerous social and political reforms, established a powerful and dynamic society to practice and represent his teachings and completely revolutionized the worlds of human thought and behavior for all times to come." - Sir Bernard Shaw.

"Muhammad is the most successful of all Prophets and religious personalities." - Encyclopedia Britannica.

"Your Lord has decreed that you worship none but Him, and that you be kind to parents. Whether one or both of them attain old age in your life period, say not to them a word of contempt, nor repel them, but address them in terms of honor." Qur'an (17:23)

{ مَرَجَ الْبَحْرَيْنِ يَلْتَقِيَانِ * بَيْنَهُمَا بَرْزَخٌ لَا يَبْغِيَانِ}

(الرحمن 19-20)

"He has made the two seas to flow freely (so that) they meet together: Between them is a barrier, which they cannot pass." – Qur'an (55:19-20)

{ وَهُوَ الَّذِي مَرَجَ الْبَحْرَيْنِ هَذَا عَذْبٌ فُرَاتٌ وَهَذَا مِلْحٌ أُجَاجٌ وَجَعَلَ بَيْنَهُمَا بَرْزَخًا وَحِجْرًا مَحْجُورًا}

(الفرقان 53)

"It is He Who has let free the two bodies of flowing water: One palatable and sweet, and the other salt and bitter; yet has He made a barrier between them, a partition that is forbidden to be passed." – Qur'an (25:53)

{أَوْ كَظُلُمَاتٍ فِي بَحْرٍ لُجِّيٍّ يَغْشَاهُ مَوْجٌ مِنْ فَوْقِهِ مَوْجٌ مِنْ فَوْقِهِ سَحَابٌ ظُلُمَاتٌ بَعْضُهَا فَوْقَ بَعْضٍ إِذَا أَخْرَجَ يَدَهُ لَمْ يَكَدْ يَرَاهَا وَمَنْ لَمْ يَجْعَلِ اللَّهُ لَهُ نُورًا فَمَا لَهُ مِنْ نُورٍ} (النور40)

"Or like utter darkness in the deep sea: there covers it a wave above which is another wave, above which is a cloud, (layers of) utter darkness one above another; when he holds out his hand, he is almost unable to see it; and to whomsoever Allah does not give light, he has no light." – Qur'an (24:40)

ABSTRACT

An experimental study examining two-layer exchange flows over a sill in a channel connecting two reservoirs at slightly different densities is presented. The experiments were designed to investigate: the generation of Kelvin-Helmholtz (K-H) instabilities in downslope currents, the reservoir-channel interaction, and mixing mechanisms in the lee of the sill.

For the downslope flow, a new entrainment and mixing mechanism was observed during the maximal exchange. In that mechanism, a low frequency oscillation of the density interface and a shear-generated K-H instability above the sill crest resulted in frequent piling and release of chunks of lower layer fluids which led to the development of large-scale breaking waves. Those waves caused significant interfacial entrainment with the entrainment coefficient about 0.1, the latter notably bigger than in turbulent wall jets. During the sub-maximal exchange, K-H instabilities were generated at bulk Richardson number, J, of about 0.05 - 0.12, which is considerably larger than theoretical predictions for parallel flows. Observations and detailed measurements of growths of those instabilities revealed two growth patterns: pattern I in which the instability was entrained into the lower layer, and pattern II where it pinched off into the upper layer.

The channel outflow revealed the existence of large-amplitude interfacial K-H instabilities that were frequently generated outside of the channel and propagated into the reservoir. The amplitude of those instabilities reached almost ¼ of the total flow depth. The internal hydraulic theory illustrated that the flow within the channel was basin-controlled. The outflow behaved like a surface plume whose densimetric Froude number, F_o, was about 0.24. Hilbert-Huang transform was used to investigate the origin of the aforementioned low frequency oscillation at the sill crest.

In the lee of the sill, a dynamically passive recirculation zone at medium density was observed between the upper and lower flowing layers. Analysis of the lower layer interface indicated the

existence of lee waves downstream of the sill base at one single frequency everywhere. The time-averaged concentration field, obtained through laser-induced fluorescence, revealed that 75% and up of the maximum concentration in the lower layer were limited only to the shallowest one centimeter.

ACKNOWLEDGEMENTS

I am greatly indebted first and foremost to God, the Almighty, Creator and Sustainer of this life and to Whom everything will return. I admit I have been extremely impressed with some of the verses in the Qur'an, three of them are in the opposite page, that deal with the phenomena of internal waves as signs from God to humanity. It is God Whom I ask that He accepts this work and that it becomes beneficial to all those who seek knowledge in this area and others. Secondly, I would like to express my sincere gratitude and thanks to my parents, brother and sister, and all family members who have been encouraging me all through; particularly my mother-in-law who took care of my daughter when both my wife and I were studying. Special thanks go to my dear wife, Noor, for her patience, encouragement, and support throughout my PhD program, and for her help in editing and printing the thesis. Although my daughter, Alaa, is only 32 months old at this time, I wish these words would compensate for the times I wished to spend with her but could not because of my study.

My thanks and acknowledgements go next to my supervisor, Dr. D. Z. Zhu for his guidance, continuous support, encouragement, and discussions during the course of this study. Special thanks go to Dr. B. Sutherland, Dr. D. J. Wilson, Dr. M. Loewen, Dr. N. Rajaratnam, and Dr. P. M. Steffler for the fruitful discussions I have had with them and for the knowledge I have gained throughout the courses they offered. I would like to further thank Dr. Sutherland who kindly accepted to replace Dr. Wilson on the examining committee, the latter having retired, and also for his useful and rich contributions that I received from him as this work was concluding. My thanks extend to Dr. N. Huang as well for his advices on the Hilbert-Huang Transform (HHT) technique. Plenty of thanks go to Dr. M. Atmane for his sincere help and productive discussions on laser-induced fluorescence (LIF).

Thank you to Mr. Perry Fedun, Instrumentation Engineering Technologist at the T. Blench Hydraulics Laboratory, for setting up the experimental arrangements and for his productive

advice and support.

Thanks to all my colleagues, the department technicians, and all the professors of the Water resources Group, Civil Engineering Department at the University of Alberta for their friendship. This provided for a pleasant working atmosphere at the T. Blench Hydraulics Laboratory. Warm thanks go to Mr. Y. Shammaa, who shared many ideas and thoughts on stratified flows with me in addition to his enormous help. Special thanks go to Dr. M. K. Siddiqui, Mr. M. Mukto, and Mr. A. Jalil for their rich discussions and support they offered during their stay at the T. Blench Hydraulics Laboratory.

I highly appreciate the financial support for this research project given mainly through the University of Alberta General Awards with special mention to the I. W. Killam Memorial Scholarship.

TABLE OF CONTENTS

LIST OF TABLES

LIST OF FIGURES

LIST OF SYMBOLS

A	Area of the instability
b	Channel width
B-i	Locations in the basin upstream to the channel exit; i being the location index
b_o	Depth or thickness of flow at the source
C	Dye concentration (g/m^3) for PLIF study
C_o	Concentration of 1 g/m^3
C1…C9	Intrinsic mode function components
CCD	Intensity of light being received by the camera
CCD$_c$	Corrected value of the initial gray scale intensity due to camera
CCD$_{Co}$	Reference concentration image (of the maximum concentration used)
CCD$_i$	Initial gray scale intensity
CH-i	Locations within the channel, where i is the location index
C_i	Propagation speed of the long interfacial gravity wave
c_i	Non-dimensional growth rate
d	Vertical shift between the shear layer center and the density interface
E	Internal energy
E_i	Energy head (or Bernoulli constant) for layer i
e_r	Entrainment rate (in Chapter 2, as defined by Parker et $al.$ 1987)
F	Densimetric Froude number
f	Frequency
F_Δ	Stability Froude number
f_0	Fundamental frequency

f_1	1st sub-harmonic related to release events
f_2	2nd sub-harmonic related to release events
f_3	3rd sub-harmonic related to K-H instability
f_4	4th sub-harmonic related to K-H instability
F_o	Densimetric Froude number at the source
g	Gravitational acceleration
g'	Reduced gravity
G	Internal Froude number
H	Total flow depth
$H_{inst.}$	Amplitude of instability
h	Sill height above the bed
h_m	Maximum amplitude of the sill at the crest
i	Layer index ($i=1$ for upper layer, $i=2$ for lower layer)
I	Gray scale value of any pixel
$\bar{I}$	Depth averaged gray scale value over the lower layer at any location
IC(i, j)	Corrected gray scale of pixel (i, j) due to vertical attenuation of Laser
IC$_o$	Mean value of the reference correction image CCD$_{Co}$
J	Bulk Richardson number
k	Wave number ($2\pi/\lambda$)
L	Length of the basin
$L_{channel}$	Length between the crest and the exit
L_s	One half of the length of the symmetric sill
L_x	Three-dimensional basin length

L_y	Three-dimensional basin width
M	Maximum number of sifting steps allowed
$n_{1...}$	Level of intermittency
n^k	Same intermittency criterion is repeatedly used for k times
p	Pressure
Q	Volumetric flow rate
q	Flow rate per unit width
R	Residual in the signal decomposition
R_e	Shear layer Reynolds number
R_i^*	Layer-based Richardson number
s	Distance from the channel exit into the channel for boundary layer calculations
S	Sifting stopping criterion
t	real time
t^*	Non-dimensional time
T	Period of wave activity, or characteristic time scale
T_{NM}	Resonant period of the internal basin oscillation at a particular mode NM
T_o	Periodic time of the fundamental frequency mode f_o
u	Horizontal velocity at any grid point
U	Uniform horizontal velocity
U_{1min}	Minimum velocity in the upper layer
U_{2max}	Maximum velocity in the lower layer
U_{avg}	Average velocity defined as $(U_{1min} + U_{2max})/2$
U_i	Horizontal velocity for layer i

U_{int}	Interfacial wave speed obtained from cross correlating neighbouring time series
U_o	Average velocity at the source
$\overline{U}_d$	Mean of the depth-averaged velocities in the upper and lower layers
ΔU	Velocity difference between the two layers
V	Total velocity
V_q	Representative velocity of the layer of interest for calculating entrainment rate
w	Vertical velocity component
x	Horizontal co-ordinate along the channel with respect to sill crest
y	Horizontal co-ordinate normal to the channel with respect to sill crest
z	Vertical co-ordinate with respect to the origin at the bed
z_b	Base interface level
z_e	Estimated equivalent excess level in the interface due to the instability
z_f	Level of the free surface
z_i	Depth or Thickness of layer i
z_t	True interface level with respect to bed
α_e	Entrainment coefficient
γ	CCD Camera correction factor
ε	Relative density difference
η	Density layer thickness
θ	Angle of tilt for the incline
λ	Wavelength
$\lambda_{\pm}$	Estimated interfacial long waves' propagation speed
ν	Kinematic viscosity

ρ	Density
$\Delta\rho$	Density difference
ρ_i	Density for layer i
ω	Vorticity
ω_y	Vorticity component within the laser sheet plane
ϵ	Non-dimensional vertical shift
δ	Thickness of the shear layer
δ_{BL}	Thickness of boundary layer

CHAPTER 1

INTRODUCTION

Exchange flow over bottom topography is a natural phenomenon that occurs mainly in straits due to density difference between the two water bodies connected through the strait. Examples of such flows include: the exchange flow through the Strait of Gibraltar (Armi & Farmer, 1988), the summer-time exchange of warmer heavily polluted Hamilton Harbor water with cooler and denser Lake Ontario water through the Burlington ship canal (Lawrence *et al.*, 2004), and the exchange between Little Sodus Bay and Lake Ontario (Rueda & Cowen, 2005). The strait or the connecting channel typically has bottom sills, lateral contractions, or combinations of both. In all density-stratified flows over bottom topography, entrainment and mixing along the interface are major issues that need to be addressed. Recent studies indicated that entrainment can change the hydraulics of exchange flows (Garret & Gerdes, 2003; Morin *et. al*, 2004; Nielsen *et al.*, 2004). Mixing is equally important since it not only affects the amount of exchange, but also because it acts as a buffer for property exchange between the two layers (Bray *et al.*, 1995).

Different mechanisms can lead to entrainment and mixing in such flows. For example: Morin *et al.* (2004), and Pawlak and Armi (2000) in their laboratory studies of stratified flows over topography attributed entrainment and mixing to large scale interfacial Kelvin-Helmholtz (K-H) instabilities. In their field study of the flow over Knight Inlet Sill, Farmer and Armi (1999) related entrainment and mixing to small-scale K-H instabilities that they observed at the density interface. Afanasyev and Peltier (2001), on the other hand, simulated the same flow over Knight Inlet Sill numerically and related entrainment and mixing to the breaking of a primary internal wave. A fundamental understanding of the interfacial processes that lead to entrainment need to be obtained (Dallimore *et al.*, 2001). As an important step towards examining entrainment and mixing, the interfacial processes that lead to them are to be studied.

The present study examines two-layer salinity-stratified exchange flows over bottom sill in a rectangular channel that connects two water reservoirs at slightly different densities. The experimental design allows the investigation of various flow phenomena that are quite important in geophysical fluid dynamics and environmental hydraulics. These include: down slope flows and the associated entrainment and mixing, interfacial shear instabilities in spatially accelerating flow field, the reservoir's impact on the flow regime and the outflow dynamics, and mixing

1

mechanisms in the lee of bottom topography. Digital particle image velocimetery (DPIV) and planar laser-induced fluorescence (PLIF) are used to obtain the velocity and concentration fields, respectively. Fast Fourier Transform (FFT) and Hilbert-Huang Transform (HHT) are used to obtain global and temporal information on the frequencies of the different interfacial activities.

At the interface between the two layers, instabilities usually form due to interactions between inertia (being destabilizing agent) and buoyancy (as a restoring force). Two common types of instabilities typically form in such flows. The first: known as Kelvin-Helmholtz (K-H) instabilities, are in the form of big rolls or vortices that cause significant interfacial entrainment and mixing between the two layers. The second type is known as Holmboe instabilities, which are in the form of upward and downward cusps that move at different speeds along the interface (Zhu & Lawrence, 2001). The latter has marginal effect on entrainment and mixing, although recently Smyth and Winters (2003) reported on numerical evidence of turbulent mixing generated through Holmboe waves which is comparable to that generated through K-H instabilities. Figure 1-1 portrays the aforementioned two types of instabilities.

In the context of two-layer exchange flow over bottom topography within a channel that connects two different density water bodies (see figure 1-2), the existence of the topography results in the establishment of an internal hydraulic control at the sill crest. An internal hydraulic control is a location at which the composite Froude number, G, equals unity ($G = 1$). The internal Froude number, G, is analogous to the traditional Froude number, F, in single layer hydraulics. Two-layer flows can have up to two controls; hence another control would form at the channel exit. The establishment of both controls defines different flow reaches along the channel from a hydraulic perspective. Within the region bounded by the two controls, the flow is internally sub-critical, whereas away from either control it is super-critical. While sub-critical flows are typically buoyancy dominated, super-critical flows are dominated by inertial effects. The existence of both controls, on the other hand, would deem the flow at maximal exchange; meaning the exchange flow rate will be at its maximum possible dictated by the two controls. The loss of any of those controls will subsequently cause the exchange flow rate to drop, hence becoming sub-maximal.

Even though considerable studies have focused on interfacial instabilities in two-layer flows, their effect on entrainment and mixing in real flows remains largely unknown. Prior to quantifying mixing, the characteristics and behavior of those instabilities are to be studied and well-understood. Previous studies on K-H instabilities focused on their generation conditions and characteristics mainly in parallel flows where topographic forcing was not considered (Lawrence *et al.*, 1991; Haigh & Lawrence, 1999; Peltier & Caulfield, 2003). Haigh and Lawrence (1999),

2

for example, indicate that K-H instabilities are generated when the bulk Richardson number, J, is less than 0.071, and the shift between the density and shear layer centers, d, is less than ¼ of the shear layer thickness, δ. In their study, the density layer thickness, η, was much smaller than that of the shear layer ($\eta \ll \delta$). In real geophysical flows though, both stratification and geometrical boundary conditions can have significant effects on the generation and characteristics of shear instabilities.

The interplay between stratification and geometry is complicated and poorly understood. One effect of geometrical boundary conditions on shear-induced mixing is the acceleration caused by the internal hydraulic response to topographic forcing (Pawlak & Armi, 1998). Unlike the results of Haigh and Lawrence (1999) for parallel flow, Pawlak and Armi (2000) reported on the generation of K-H instabilities when $J \approx 0.08\text{-}0.33$. In their hydraulically controlled wedge flow setting, they observed a shift between the core of the growing vortices and the vorticity source at the interface when $\delta \approx \eta$. More recently, Morin et al. (2004) studied K-H instabilities in downslope exchange flow and reported $J \approx 0.07\text{-}0.1$ when δ/η is $O(10)$. However, they did not investigate the effect of displacement between the shear and density layer centers. The latter two studies focused on the steady flow situation only. Obviously, the generation conditions of K-H instabilities seem to be different from the parallel flow case, hence the need to further study their characteristics in situations matching real flow conditions does exist. Downslope currents are typical real flows in which these phenomena are valid. Chapter 2 of this study is devoted to investigate such effects in an accelerating exchange flow down an incline. The study examines these phenomena within both the steady maximal and the unsteady sub-maximal exchange regimes. For that, exchange flow was modeled in the laboratory as shown in figure 1-2a.

The second motivation of the current study has been to explore the reservoir-channel interaction and its effect on the flow regimes and how these influence the concurrent generated interfacial waves. While abundant studies have focused on the hydraulics of exchange through straits connecting adjacent reservoirs (Armi & Farmer, 1988; Lawrence, 1993; Helfrich, 1995; Zhu, 2002), only few recent studies discussing the reservoir-strait interaction exist (Finnigan et al. (2001); Rueda & Cowen, 2005). The mechanisms through which the strait communicates with the neighboring reservoir and whether the exchange is reservoir-controlled or channel-controlled are key issues that are relatively poorly understood and need to be addressed. Chapter 3 of the present study discusses these issues along the sub-critical reach upstream to the sill crest and within the salt water reservoir. A complementary objective has been to resolve the existence of a long wave low frequency oscillation that was reported in earlier studies performed in the same facility (Zhu et al. (2002); Morin et al. (2004)). In both studies, that low frequency oscillation

3

was referred to the internal basin seiching, yet there has been no concrete evidence for this notion. For this part, the sill had the profile shown in figure 1-2b with its crest located a bit far from the exit to allow for the formation of a tangible sub-critical region between the two controls.

The third objective of the present study is to examine the entrainment and mixing that occur beyond the topography due to the breaking of the interfacial waves that were generated along the slope. In the lee of the topography, different mechanisms and flow phenomena could occur depending on various factors like the head and tail water conditions of the lower layer, the height of the sill, the strength of the approach flow and the nature of the existing stratification (Staquet & Sommeria, 1996). Among those mechanisms are: internal hydraulic jumps (Yih & Guha, 1955; Rajaratnam *et al.*, 1991), wall jets, lee waves (Sutherland, 2002), separation and subsequent recirculation zone, turbulent wakes and internal waves. The flow may transition, as in the case of an internal jump, from super- to sub-critical state. Recently, though, there has been a debate among the stratified flow community as to whether such transition occurs through an internal jump or breaking internal waves (Farmer & Armi, 1999; Afanasyev & Peltier, 2001). In most of those flow phenomena, an intermediate layer of medium density usually forms and the interaction of such layer with the upper and lower layers is still not well understood. Chapter 4 discusses this flow reach within the maximal regime. In addition, it sheds the light on some effects that occur in the late sub-maximal regime, and explores the effect of the density difference on the flow field.

Chapter 5 presents summary of the findings of the current research, and recommendations for future research in this field. The final appendices include: a) results from an earlier study on exchange flow through openings in which the author was part of, b) a brief account on the estimation of the density as a function of temperature and salinity, c) a short report on PLIF and sample calibration for the technique using a circular buoyant jet in quiescent flow, and d) an account on error analysis.

While the current study focuses on exchange flows, the results may be applicable to other flows which feature instability-induced entrainment and mixing such as gravity currents, cold river water into lakes, river mouth discharges into oceans, and intrusion of seawater in reservoirs and estuaries. The study could also relate to atmospheric flows over mountains and oceanographic hydraulic flows at inlets. The results herein can help improve our understanding of geophysical flows such as that over Knight Inlet Sill where interfacial instabilities were thought to be the cause of mixing (Farmer & Armi, 1999). Likewise, the obtained results for the fresh water outflow into the reservoir can simulate river mouth discharges into oceans, which have been recently reported as a new mechanism for the generation of internal waves (Nash & Moum, 2005).

4

REFERENCES

AFANASYEV, Y. D. & PELTIER, W. R. 2001 On breaking internal waves over the sill in Knight Inlet. *In Proc. Royal Society, series A* **457**, 2799-2825.

ARMI, L. & FARMER, D. M. 1988 The flow of Mediterranean water through the Strait of Gibraltar. *Progress in Oceanography*, **21**, 1-105.

BRAY, N. A., OCHOA, J. & KINDER, T. H. 1995 The role of the interface in exchange through the Strait of Gibraltar. *J. Geophys. Research* **100** (C6), 10,755-10,776.

DALLIMORE, C. J., IMBERGER, J. & ISHIKAWA, T. 2001 Entrainment and turbulence in saline underflow in Lake Ogawara. *Journal of Hydraulic Engineering* **127**, 937.

FARMER, D. & ARMI, L. 1999 Stratified flow over topography: the role of small-scale entrainment and mixing in flow establishment. *Proc. R. Soc. Lond.* A **455**, 3221-3258.

FINNIGAN, T. D., WINTERS, K. B. & IVEY, G. N. 2001 Response characteristics of a buoyancy-driven sea. *J. Physical Ocean.* **31**, 2721-2736.

GARRET, C. & GERDES, F. 2003 Hydraulic control of homogeneous shear flows. *J. Fluid Mech.* **475**, 163-172.

HAIGH, S. & LAWRENCE, G. A. 1999 Symmetric and non-symmetric Holmboe instabilities in an inviscid flow. *Phys. Fluids* **11**, 1459-1468.

HILFRICH, K. R. 1995 Time-dependent two-layer hydraulic exchange flows. *J. of Physical Oceanogr.* **25**, 359-373.

LAWRENCE, G. A., BROWAND, F. K. & REDEKOPP, L. G. 1991 The stability of a sheared density interface. *Phys. Fluids* A **3** (10), 2360-2370.

LAWRENCE, G. 1993 The hydraulics of steady two-layer flow over a fixed obstacle. *J. Fluid Mech.* **254**, 605-633.

LAWRENCE, G., PIETERS, R., ZAREMBA, L., TEDFORD, T., GU, L., GRECO, S. & HAMBLIN, P. 2004 Summer exchange between Hamilton Harbour and Lake Ontario. *Deep-Sea Research II* **51**, 475-487.

MORIN, V. M., ZHU, D. Z. & LOEWEN, M. R. 2004 Super Critical Exchange Flow Down a Sill. *J. Hydraulic Engineering* **130** (6), 521-531.

NASH, J. D. & MOUM, J. N. 2005 River plumes as a source of large-amplitude internal waves in the coastal ocean. *Nature* **437**, 400-403.

NIELSEN, M. H., PRATT, L. & HELFRICH, K. 2004 Mixing and entrainment in hydraulically driven stratified flows. *J. Fluid Mech.* **515**, 415-443.

PAWLAK, G. & ARMI, L. 1998 Vortex dynamics in a spatially accelerating shear layer. *J. Fluid Mech.* **376**, 1-35.

5

PAWLAK G. & ARMI L. 2000 Mixing and entrainment in developing stratified currents. *J. Fluid Mech.* **424**, 45-73.

PELTIER, W. R. & CAULFIELD, C. P. 2003 Mixing efficiency in stratified shear flows. *Ann. Rev. Fluid Mech.* **35**, 135-167.

RAJARATNAM, N., TOVELL, D. & LOEWEN, M. 1991 Internal jumps in two moving layers. *J. of Hydraulic Res*, **29**, 91-106.

RUEDA, F. G. & COWEN, E. A. 2005 Exchange between a freshwater embayment and a large lake through a long, shallow channel. *Limnil. Oceanogr.* **50** (1), 169-183.

SMYTH, W. D. & WINTERS, K. B. 2003 Turbulence and mixing in Holmboe waves. *J. Phys. Oceanog.* **33**, 694-711.

STAQUET, C. & SOMMERIA, J. 1996 Internal waves, turbulence and mixing in stratified flows: A report on Euromech Colloquium 339. *J. Fluid Mech.* **314**, 349-371.

SUTHERLAND, B. R. 2002 Large-amplitude internal wave generation in the lee of step-shaped topography. *Geophysical Research Letters* **29** (16), art. no. 1769.

YIH, C. G. & GUHA, C. R. 1955 Hydraulic jump in a fluid system of two layers. *Tellus*, **7** (3), 358-366.

ZHENG, Q., SHEN, S. S. P., YUAN, Y., HUANG, N. E., KLEMAS, V. et al. 2004 Evidence of the coexistence of upstream and downstream solitary wavetrains in the real atmosphere. *Int. J. Remote Sensing* **25** (21), 4433-4440.

ZHU, D. Z. & LAWRENCE, A. G. 2001 Holmboe's instability in exchange flows. *J. Fluid Mech.* **429**, 391-409.

ZHU, D. Z., FOULI H. & OKYERE, Y. A. 2002 Exchange flow through an opening. *J. Hydraulic Research*, **40** (3), 341-350.

ZHU, D. Z. 2002 Control curves for two-layer flows. *J. of Hydraulic Engineering*, ASCE, **128**(1), 113-116.
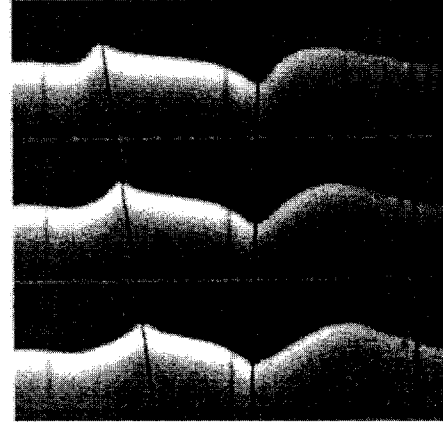
FIGURE 1-1. K-H instabilities in the form of rolls at the interface are shown to the left (quoted from Morin *et al.*, 2004). To the right are few images showing Holmboe instabilities as cusps moving at different speeds (reproduced from Zhu *et al.*, 2001).

7
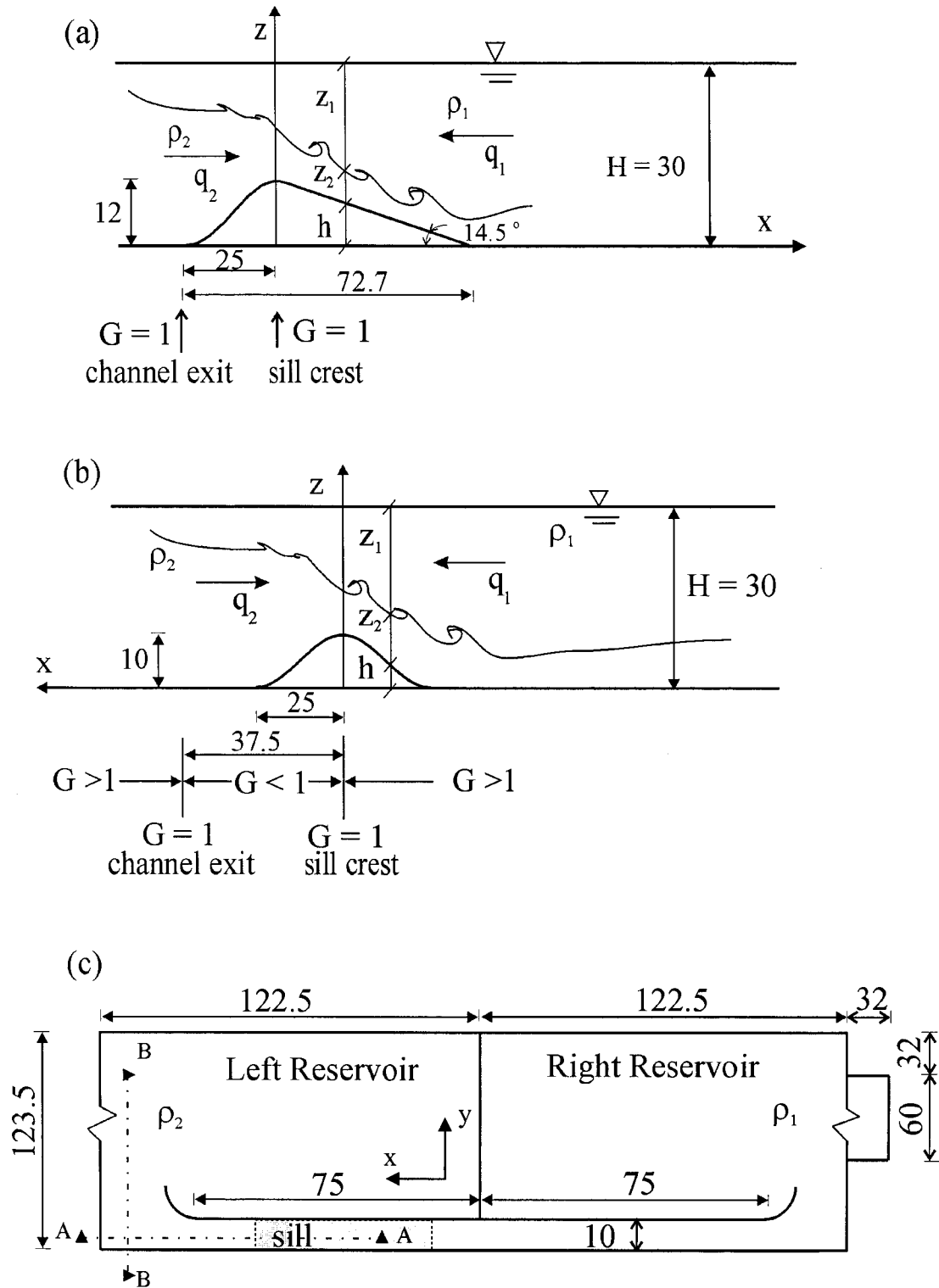
FIGURE 1-2. Schematic of the experimental facility used throughout the study: (a) side view of the setup used in chapter 2 and 4, b) side view of the setup used in chapter 3, and (c) general plan view. All dimensions are in centimeters. G is the composite Froude number.

8

CHAPTER 2

INTERFACIAL WAVES AND INSTABILITIES DOWN A SMOOTH SLOPE[1]

2.1 INTRODUCTION

Exchange flows can be generated when two fluids of slightly different densities are brought in contact. The difference in densities could be due to differences in salinity, temperature and/or sediment concentration of these fluids. Of particular interest is the exchange flow which occurs over bottom topography due to its existence in many natural flows. Examples of such flows in the aquatic environment include: the exchange of the more saline Mediterranean water with the less saline Atlantic Ocean water through the Strait of Gibraltar (Armi & Farmer, 1988; Baringer & Price, 1997), and the summer time exchange of warmer heavily polluted Hamilton Harbor water with cooler (denser) Lake Ontario water through the Burlington Ship canal (Hamblin & Lawrence, 1990; Lawrence *et al.*, 2004). These flows can be easily generated in the laboratory, which is one of the most effective ways to study them.

In all density-stratified flows over bottom topography, entrainment and mixing along the interface are major issues that need to be addressed. Recent studies indicated that entrainment not only affects the interface height and flow rate along the topography, but also causes a horizontal shift in the location of the critical section from its assumed position at the topography crest as predicted by the internal hydraulic theory (Pawlak & Armi, 2000; Morin *et al.*, 2004; Nielsen *et al.*, 2004). Mixing is equally important since it controls the vertical transfer of mass, heat, and nutrients, in addition to controlling the exchange flow rate between the water bodies. Bray *et al.* (1995) reported in their study of exchange flow through the Strait of Gibraltar that mixing between the inflow and outflow causes the formation of an intermediate layer which significantly contributes to the exchange and acts as a buffer layer for property exchange between the upper and lower layers.

---

[1] The contents of this chapter in part has been presented in the 4th International Symposium on Environmental Hydraulics and the 14th Congress of Asia and Pacific Division, International Association of Hydraulic Engineering and Research (IAHR), Hong Kong, 2004.

9

Different mechanisms can lead to entrainment and mixing in such flows. For example, Morin *et al.* (2004) and Pawlak and Armi (2000), in their laboratory studies of stratified flows over topography, attributed entrainment and mixing to large scale interfacial Kelvin-Helmholtz (K-H) instabilities. In their field study of the flow over Knight Inlet Sill, Farmer and Armi (2001) related interfacial entrainment and mixing to small-scale K-H instabilities that they observed at the density interface. Afanasyev and Peltier (2001a), on the other hand, simulated the same flow over Knight Inlet Sill numerically and related interfacial entrainment and mixing to the breaking of a primary internal wave. A fundamental understanding of the interfacial processes that lead to entrainment need to be obtained (Dallimore *et al.*, 2001). This chapter presents an experimental study of two-layer exchange flow over mild slope topography (slopes < 20° to the horizontal). Most bottom slopes in the ocean lie within this range of slope angles (Baines, 2001). A major goal of the study is to further improve our understanding of the mechanisms that lead to interfacial entrainment and mixing, particularly in oceanic exchange flows experiencing spatial acceleration.

While there is considerable knowledge on K-H instabilities in parallel flows (Lawrence *et al.*, 1991; Haigh & Lawrence, 1999), their generation conditions and characteristics in real flows, where geometrical boundary conditions interact with stratification, are largely unknown. One effect of the geometrical boundary conditions is the acceleration due to the internal hydraulic response to topographic forcing (Pawlak & Armi, 1998). Recently, Pawlak and Armi (2000) and Morin *et al.* (2004) reported larger values of the bulk Richardson number, J, for the generation of K-H instabilities down an incline than for the parallel flow case. Their studies focused on the steady state situation only and lacked measurements of the vertical shift between the shear and density layers' thicknesses.

In this study, we examine different interfacial wave activities that lead to entrainment and mixing. We investigate the characteristics of these waves with emphasis on the large-scale interfacial K-H instabilities. The study serves as an important step towards understanding the behavior of those instabilities in spatially accelerating flow fields. The results provide better understanding of the concerned mechanisms, and lend data for validating future numerical modeling of such flows. While the current study focuses on two-layer exchange flows over bottom sills, the results may be applicable in many other flows that feature similar entrainment and mixing mechanisms. Examples of such flows include gravity currents and turbidity currents entering lakes and reservoirs (Alavian *et al.*, 1992; Altinakar *et al.*, 1992), intrusion of seawater into reservoirs (Dallimore *et al.*, 2001) and estuaries (Arita & Jirka, 1987). Section 2 provides

10

review of the topic, while Section 3 describes the experimental setup and techniques. In Section 4, the results are presented, and the discussion and conclusions are in Sections 5 and 6, respectively.

2.2 BACKGROUND AND LITERATURE REVIEW

At the interface between two fluids of slightly different densities, both shear and gravity effects interplay resulting in various modes of instabilities. Depending upon the strength of shear, buoyancy, thickness of the interface, and its displacement from the shear layer center, either of Holmboe or Kelvin-Helmholtz modes may form in stably stratified shear flows (Ortiz *et al.*, 2002). Although considerable studies have focused on these instabilities, their effect on mixing and entrainment in real flows remains largely unknown. A common and special example of real flows that exhibit the generation of shear instabilities is that of stratified flow over topography. Stratified flow over topography has been an outstanding topic in geophysical fluid mechanics since the forties of the last century. The problem is complicated due to the interference of many parameters whose interplay is still not well understood. Such parameters include: the background stratification, the geometry of the topography, the state of flow at either side of the topography be it sub- or super-critical, the spatial domain of the flow field, and the flow regime whether it is at maximal or sub-maximal exchange when it comes to exchange flows over sills. The change of any of these parameters can cause different flow phenomena to occur along the topography. For instance, a streamlined topography may cause the flow to behave like a wall jet experiencing no separation at its lee side. A bluff body on the other hand would cause the flow to separate at its boundary resulting in circulation zones and undular waves at its lee side.

The strength of the shear can be described using the bulk Richardson number, $J = g'\delta/\Delta U^2$, where $g' = \varepsilon.g$ is the reduced gravity in which g is the gravitational acceleration, $\varepsilon = (\rho_2-\rho_1)/\rho_2$ with ρ_1 and ρ_2 being the densities of the upper and lower layers, respectively, $\delta = \Delta U/(\partial U/\partial z)_{max}$ the thickness of the shear layer, and $\Delta U = U_2-U_1$ is the velocity difference between the two layers (see figure 2-1). We restrict ourselves to flows with $\varepsilon \ll 1$, thus the Boussinesq approximation is valid. Our study focuses on K-H instabilities, which form as rolled vortices or billows separated by thin braids, along the interface between two fluids in a down slope accelerating current. These billows can grow temporally as well as spatially until they reach a maximum size limited by stratification and boundary effects. Eventually, they break generating turbulence and irreversible

11

mixing of the two fluids leading to the formation of a mixing layer. In what follows, a review of existing literature on the topic is presented.

The hydraulics of two-layer exchange flows over a smooth bottom sill in a constant-width channel has been studied by Morin et al. (2004) using the internal hydraulic theory; an overview of which is presented in chapter 3. In brief, the internal Froude number, G ($G^2 = F_1^2 + F_2^2$), describes the criticality of two-layer flows to interfacial waves, where F is the densimetric Froude number ($F_i^2 = U_i^2/g'z_i$) for layer i, and the mean horizontal velocity $U_i = Q_i/bz_i$, Q being the volumetric flow rate, b the channel width, z_i the thickness of layer i, and g' the reduced gravity. Locations where $G = 1$ are called internal hydraulic controls. Two-layer exchange flows can have up to two controls. With two controls, the flow is at maximal exchange; whereas with one control only, it is sub-maximal (Farmer & Armi, 1986). For the current flow setup, a schematic of which is presented in figure 1-2, the two controls can occur at the sill crest and the channel left-hand exit (Morin et al., 2004).

The generation of K-H instabilities in spatially accelerating stratified down slope flows has received significant attention among the geophysical community only recently. Perhaps motivated by the observations of Farmer and Armi (1999) of the flow over Knight Inlet Sill in which they related interfacial mixing to small scale K-H instabilities, few other researchers started to investigate the different mechanisms and phenomena involved in these flows. For example, Pawlak and Armi (1998, 2000) examined the vortex mechanisms developed in a stratified shear layer subject to spatial acceleration and the subsequent interfacial entrainment and mixing in their physical experiments of down slope currents. Their outer flow was dictated by a hydraulically controlled wedge flow that provided a spatially accelerating shear layer and baroclinic generation of interfacial vorticity along the density interface above a mild sloping topography. They observed organized separation and pinching off of the vortex core of K-H instabilities from the vorticity source at the interface. They reported the existence of a new finite-amplitude vortex mechanism, which they referred to as leap-frog pairing. They observed large scale K-H instabilities at $J = 0.08 - 0.33$ when $\delta \approx \eta$. However, they based their measurements on time-averaged velocity profiles, which would overestimate J by a factor of 3 (Morin et al., 2004).

More recently, Morin et al. (2004) studied interfacial K-H instabilities in the super-critical region of two-layer exchange flows over a smooth bottom sill within the maximal exchange. Their flows were dictated by the establishment of two hydraulic controls at the sill crest and the exit of a channel which connected two reservoirs at different densities. The instabilities caused large periodic fluctuations in their measurements of the flow rate and interface positions along the

12

sill. They reported K-H instabilities at $J = 0.07 - 0.1$ when δ/η is O(10), but did not investigate the effect of density interface displacement from the shear layer center. They reported on the existence of multiple modes of K-H instabilities down the slope at higher order harmonics of a primary K-H instability that occurred roughly within the upper third of the slope.

The stability of two-layer stably stratified flows has been studied using the linear stability theory. While recent studies have focused on the stability of parallel stratified flows, there are only a limited number of studies on spatially accelerating flows. The interfacial region is described by the thickness of the shear layer, δ, the vertical shift between the shear layer center and the density interface, d, and the density layer thickness, $\eta = \Delta\rho/(\partial\rho/\partial z)_{max}$ (refer to figure 2-1). Lawrence et al. (1991) investigated theoretically and experimentally the stability of two-layer shear flows when $\delta \gg \eta$ and the density interface is displaced with respect to the velocity interface by a non-dimensional vertical shift, $\epsilon (= d / (\delta/2))$ in which d is the dimensional shift. They reported K-H instabilities to have occurred when $J < 0.1$ for an initial displacement of $\epsilon_o \approx 0.5$.

In continuation to these efforts, Haigh and Lawrence (1999) studied the effect of displacing a thin density interface with respect to the center of the shear layer on the stability of an inviscid, stably stratified parallel flow. Their studies focused mainly on flows with $\delta \gg \eta$. They showed that for symmetric flows where the interface displacement is zero ($d \approx 0$), K-H instabilities are possible for $J < 0.071$; however when $0.046 < J < 0.071$, Holmboe instabilities are more unstable than K-H instabilities. In addition, they found that when $d > \frac{1}{4} \delta$, the symmetry of the background flow is broken and K-H instabilities are no longer observed. Experiments by Zhu and Lawrence (2001) showed that Holmboe instabilities disappear when J exceeds about 0.7.

Pawlak and Armi (1998) applied spatial linear stability analysis and described two modes of instabilities whose centers of vorticities could be displaced upwards or downwards from the density interface at different growth rates. They compared these two modes to the positive and negative Holmboe instabilities which were found as solutions to the temporal problem (Lawrence et al., 1991). Their positive K-H mode had a higher phase speed, hence slower growing rate. The faster growing mode corresponded to the upstream propagating negative Holmboe solution. While the faster growing mode showed significant upward displacement of its centre of rotation into the lower momentum stream, the slower growing mode had a less significant bias into the higher momentum stream.

13

The generated K-H instabilities in stratified flows down an incline have been considered as the main cause of interfacial entrainment and mixing by many researchers (Farmer & Armi, 1999; Pawlak & Armi, 2000; Baines, 2001; Morin et al., 2004). Many studies quantified entrainment using the classic model of Ellison and Turner (1959). Entrainment causes the flow rate to increase spatially as parcels from the lower momentum stream are entrained into the higher momentum stream. Pawlak and Armi (2000) identified two distinct regions with high and low entrainment rates, respectively, in their study of hydraulically controlled wedge flow down a sill. They reported values for the entrainment coefficient, based on Ellison and Turner's definition, decreasing from about 0.08 up the slope in the initial unstable accelerating region to around 0.01 where the flow became fully developed in the final region down the slope. More recently, Morin et al. (2004) reported on an increase of about 20% in their time-averaged measurements of the flow rate downstream of the sill crest. Their entrainment coefficient increased initially up to about one third of the sill length, where the primary instabilities were generated, and then was followed by a decaying fold over the rest of the sill. They reported values of the entrainment coefficient varying between 0.05 and 0.09.

Baines (2001) studied mixing and entrainment in dense flows down gentle slopes into linearly stratified ambient fluid. He identified three regions in the down slope current as follows: an initial adjustment region closest to the source, an intermediate region in which the flow had almost uniform thickness where it experienced continuous detrainment and entrainment with the ambient fluid, and a final region where the flow left the slope as it found its own neutral density level. He expanded Ellison and Turner's (1959) entrainment model to describe turbulent transfers of mass and momentum at the upper interface of the dense current in terms of entrainment, detrainment and drag coefficients. Those coefficients could be determined in terms of local values of Richardson number and a parameter that involves the volume flux, the buoyancy frequency and the reduced gravity.

Entrainment can cause other effects in stratified flows over topography. For example, Morin et al. (2004) found that the time-averaged interface profile along the sill was higher than that predicted by the internal hydraulic theory; the latter neglects the effect of entrainment. Nielsen et al. (2004) analytically and numerically studied mixing and entrainment in hydraulically driven stratified sill flows. They postulated an approach based on shallow-water theory for reduced gravity flows with a cross-interface entrainment. They ran numerical simulations using another model with continuously varying stratification and velocity but found poor agreement for the location of the hydraulic control between the two models. They quantified such differences by

14

shape coefficients which measured the vertical non-uniformities in the density and velocity profiles as a result of incomplete mixing of entrained mass and momentum over the lower layer depth. Their prediction of the location of the hydraulic control based on the continuously varying model showed an upstream shift compared to that obtained through the reduced-gravity model.

Stratified flow over topography is usually accompanied by the formation of a relatively thick downstream intermediate layer at a medium density between the upper and lower layers on the lee side of the topography. Intermediate layers were observed in earlier experimental work, for example, Wilkinson and Wood (1983). A key question in such flows has been: what forms such intermediate layer. While Farmer and Armi (1999) referred its formation to small scale interfacial K-H instabilities that break and provide a source of fluid entering the intermediate layer, Afanasyev and Peltier (2001a) emphasized the role of a primary internal breaking wave, which leads to the formation of that intermediate layer. Within the phase of flow establishment, Farmer and Armi (1999), in their study on stratified tidal flow in Knight Inlet, observed boundary layer separation that was suppressed as the intermediate layer grew full. They observed no internal breaking wave in their field study.

Afanasyev and Peltier (2001a) on the contrary did not account for boundary layer separation and therefore, according to Farmer and Armi (2001), did not analyze this phase of flow establishment. Rather, their analysis was mainly within the hydraulic end state. Afansyev and Peltier's assumption of no boundary layer separation is supported by theory which predicts that stratification acts to accelerate the flow in the lee of the sill and suppress boundary layer separation (Sutherland, 2002). The analyses of the observations and numerical results of both parties have been subject to controversy (Afanasyev and Peltier, 2001b). More recently, Lamb (2004) used a non-hydrostatic two-dimensional model to numerically simulate the flow over Knight Inlet sill. He assumed a no-slip bottom boundary condition which resulted in boundary layer separation from near the top of the sill. The latter remarkably reduced the amplitude of a generated lee wave during the initial stages of the flow development.

Previous studies which investigated the evolution of mixing layers due to generated shear instabilities considered their temporal evolution as in the titling tube experiments of Thopre (1968), or their spatial evolution in splitter-plate configurations. Thorpe (1968) studied experimentally the temporal evolution of mixing layers in his well known tilting tubes. He obtained information on the structure and evolution of K-H billows especially their growth rates, maximum amplitude, wavelength, and their breakdown mechanism (Thorpe, 1969a, 1969b, 1971, 1973, 1987). In his series of work on mixing layers due to shear instabilities he found that their

15

wavelength, λ, and the time at which they first occurred were remarkably repeatable for given density difference, $\Delta\rho$, angle of tilt, θ, and total depth, H. He also found that the instabilities reached their maximum height before they broke when the wave slope, defined as $2\pi a/\lambda$ in which a is the wave amplitude, was about 1.1. He then developed a theory to predict the onset and wavelength of K-H instabilities in uniformly accelerating flow and while his theory could fairly predict the onset time, it underestimated the wavelength compared to observations. He concluded that acceleration had the effect to decrease the wavelength, λ, of the fastest growing wave to lower values than predicted for steady flows. He then studied the effect of the thickness of the interface on the growth rates of the instabilities and could find that the observed growth rates were on average 25% less than the predictions. Scorer (1969) considered the mechanics of billows that are formed due to the tilting of stably stratified layers as in the wavy airflow produced by hills. He showed that the mixed layer due to the instabilities could be five times as thick as the statically stable layer prior to tilting.

Experimental studies that examined the spatial evolution of mixing layers include those of Scotti and Corcos (1969) in which they imposed small periodic disturbances at the interface between two uniform streams of air at different temperatures in a horizontal wind tunnel. In their experiments, the shear layer Reynolds number, R_e ($=\delta.\Delta U/\nu$) in which ν is the kinematic viscosity, ranged between 50 and 150. They presented results that showed the growth rates of the generated instabilities were in reasonably good agreement with theoretical predictions based on inviscid parallel flow. Brown and Roshko (1974), and Winant and Browand (1974) studied the spatial evolution of mixing layer through splitter-plate experiments. Those studies documented the existence of two-dimensional organized vortical structures in the mixing layer and referred to their interactions as a main cause for the mixing layer growth. Brown and Roshko (1974) investigated the density effects on the turbulent mixing layer. They attempted to extend ideas like that in the problem of Helmholtz instability of a vortex sheet in which the density ratio would affect the amplification rate of the mixing layer through increasing the vortex strength by the square root of the density ratio. Those attempts were not much successful though. Winant and Browand (1974) reported in their experiments on vortex pairing and showed how two successive instabilities originally separated at a wavelength, λ, would pair to form a larger structure separated at twice the original wavelength from another successive large structure. In their experiments the shear layer Reynolds number, R_e ($=\delta.\Delta U/\nu$) in which ν is the kinematic viscosity, ranged from 45 where the shear layer originated to 850 over 50 cm span.

Patnaik *et al.* (1976) carried out numerical simulations of K-H waves of finite amplitude in equal-depth two-layer exchange flows. They investigated the growth and interaction of those waves and the effect of some parameters including R_e, J, and λ on their behavior. Other numerical studies of down slope windstorms over mountain ridge revealed the generation of K-H instabilities accompanied by a pulsation phenomenon in the flow field. Clark and Farely (1984) earliest reported on surface gustiness while studying strong down slope windstorm events. They combined two- and three-dimensional model simulations in which they assumed dynamic stability of the two-dimensional down slope flow. The periodic gustiness was a result of three-dimensional instability of the two-dimensional background stable state. Later, however, Scinocca and Peltier (1989) criticized the initial assumption that the two-dimensional state was stable and delivered no such oscillations, even though Peltier and Halle (1978) used the same assumption in their study on the evolution of finite amplitude K-H billows. Scinocca and Peltier (1989) proved that such gustiness was an intrinsically two-dimensional phenomenon. They showed as well that whenever a down slope windstorm is generated through wave breaking mechanism in two spatial dimensions, oscillations in the surface wind speeds will occur to the lee of the topography. This gustiness is manifested as series of pulses of high velocity that propagate downstream at fixed phase speed.

Early theoretical modeling of linearly stably-stratified flow over topography dates back to Long (1955) who studied stratified flows over obstacle and provided a solution for the flow field, *Long's model*, when the upstream depth was infinite compared to the height of the obstacle. Baines (1977) investigated the problem experimentally and showed that Long's model was approximately applicable only for $Nh/U \leq 0.75$, in which N is the background stratification, h is the height of the topography, and U is the uniform upstream free flow speed. Baines' observations with larger obstacles having $Nh/U \geq 0.75$ revealed a new phenomenon which he called '*upstream influence*'. When the topography is large enough, partial blocking of the flow upstream to the obstacle would cause its rising up, thereby altering the stratification and velocity arbitrarily far upstream. The idea is that some fluid in the flow would not have enough kinetic energy to initially make it over the obstacle. The denser fluid would decelerate and accumulate behind the obstacle in an exchange process between kinetic and potential energies. The elevated fluid would pour then over the sill forming a jet along the downstream side of the sill crest.

The importance of the upstream influence is becoming more obvious since it not only causes the generation of large scale breaking waves down the slope (those waves can severely damage downstream structures in the lee of mountains and generate extensive mixing both in air and water flows), but also affects the upstream region. Recently, Cummins *et al.* (2003) in their study

17

of Knight Inlet sill reported on observations of upstream-propagating solitary like internal waves as the tidal flow relaxes, a consequence of upstream influence. Those waves could propagate hundreds of kilometers and appear to play a role in the mixing of surface waters, in modifying the biological environment, as well as in re-suspending sediment (Cummins *et al.*, 2003). Chapter 3 of this thesis elaborates more on the upstream effects that were observed upstream to a symmetric bottom sill.

When the topography's height is large compared to the flow depth, a high-drag state forms along the topography. A high-drag state consists of a strong, super-critical down slope jet of fluid beneath a large breaking lee wave (Lamb, 2004). In the atmospheric terminology, this jet is commonly termed down slope windstorm. While there are many atmospheric realizations of down slope windstorms (Baines, 1995), oceanic observations of the phenomenon are more recent and rare (Farmer & Armi, 1999; Nash & Moum, 2001). The high-drag state is explained hydraulically as a consequence of the flow transitioning from sub-critical upstream to the sill crest to super-critical at its downstream side. The strong super-critical jet stream creates a region of low pressure at the lee side of the sill; hence a net horizontal drag on the topography is formed.

In this study, our interest is mainly in the K-H instabilities and other interfacial wave activities observed in experiments of two-layer exchange flows over a bottom sill within the super-critical reach downwind the sill crest at its lee side. After examining the flow conditions, we will then study the entrainment due to these interfacial waves and instabilities and its effect on the flow rate. The instability characteristics including their frequencies, generation conditions, wavelengths, and growth rates and patterns are also investigated.

2.3 EXPERIMENTAL SETUP

Two-layer exchange flow over a smooth sill in a rectangular channel was modeled in the laboratory (refer to figure 1-2: a, c). The sill has the shape: $h(x) = h_m \cos^2 (\pi x/2L_s)$, with $h_m = 12$ cm, and $L_s = 25$ cm within $-25 < x < 2.8$ cm with the crest at $x = 0$. The downstream part of the sill ($2.8 < x < 47.7$ cm) has a flat slope at $14.5°$ to the horizontal, matching that of Pawlak & Armi (2000), and allowing for a longer slope length than that of Morin *et al.* (2004), hence better capturing multiple wavelengths of the generated instabilities down the slope. The left toe of the sill coincides with the channel left exit. A side compartment was appended to the right fresh water reservoir to allow for longer duration of the experiments; thus longer duration within the sub-maximal regime could be recorded. Three main experiments were conducted with $g' = 1.62$,

18

3.23, 6.47 cm/s^2 for Exp 1, 2, and 3, respectively. Exp 1 was repeated with a smaller field of view to attain higher spatial resolution and more accurate measurements, especially for the shear layer along the interface, the repeat of the experiment is labeled Exp 1a. A fourth experiment, Exp 4, was conducted at much higher g' ($\approx$ 18.03 cm/s^2) to explore the effect of Reynolds number on the interfacial wave activities. Exp 1, 1a, 2, and 3 provided simultaneous measurements for the density and velocity fields, while Exp 4 provided qualitative images for the density field only. The experiments along with their properties are listed in Table 2-1.

In all main experiments, the tank was filled with fresh water to a depth of 30 cm. A vertical barrier was placed at the left toe of the sill to divide the tank into two reservoirs. NaCl salt was added in the left reservoir. Silver-coated spherical glass particles (mean diameter of 15 μm and specific gravity of 1.65, Potters Industries, Paoli, Pennsylvania) were seeded in both reservoirs for PIV measurements. Rhodamine 6G dye (has excitation and emission wavelength peaks in water at $\approx$ 526 and 550 nm, respectively (Bindhu *et al.*, 1999)) was mixed with the water in the left reservoir to visualize the lower layer for the determination of the density interface. A laser sheet was produced through a 5W argon-ion laser operating at 488 nm (Stabilite 2017, Spectra-Physics Lasers, Mountain View, California). A fiber optical cable (OZ Optics Ltd., Nepean, Ontario) transmitted the light to a top-located lens that produced a 2 mm laser sheet at the center of the channel where measurements were made.

In Exp 1 and 3, two TK-1280U JVC CCD cameras were synchronized and used during the measurements at a shutter speed of 1/60 s. The produced images (640x480 pixels) were grabbed at a rate of 30 Hz both for PIV and interface analysis. In Exp 2, a digital CCD Dalsa camera (DS-21-02M30-SA, DALSA, Waterloo, ON) was used at a rate of 60 Hz and spatial resolution of 1600x1200 pixels for the PIV measurements, while a digital CCD Pulnix camera (TM – 1040, Pulnix America Inc., Sunnyvale, California) running at 30 Hz with 1008x1008 pixels spatial resolution was used for the interface images. Exp 1a was recorded using the TM - 1040 Pulnix camera at 30 Hz for the PIV images, while a digital Sony Hi-8 video camera was used to produce the interface images at 5 Hz. In all recordings, a band-pass filter with a rejection range of 525 - 800 nm (Edmund Industrial Optics, Barrington, NJ, USA) was used with the PIV camera to filter out the dye. A high-pass filter with a cutoff at 520 nm (Melles Griot Inc., Irvine, California) was used with the interface camera to filter out the PIV particles. The PIV camera was connected to a personal computer which had image acquisition software (Video Savant, I.O. Industries Inc., London, Ontario) and a frame grabber (Road Runner, Bitflow, Woburn, Massachusetts), both of which allowed capturing and streaming the PIV images onto a Redundant Array of Independent

19

Drives (RAID) at a rate of 30 Hz. Exp 4 was recorded using the same digital Sony Hi-8 camera used for Exp 1a, but with no filters.

The average error in the instantaneous velocity measurements was estimated at 4%. The velocity fields in Exp 1, 2 and 3 were computed using a direct cross-correlation PIV algorithm (Marxen, 1998) with a search and interrogation windows of 32 and 16 pixels at 50% overlap allowing a velocity measurement each 8 pixels. Velocity vectors were post-processed to remove any spurious vectors using a local median test (Morin, 2002). All vectors were corrected and interpolated onto the grid points using Adaptive Gaussian Window (AGW) interpolation. The generated velocity fields were at 15 Hz in Exp 1 and 3, and at 30 Hz in Exp 2. In Exp 1a, however, an iterative multi-grid cross-correlation PIV algorithm (Scarano & Riethmuller, 1999) was used to generate the velocity fields at 10 Hz.

The density interface, on the other hand, was detected based on the differing gray scales of the upper and lower layers. An algorithm based on the differing gray scale values of the upper and lower layers was used to estimate the interface position. Because of the existence of rolling interfacial K-H instabilities (see figure 2-2: image f), a base interface level, z_b, which would border the lower part of the instability, is first determined at all locations through a bottom-top scheme. To account for the rolls, we integrate the pixels above the base interface, z_b, having bright gray scale values as part of the lower layer and estimate an equivalent excess level, z_e, as follows:

$$z_e = \frac{\sum_{z_b}^{z_f} I \cdot dz}{\bar{I}} \tag{2.1}$$

in which z_f is the level of the free surface, I is the gray scale value of any pixel, dz is the vertical discretization (one pixel), and $\bar{I}$ is the depth averaged gray scale value between the channel bed and z_b at any location. The true interface, z_t, is then predicted as:

$$z_t = z_b + z_e \tag{2.2}$$

Where no interfacial waves or K-H instabilities occurred, the interface was sharp and both z_t and z_b coincided. Errors of about 2-3 pixels (1.4-2 mm) were estimated in detecting the interface position. The interface images were also used to estimate the density layer thickness, η, through vertical profiles of the gray scale intensity at different locations along the sill.

20

2.4 RESULTS

2.4.1 Overview of the wave activities and their generation mechanism

As the barrier separating the two fluids was removed, exchange flow started (figure 2-2) with the upper fresh water layer flowing from right to left, whereas the lower more dense layer flowing in the opposite direction. The flow was unsteady for some time, after which an internal hydraulic control was first established at the channel exit followed at a later time by a second control at the sill crest. The initial unsteady period was about 30 and 60s in Exp 3 and 1, respectively. Once the two controls were established, the flow was at maximal exchange. Since velocities scale with $\sqrt{g'}$ and the tank has fixed volumes of fluids in all experiments, the duration of the maximal exchange is expected to vary inversely with $\sqrt{g'}$. The maximal exchange lasted for about 6.2, 4.4 and 2.4 min, for Exp 1, 2 and 3, respectively. As the experiment proceeded, the upper layer flow filled the left reservoir and flooded the left-hand exit control; hence the flow became sub-maximal. Sub-maximal exchange flow continued to decrease gradually until the end of the experiment when the fresh water totally overlaid the salt water in the whole tank.

As can be seen in figure 2-2, the lower layer continually accelerates as it flows over the sill. During the steady maximal regime, frequent releases of large lumps of lower layer fluid that occur around the sill crest (see image a) are observed. These lumps grow bigger as they travel down the slope and attain very steep fronts along which parasitic K-H instabilities are generated (images b, c). Eventually they break and leave in their wakes remarkable mixing (images d, e). The mixed layer is then entrained into the lower layer and flushed away leaving behind a steep sharp interface along which fresh larger K-H instabilities are generated (image f). K-H instabilities are also frequently generated around the sill crest and would propagate upstream or downstream the sill crest depending on the mean flow field conditions. This pattern widely persists during the maximal regime, although sometimes those released lumps may form successively with no K-H instabilities in their wakes, hence occurring more frequent. Note also the huge fluctuation that occurs to the density interface at the sill crest in a cyclic fashion (compare images a – e that indicate a continual decay in the interface level at the crest, followed by a successive rise in image f). The reader is advised to refer to chapter 3 for the upstream propagating instabilities. It may be worth mentioning here that the two sets of waves propagating in opposite directions around the crest in our experiments are similar to a recent observation of coexisting upstream and downstream propagating wave trains in the atmosphere around the Hainan Island which was reported by Zheng et al. (2004).

21

Later in the sub-maximal regime, a thin intermediate layer is formed upstream to the sill crest as a result of interfacial mixing. Then, this layer and the weakened shear do not favor the generation of K-H instabilities upstream to the sill crest. At this stage as well, we do not observe those downstream frequently released lumps anymore. The interfacial fluctuations upstream and at the sill crest fade remarkably at this stage. However, more frequent and organized K-H instabilities are formed at the tip of the intermediate layer (figure 2-3). They grow larger in amplitude as they travel along the interface and once they reach their maximum size, they are either pinched-off the lower layer into the upper layer, or distorted in shape and may pair with a following K-H instability into the lower layer. The location of the point at which those instabilities are generated constantly shifts further downstream with time. Due to the excessive interfacial mixing resulting from the breaking of the interfacial waves and instabilities in the downstream, a larger intermediate mixed layer also forms around the right toe of the sill and progresses towards the crest. The flow field attains then a three-layer structure with the intermediate layer being almost stagnant compared to the upper and lower dynamically more active layers. This study investigates both flow regimes, namely the maximal and sub-maximal, but up to the time where there existed clear two-layer structure within the flow field. Figure 2-4 shows an instantaneous density field image from Exp 1 over which the corresponding velocity profiles at few locations are plotted. The density interface defined previously in Section 2-3 is also over plotted and seen to capture the interfacial K-H instabilities and waves that occur along the interface.

The present set of experiments reveals a new finite-amplitude mechanism through which large interfacial breaking waves occur during the maximal regime along the slope of the topography. In this mechanism, shear-generated K-H instability forms along the sharp density interface above the crest of the topography when the interface is low (figure 2-5: images a-d in the first cycle, and i-l in the second cycle). A pair of other K-H instabilities is symmetrically generated at either side of the former crest instability. The crest instability stalls in place for some time while growing bigger in amplitude causing piling up of lower layer fluid upstream and up to the crest; hence the interface attains higher elevations. Meanwhile, the two instabilities that formed at either side of the crest would propagate in opposite directions with the upstream propagating instability smaller in amplitude than the downstream propagating one. As the interface level reaches a climax elevation at the sill crest, it starts to drop down releasing the lower layer fluid down the slope (images g-j in the first cycle, and o-v in the second cycle). The lowering of the interface in this phase results in the shallowness of the lower layer and possible shift of the density interface below the shear layer center. This causes the crest instability to accelerate down the slope and the

22

released lower layer fluid helps its development into large scale breaking wave (see image a from a previous cycle, j and v from the 1st and 2nd cycles, respectively). Sometimes parasitic K-H instabilities may form atop of those breaking waves (image i). The whole structure, as a cluster of instabilities, overturns and breaks generating intensive mixing and entrainment of the upper layer fluids into the lower layer stream. The accelerating flow field washes out the mixing and a steep sharp interface is once more formed along which a new cycle begins (image b from a previous cycle, i and w-x from 1st and 2nd cycles, respectively). During the rise-fall cycle of the interface, more frequent K-H instabilities may form at either side of the sill crest.

2.4.2 Velocity field and entrainment

The instantaneous velocity profiles at the sill crest were used both to validate our velocity measurements and to help estimate the different flow regimes. The horizontal velocity profiles in Exp 1 and 3 were integrated across depth to obtain the instantaneous flow rate per unit width, q $(=Q/b)$. Figure 2-6 shows the time series of the flow rate in both experiments for the upper layer. Clearly the initial unsteady period is seen followed by the steady maximal regime. Once the hydraulic control is lost ($G < 1$), the sub-maximal regime starts with the flow rate decaying with time. The mean flow rate during the maximal exchange measures 21.73 and 42.41 cm/s^2 in Exp 1 and 3, respectively. These measurements compare well with the predictions of the internal hydraulic theory that can be graphically obtained through the control curve approach (the reader is to refer to Zhu (2002) for more details on the approach. Predictions of the flow rate are 20.71 and 41.39 cm/s^2 for Exp 1 and 3 respectively. These are within 5% from the measured upper layer values. Both the time series of the interface positions (a sample of which is presented later in figure 2-21 for Exp 1) and that of the flow rate at the sill crest were used to estimate the duration of the steady maximal exchange.

The instantaneous velocity fields were time-averaged over the steady maximal exchange period and the results are shown in figure 2-7. The gradual spatial increase in velocities within each layer clearly shows the accelerating behavior of the flow. The time-averaged density interface position along the sill is over-plotted and shows the same effect. The velocity profiles exemplify self-similarity in the stream wise direction although there is some change in the shape of the profile in terms of its uniformity within the lower layer beyond $x \approx 12.5$ cm. In addition, the lower layer velocity profiles reflect no signatures of boundary layer separation. The time-averaged velocity fields shown in figure 2-7 were obtained based on 30 and 10 Hz instantaneous velocity fields in Exp 2 and 1a, respectively.

23

The different velocity profiles in Exp 1a were used to calculate the velocity shear, ΔU ($\Delta U = U_{2max}-U_{1min}$), and the average velocity, U_{avg} ($U_{avg} = (U_{2max}+U_{1min})/2$). The results are shown in figure 2-8 along with the interfacial wave speeds obtained from cross-correlating successive neighboring interface positions time series data over the maximal exchange period. Although the definition of the density interface is somewhat subjective, yet the measurements indicate that the interfacial K-H instabilities are moving at a convective speed close to that of the mean flow. This agrees with the existing knowledge in horizontal parallel flows that K-H instabilities have zero phase speed with respect to the mean flow. It is noteworthy mentioning here that Pawlak and Armi (2000) in their experiments with wedge-controlled downslope stratified currents also reported that the flow structure throughout the depth of the shear layer is essentially advected with the mean velocity. The velocity shear, ΔU, on the other hand, shows an initial constant zone for up to about $x = 8$ cm, beyond which it constantly increases with distance down the incline. The variation of the velocity shear, ΔU, would suggest a decay in the bulk Richardson number, J, with distance since its effect is more emphasized than the shear layer thickness, δ.

The horizontal u-component velocity profiles were integrated across depth to obtain the flow rate per unit width, q. Results from Exp 2 and 1a for the upper layer flow rate are shown in figure 2-9, where a significant increase of up to about 40% in comparison to the value at the sill crest is observed. Morin *et al.* (2004) reported an increase in flow rate of about 20% in a similar setup but with a symmetric topography to the left part of the current one. In their setup though, such increase happened over a length of 25 cm down the crest and the sill had amplitude of 10 cm, hence allowing higher flow rates for the same g'. In their setup, the sill was located such that its crest was at 37.5 cm to the right of the channel left exit (refer to figure 1-2b). It appears that the interfacial K-H instabilities and the huge wave structures resulting from the frequent releases of the lower layer fluid cause significant interfacial entrainment from the upper lower momentum stream into the lower higher momentum one. As the flow rate becomes higher, the lower layer has higher momentum; hence the capacity of entrainment decreases. This could explain the differences in the results of Exp 2 and 1a in figure 2-9. That we measure 40% increase in q in Exp 1a, almost twice what Morin *et al.* (2004) reported over the same length with the same g', may be due to the lower momentum in our case. It is known that plumes, with lower momentum fluxes as compared to jets, have higher entrainment capacity. Upstream to the sill crest where the flow is internally sub-critical, the flow rate seems to be fairly constant with distance.

From the perspective of downslope gravity currents and turbulent wall jets, the primary entrainment rate of interest is that of the lower momentum ambient fluid into the higher

24

momentum stream. Following Ellison and Turner (1959), the entrainment rate, α_e, can be defined as:

$$\alpha_e = \frac{1}{V_q}\frac{dq}{dx} \qquad\qquad (2.3)$$

in which V_q is a representative velocity of the layer of interest. Over an interval of dx, the mean flow rate in the upper layer has been used on the assumption that it is equal to that of the lower layer. During the steady maximal exchange period, the interface was sharp and any mixing was flushed down; hence no accumulation or storage of fluids existed between the two layers. A nine-point moving average operator was applied to the flow rate data presented in figure 2-9 to smooth the data and obtain a better estimate for the gradient dq/dx in equation 2.3. While Morin *et al.* (2004) simply used the mean of the u-component velocity (obtained through dividing the upper layer flow rate over the lower layer thickness) within the lower layer for V_q, Ellison and Turner (1959) made use of the integral continuity, momentum and conservation of flux of density difference equations to define V_q as follows:

$$V_q = \frac{\int u^2(z)dz}{\int u(z)dz} \qquad\qquad (2.4)$$

In this way, any assumption regarding the shape of the velocity profiles is avoided.

Both values for estimating V_q were used in computing the entrainment rate, α_e, in Exp 2 and 1a and the results are shown in figure 2-10. Although the data have huge scatter, both approaches clearly indicate that the entrainment coefficient in such flows is significantly higher than turbulent wall jets. On average, α_e has values of approximately 0.079 and 0.101 in Exp 2 and 1a, respectively, using the average lower layer velocity for V_q. Using Ellison and Turner's approach, α_e is around 0.1 on the mean for both experiments. These are significantly higher values than that of 0.035 reported by Rajaratnam (1976) for plane turbulent wall jets. On closely looking at the data, it appears there is an initial zone of increasing entrainment coefficient, α_e, for up to about x $\approx$ 10 cm in Exp 1a, $x \approx 7.5$ cm in Exp 2. This is where about the large scale interfacial waves are about to overturn and break (refer to figure 2-2) and also where the velocity profiles are more or less uniform within the lower layer (figure 2-7). Beyond that zone, the entrainment coefficient data show fluctuating behavior around almost a constant value; possibly due to the breaking of the downslope waves. With the formation of the large scale interfacial waves and instabilities

25

right down the sill crest, they engulf large amounts of the upper layer fluid and entrain them into the lower layer. Later as they travel further downstream the waves break and the entrainment capacity possibly stalls as it may be inferred from the data and visual observation of the experiment.

Using Ellison and Turner's entrainment model did not show a significant difference when compared with the results obtained from using the depth-averaged velocity of the lower layer in equation 2.3. However, it is to be noted that the nature of the exchange flow down the slope, affected by the low oscillations of the density field around the sill crest, is different from the gravity currents that Ellison and Turner (1965) considered. The current flow is dominated by large scale interfacial instabilities which make the flow highly unsteady and turbulent especially along the interface. The flow can be investigated in future studies from energy point of view since the turbulent kinetic energy and the associated mixing are directly related to the change of the potential energy around the sill crest.

It is to be mentioned that many researchers attempted to quantify entrainment in gravity currents flowing down a constant slope using empirical formulae that would involve a layer-based Richardson number, R_i^* ($R_i^* = g'.z_2.\cos \theta/U^2$), in which U is the mean velocity within the turbidity current. For example Parker et $al.$ (1987) used this approach and expressed the entrainment rate, e_r, as:

$$e_r = 0.075 \Big/ (1 + 718 R_i^{*2.4})^{0.5} \tag{2.5}$$

Our data from Exp 1a provide values for R_i^* of about 1.35 at the sill crest in a decaying trend to about 0.55 at $x = 25$ cm. These result in e_r increasing from about 0.002 at the sill crest to about 0.005 at $x = 25$ cm. Apparently the results using such approach are an order of magnitude underestimated. It is to be mentioned that equation 2.5 is a relation derived for gradually varied flow. The present exchange flow is rapidly varying which could explain the large discrepancy in estimating the entrainment rate using equation 2.5.

2.4.3 Interfacial waves and characteristics of the release events

The density interface positions, obtained as explained previously in Section 2.3, at all times and locations were used to generate a wave characteristics' plot (see figure 2-11) that shows the different wave activities during the experiment. The time-averaged interface profile over each

26

minute was subtracted from the instantaneous interface data set within the same minute, and the differences were plotted after applying a contrast scheme. This way the waves were referenced with respect to the time-varying mean interface that dropped gradually; and even at late times of the experiment the wave activities were still obvious as can been seen in the third panel to the right. Bright spots resemble instants at which the instantaneous interface position was higher than the mean interface, while darker spots correspond to depressions below the mean interface. It can be clearly seen that during the maximal exchange regime (the first two panels from the left in figure 2-11), two sets of waves are generated in the close proximity of the sill crest ($x = 0$) and propagate in two opposite directions. The waves propagating upstream are smaller in amplitude than those traveling downstream. This is envisaged through the color intensity and by tracing any wave through its characteristic line. The large lumps that we reported earlier appear to be generated at a frequency of roughly about 25 s within $0 < x < 5$ cm beyond which K-H instabilities are generated on their steep fronts causing more wave activities to occur at higher frequencies.

Within the sub-maximal regime (approximately $t > 600$ s), almost no K-H instabilities are generated in the upstream. This is reflected through the flattening of the interface and the regularity of the color as portrayed in the third panel of figure 2-11. On the other hand, we begin to see more frequent interfacial waves downstream to the sill crest than before although may be at smaller amplitudes. The downstream horizontal shift of the point at which the late sub-maximal K-H instabilities are generated from the crest is also obvious ($800 < t < 900$ s). The wave characteristics' plot could be used to assess the speed of propagation of any interfacial wave by tracing its wave characteristic line; whereby the speed is the slope of that line. This speed could serve as a physically meaningful velocity scale that can be used in concurrence with the corresponding frequency to estimate the wavelength as will be discussed later. In the following, the bulk characteristics of the large scale down slope wave structures within the maximal regime are investigated.

The current set of experiments and those of Morin (2002) provide a clear experimental evidence of those release events described earlier which result into the formation of large scale breaking interfacial waves in two-layer exchange flow over bottom topography. Both sets of experiments were performed at reduced gravity, g', of 1.32, 3.23 and 6.47 cm/s^2 for experiments: Exp 1, 2, and 3, respectively. The shape, amplitude and location of the topography in the channel were different though in the two sets. Figure (1-2) shows a schematic of the two sills used in both studies. The additional experiment Exp 4 at g' of ≈ 18 cm/s^2 showed similar effect. Despite the different geometry and large variations in the density differences among those experiments, those

27

release events and the associated large scale breaking waves were a dominant feature as will be shown shortly. This indicates that Reynolds number has insignificant effect on such phenomenon of large scale breaking waves down the slope.

Figure 2-12 shows a sequence of images from the current Exp 1 portraying two events of large scale interfacial down slope breaking waves. The first of these (images a – f) appears to have started as an interfacial K-H instability during the pilling up of the lower layer upstream to the sill crest. It stretches in the stream wise direction and develops into a breaking wave, yet of relatively moderate height ($\approx$ 5 cm). The second event, although it seems to start as a small K-H instability (image d), is coupled with the relaxation of the lower layer. It results in the formation of a larger breaking wave with a steep front along the slope (image h). Small amplitude parasitic K-H instabilities form atop of these steep fronts. The wave reaches a height of around 7 cm as it breaks (image l). In the wake of those down slope breaking waves, K-H instabilities may form along the interface prior to the following pilling of the lower layer upstream to the sill crest. Image d can be used to measure the slope of the interface as an incipient condition prior to the generation of those large down slope waves. The slope measures roughly 40° to the horizontal.

Figure 2-13 shows another sequence of images from the current Exp 3 demonstrating the same effect. The higher density difference though causes the interface to become rougher and the velocities are larger than in Exp 1; hence K-H instabilities could not form as big in the wake of the down slope breaking waves neither atop of their steep fronts before they break. The slope of the interface at which the wave started to develop measures approximately 60° to the horizontal (image b). The wave grew and deformed due to the accelerating flow field pretty much similar to Exp 1 with the amplitude almost the same. As g' increased further to $\approx$18 cm/s^2 in Exp 4, the interface became even rougher and K-H instabilities were not as observable (figure 2-14). The dominant and only feature was that of the down slope breaking wave as a consequence of the release in the lower layer following a pile up due to cluster of tiny instabilities above the crest. The generation frequency of the release events was much higher, yet their amplitude seemed not to change much. The slope of the interface prior to the formation of the wave was about 58° to the horizontal (image c); although at some instants it attained slopes of up to $\approx$ 70° and higher. The relatively long and mild slope of the topography at its downstream side has its effect on the wave development. The continuous spatial acceleration of the flow field causes the wave to stretch in the stream wise direction and hence limits its amplitude development.

The experiments of Morin (2002) were re-examined for the release events and the large scale interfacial breaking waves. Figure 2-15 shows a series of images from their Exp 3 (g' = 6.47 cm/s^2) in which images (a – c) portray a passing fully developed wave after an earlier relaxation

of the interface. In image b, the lower layer piles up behind the topography due to the growth of a quasi-stagnant K-H instability above the sill crest, and a new down slope wave is about to form following the subsequent release of the lower layer fluid. The interface attains a slope of about 70° to the horizontal prior to the development of the wave (image c). The wave then grows gradually until it reaches its maximum amplitude before it breaks (images d – h). The relaxation of the lower layer is quite obvious in images (f, g), after which a new cycle of the piling up starts behind the crest. The maximum amplitude of the wave is almost in the order of the height of the topography ($\approx$ 10 cm). Additionally, the short span of the sill (25 cm) over which the flow is accelerating seems not to allow for the stream wise stretching that was observed in figures (2-12 – 2-14). The higher value of g' again causes the interface to be rougher than in Exp 1, 2 and so less clear signatures of K-H instabilities were observed down the slope; although some small amplitude ones may form in the wake of the large breaking waves. In what follows, the variation of the height of those large-scale down slope waves during the course of an experiment is examined.

The generated down slope large-scale waves were observed closely as they traveled along the topography. They start initially as K-H instabilities that develop into rolls separated from the lower layer stream. As the time passes, they grow into large scale structures that form an interfacial breaking wave. Those waves were tracked over the course of the experiment until they achieved their maximum vertical heights, after which they break and stretch in the stream wise direction due to the accelerating flow field. The variation of the wave heights and their times of occurrence are shown in figure 2-16 for the current Exp 3. In the maximal regime, when the interfacial fluctuations at the sill crest were high, those waves grow to about 7 ± 1 cm (almost 60 % of the height of the topography). Their periodic times varied from 8 to 15 s and on average 11.3 s could be considered a representative value. Once the sub-maximal regime started, the interface at the sill crest became less fluctuating and consequently a drop in the heights of those down slope waves occurred. Observed heights were about 4.5 ± 1 cm and the periodic times were about 8.9 s on the mean. The wave heights gradually decreased afterwards, although those structures were still observable. In the late sub-maximal regime, the interface almost leveled off upstream to the sill crest, and the regular and frequent K-H instabilities that were described earlier (see figure 2-3) were the only wave activity occurring along the slope. The height of those late instabilities was approximately 2- 3 cm. More details on those late K-H instabilities are included in section 2.4.5.

29

2.4.4 Frequency analysis and the Hilbert-Huang transform

In interpreting any physical data, both the time scales and the energy distributions relevant to them are of great importance (Huang et al., 1999). In the Fourier analysis, the time scales are defined as the periods of continuous and constant-amplitude trigonometric components. This results in providing only global time-averaged estimates of the energy and the time scales. In the Hilbert analysis, however, the data are decomposed according to their intrinsic characteristic scales into a number of intrinsic mode function components (IMFs), later will be denoted by C. This is done using the method of empirical mode decomposition (EMD), which aims at expanding the data in a basis derived from the data itself. Hilbert transform is then applied to those components with the result that the time localities of events are preserved. The empirical mode decomposition method is necessary to deal with both non-stationary and nonlinear data (Huang et al., 1996, 1998). For a complete description of the Hilbert technique and its application, the reader is referred to Huang et al. (1998). Because our data are both non-stationary and nonlinear, we believe the Hilbert-Huang Transform (HHT) is rather more appropriate than the Fast Fourier Transform (FFT). However, in what follows we will present the results of both techniques and compare between them.

The time series of the interface position obtained as described in the previous section at five sample locations (x = -10, 0, 10, 20, and 30 cm) in Exp 1 were extracted. The horizontal u-velocities at the closest grid points to the mean density interface at the corresponding locations in the PIV images were also obtained. The u-velocity data along with its spectra and that of the density interface using FFT are shown in figure 2-17. The time series shows the amplitude and frequencies to increase with x. With the lower layer flow accelerating down the sill and being internally super-critical, and with more wave activities occurring as we move further downstream, this can be expected. A dominant low frequency though exists upstream to and at the crest which then seems to fade down the slope being overtaken by higher frequencies. This agrees with what Morin et al. (2004) found in their analysis of the interface fluctuations (refer to their figure 10). Note that such low frequency mode is also reported in chapter 3, discussed therein in more depth, for the flow within the sub-critical region upstream to the sill crest where it persisted along the channel.

Because of the ambiguity in defining the density interface, we expect the frequency analysis of the velocity time series to be more accurate than that of the density interface data. Both time series were analyzed using Fourier power analysis to investigate the different interfacial wave activities in a global sense. The two spectra appear similar except for few differences at some locations. The lowest peak, f_0 of 0.0147 Hz (T_o = 68 s), exists only at and upstream to the crest (x

30

= -10 cm) where the flow is internally sub-critical and both spectra confirm that. Morin *et al.* (2004) referred f_0 to the basin internal seiching whose period can be estimated as $T=2L/C_i$ with L being the length of the basin (123 cm) and C_i the propagation speed of the interfacial wave $(=\sqrt{g'z_1z_2/H})$. They measured T_o as 60 s in the same tank but with a different sill geometry which we expect would not affect much the basin seiche period. With $z_1 = z_2 = 15$ cm, T is ≈ 70 s. Our measurement of T_0 is closer to the prediction given the longer time of the experiment and the finer frequency resolution. Notice that in an earlier study of exchange flow through openings using the same tank, Zhu *et al.* (2002) also reported this same value of f_0. While both studies related f_0 to the internal basin seiching, which is a basin characteristic frequency, the study in chapter 3 shows that such low frequency mode could be of a long wave generated within the channel due to interfacial perturbation because of the topography. Many studies support the opinion that interfacial level changes in the two reservoirs can not propagate through the connecting channel within the maximal regime (see for example: Hogg *et al.* (2001); Tedford *et al.* (2005)). In other terms, the hydraulic controls, with the flow being internally super-critical in their outer regions, would be expected to isolate their inter-region and block the transfer of information from either side into the domain bounded by the controls. The reader is to refer to chapter 3 for more details on that.

Upstream to the crest ($x = -10$ cm), a second peak of 0.0370 Hz (27 s) is measured and seems to be in line with that of the release events described earlier in figures 2-5 and 2-11. At $x = 0$, a second peak of 0.0295 Hz ($\approx 2f_0$) and 34 s is dominant in the u-spectrum; although the interface spectrum shows a matching smaller peak at almost the same period of 27 s for f_1. This peak could either be a sub-harmonic of f_0 or a mode of the release events of the lower layer as we will see later on. This second peak shifts further downstream to 0.0223 Hz ($\approx 1.5f_0$) and 45 s ($10 \le x \le 30$ cm). It is not clear yet why there is a shift in this peak as x increases. Two other higher peaks overtake though as x increases; these are f_1 (0.0438 – 0.0370 Hz) at about 23 – 27 s, and f_2 (0.0661–0.0589 Hz) at about 15 – 17 s. We relate both f_1 and f_2 to the release events of the lower layer lumps that we reported earlier as either occurring successively at higher frequency or separated by a train of K-H instabilities in their wakes, hence at lower frequency. The measurement of f_1 with its relatively higher energy component in the spectrum at both sides of the sill crest might indicate the ability of such wave to propagate in both directions. With the K-H instabilities observed to occur at shorter periods and higher frequencies, we would match them with the higher frequencies of f_3 (0.0809 Hz or 12 s) and f_4 (0.1250 Hz or 8 s) in the spectrum. Therefore, we report three main interfacial wave modes in the course of the experiment, namely: a) K-H instabilities occurring at the highest frequencies whose periods are about 12 s and less, (b)

large scale down slope breaking wave due to release events of lumps of lower layer fluid at frequencies with periods ranging from 15 to 45 s, and (c) the lowest frequency of about 70 s, which we elaborate on more in chapter 3. It is noteworthy here mentioning that by $x = 30$ cm, the peak energy (especially in the interface spectrum) is shifted towards the frequency f_2 (17 s). In chapter 4, which deals with the field of view further downstream in the lee of the topography, the frequency analysis of the interface positions' time series revealed a single dominant peak whose period is 17 s for the same g'.

To gain an idea about the periods of the observed wave modes, reconstructed images at sample locations were obtained during both the maximal and sub-maximal regimes. Figure 2-18 shows such images where the top three panels portray the wave activities at $x = 10$ cm during the first 6 ½ minutes of Exp 1. The lowermost panel reflects those activities at $x = 15$ cm when the late K-H instabilities start to form. Within the maximal regime, the release events are obvious with their huge amplitudes and broadened-top patterns. They are sometimes successive with shorter periods of about 15 and 17 s as was indicated by the Fourier spectrum. However, they are often separated by a series of $1 - 3$ K-H instabilities that cause them to have longer periods ranging between 27 and 45 s. The late K-H instabilities are on the other hand more frequent with initial periods of about 12 s. As time proceeds and the interfacial shear drops, they start to grow smaller in amplitude and form more frequently with periods as low as 2 s. In the following, the frequencies of the large scale breaking waves due to the release events are examined as these structures are a dominant feature in the maximal regime and probably the major cause of entrainment. They do have the highest share of energy in the spectrum as was shown in figure (2-17).

To quantify the frequency of those down slope breaking waves, the interface positions' time series, at the same discrete locations as in figure (2-17), in different experiments were analyzed in the frequency domain within the maximal regime using FFT. Their frequencies were also estimated from repetitive observations of recorded movies of the experiments and compared with the FFT results. Figure 2-19 shows sample interface positions' time series and their spectra for the current Exp 3. As mentioned earlier, when g' became larger, no clear signatures of K-H instabilities were observed and only small amplitude ones were occasionally formed along the interface (figure 2-13). The dominant feature was that of the large scale breaking waves generated down the slope. This is reflected in the spectrum of figure 2-19 where a dominant single peak of a period ≈ 11.4 s is obvious at either side of the crest. This is in agreement with the estimate obtained through repeatedly watching the movie of Exp 3. The lowest frequency f_o with a period of 32.4 s is again only observed at the sill crest and upstream. This frequency f_o is close enough to that reported in Morin *et al.* (2004) as equals to 36 s for the same g'; the

32

discrepancy again is likely due to the different topography and frequency resolution. Note that figure 10b in Morin *et al.* (2004) shows a similar pattern to that in figure 2-17 and 2-19. The repetitive observation of their movies indicates that the frequency at which most of the energy is concentrated in the spectrum is that of those large-scale down slope breaking waves and not of the K-H instabilities as reported. A period of about 19 s for those events was observed, which is very close to their reported value of 18 s in their Table 2. They report on a measured frequency f_l of 24 s, which we find very close to our measured f_l of 27 s (note that the frequency resolution and the different topography could cause this little variation). There is a difference though between their f_l and observation, which we did not find in the current set of experiments.

The frequency f_l, as related to the large scale down slope breaking waves, was obtained in all experiments both as measured and observed. The periodic times ($1/f_l$) are plotted in figure 2-20 versus the reduced gravity, g'. It is obvious that as g' increases, the frequency of those events increases, too. In some experiments, f_l was a little varying down the slope though (as shown previously in figure 2-17 herein; and figure 10b in Morin *et al.* (2004)). In those experiments, the mean value of the measured f_l was taken as a representative of the event and the error bars indicate the standard deviation then. In general, the measured and observed values are in good agreement within the current set of experiments; although the measured values in Exp 2 and 3 are identical. The observed periods in Exp 2 and 3 of Morin *et al.* (2004), as per our observation, are shorter than those reported in their Table 2. Both observations match for their Exp 1; even though they show higher discrepancy compared to the measurement. Generally, the rate of decay of the period seems to decrease remarkably as g' increases. In the following, the analysis of the time series using HHT is presented to enable us have more details on the temporal evolution of frequencies.

To trace the temporal development of the frequencies of the existing wave activities, we now implement HHT. For simplicity, we have performed all the decompositions herein at no intermittency, a criterion which could be viewed as a variation of low-pass filtering, hence may allow avoiding mode mixing and separating the different modes within a signal. However, in chapter 3 we show how it is possible to isolate the different modes through the application of intermittency. The reader is to refer to Huang *et al.* (2003) for more details on HHT and intermittency. A sample decomposition of our data for the interface positions' time series at the sill crest in Exp 1 is shown in figure 2-21. The signal, sampled at 5 Hz, is sifted into nine intrinsic mode functions (IMFs) or components (C1 ... C9) and a monotonic residual, R; the latter clearly represents the trend. To obtain physically meaningful IMFs, the sifting cannot go on forever; otherwise the IMFs will become simple modulated sinusoidal waves and may lose their

33

physical meaning. On the other hand, if the sifting is stopped too early, the riding waves cannot be separated. Therefore, to have physically meaningful IMFs, one should select the criteria in EMD carefully such that the resulting IMFs represent the underlying physical processes (Wen and Gu, 2004).

The reconstructed signal of the components (C4 … C8) and the residual, R, is shown at the bottom of figure 2-21 with the original data over-plotted. Evidently, both signals match well. The choice of the components (C4 … C8) is based on their frequencies, whose periods varied on average between 5 and 80 s, as well as on the power contained in their time series. These periods are in line with our observations of the different wave activities in the experiment in addition to them being measured in the Fourier spectra. C4 and C5 have periods of about 5 and 9 s, respectively. We relate them to two modes of the K-H instabilities. C6 and C7 have periods of about 23 and 47 s, correspondingly, which we relate to the release events of the lower layer fluid. C8 has a period of about 82 s on average, which could be related to the low-frequency long-wave mode observed in the Fourier spectra (figure 2-17b). The residual, R, represents the trend and can be used to estimate the duration of the maximal exchange. Our estimate for the maximal exchange period based on the trend, R, is about 400 s. The standard deviation, σ, of each mode was calculated over the maximal exchange duration and taken as a measure of its power. The ratio (σ/σ_{total}), in which σ_{total} is the sum of standard deviations of all modes, is included in Table 2-2. From the table, it is clear that C1 and C2 have lower power and therefore were not considered in reconstructing the signal. Although C3 has comparable power to C4, it was not included based on its high frequency that does not match with observation. Similarly, C9 has very low frequency that we do not consider as physically important in the experiment and is possibly a result of the sifting process. Clearly, C6 and C7 have the highest share of the power and this is in line with the piling and release events that had the maximum fluctuations. It is to be noted that the sampling frequency of the data has its effect on the results. For example, the same time series when analyzed at 30 Hz produced relevant components whose periods were 7, 17, 40 and 72 s. These still match with the different wave modes that we observe in the experiment in addition to the measurement of the low-frequency wave of $\approx$ 68s.

Different from the Fourier analysis, each component retains both frequency and amplitude modulations. For example, the 8th component C8, which we relate to the long-wave mode, clearly fades in amplitude by the time the sub-maximal regime starts ($t \cong 600$ s). Similarly C6 and C7 describing the release events of the lower layer fluid decay in amplitude within the sub-maximal regime. This is in line with observation. On the other hand, if we examine the development of the amplitudes in C4 and C5, we could find that the K-H instabilities seem to

34

maintain their amplitudes and frequencies although those occurring during the late sub-maximal regime become more evident at later times. Those components (C4, C5, C6, and C8) were extracted as we analyzed different time series at sample locations down the incline to trace the development and behavior of those wave modes both in space and time. The results are shown in figure 2-22.

By tracing the component C8, which we relate to the low-frequency long-wave, with distance down the slope, it can be clearly seen that the amplitudes of oscillations decay with increasing x. This is because the flow becomes internally super-critical as well as due to the more frequent wave activities that overtake as x increases; a finding that agrees with what we obtained earlier in the FFT. The same finding can be observed with the component C6, which we relate to the release events of the lumps of the lower layer fluid, although they persist for longer distances. While those two modes decay in time and space, the other two modes (C5 and C4), which reflect the K-H instabilities, seem to grow. For instance in C4, the amplitudes grow abruptly at $x = 5$ cm as the sub-maximal regime starts and frequent organized K-H instabilities start to dominate the wave modes. Also the amplitudes are clearly minimal at $x = 0$ since it is the source at which the two sets of waves propagating upstream and downstream are initially generated.

The Hilbert power spectrum of the original time series at the location ($x = 10$ cm) was generated and is shown in figure 2-23. It clearly indicates that most of the power is concentrated below the frequency of about 0.3 Hz, which justifies our exclusion of the high frequency components (C1 – C3) when reconstructing the signal in our earlier discussion. Since the high frequency components and the component C9 have no meaningful physical significance, we exclude them and further generate the Hilbert power spectrum of the re-constructed signal (C4 ... C8) along with its energy distribution (figure 2-24). The trend R was not included in this step as we know it reflects the trend of the data. This refines the spectrum and its energy distribution to better trace the behavior of each mode. It is obvious that the lowest frequency component (C8) degrades in power at about $t \approx 600$ s which marks the start of the sub-maximal regime. The component C6 is persistent at almost all times and only starts to fade at $t \approx 700$ s when the late K-H instabilities become the most dominant mode then. The energy distribution is relatively spread but it appears that the frequencies of 0.07 – 0.12 Hz (or periods of about 8 – 15 s) have the major contribution.

To better track the spectral power evolution of those components (C4 .... C8), we isolate each of them as shown in figure 2-25. It is obvious that there are relatively huge temporal fluctuations in the instantaneous frequencies especially for that of C8. However, the mean of these frequencies for C8 is about 0.0117 Hz (or 85.47 s), and clearly the power degrades at $t \approx 600$ s as

35

indicated earlier. The color bar which reflects the power embedded in the signal also indicates that the low-frequency mode has almost ½ of the power of the release events (C6 and C7) and about ¼ of the power contained in the K-H instabilities (C4 and C5). The mean of the frequency fluctuations for the other modes reads 0.0247, 0.0415, 0.0838, and 0.2085 Hz which corresponds to periodic times of approximately 40.5, 24.1, 11.9 and 4.8 s for C7 – C4, respectively. These values are in close agreement to those observed and measured previously through FFT, which justifies our matching of the modes to the IMF. The HHT has the advantage though that it tells us which mode has more power in addition to when and how the frequency or the amplitude changes.

To further appreciate the technique, we zoom-in to capture a smaller time interval within the sub-maximal regime when the regular K-H instabilities were generated. Figure 2-26 shows the reconstructed image of the interfacial fluctuations in Exp 1 at $x = 15$ cm for about 70 s, along with its corresponding HHT spectrum. It is obvious that there is a clear gradually uprising trend of the frequencies from about 0.10 to 0.33 Hz, which corresponds to periodic times of about 10 – 3 s. This is clearly reflected in the real time development of the K-H instabilities as shown in the image on top. The image also tells that the amplitude drops remarkably in time as the shear weakens. A decay of about ¼ happens to the amplitude over about a minute, while the lower layer maintains its thickness. The information on the frequency from figure 2-26 and on the speed of propagation of those instabilities from the wave characteristics' plot in figure 2-11 will be used to obtain the wavelength as will be discussed afterwards.

2.4.5 K-H instabilities and their characteristics

2.4.5.1 Generation conditions

Before investigating the generation conditions of the instabilities, it is of interest to see the overall temporal development of some parameters including δ, J, and the shear layer Reynolds number, R_e $(=\delta.\Delta U/\nu)$ in which ν is the kinematic viscosity. Figure 2-27 portrays how these parameters vary at the sill crest in Exp 1a. It is obvious that a change occurs around the transition from maximal to sub-maximal regimes. While δ has a mean value of about 2 cm within the maximal regime, it starts to fade gradually into the sub-maximal regime. The frequent spikes that are seen reflect the instants when instabilities occur thereby distorting and stretching the velocity profiles. With δ decreasing during the sub-maximal regime and J on the contrary increasing, it is concluded that the shear, ΔU, must be decreasing then, which agrees with the nature of this

36

regime. The effect of ΔU, being squared, on J would override that of δ. J as can be seen fluctuates about 0.1 during the maximal regime, and gradually increases within the sub-maximal regime. Given the decrease in both ΔU and δ within the sub-maximal regime, R_e is expected to decrease at a faster rate as reflected in figure 2-27.

Now to investigate the generation conditions of the K-H instabilities, various instantaneous horizontal velocity profiles prior to the generation of the late downstream K-H instabilities in the sub-maximal regime were used. Although these instabilities occur after our estimate for the maximal regime to end at $t \approx 600$ s, we expect that Richardson number J then will be a good representative for the generation conditions of K-H instabilities in two-layer flows. In fact, at those late times the flow rate has decreased and the three dimensional effects, an account of which is given in chapter 4, would be minimal, hence providing for ideal conditions to study such instabilities. For upstream to the sill crest, few instabilities were investigated during the maximal regime since within the sub-maximal regime no instabilities formed and the interface was stable. An optimized hyperbolic tangent profile was fit to the velocity data around the shear layer to estimate the shear layer thickness, δ, and the shear ΔU, hence the Richardson number, J. The instants and locations at which the instabilities were about to form were determined from the LIF images and the corresponding velocity profiles for one second prior to their generation were selected to obtain an average value for these parameters. A threshold least square error was set and only those profiles that achieved errors less than the threshold were used to obtain an average for those parameters.

Our measurements for δ and J are shown in figure 2-28 for numerous instabilities at different locations downstream to the crest in different experiments. Our estimates for η show δ/η is $O(10)$ whereas our measurements for δ read values ranging between $0.7 - 2.4$ cm. While Pawlak & Armi (2000) report δ ranging from $2.5-8$ cm along the same slope for g' of 1.75 cm/s^2, Morin *et al.* (2004) in their experiments with variable slope sill report δ to vary from $1.7 - 3.2$ cm, which overlap with our measurements. Our J data on the other hand shows that K-H instabilities were generated at $J = 0.04 - 0.22$. These values are considerably higher than the theoretical predictions of Haigh & Lawrence (1999) for parallel flows. The spatial variation of J along the sill shows a decaying trend, which agrees with Pawlak & Armi (2000) although they report values relatively higher than our measurements. With the measurements of δ indicating almost a constant value of about 1.3 cm with x, however the scatter of the data, it is not surprising to see J decaying with distance since a spatially accelerating flow will impose an increasing velocity shear (ΔU) with x (recall figure 2-8). This contradicts though with the trend reported by Morin *et al.* (2004) for J to increase down the slope. It is noticeable that our measurements in Exp 1a are

37

somewhat lower than those in Exp 1 and 2. This is referred to the difference in spatial and temporal resolution among the different experiments. With Exp 1a having higher spatial resolution and lower sampling frequency, its measurements are more credible. Upstream to the sill crest, δ has values ranging from 1.5 – 3.2 cm, while J varies between 0.12 and 0.22.

It is of interest now as well to investigate J within the sub-maximal regime when no instabilities were generated. This may answer the quest at what J the instabilities will not form in such a flow setup. Five locations upstream to and including the crest were selected to evaluate J at which instabilities were suppressed. The five locations are: 0, -3, -6, -9 and -11 cm. Velocity profiles at the time of about 14 minutes and later were selected and again an optimal hyperbolic function was fit to the data around the shear layer. It is obvious in figure 2-29 that J was about 0.24 at the crest in Exp 1 and had an uprising trend as we move further upstream to J of as high as 0.56. The decreasing shear (ΔU) for the increase in layer depths as we move further upstream from the crest explains the increasing trend of J. The shear layer thickness, δ, at that stage was a little higher than downstream the crest and had a value of approximately 2 cm on average. Downstream to the crest though, both δ and J appear to have similar values to when K-H instabilities were generated. It is not clear yet why the instabilities would not be generated at those late times even though the conditions would still be favorable. One possible parameter could be the vertical shift, d, between the density and shear layer centers.

Before investigating the shift though, it would be beneficial first to explore the temporal variation of J at sample locations down the crest. Figure 2-30a and 2-30b portray reconstructed images of the interfacial fluctuations in the late sub-maximal regime at $x = 8$ and 15 cm, respectively, in Exp 1a. The K-H instabilities are quite obvious in both images and the increase in the frequency of interfacial fluctuations is also notable as x increases. Equally important to note is the recession of the fluctuations and instabilities at $x = 8$ cm earlier than at $x = 15$ cm. At $t \approx 840$ s, no more K-H instabilities were generated at $x = 8$ cm, whereas they continue to form until $t \approx 875$ s for $x = 15$ cm. This confirms the phenomenon of the horizontal downstream shift of the point of generation of those instabilities as was presented earlier in the wave characteristics' plot in figure 2-11 for Exp 1.

The temporal variation of δ, J, and Re during the course of Exp 1a is shown in figure 2-31 for the location of $x = 8$ cm. Clearly during the generation of the instabilities, the measurements fluctuate as we saw earlier in figure 2-27 for $x = 0$ (crest) due to the stretching and distortion of the velocity profiles. However, the uprising trend in J that was found at the crest at later times, at which we think J was high enough not to favor K-H instabilities to be generated, is not remarkable at $x = 8$ cm. Rather it is noticeable that J stagnates at about 0.05 for $t \geq 840$ s, at

which time no more K-H instabilities were formed at this location ($x = 8$ cm). It is good to find an agreement of this time ($t = 840$ s) at which J almost attained a constant value and that at which no more instabilities were observed in figure 2-30a. Both δ and Re show a similar pattern to J although it appears there is a decaying trend in Re as the experiment evolves. Figure 2-32 shows a zoomed-in plot of the same parameters at $x = 15$ cm for $t = 600 - 885$ s. It is noticeable that the amplitude of fluctuations, especially in δ and Re, remarkably fades at $t \approx 850$ s. This is when the instabilities started to form at smaller amplitudes than at earlier times as can be depicted from figure 2-30b. There is also a noticeable correlation in the pattern of the data of the three parameters during the shown time span.

2.4.5.2 The vertical shift, d

To measure the vertical shift, d, between the density and shear layer centers, a grid fixed at the front glass wall of the tank was imaged through both the PIV and interface cameras in Exp 1a for the scaling of both the density and velocity profiles into real world co-ordinates. The scaling to real world co-ordinates was also done using the water depth as both the free surface and the bed profile appeared as white lines in the images with few pixels of thickness (typically 2-3 pixels). Over 15 instabilities that formed between $t = 760$ and 880 s at different locations down the incline were selected through the interface images and the instants prior to their generation were recorded. The corresponding velocity field data from the PIV set of images were identified and each pair of density and velocity field data were used to determine the density and shear layer centers, respectively. At $t > 870$ s, no more instabilities were observed within the field of view for a clear two-layer structure. Sample locations at those later times when no instabilities formed were also selected to investigate if the shift would change from when the instabilities were being generated. This was in attempt to answer the quest why the instabilities did not form at the later times even though J would be favorable (refer to figures 2-30, 2-31 and 2-32).

In estimating the shift, the density layer center was obtained from the density filed images by tracing the instabilities backwards in time until the images prior to their generation were obtained. In those images, the interface was very sharp and the density layer centers could be determined to the nearest pixel. The shear layer centers were obtained, on the other hand, by fitting an optimized hyperbolic tangent profile to the velocity data around the interface. In doing so, the original velocity profiles were first shifted by the mean velocity of the layers considering the velocity measurements away from the shear layer. The intercept of the optimized profile with the z-axis then provided the shear layer center's elevation. Figure 2-33 shows sample velocity

39

profiles at different locations down the slope with the optimized hyperbolic functions over-plotted. As can be seen, the velocity difference, ΔU, increases with distance down the slope and the accelerating flow field appears to stretch the velocity profiles in the stream wise direction; hence the shear layer thickness, δ, decreases.

The maximum velocity gradient, $\partial U/\partial z$, and the velocity difference, ΔU, were obtained from the optimized profile for the calculation of δ and the bulk Richardson number, J. Figure 2-34 presents the variation of δ and ΔU for 15 instabilities that were observed down the slope. While δ shows clearly a decreasing trend with x, some scatter in the data is obvious. For that, and to have reliable representation of δ, a linear function was fit to the data to be used when non-dimensionalizing the shift values of d into ϵ using ½ of the shear layer thickness $\delta/2$ (i.e. $\epsilon = d/(\delta/2)$). The velocity difference, ΔU, however, shows a consistent less-scattered increasing trend with x. The individual data points for δ and ΔU were used to estimate J as shown in figure 2-35a. Clearly, J decays with x as the effect of ΔU overrides that of δ in its calculation. The values of J, although on instantaneous basis, are in line with those in figure 2-28b and confirm that the instabilities were generated at larger values than 0.0461 as reported by Haigh and Lawrence (1999) for parallel flow. Figure 2-35b shows the elevations of the density and shear layer centers for the traced instabilities. It can be seen that generally the density layer center was displaced vertically downwards below the shear layer center, even though that the differences were really small in the order of 2-3 mm. It is to be mentioned that the data presented in figure 2-35b were obtained through using the water depth in the laser plane as a physical scale to convert to real co-ordinates. This provided more accurate and consistent results than using the grid, which was off the central plane of the laser in the channel. With the grid not positioned within the central laser plane, bigger errors with large scatter in the data when estimating the shift were obtained. Using the grid resulted in errors of about 15 pixels compared to 2-3 pixels when using the water depth. Ideally, the grid should be placed in the central plane and a single camera for both PIV and density field measurements should be used, preferably with a zoomed-in field of view around the density interface profile.

The shift, d, was computed then as the difference between the elevations of the density and shear layer centers with a negative value indicating a lower density center than a shear center. The values of d were non-dimensionalized into ϵ using ½ of the shear layer thickness $\delta/2$ (i.e. $\epsilon = d/(\delta/2)$) as stated previously. Figure 2-36 shows the measurements of the shift both prior to the generation of the instabilities and later at times when no instabilities would form. It can be seen, given the scatter in the data, that the majority of the data points show a consistent downward shift of the density interface below the shear layer center. With the exception of a few instabilities that

40

have $\epsilon \leq$ -0.5 and those which have $\epsilon >$ 0, the shift seems to be about -0.14±0.08. The measurements of the shift at the later times when no more instabilities were generated and the interface became stable are shown in figure 2-36b. It can be seen that almost all of the data points have a negative shift. Again excluding few points that have $\epsilon \leq$ -0.5 or $\epsilon >$ 0, the shift is on the average about -0.25±0.11. This suggests that at those later times the density interface became stabilized at lower elevations and dropped faster than the shear layer center. Although J is favorable for the generation of instabilities as we saw earlier in figures 2-31 and 2-32, no instabilities are formed. That ϵ almost doubled (from -0.14 to -0.25) suggests that it could be a reason for the instabilities not to form. Note that this is in line with the results of Haigh and Lawrence (1999) who indicated that for $\epsilon >$ 0.25, no K-H instabilities could be predicted for parallel flows. However, our measurements for J indicate that K-H instabilities are possible to occur at higher values than that of 0.0461 predicted by them for parallel flows. As stated earlier, higher resolution experiments preferably with a single camera for PIV and density fields are recommended to confirm the effect of the shift in accelerating flows.

2.4.5.3 The wavelength, λ

The wavelength, defined as the distance between two successive wave crests, can be estimated using a velocity scale, U, and a time scale, T, or a frequency, f (i.e. $\lambda = U/f$). While the frequency or time scale is clear and can be taken as the periodic time between two successive waves or their frequency of occurrence, the velocity scale can be chosen arbitrarily. Pawlak and Armi (2000) used the convective speed ($\Delta U/2$) as the velocity scale. They obtained wavelengths of as large as 40 cm in their wedge-flow setup at g' of 1.75 cm/s^2 and similar slope to ours. We rather find the interfacial speed of propagation, which can be obtained by tracing the instability and is reflected in the wave characteristics' plot in figure 2-11, physically more meaningful to use. Another velocity scale could be the mean of the depth-averaged velocities in the upper and lower layers defined by: $\overline{U}_d = \frac{1}{2}(\frac{q_1}{y_1} + \frac{q_2}{y_2})$, in which the flow rate per unit width, q, is obtained by integrating the upper and lower layers' velocity profiles. We use both velocity scales to estimate the wavelength, λ, in our experiments. Note that the convective speed ($\Delta U/2$) that Pawlak and Armi (2000) used in their wedge flow setup would provide remarkably higher values for λ in our exchange flow.

A zoomed-in detail of the wave characteristics' plot in the late times of Exp 1 is shown in figure 2-37. Clearly the characteristic lines show the accelerating flow field. The sample

41

location at $x = 15$ cm, which we used earlier to show the variation in frequency with time in figure 2-26, is selected to estimate the wavelengths. The wave speeds are the slopes of the wave characteristic lines at the respective times. The information from both plots (figures 2-26 and 2-37) were used to provide a first estimate for λ. On the other hand, the instantaneous velocity profiles between two successive instabilities were time-averaged over their inter-periodic time and the velocity scale ($\overline{U}_d$) was used to provide a second estimate for λ. The results are shown in figure 2-38 from which we report λ to vary between 4 and 16 cm, using the interfacial wave speeds as the velocity scale, in a decreasing fashion with time. These values could also be estimated from the wave characteristics' plot (figure 2-37) if we trace the distance between two successive wave-characteristic lines at any given time should the field of view and the spatial domain of the slope allow. This is shown by the horizontal dashed line between the two arrows at $t = 840$ s, which reads λ of about 15 cm. It is nice to see it agreeing with our calculation at the same time in figure 2-38. From figure 2-37, it is also depicted that the wavelengths decrease as time increases matching our data in figure 2-38. The wavelengths based on $\overline{U}_d$ are clearly underestimated when compared to observations. The instabilities marked (i – v) in figure 2-37 were selected to study their growth patterns and rates in what follows.

2.4.5.4 The growth patterns and rates

Five selective K-H instabilities, those marked (i – v) in figure 2-37, from Exp 1 were traced to investigate their growth. Density field images digitized at the rate of 5 Hz were used to trace their temporal development as they traveled down the incline. Those instabilities were carefully selected where no pairing occurred to be representative of typical individual K-H instabilities. An algorithm similar to the one previously presented to identify the density interface was implemented to detect the upper and lower density interfaces that would encapsulate the instabilities. The threshold gray scales and gradient conditions were modified to match the observed instability as it grew in time. Figures 2-39 (i – v) show sequences of images reflecting those selected instabilities.

Two main patterns for the growth of those instabilities could be recognized. Pattern I: in which the instability would gradually grow in size until it attains a maximum amplitude after which it will stretch in the stream wise direction until it collapses and is washed away or entrained into the lower high momentum stream. Pattern II: in which the instability would continuously grow in size and amplitude until its braid becomes very thin when it will detach or pinch-off into the upper lower momentum stream. Figures 2-39: i, iii, iv and v portrays pattern I,

42

while figure 2-39ii shows pattern II. The upper and lower density interfaces are over-plotted in all images and seem to pretty well capture the instabilities. It is noteworthy mentioning that at the early times of the birth of the instability, it is sometimes difficult to decide upon its size, and where needed an eye judgment may interfere to observe a zoomed-in view of the pixels. The difference between the upper and layer interfaces that encapsulated the instability was used to estimate its size. It basically represents the area of the instability, A. A representative length scale, defined as the square root of the area, $\sqrt{A}$, was used to track the growth of the billows. Because of the different growth patterns of those instabilities, it would be more meaningful to measure the amplitude, H, being the maximum difference between the upper and lower interfaces that would envelope an instability. Both the size represented by $\sqrt{A}$ and the amplitude, H, would provide full picture of how the instability grows.

Figures 2-40 (i – v) show typical growth curves over the lifespan of the 5 instabilities. The horizontal axis represents the time of the growth of the instability with respect to its moment of birth as a starting moment. Figure 2-40i portrays the growth curve for pattern I. In figure 2-40i:a it can be seen that the size of the instability increases continuously with time in an initial exponential fashion at a faster growth rate followed by a later slower rate. Figure 2-40i:b portrays the corresponding development in the amplitude, H, in which there is a similar initial period with exponential growing fashion followed by a linear growth rate until the amplitude attains its maximum value. At this stage, stream wise vortex stretching starts to dominate with the amplitude kept constant. Later, the instability starts to collapse with linear decaying amplitude until it breaks and gets entrained into the lower layer. The late rising amplitude after about the 6th second is due to the downstream effect of an intermediate layer that caused the instability to accumulate as can be seen in figure 2-39i (image h).

The growth development of pattern II is reflected in figure 2-40ii which corresponds to instability ii. The same pattern of the growth in size, $\sqrt{A}$, can be seen (figure 2-40ii, a). However, the amplitude, H, although experiencing the same initial exponential growth which is followed by a linear one, does not reach a constant step but rather increases monotonically until the instability pinches off. The remaining three instabilities (iii – v) follow primarily pattern I, even though there are minor deviations due to some changes in the flow field. For instance instability iii experienced a delayed initial exponential growth in its amplitude H (refer to figure 2-40iii, b). A closer look into figure 2-39iii (images a – d) reveals the existence of an earlier neighboring instability downstream to instability iii. This is within the same spatial spans as those for instabilities i and ii in figures 2-39ii and 2-39iii, when no close downstream instability would affect them though. Instability iii was affected by the close downstream earlier instability in that

43

it was initially stretched with its size growing but its amplitude almost constant. Only after the 2nd second that its amplitude started to grow exponentially. It is also noticeable that the exponential growth period of the amplitude, H, seems to last for about 3 seconds as can be seen from the growth of all five instabilities. Instability iv shows the typical pattern I growth that was described earlier (see figure 2-40iv). Back tracing the images of figure 2-40iv, it is obvious that after the 7th second, the instability got distorted and it is obvious that the increase in amplitude shown in figure 2-40iv after that time is not real. Instability v has a typical pattern I growth (see figure 2-40v). It is noteworthy mentioning that the same amplitude growth pattern I which is characterized by the initial monotonic exponential growth followed by a leveling off saturation level is also reported in a theoretical study on non-linear spatial stability analysis in incompressible flows as was discussed by (Ladeinde & Wu, 2002) in their figure 2.

To estimate the initial growth rate of the amplitude of the instabilities, an optimized exponential function was fit to the initial set of data points prior to the successive linear portion. The initial growth rates of instabilities i – v were estimated as 1.76, 1.65, 1.99, 2.33 and 1.61 mm/s, respectively. An overall linear growth rate over the whole life time of the instabilities was also estimated from the growth curves of their sizes, $\sqrt{A}$, and found to be 3.11, 5.04, 3.03, 3.57 and 3.73 mm/s for instabilities i – v, respectively. An overall look at those instabilities suggests that they attained maximum amplitude that ranged between 19 and 28 mm. The initial exponential amplitude growth would last for about 3 s, followed by the linear growth phase lasting for 1 – 3 s after which the amplitude would level off for about 3 s in the case of pattern I. The maximum size of the instability, $\sqrt{A}$, would range between 28 and 35 mm.

2.5 DISCUSSIONS

For two-layer parallel flows with $\delta/\eta > 2.4$ and zero shift $(d=0)$, Haigh and Lawrence (1999) predicted that K-H instabilities will be generated when the bulk Richardson number $J < 0.071$. However, they showed that when $0.0461 < J < 0.071$, Holmboe instabilities have a larger growth rate. Our estimates for δ and η provide $\delta/\eta \approx 10 >> 2.4$. Additionally, J varies in our experiments as 0.05 - 0.12 in Exp 1a which had a good enough spatial resolution and sampling frequency for the measurements to be precise. These J values are significantly larger than those predicted for parallel flows. Our estimates for the shift, ϵ, and prior to the generation of instabilities, are on the average 0.14±0.06. At later times into the sub-maximal regime, ϵ seems to have increased to about 0.25±0.11 and no instabilities were observed even though J was favorable. This is in line

with Haigh and Lawrence (1999) who did not predict any K-H instabilities when the shift was larger than 0.25. On the other hand, Pawlak and Armi (2000) observed large scale K-H instabilities in their accelerating wedge flow at J = 0.08 – 0.33, which is well above the upper limit of 0.071 predicted earlier for J by Haigh and Lawrence (1999). However, their flows had $\delta \approx \eta$, which is remarkably different from our flows. They based their estimates though for J, δ, and η on time-averaged velocity and density profiles, which we think is not appropriate for this kind of study. Even with the consideration of the factor of 3 that Morin *et al.* (2004) reported to overestimate J when using time-averaged measurements, the modified J values for Pawlak and Armi's (2000) flows would still be higher than for parallel flows.

Our measurements and observations of upstream and downstream propagating K-H instabilities can be compared to the two modes that Pawlak and Armi (1998) reported in their spatial linear stability analysis. That Pawlak and Armi (1998) had hydraulically controlled wedge flow with the upper layer almost dynamically inactive prevented the realization of the upstream propagating mode in the experiments. Although their slower growing mode propagated downstream, which matches with our observations of the instabilities down the incline, they reported that such mode had less significant bias into the higher momentum stream. Our measurements of the shift indicate though that downstream propagating instabilities could have shifts in both streams. Pawlak and Armi's (1998) stability analysis considered parallel flow with the assumption that acceleration would not significantly affect the nature of possible modes. We think that further research is needed to expand the linear stability theory to include the effect of acceleration.

The downstream horizontal shift of the point at which the late K-H instabilities in the sub-maximal regime were generated down the incline is a unique phenomenon. It could be explained though in terms of the spatial acceleration of the flow field and the continuous decaying flow rate. Given that the changes in the lower layer depths in the late sub-maximal exchange were negligible, the decay in flow rate as time elapses will require the fluid to travel longer distances down the slope to reach high enough shear for Richardson number, J, to be favorable for the instabilities to be generated. Upstream to the sill crest, J increases remarkably as a result of the decay in the flow rate resulting in a weakened shear and a stable interface. As stated previously, at later times into the sub-maximal regime no K-H instabilities were observed down the slope. We think the increase in the shift, ϵ, could be a reason. No signatures of other types of instability, like Holmboe instability for example, could form either at those late times even though the conditions were favorable. Zhu and Lawrence (2001) reported on Holmboe instabilities to have occurred when $\epsilon \approx 0.25$, but within the sub-critical flow region upstream to

45

the sill crest. We think that the stability of the flow should be studied along with the hydraulics to have a complete picture of the phenomenon.

Considering the wavelength λ, an estimate of the most unstable wavelength for parallel horizontal stratified shear flow may be: $\lambda = 7.5\ \delta$ (Turner, 1973). Note that the most unstable wavelength is insensitive to the precise shape of density and shear profiles (Farmer and Armi, 1999). In our experiments, with δ varying from about 0.8 - 1.8 cm down the incline, λ would vary as 6 – 13.5 cm along the sill. These values are relatively in line compared to our observations and measurements in figure 2-38 based on the interfacial wave speed obtained from the wave characteristics' plot as a velocity scale. It is worth considering then to compare our results to those of Pawlak and Armi (2000) where their accelerating wedge flow had g' of 1.75 cm^2/s, pretty close to our Exp 1 and 1a. Their measurements for a constant slope of 10.8° over a length of about 80 cm show wavelengths varying from about 7 cm at the crest to 40 cm at the end of the slope (refer to their figure 10). This increasing trend in wavelength down the slope is contradicting with our trends that down the sill the instabilities occur at higher frequencies resulting in shorter wavelengths.

The growth rates of shear instabilities in parallel stratified flows were discussed theoretically and experimentally (Turner, 1973). Scotti and Corcos (1969) found that the growth rate could be described by $0.5k\delta c_i \approx 0.1$, where k is the wave number ($k = 2\pi/\lambda$) and c_i is the non-dimensional growth rate normalized by the shear ΔU. Based on mean values of the shear along the sill, we get a growth rate c_i for Exp 1 of about 15 mm/s. This estimate is remarkably higher compared to that obtained earlier from our measurements.

While it is often argued that interfacial mixing is caused by the instabilities that are generated along the density interface when they break, we would like to point out that in accelerating flow fields as that presented here down the incline this effect is only temporarily. The super-critical nature of the flow down the sill would always act to wash out any mixing layer and entrain it into the lower higher momentum stream. Mixing does persist though beyond the toe of the sill causing an intermediate layer that is dynamically almost inactive. It experiences circulation and progresses upstream as the flow evolves and only at very late times that it overtops the incline when basically there is almost no flow anymore.

During the steady maximal exchange, our results for the interfacial entrainment confirmed those obtained earlier by Morin et al. (2004). It has been shown that the entrainment coefficient of such flows is significantly higher than that of a plane turbulent wall jet. We believe the cause of such high entrainment capacity is the breaking of the large scale down slope interfacial waves that were a dominant feature in all experiments. It has been experimentally proven that such

46

large scale structures were dominant even at higher values of g'. Exp 4, with g' reaching ≈ 18 cm/s^2, proves that Reynolds number does not seem to be significant for those large scale structures. This is unlike what one would expect when the flow is highly turbulent at such high density differences. The narrow width of the channel may have its effect on the computations of the flow rate per unit width, q, since the boundary layer thickness would decrease the effective width of the channel. However, because of the short span of ≈ 30 cm down the topography, it is less likely that the boundary layer thickness would change significantly. The entrainment coefficient, α_e, would still be much higher than turbulent wall jets. The following chapter estimates how the boundary layer thickness varies along the reach upstream of the sill crest.

While it has been shown that those large scale down slope breaking waves were predominantly generated in events of release of lower layer fluids due to relaxation of the density interface after it reached a climax elevation following the development of K-H instability above the crest, that similar frequencies to those events were measured upstream to the sill crest is worth further investigation. The repeated concurrence of the generation of two K-H instabilities at either side of a central instability at the sill crest (refer to figure 2-5: images c, k, and x), when the piling of the lower layer and the rise of the interface occur subsequently, brings into mind a notion of harmonic behavior. The results in figures (2-17, 2-19) might indicate that the low frequency oscillation, f_o, at the sill crest is at a factor of 3 when compared to that of the large scale down slope breaking waves, f_l. Further studies might explore such ideas.

With regards to boundary layer separation, repeated observations of movies of the PIV experiments indicated that there might be some flow separation very close to the boundary within the shallowest 2-3 mm. The PIV tracer particles seem to reflect some sort of saltation close to the bed down the slope. These motions are, however, suppressed by the lower layer flow and can highly unlikely be thought of as the cause of the interfacial instabilities. We believe that the generated instabilities are purely due to interfacial shear. Figure 2-5 presenting a snap shot of sample instantaneous velocity profiles, and figure 2-7 that shows the time-averaged velocity fields both indicate clearly that the streamlines are very much adhering to the bed. We do not think there is any clear boundary layer separation which would be considerable.

The oscillatory motion at the sill crest and the continuous rising of the lower layer upstream to the crest followed by a subsequent release and formation of large scale breaking waves may also draw into consideration analytical formulations of the phenomenon based on the energetics of the flow. An exchange of potential to kinetic energy during the maximal regime along the topography is another point that needs to be addressed. While this motion might be thought of in terms of 'upstream influence' as suggested by Baines (1977), we think it is rather due to an

47

instability that forms at the sill crest where the mean flow speed almost vanishes; hence the instability stalls but grow bigger in amplitude until the interface reaches a climax elevation. The subsequent release of the lower layer fluid would cause the instability to travel at the mean flow speed, now that it is more affected by the lower layer as the interface drops down. The instability develops into large scale structures as it advects down the slope. It temporarily separates from the lower layer, entrains chunks of the upper layer fluid then breaks and merges with the lower layer inducing high momentum into the stream.

2.6 SUMMARY AND CONCLUSIONS

A detailed experimental laboratory study was conducted to investigate interfacial waves and instabilities in two layer spatially accelerating exchange flows over bottom topography at its lee side. The experiments provided a unique opportunity to study different phenomena under conditions of maximal and sub-maximal exchange. A new finite-amplitude mechanism through which large scale down slope breaking interfacial waves are formed within the maximal regime is described. In this mechanism, low frequency shear-generated K-H instabilities develop along the sharp density interface above the crest of the topography. The growth of these instabilities causes the interface to rise up; hence the lower layer accumulates upstream to the crest in an exchange of kinetic to potential energy process. In the ascend phase of the interface, symmetric more frequent K-H instabilities would form at either side of the central stalling instabilities above the crest. While these instabilities propagating downstream would grow large in amplitude, those traveling upstream are of finite amplitude and get squeezed due to the shallow accelerating lower layer. As the interface reaches a climax elevation above and upstream to the crest, it relaxes resulting in the release of bulk fluids of the lower layer. In this descending phase above the crest, the lower layer becomes shallower than the upper layer and the quasi-stalling instabilities would subsequently shift downwind the crest. The release of bulk fluids of the lower layer then causes these instabilities to grow remarkably big into a large scale interfacial breaking wave. Those large scale waves have steep fronts atop of which parasitic K-H instabilities would form and the whole cluster would engulf chunks of the upper layer, overturn then break resulting in significant interfacial entrainment. Temporary intensive mixing layer would form but the accelerating flow field would wash it out and a fresh sharp interface will form in the wake of those structures. The cycle repeats and the phenomenon was observed in all experiments covering a range of g' that varied between about 1.6 and 18 cm/s^2.

48

Large entrainment coefficients of about 0.1 on average were estimated. This is almost three times as big compared to the plane turbulent wall jet. An increase in the flow rate of up to 40% of its value at the sill crest occurred over a distance of about 30 cm. The entrainment coefficient gradually increases in the near field downstream to the sill crest where the large scale waves and instabilities are generated. Further downstream, the coefficient drops since the waves are simply transported without breaking and therefore cause no more significant entrainment.

During the sub-maximal regime, the interface becomes less fluctuating at and upstream to the sill crest. The cyclic process described above could still be observed although less significant. The fluctuations gradually fade and in the late sub-maximal regime the interface becomes almost leveled upstream to the topography. No K-H instabilities are observed at the sill crest. At the downstream side though, frequent K-H shear instabilities are generated along the interface and their generation location constantly shifts down the slope.

The results indicate that K-H instabilities are generated at bulk Richardson number, $J \cong 0.05$ - 0.12, with a downward shift of the density interface from the shear layer center, ϵ, within 0.14 ± 0.06. Theoretical results by Haigh and Lawrence (1999) for parallel horizontal flows do not predict K-H instabilities for flows with a sharp density interface when it is shifted from the shear center. In their study, they had an upper limit for J of about 0.071 for the case of zero shift, although they indicated that when $0.0461 < J < 0.071$ Holmboe instabilities have larger growth rates. Cross correlation of the interface positions' time series during the maximal exchange regime indicated that those instabilities propagated at the mean flow velocity; hence had zero phase speed in concurrence with the existing knowledge. Two growth patterns were observed for the late instabilities in the sub-maximal regime: a) pattern I, in which the instability grows initially exponentially then levels off and experience stream wise vortex stretching until it is entrained into the lower layer, and b) pattern II, in which the instability would grow continuously until it pinches off into the upper layer. Our measurements for the growth rate were much smaller (a factor of 8) than predictions based on parallel flow assumption. Estimates based on parallel flow for the wavelengths were in line though with our measurements. A wave characteristics' plot which described the characteristics of the different interfacial waves in the course of an experiment was generated. The plot showed a gradual horizontal downstream shift in the point at which the late K-H instabilities first occurred.

Spectral analysis of the interface positions' and velocity time series using both FFT and HHT were in good agreement with observations. The application of HHT proved beneficial in tracing the interfacial fluctuations and the evolution of the different frequency modes.

REFERENCES

AFANASYEV, Ya. D. & PELTIER, W. R. 2001a On breaking internal waves over the sill in Knight Inlet. *Proc. Royal Society of London, series* A **457**, 2799-2825.

AFANASYEV, Ya. D. & PELTIER, W. R. 2001b Reply to comment on the paper 'On breaking internal waves over the sill in Knight Inlet'. *Proc. Royal Society of London, series* A **457**, 2831-2834.

ALAVIAN, V., JIRKA, G. H., DENTON, R. A., JOHNSON, M. C. & STEFAN, H. G. 1992 Density currents entering lakes and reservoirs. *Journal of Hydraulic Engineering* **118**, 1464.

ALTINAKAR, M. S., GRAF, W. H. & HOPFINGER, E. J. 1992 Flow structure in turbidity currents. *Journal of Hydraulic Research* **34** (5), 713.

ARITA, M. & JIRKA, G. H. 1987 Two-layer model of saline wedge I: entrainment and interfacial fristion. *Journal of Hydraulic Engineering* **113**, 1229-1248.

ARMI, L. & FARMER, D. M. 1988 The flow of Mediterranean water through the Strait of Gibraltar. *Progress in Oceanography* **21**, 1-105.

BAINES, P. G. 1977 Upstream influence and Long's model in stratified flows. *J. Fluid Mech.* **82**, 147-159.

BAINES, P. G. 1995 Topographic effects in stratified flows. 1st edition, Cambridge University Press, New York, USA.

BAINES, P. G. 2001 Mixing in flows down gentle slopes into stratified enviroenments. *J. Fluid Mech.* **443**, 237-270.

BARINGER, M. O. & PRICE, J. F. 1997 Mixing and spreading of the Mediterranean outflow. *Journal of Physical Oceanography* **27**, 1654.

BINDHU, C. V., HARILAL, S. S., NAMPOORI, V. P. N. & VALLABHAN, C. P. G. 1999 Solvent effect on absolute fluorescence quantum yield of Rhodamine 6G determined using transparent thermal lens technique. *Modern Physics Letters B*, Vol. **13 (16)**, 563-576.

BRAY, N. A., OCHOA, J. & KINDER, T. H. 1995 The role of the interface in exchange through the Strait of Gibraltar. *J. Geophys. Research* **100** (C6), 10,755-10,776.

BROWN, G. L. & ROSHKO, A. 1974 On density effects and large structure in turbulent mixing layers. *J. Fluid Mech.* **64**, 775.

CLARK, T. L. & FARELY, R. D. 1984 Severe downslope windstorm calculations in two and three spatial dimensions using anelastic interactive grid nesting: A possible mechanism for gustiness. *J. Atmos. Sci.* **41**, 329.

50

CUMMINS, P. F., VAGLE, S., LAURENCE, A. & FARMER, D. M. 2003 Stratified flow over topography: upstream influence and generation of non-linear internal waves. *Proc. R. Soc. Lond.* A **459**, 1467-1487.

DALLIMORE, C. J., IMBERGER, J. & ISHIKAWA, T. 2001 Entrainment and turbulence in saline underflow in Lake Ogawara. *Journal of Hydraulic Engineering* **127**, 937.

ELLISON, T. H. & TURNER, J. S. 1959 Turbulent entrainment in stratified flows. *J. Fluid Mech.* **6**, 423-448.

FARMER, D. & ARMI, L. 1986 Maximal two-layer exchange over a sill and through a combination of a sill and contraction with barotropic flow. *J. Fluid Mech.* **164**, 53.

FARMER, D. & ARMI, L. 1999 Stratified flow over topography: the role of small-scale entrainment and mixing in flow establishment. *Proc. Royal Society of London, series* A **455**, 3221-3258.

FARMER, D. & ARMI, L. 2001 Stratified flow over topography: models versus observations. *Proc. Royal Society of London, series* A **457**, 28272830.

HAMBLIN, P. F. & LAWRENCE G. A. 1990 Exchange flows between Hamilton Harbour and Lake Ontario. *Proc. of 1990 Annual Conf. of Canadian Society for Civil Eng.* V, 140-148.

HAIGH, S. & LAWRENCE, G. A. 1999 Symmetric and non-symmetric Holmboe instabilities in an inviscid flow. *Phys. Fluids* **11**, 1459-1468.

HOGG, A. McC., WINTERS, K. B. & IVEY, G. N. 2001 Linear internal waves and the control of stratified exchange flows. *J. of Fluid Mech.* **447**, 357-375.

HUANG, N. E., LONG, S. R. & SHEN, Z. 1996 The mechanism for frequency downshift in non-linear wave evolution. *Adv. Appl. Mech.* **32**, 59-111.

HUANG, N. E., SHEN, Z., LONG, S. R., WU, M. C., SHIH, H. H. et al. 1998 The empirical mode decomposition and the Hilbert spectrum for non-linear and non-stationary time series analysis. *Proc. Royal Society of London, series* A **454**, 903-995.

HUANG, N. E., SHEN, Z. & LONG, S. R. 1999 A new view of nonlinear water waves: The Hilbert spectrum. *Annu. Rev. Fluid Mech.* **31**, 417-457.

HUANG, N. E., WU, M. C., LONG, S. R., SHEN, S. S. P., QU, W. et al. 2003 A confidence limit for the empirical mode decomposition and the Hilbert spectral analysis. *Proc. R. Soc. London Ser. A* **459**, 2317-2345.

LADEINDE, F. & WU, J. 2002 Second order non-linear spatial stability analysis of compressible mixing layers. *Physics of Fluids* **14** (9), 2968-2986.

LAMB, K. G. 2004 On boundary-layer separation and internal wave generation at the Knight Inlet sill. *Proc. Royal Society of London, series* A **460**, 2305-2337.

51

LAWRENCE, G. A., BROWAND, F. K. & REDEKOPP, L. G. 1991 The stability of a sheared density interface. *Phys. Fluids* A **3** (10), 2360-2370.

LAWRENCE, G., PIETERS, R., ZAREMBA, L., TEDFORD, T., GU, L., GRECO, S. & HAMBLIN, P. 2004 Summer exchange between Hamilton Harbour and Lake Ontario. *Deep-Sea Research II* **51**, 475-487.

LONG, R. R. 1955 Some aspects of the flow of stratified fluids, III. Continuous density gradients. Tellus 7, 341-357.

MARXEN, M. 1998 Particle Image Velocimetry in Stromugen mit staken Geschwindigkeitsgradienten, *Diplom Thesis*, Fakultat fur Physik und Astronomie, Ruprecht-Karls-Universitat Heidelberg, Germany.

MORIN, V. M. 2002 An Experimental Investigation of Interfacial Instabilities and Entrainment in Exchange Flow over a Smooth Sill. M.Sc. thesis, University of Alberta.

MORIN, V. M., ZHU, D. Z. & LOEWEN, M. R. 2004 Super Critical Exchange Flow Down a Sill. *J. Hydraulic Engineering* **130** (6), 521-531.

NAKOS, J. T. 1994 The prediction of velocity and temperature profiles in gravity currents for use in chilled water storage tanks. *Journal of Fluids Engineering* **116** (1), 83.

NASH, J. D. & MOUM, J. N. 2001 Internal hydraulic flows on the continental shelf: High drag states over a small bank. *Journal of Geophysical Research* **106**, 4593-4611.

NIELSEN, M. H., PRATT, L. & HELFRICH, K. 2004 Mixing and entrainment in hydraulically driven stratified flows. *J. Fluid Mech.* **515**, 415-443.

ORTIZ, S., CHOMAZ, J-M. & LOISELEUX, T. 2002 Spatial Holomboe instability. *Phys. Fluids* **14** (8), 2585-2597.

PARKER, G., GARCIA, M., FUKUSHIMA, M & YU, W. 1987 Experiments on turbidity currents over an erodable bed. *J. Hydraulic Research* **25**, 123-147.

PATNAIK, P. C., SHERMAN, F. S. & CORCOS, G. M. 1976 A numerical simulation of Kelvin-Helmholtz waves of finite amplitude. *J. Fluid Mech.* **73**, 215-240.

PAWLAK G. & ARMI L. 1998 Vortex dynamics in a spatially accelerating shear layer. *J. Fluid Mech.* **376**, 1-35.

PAWLAK G. & ARMI L. 2000 Mixing and entrainment in developing stratified currents. *J. Fluid Mech.* **424**, 45-73.

PELTIER, W. R. & HALLE, J. 1978 The evolution of finite-amplitude Kelvin-Helmholtz Billows. *Geophys. Astrophys. Fluid Dynamics* **10**, 53-87.

RAJARATNAM, N. 1976 Turbulent jets. Elsevier Publishing Co., Amsterdam and New York.

SCARANO, F. & RIETHMULLER, M. L. 1999 Iterative multigrid approach in PIV image processing with discrete window offset. *Experiments in Fluids* **26**, 513-523.

SCINOCCA, J. F. & PELTIER, W.R. 1989 Pulsating downslope windstorms. *J. Atmosph. Sci.* **46** (18), 2885.

SCORER, R. S. 1969 Billow mechanics. *Radio Science*, Volume 4, Number 12, 1299-1308.

SCOTTI, R. S. & CORCOS, G. M. 1969 Measurements on the growth of small disturbances in a stratified shear layer. *Radio Science*, Volume 4, Number 12, 1309-1313.

SUTHERLAND, B. R. 2002 Large-amplitude internal wave generation in the lee of step-shaped topography. *Geophysical Research Letters* **29** (16), art. no. 1769.

TEDFORD, E. W., LAWRENCE, G., and PIETERS, R. 2005 Interfacial Waves in a Laboratory Exchange Flow. *Proceedings of the 17th Canadian Hydrotechnical Conference,* CSCE, Edmonton, Canada.

THORPE, S. A. 1968 A method of producing a shear flow in a stratified fluid. *J. Fluid Mech.* **32**, 693-704.

THORPE, S. A. 1969 Experiments on the instability of stratified shear flows: immiscible fluids. *J. Fluid Mech.* **39**, 25-48.

THORPE, S. A. 1969 Experiments on the stability of stratified shear flows. *Radio Science* **4**, Number 12, 1327-1331.

THORPE, S. A. 1971 Experiments on the instability of stratified shear flows: miscible fluids. *J. Fluid Mech.* **46**, 299-319.

THORPE, S. A. 1973 Experiments on instability and turbulence in a stratified shear flow. *J. Fluid Mech.* **61**, 731-751.

THORPE, S. A. 1987 Transitional phenomena and the development of turbulence in stratified fluid: a review. *J. Geophys. Res.* **92**, 5231.

TURNER, J. S. 1973 Buoyancy effects in fluids. Cambridge University Press, New York, USA.

WEN, Y. K. & GU, P. 2004 Description and simulation of nonstationary processes based on Hilbert spectra. *J. Engineering Mech.* **130** (8), 942-951.

WINANT, C. D. & BROWAND, F. K. 1974 Vortex pairing: the mechanism of turbulent mixing-layer growth at moderate Reynolds number. *J. Fluid Mech.* **63**, 237.

WILKINSON, D. L. & WOOD, I. R. 1983 The formation of an intermediate layer by horizontal convection in a two-layered shear flow. *J. Fluid Mech.* **136**, 167.

ZHENG, Q., SHEN, S. S. P., YUAN, Y., HUANG, N. E., KLEMAS, V. et al. 2004. Evidence of the coexistence of upstream and downstream solitary wavetrains in the real atmosphere. *Int. J. Remote Sensing* **25** (21), 4433-4440.

53

ZHU, D. Z. & LAWRENCE, G. A. 2001 Holmboe's instability in exchange flows. *J. Fluid Mech.* **429**, 391-409.

ZHU, D. Z. 2002 Control curves for two-layer flows. *J. of Hydraulic Engineering*, ASCE, **128**(1), 113-116.

ZHU, D. Z., FOULI H. & OKYERE, Y. A. 2002 Exchange flow through an opening. *J. Hydraulic Research*, **40** (3), 341-350.
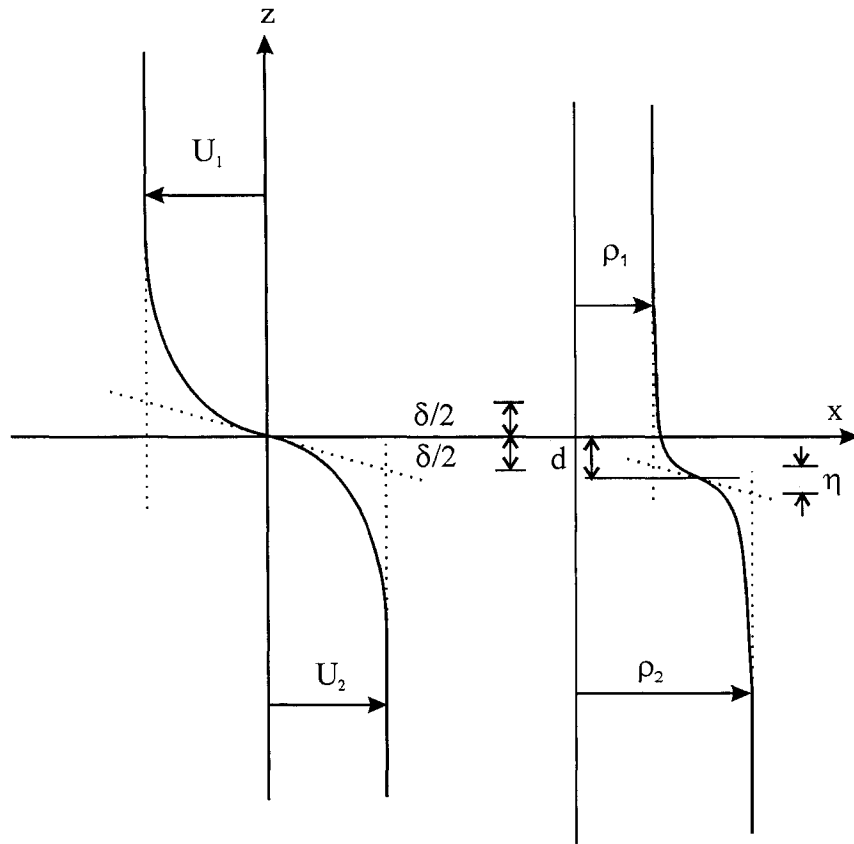
FIGURE 2-1. Definition diagram of velocity and density profiles in two-layer exchange flows. δ and η are the shear and density layer thickness, respectively. d is the vertical shift of the density interface from the shear layer center.
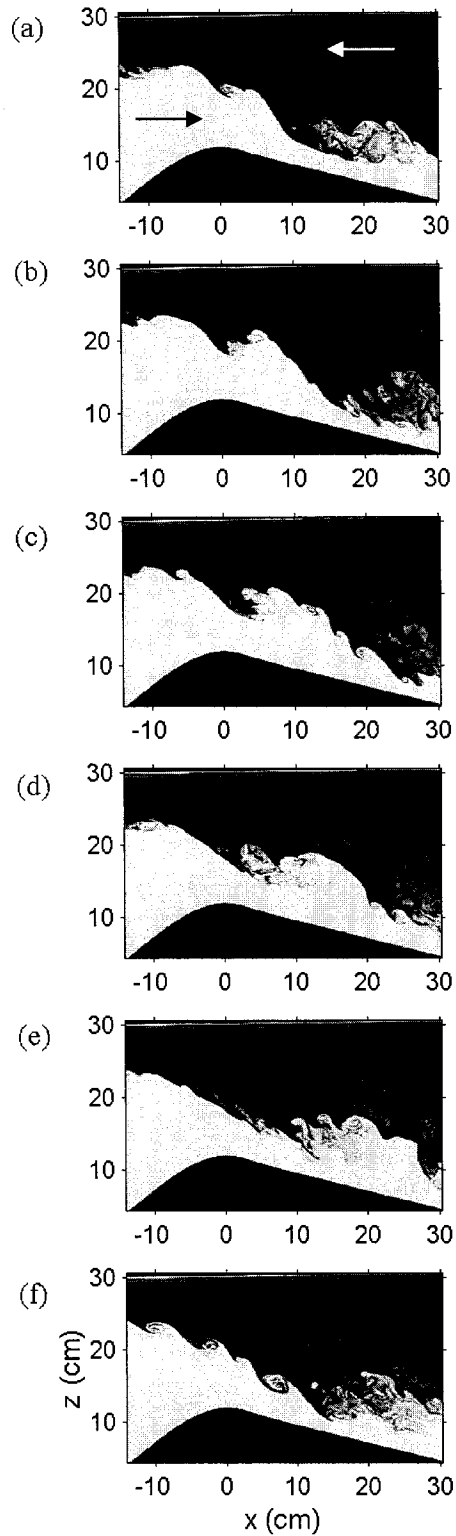
FIGURE 2-2. Sequence of images showing the frequent release of lumps of lower layer fluid during maximal exchange in Exp 1. The arrows indicate the flow direction in each layer. K-H instabilities are generated both on top of those release events as well as in their wakes and propagate in both directions. The images are 4 s apart.

56
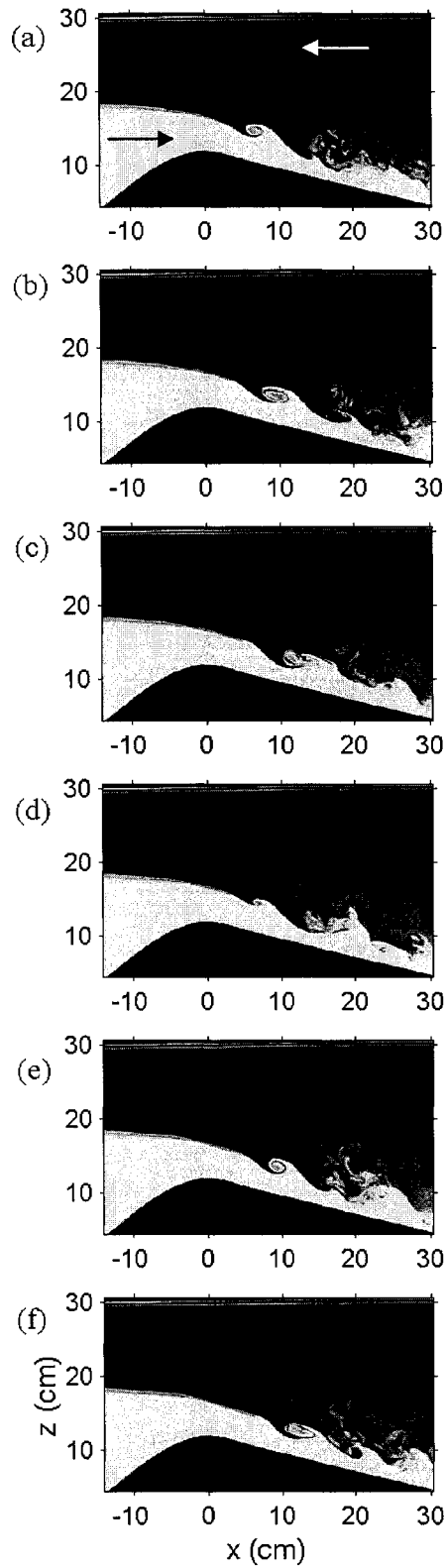
FIGURE 2-3. Sequence of images from Exp 1 showing the frequent and organized K-H instabilities that form in the late sub-maximal regime. The images are 14.5 minutes into the experiment and are 2 s apart. The subtle wave activity upstream to the sill crest is obvious.

57
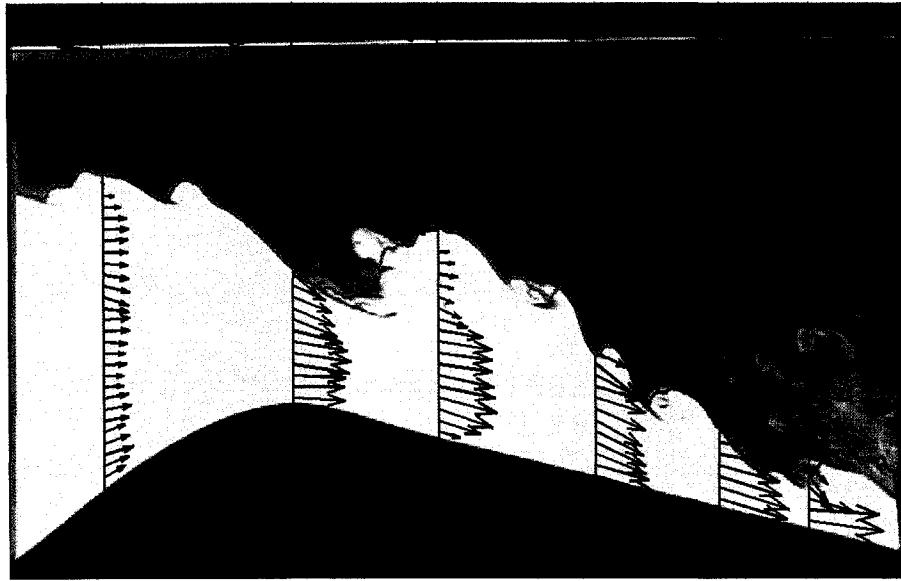
FIGURE 2-4. Instantaneous snapshot of the density field in Exp 1. The estimated density interface position and sample simultaneous velocity profiles are over plotted.

58
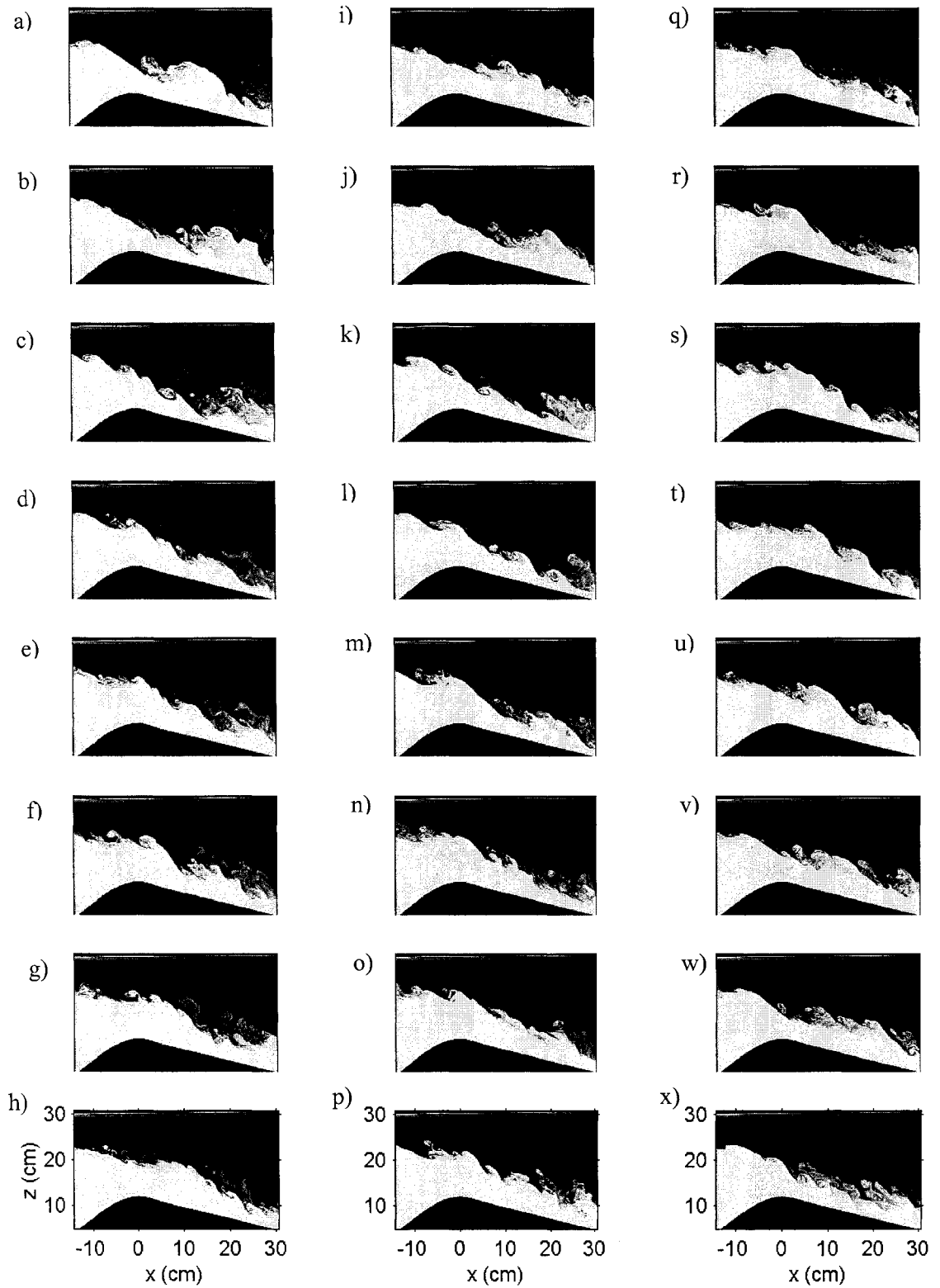
FIGURE 2-5. Two cycles of the oscillatory motion of the interface at the sill crest in Exp 1 and the associated instabilities and wave activities along the sill. Images are about 87 s into the experiment and are 4 seconds apart.

59
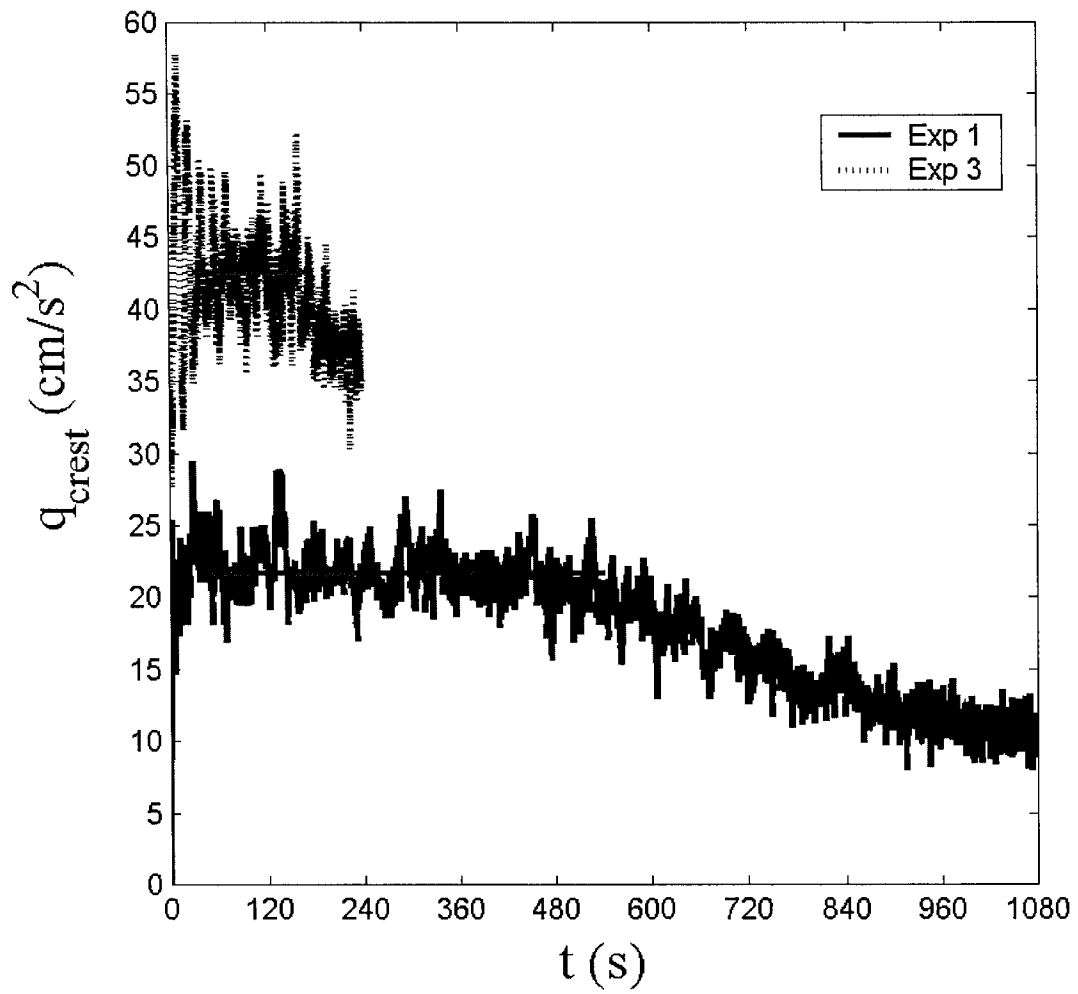
FIGURE 2-6. Time series of the flow rate per unit width, q, at the sill crest in Exp 1 and 3. The maximal and sub-maximal regimes are quite obvious.

60
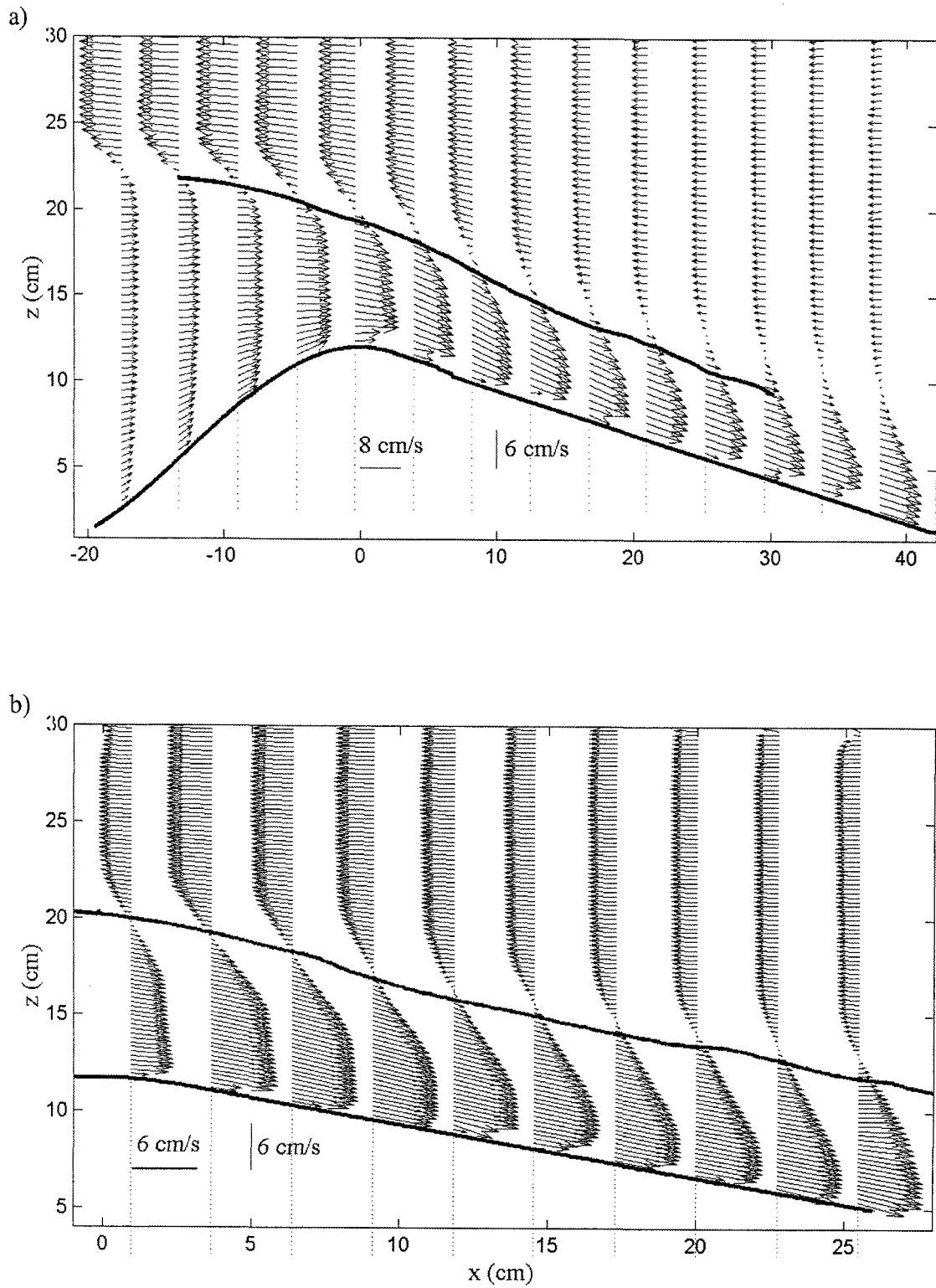
FIGURE 2-7. Sample velocity profiles time-averaged over the steady maximal exchange period along the topography in: a) Exp 2; and b) Exp 1a. The corresponding time-averaged density interface is over plotted.

61
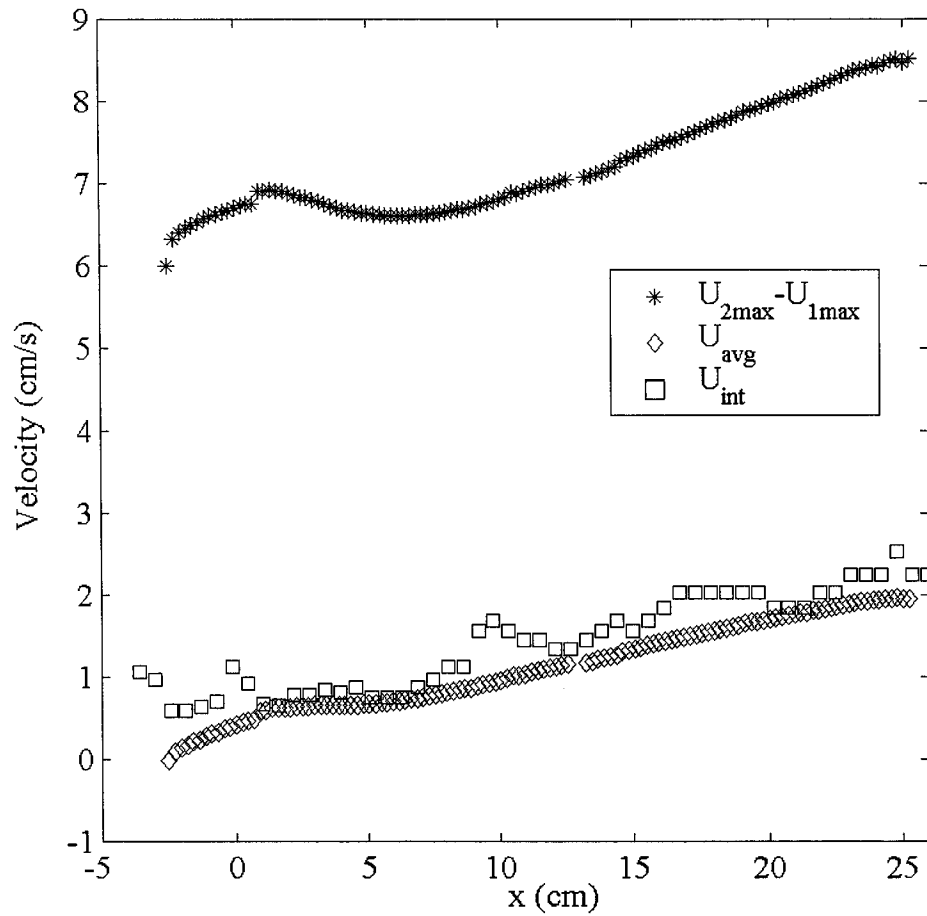
FIGURE 2-8. The spatial variation of the time-averaged velocity shear, ΔU; the average velocity, U_{avg}, and the interfacial wave speed, U_{int}, the latter obtained from cross correlating the interface positions' time series. Data are from Exp 1a.
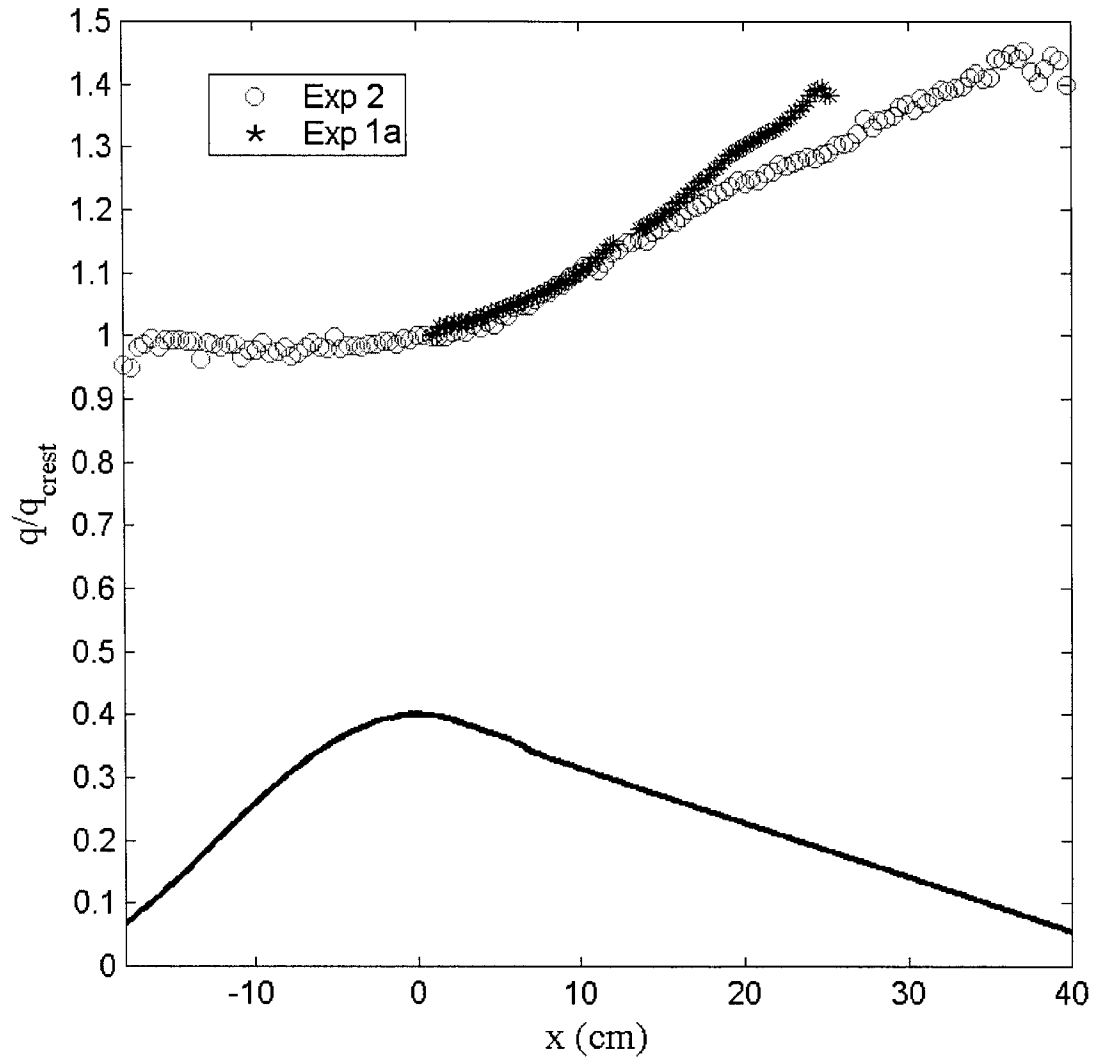
FIGURE 2-9. The spatial variation of the time-averaged upper layer flow rate intensity, q, with respect to its value at the sill crest in Exp 2 and 1a.

63
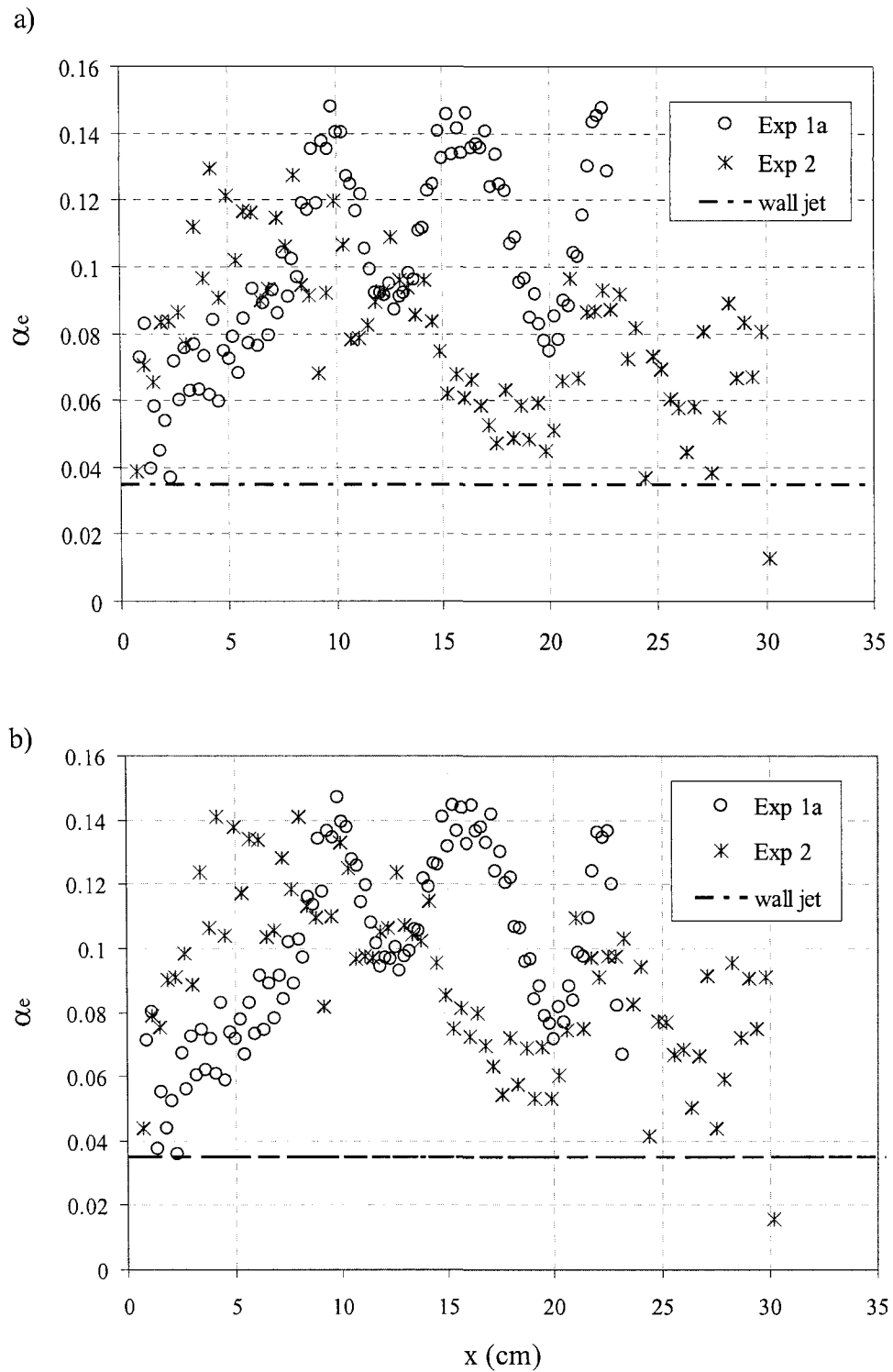
FIGURE 2-10. The spatial variation of the entrainment coefficient, α_e, based on time-averaged data over the steady maximal regime using two different representative velocities of the lower layer: a) using the average velocity; b) following the definition of Ellison and Turner (1959). The dashed line represents that of a plane turbulent wall jet (Rajaratnam, 1976).
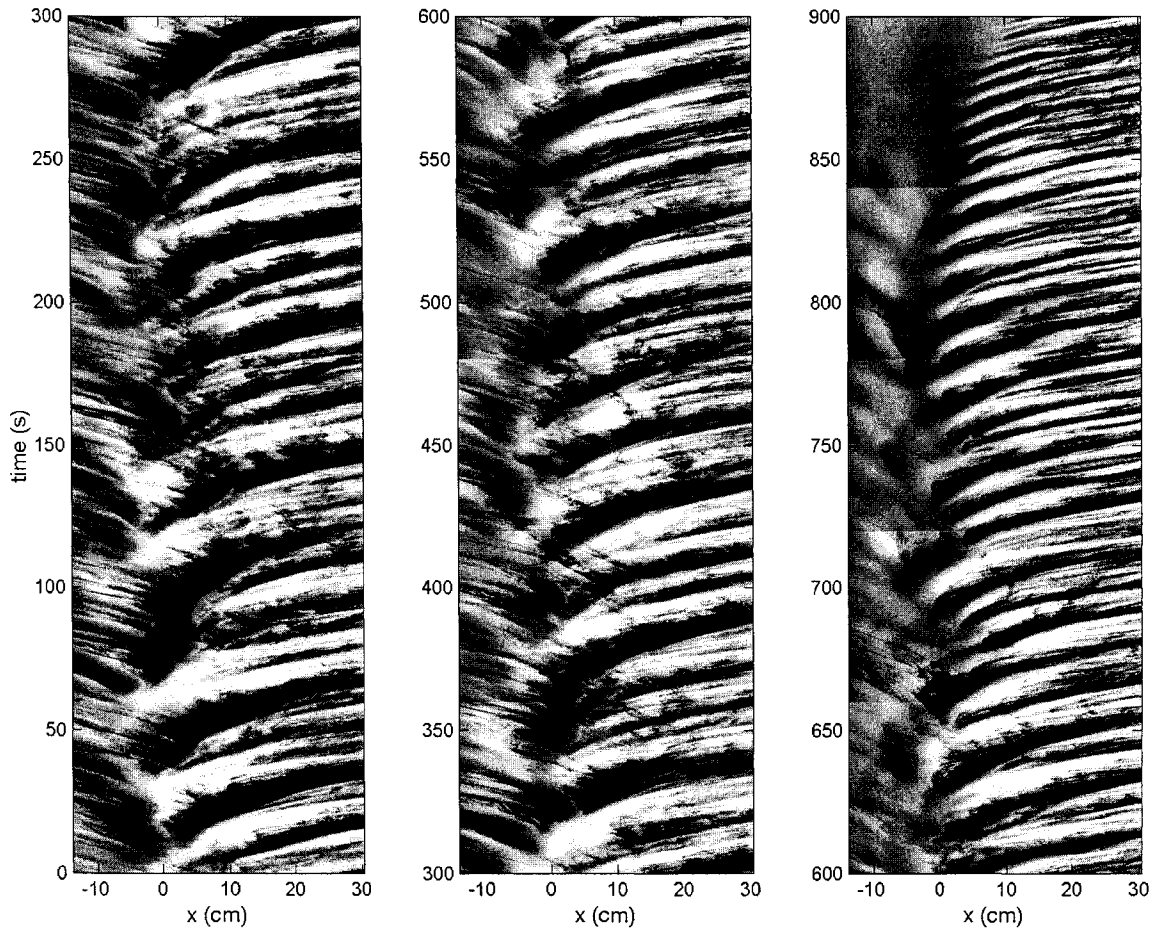
FIGURE 2-11. The wave characteristics' plot for Exp 1. The sill crest is at $x = 0$. Two sets of waves originate about the crest: upstream propagating small-amplitude waves, and downstream propagating large-amplitude ones. The two panels to the left reflect the maximal regime, while the rightmost panel represents the sub-maximal regime. The downstream shift of the point of generation of the late K-H instabilities can be clearly seen in the rightmost panel.

65
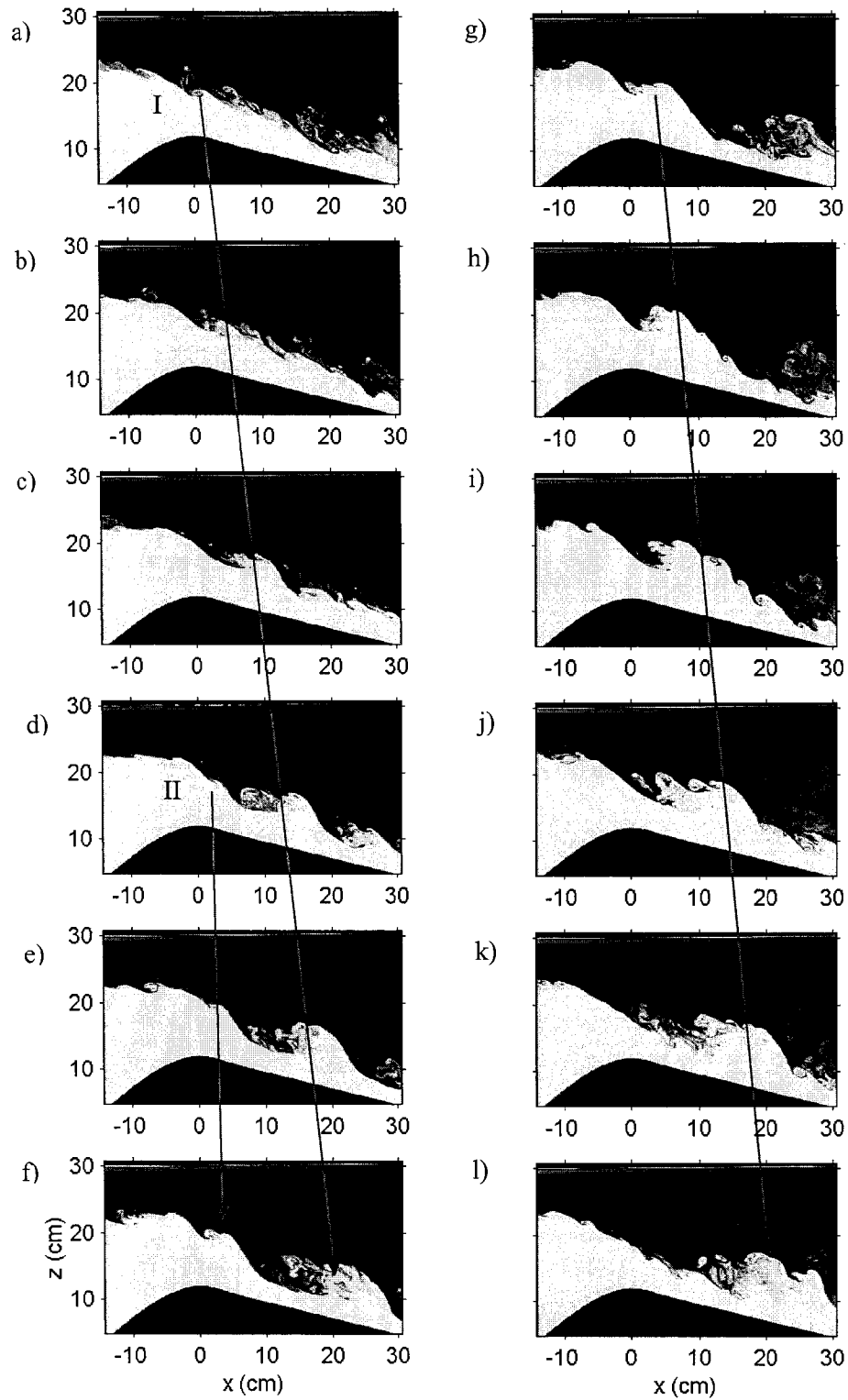
FIGURE 2-12. Sequence of images from Exp 1 showing the development of two large-scale interfacial down slope waves: wave I due to shear instability, whereas II due to lower layer relaxation. Images are about one minute into the experiment and are 3 seconds apart.
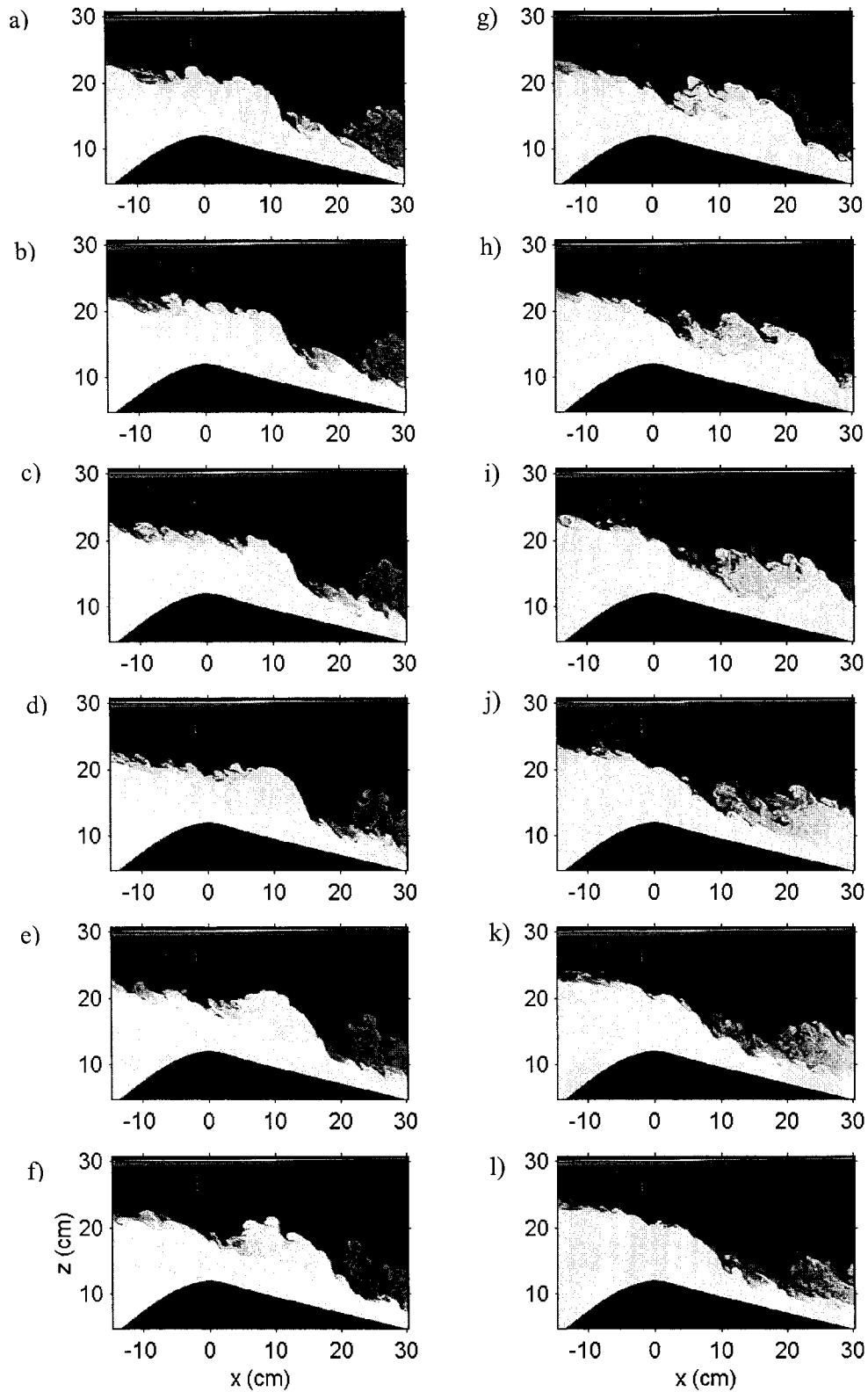
FIGURE 2-13. Sequence of images from Exp 3 at about 68 s into the experiment and are one second apart. They clearly show the development of a release event as the interface relaxes at the sill crest.

67
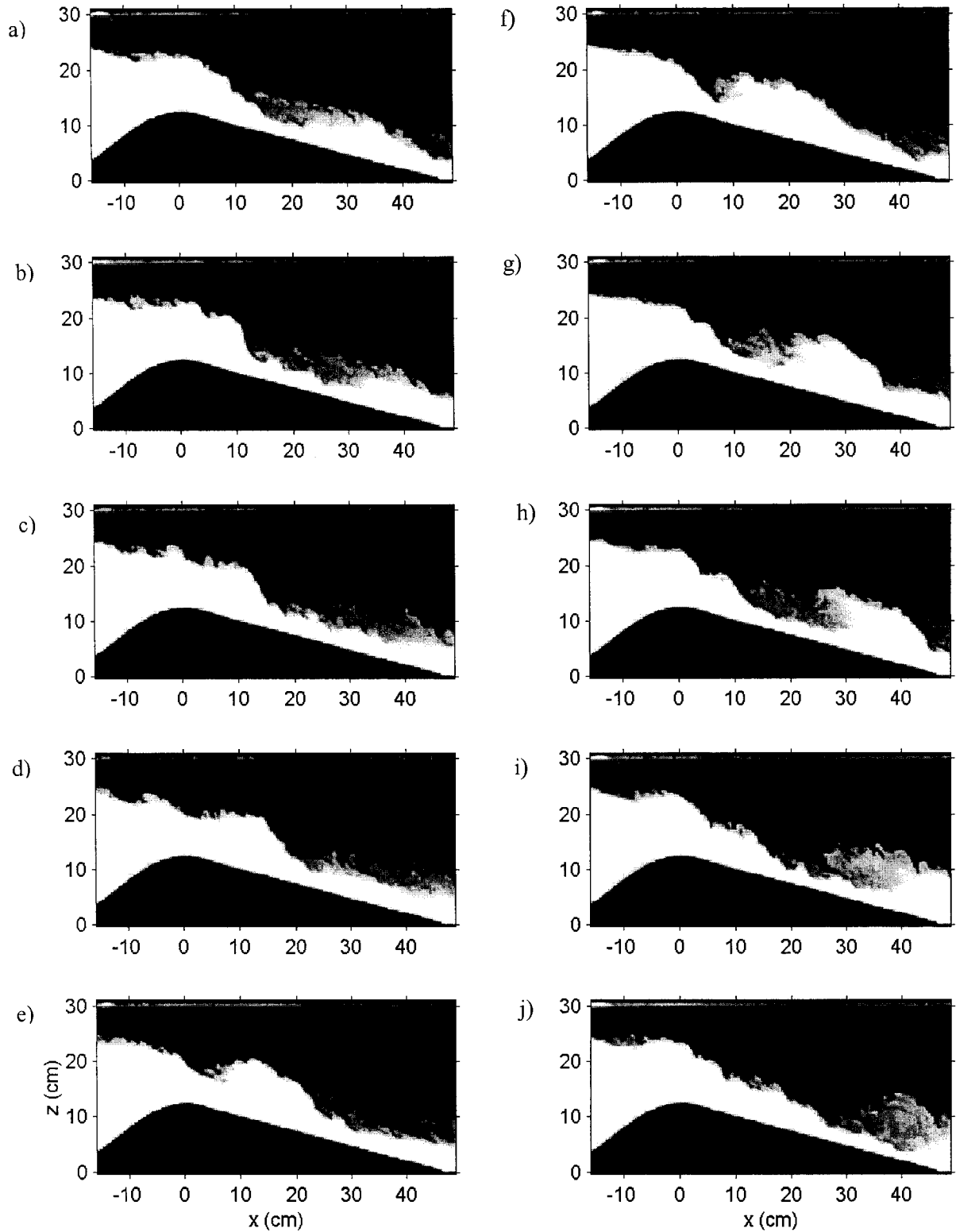
FIGURE 2-14. Sequence of images from Exp 4 at about 39 s into the experiment and are one second apart. The oscillatory fluctuation of the interface at the sill crest is quite obvious and the formation of a large down slope breaking wave is still obvious.
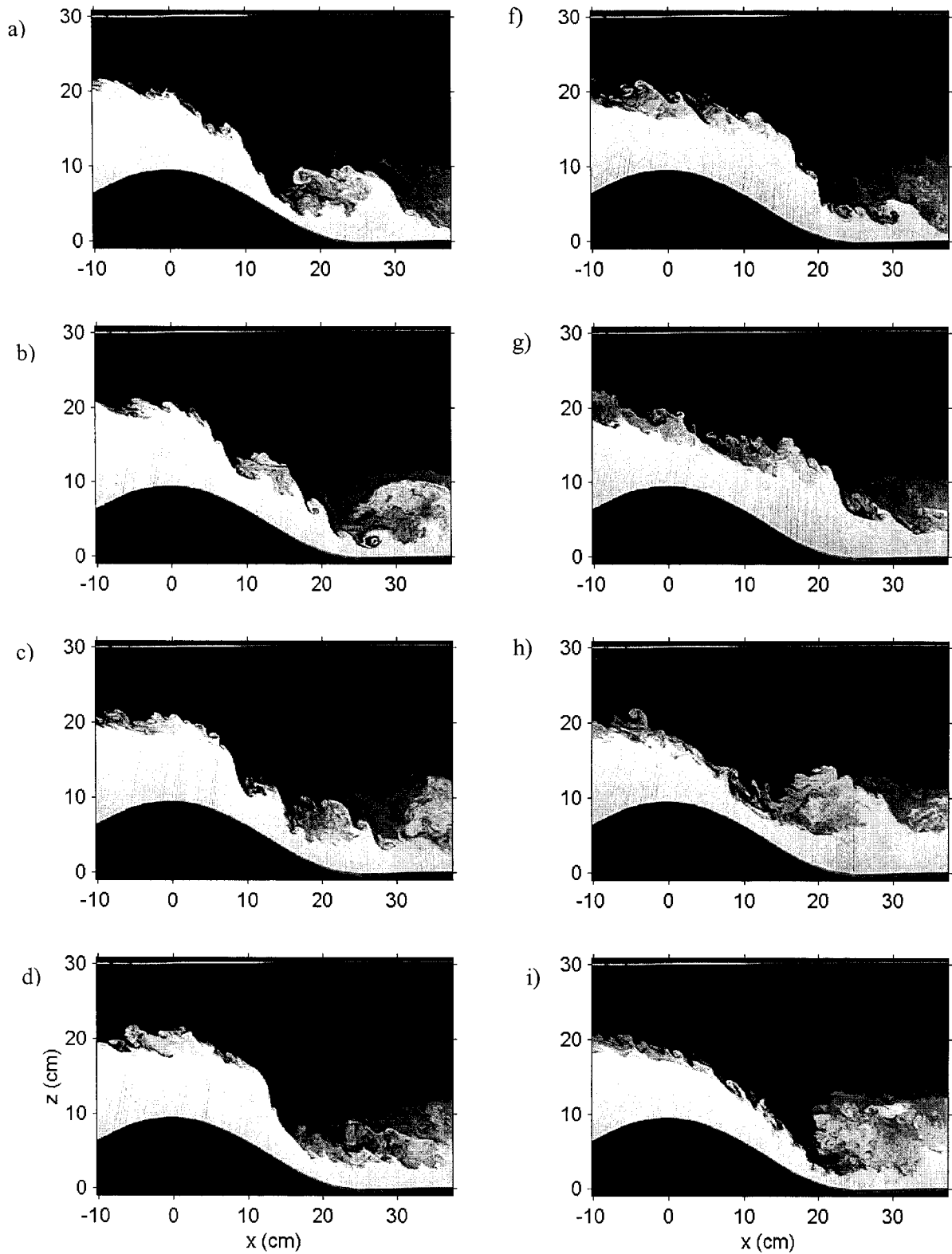
FIGURE 2-15. Sequence of images from Exp 3 of Morin (2002) with $g' = 6.47$ cm/s^2 and $h_{sill} = 10$ cm showing the same effect of the formation of a large scale breaking wave as the interface position drops at the sill crest. Images are two seconds apart.

69
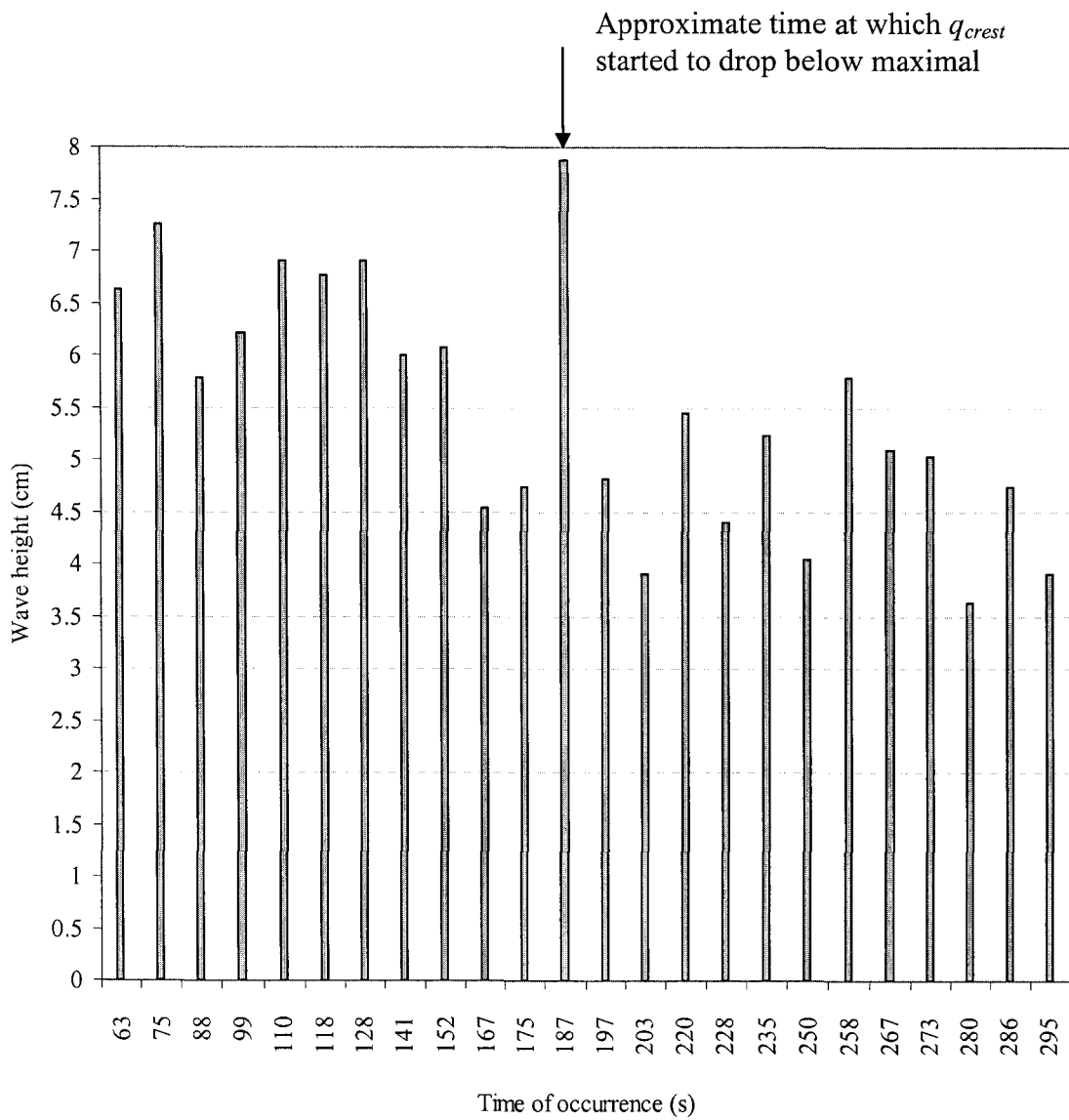
FIGURE 2-16. The temporal variation of the height of the large scale down slope breaking waves in Exp 3.

70
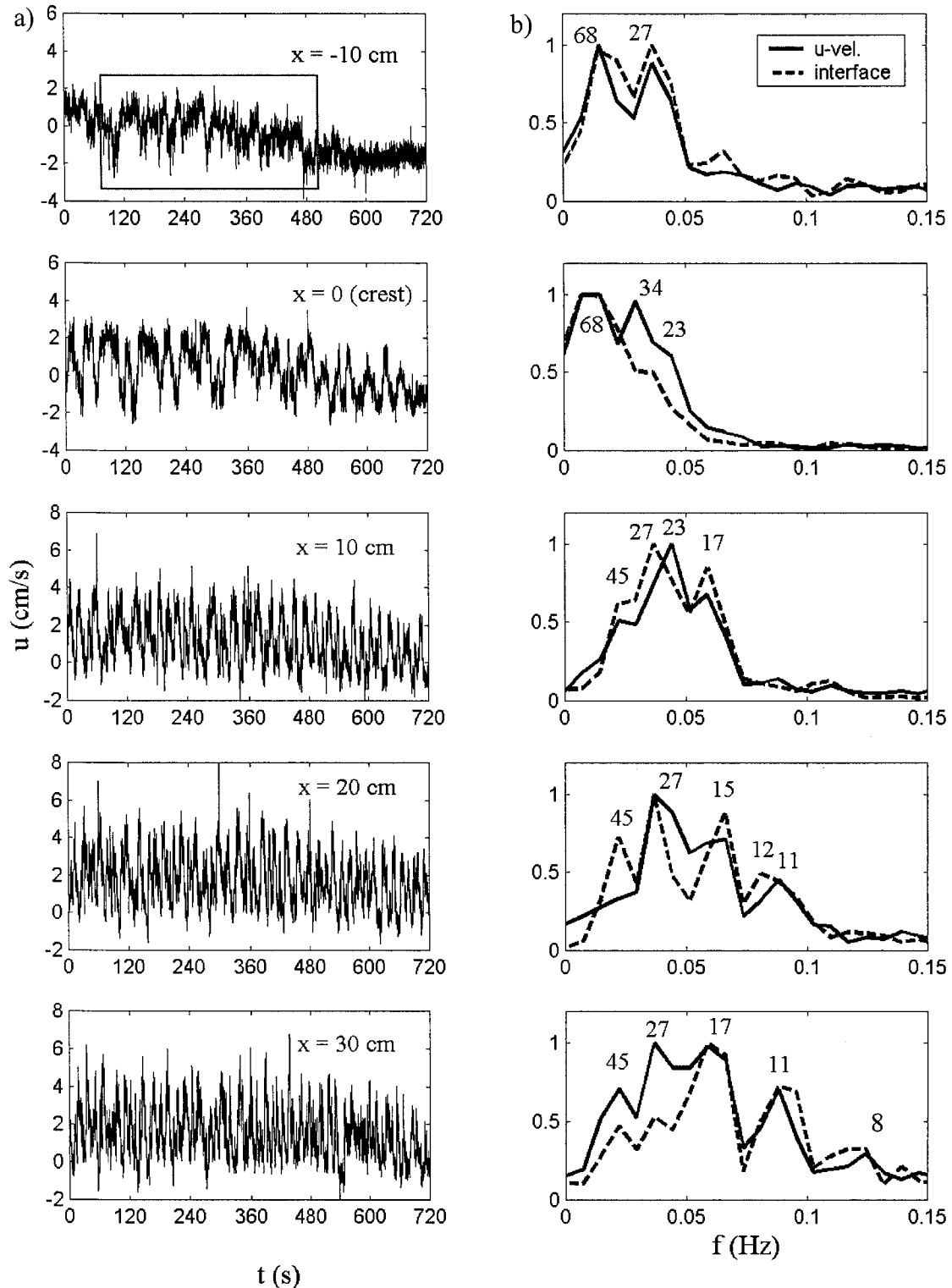
FIGURE 2-17. a) Time series of the u-velocity along the mean density interface, and b) its corresponding Fourier spectra along with that of the interface during maximal exchange in Exp 1 ($\Delta f = 0.0073$ Hz). The numbers in (b) are the periodic times ($1/f$) in seconds. The box in the top panel of a) defines the maximal regime data over which FFT operated.

71
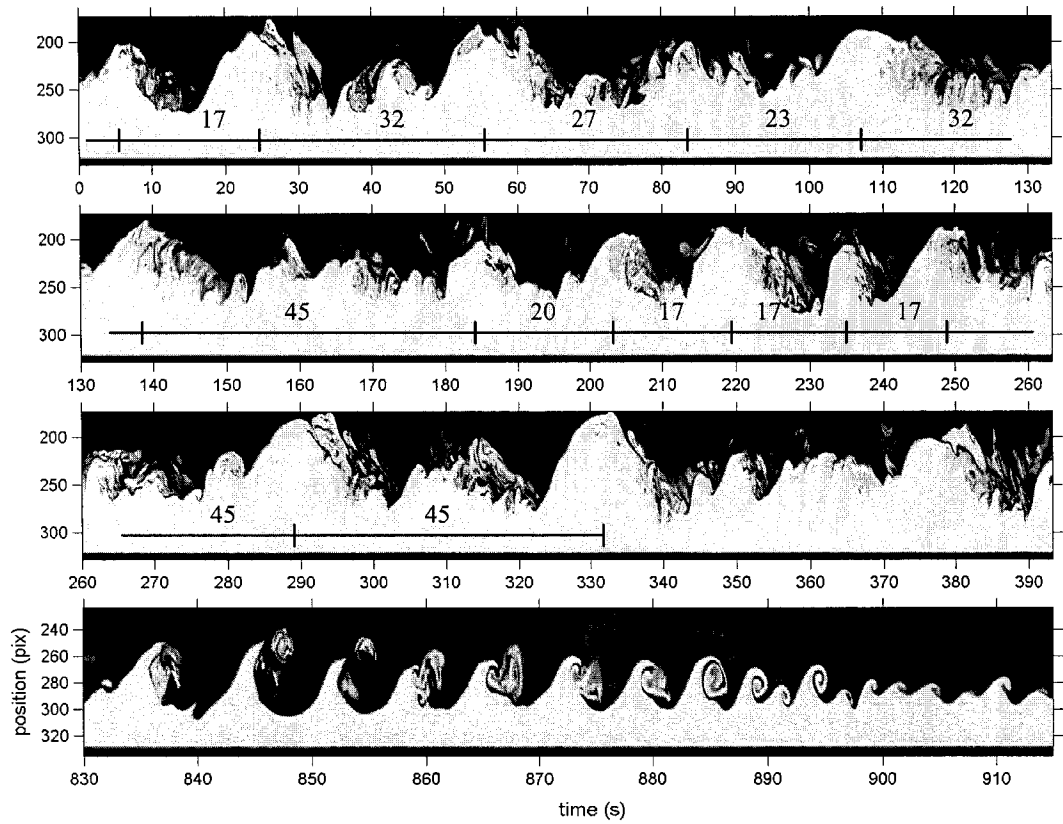
FIGURE 2-18. Reconstructed images of the interfacial fluctuations in Exp 1. The three top images are at $x = 10$ cm and show the release events of lumps of lower layer fluid at variable periodic times along with K-H instabilities in the maximal exchange. The lowermost image shows a train of K-H instabilities at $x = 15$ cm in the sub-maximal regime.

72
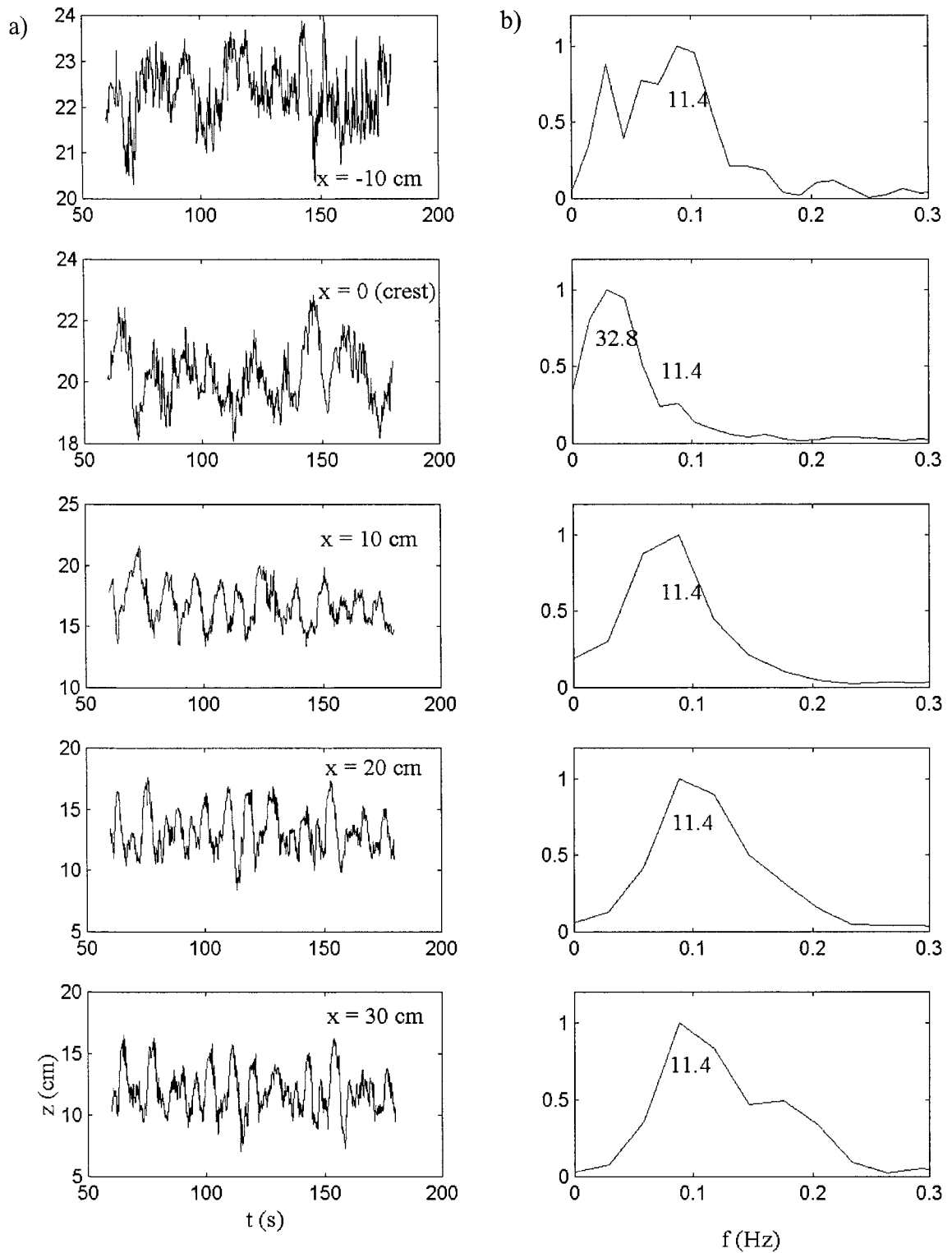
FIGURE 2-19. a) Time series of the interface positions at sample locations in Exp 3 over about 2 minutes during the maximal exchange regime, and b) its corresponding Fourier spectra. The numbers in (b) are the periodic times $(1/f)$ in seconds.

73
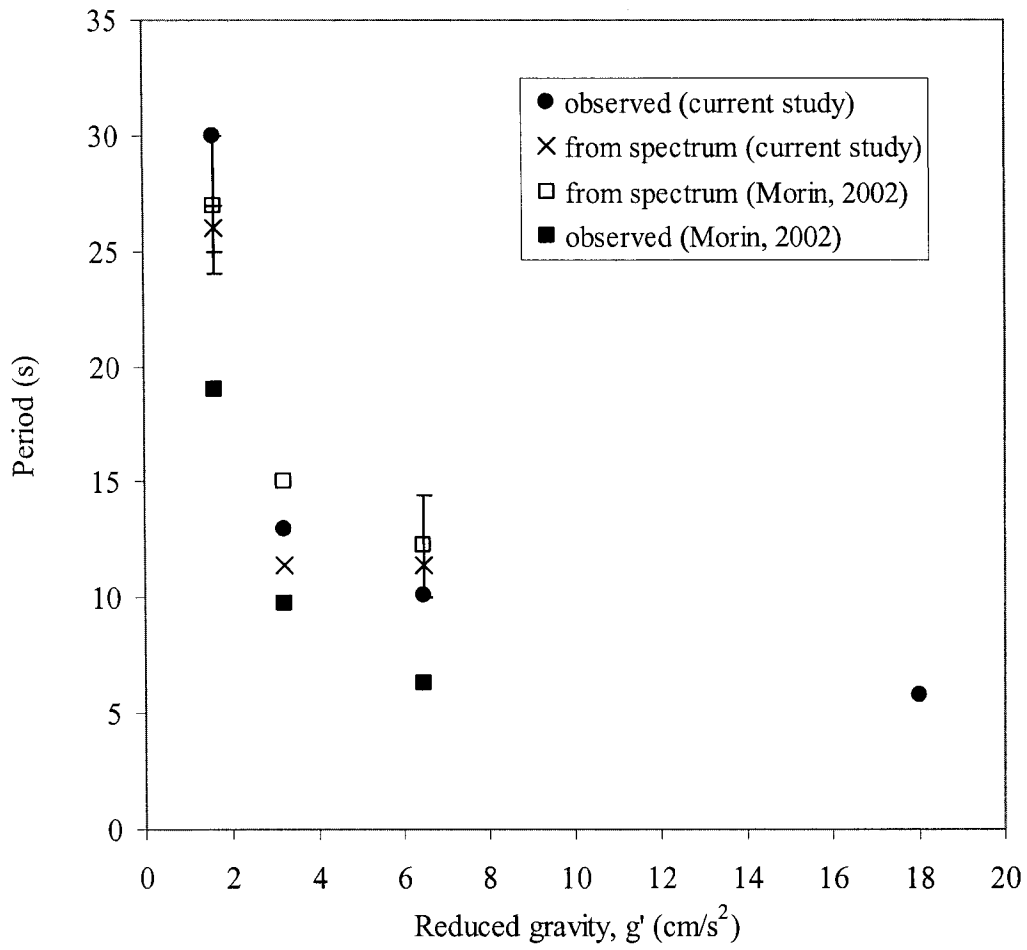
FIGURE 2-20. Comparison between observed periods of the release events in different experiments and those obtained from the Fourier spectra of the interface positions' time series over the maximal regime.

74
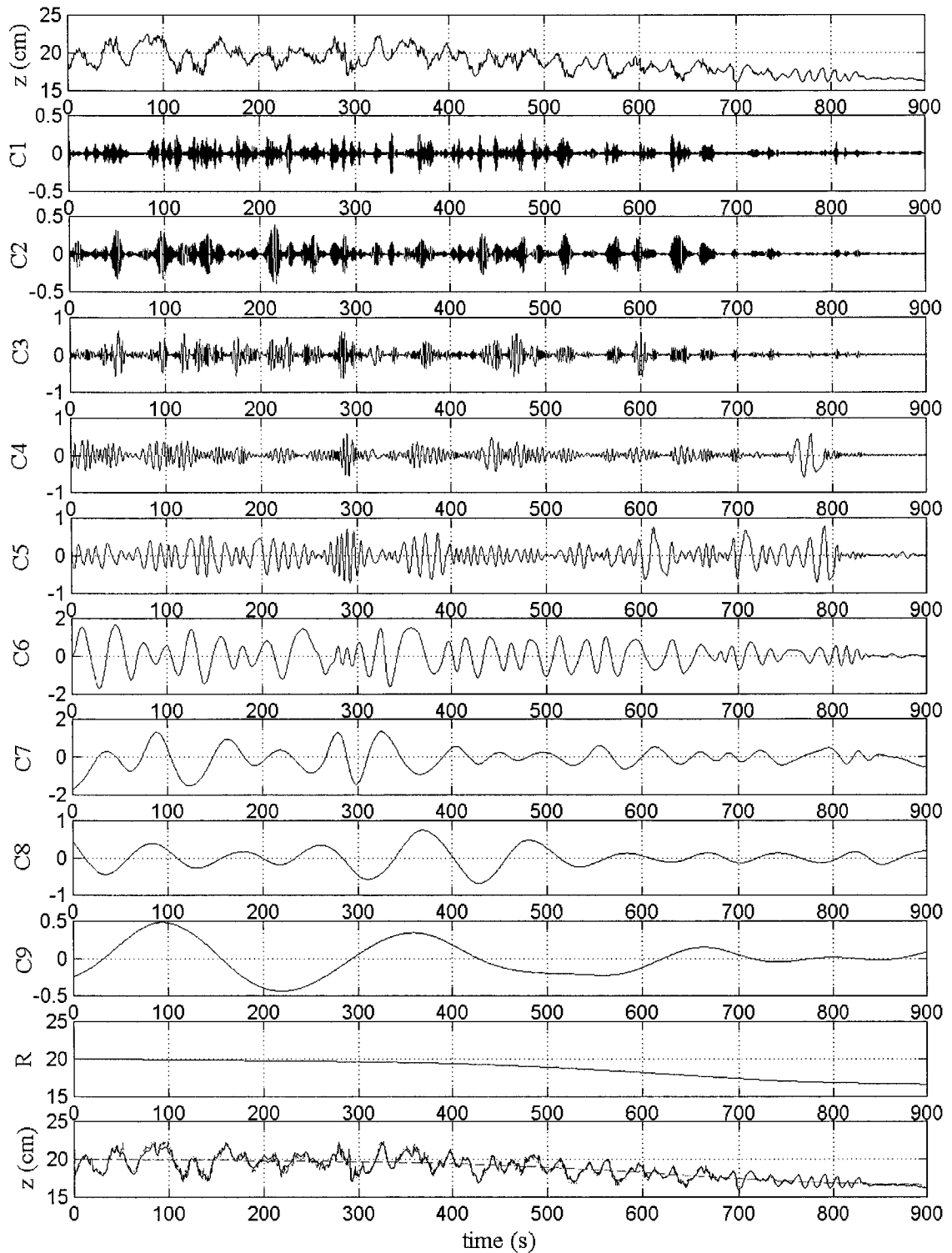
FIGURE 2-21. The original interface positions' time series at the sill crest in Exp 1 and its intrinsic mode functions (C1 ... C9) and the residual, R, using HHT. The reconstructed signal composed of (C4 ... C8) and R is plotted at the bottom and compared with the original series. A coherent match is observed between the two signals. The data are sampled at 5 Hz.

75
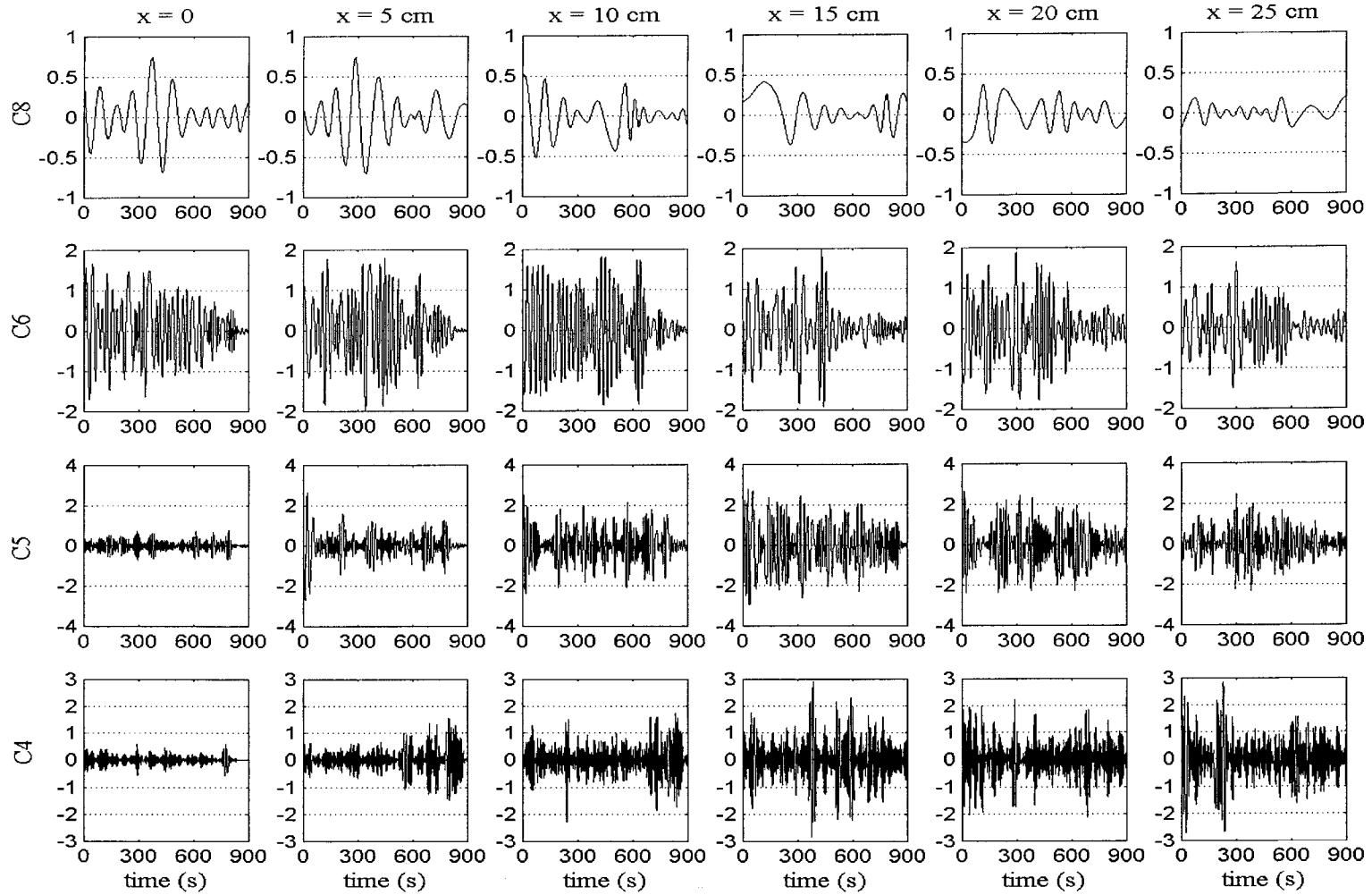
FIGURE 2-22. The temporal and spatial variation of the main intrinsic modes (C4, C5, C6, and C8) in Exp 1. Clearly C8 decays in amplitude with distance and once the sub-maximal regime starts. C4 and C5 on the contrary grow in time and space.
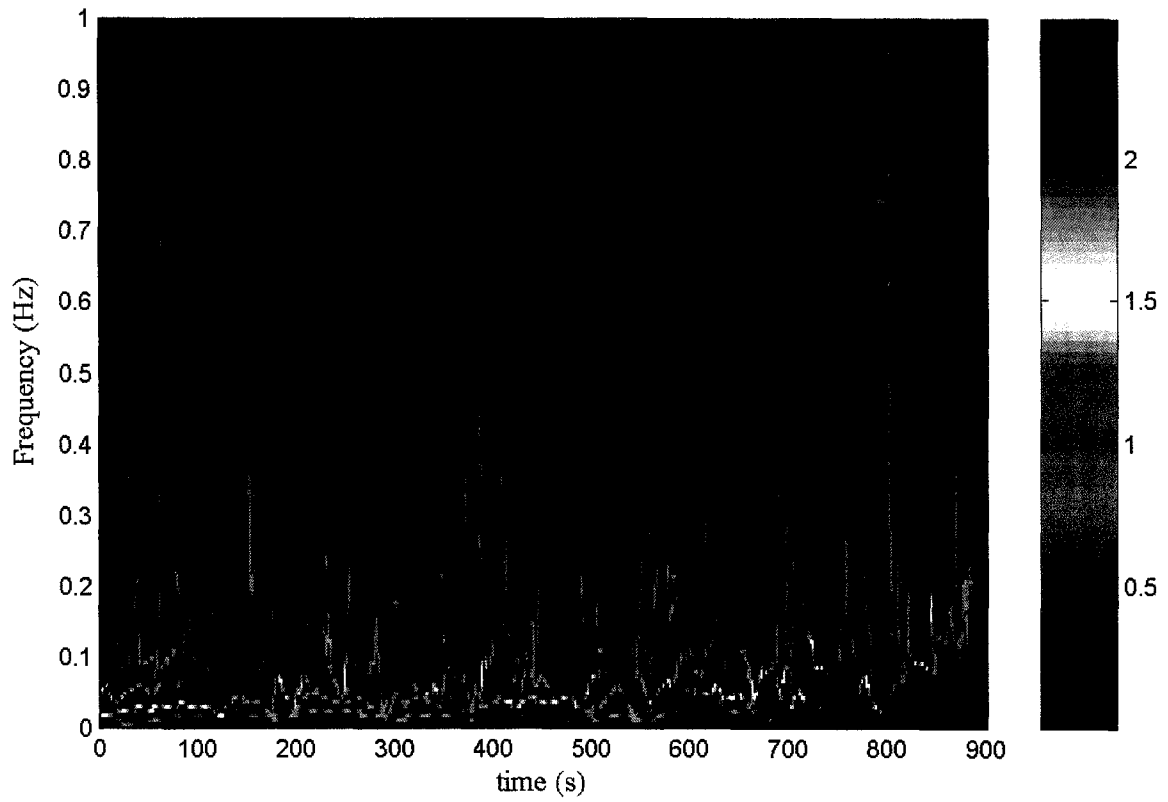
FIGURE 2-23. The Hilbert-Huang power spectra of the original time series of the interface positions at $x = 10$ cm in Exp 1.

77
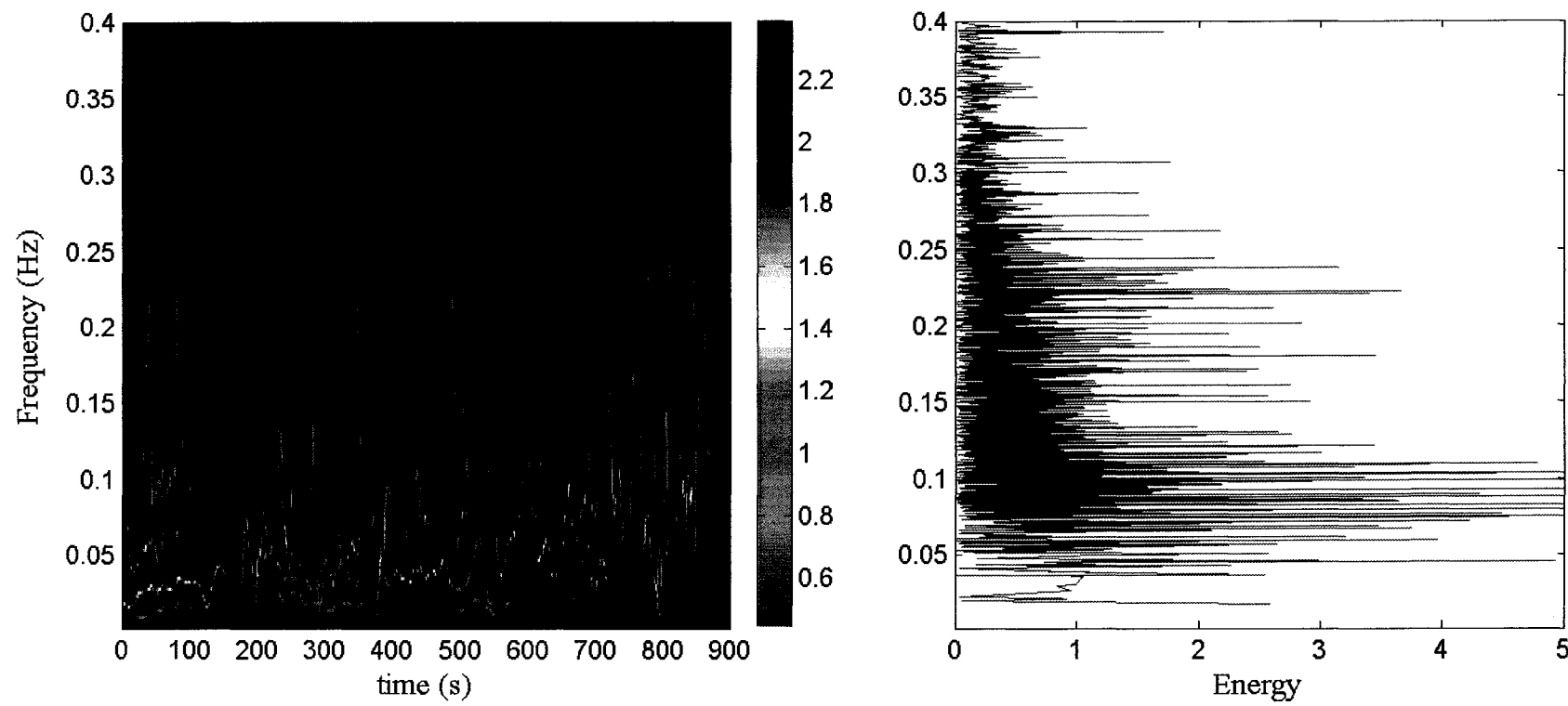
FIGURE 2-24. Hilbert-Huang power spectra and the corresponding spectral energy distribution of the reconstructed time series (C4 … C8) of the interface positions at $x = 10$ cm in Exp 1.
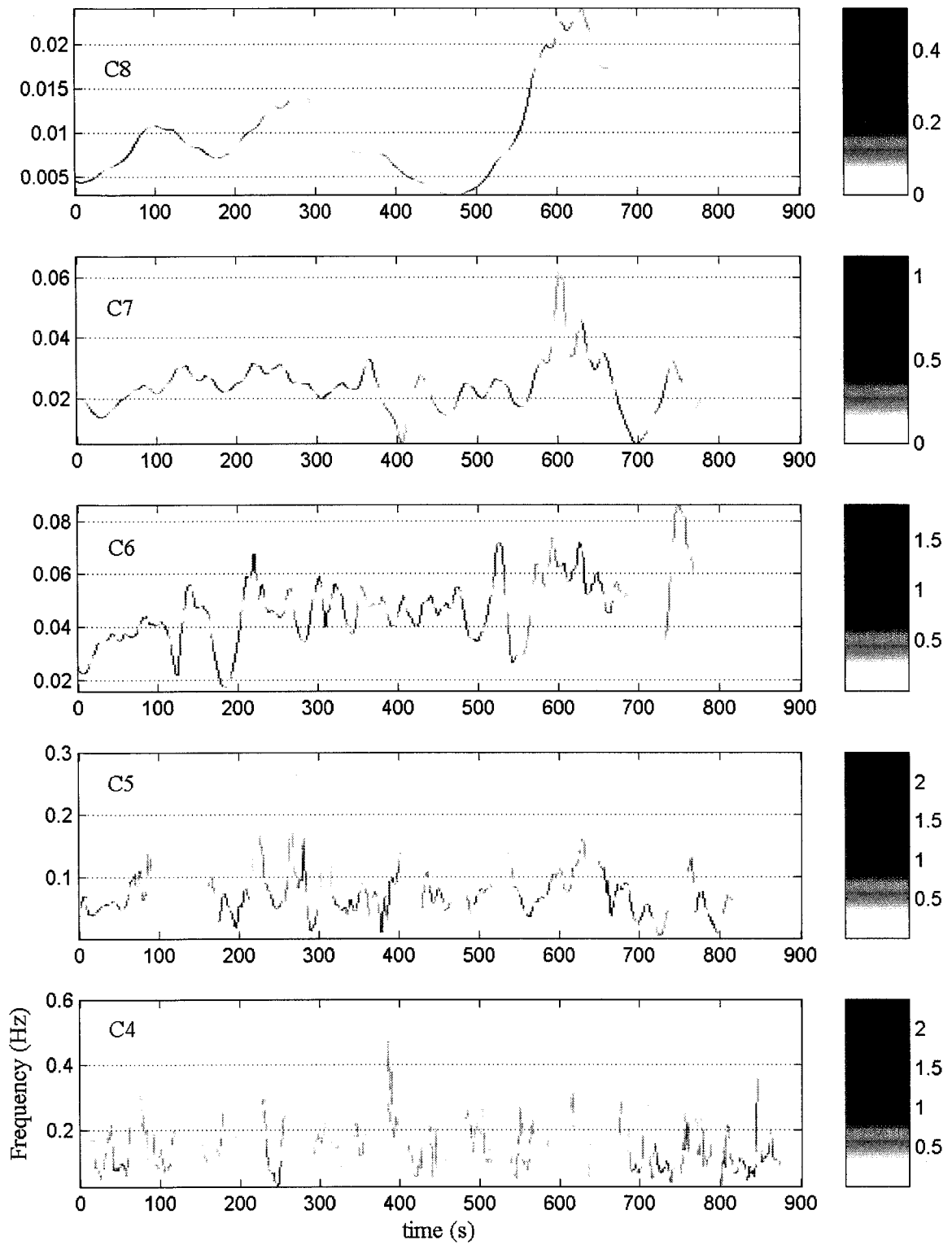
FIGURE 2-25. The Hilbert-Huang power spectra of the individual components C4 ... C8 for the interface positions' time series at $x = 10$ cm in Exp 1.
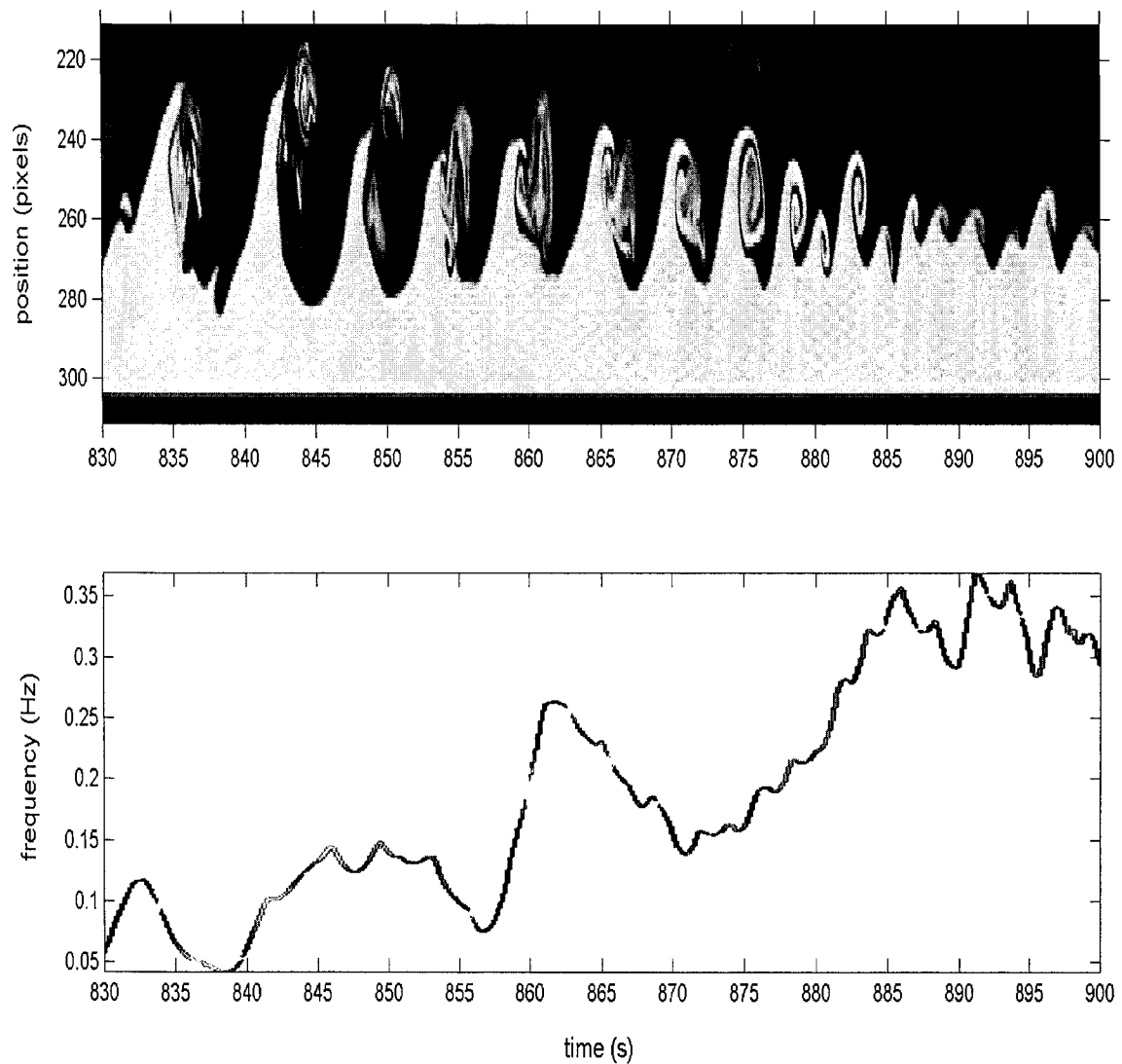
FIGURE 2-26. A zoomed-in reconstructed image of the interfacial fluctuations and the corresponding HHT power spectra showing the evolution of the frequency with time. Quite good match is observed between the observed and measured frequencies, which reflects the merit of the technique. The data are from Exp 1 at x = 15 cm in the sub-maximal regime.

80
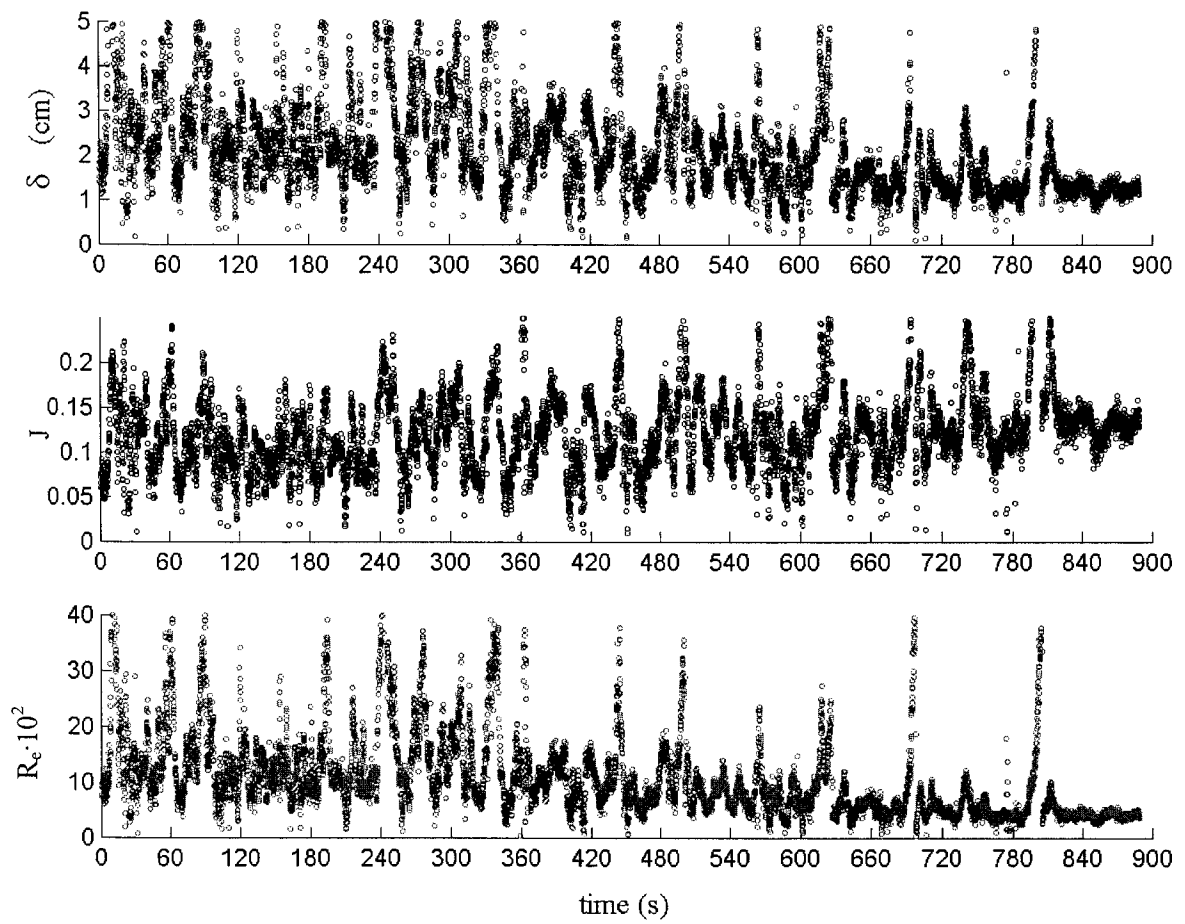
FIGURE 2-27. The temporal variation of the shear layer thickness, δ, the bulk Richardson number, J, and the shear layer Reynolds number, R_e, in Exp 1a at the sill crest ($x = 0$) throughout the whole experiment.

81
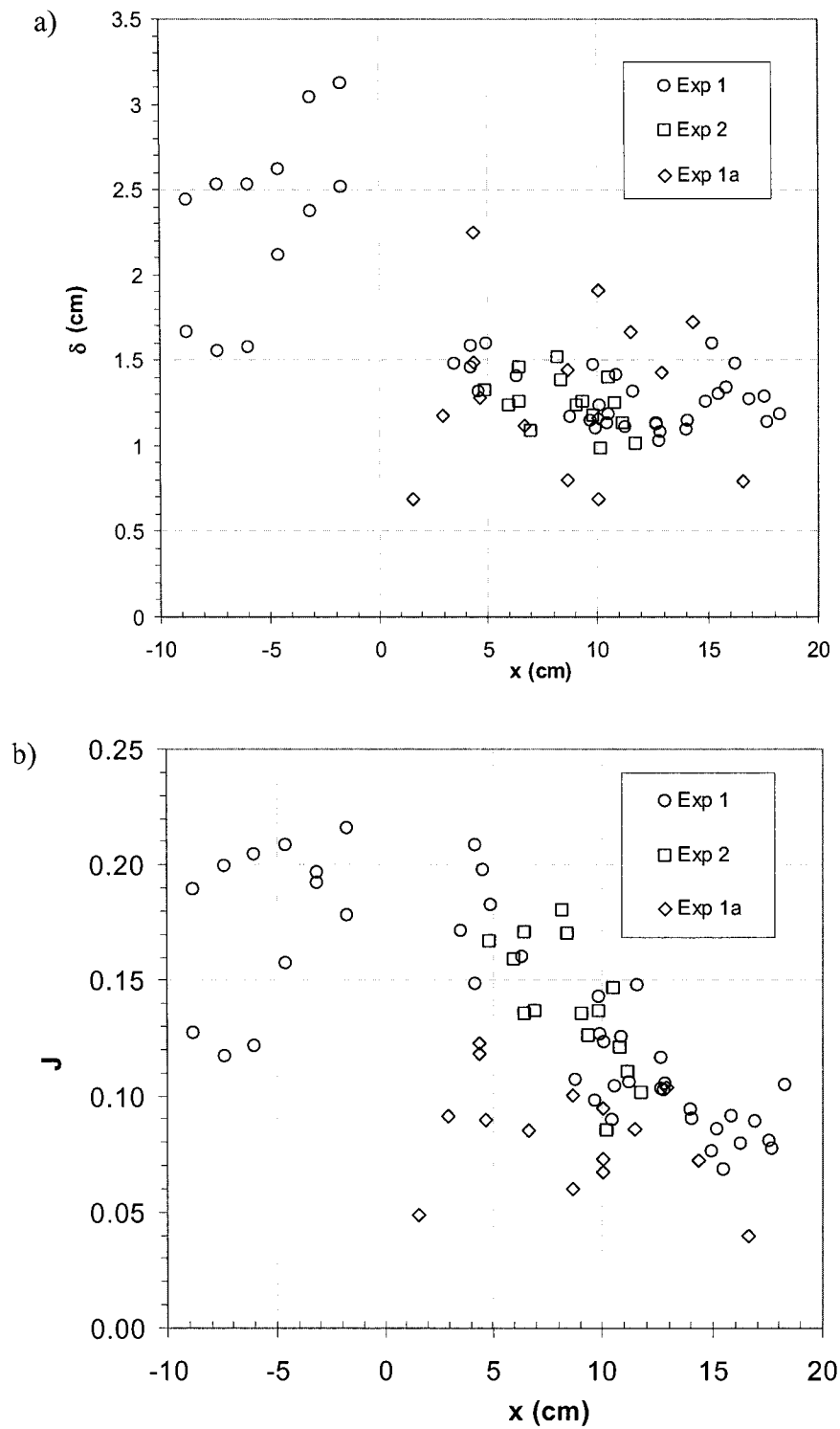
FIGURE 2-28. The spatial variation of: a) the shear layer thickness, δ, and b) the bulk Richardson number, J, along the sill prior to the generation of the K-H instabilities. The data were time-averaged over about one second before the instability was generated.

82
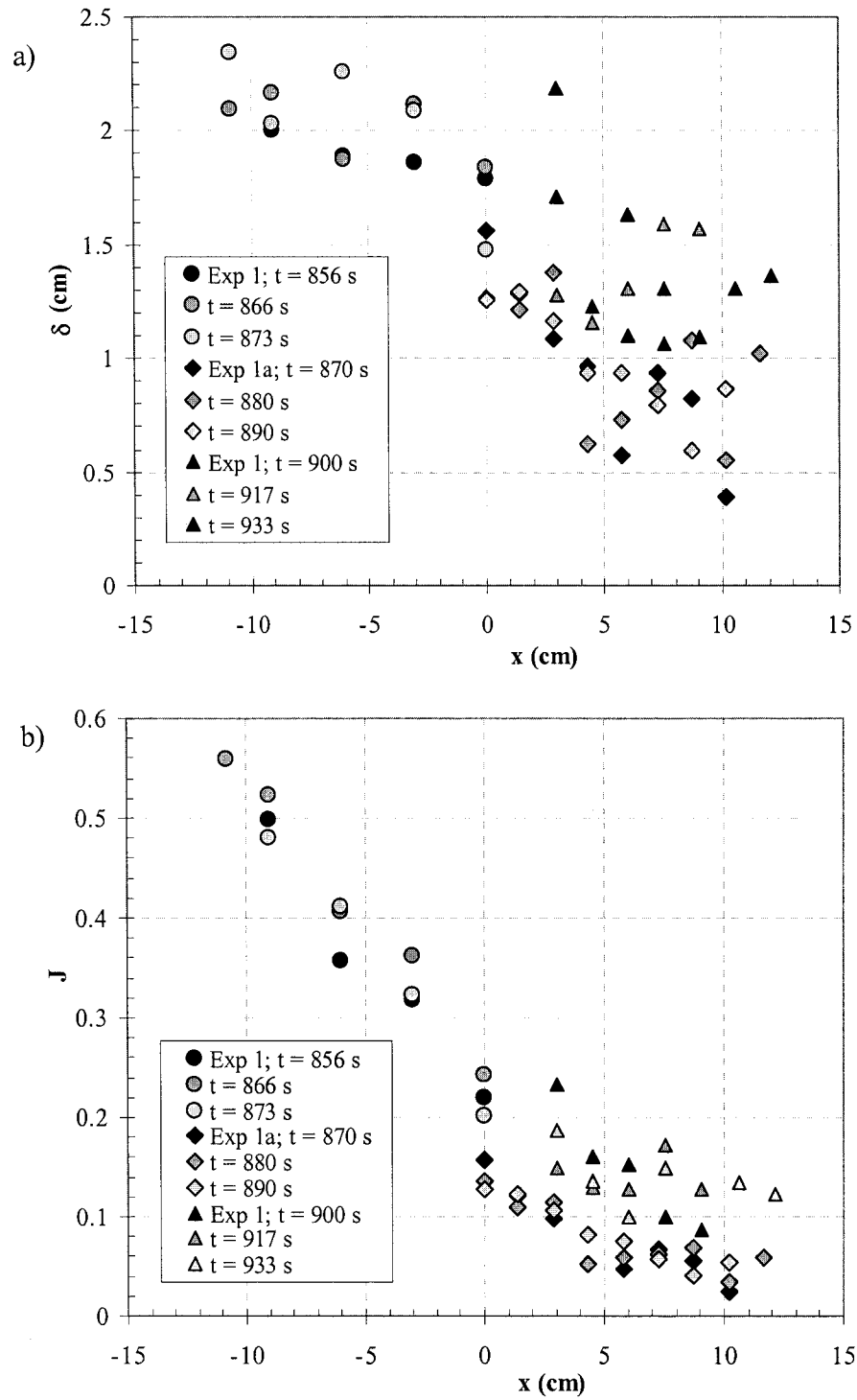
FIGURE 2-29. The spatial variation of: a) the shear layer thickness, δ, and b) the bulk Richardson number, J, along the sill at later times when no K-H instabilities were observed. The data were measured and time-averaged over about one second.

83
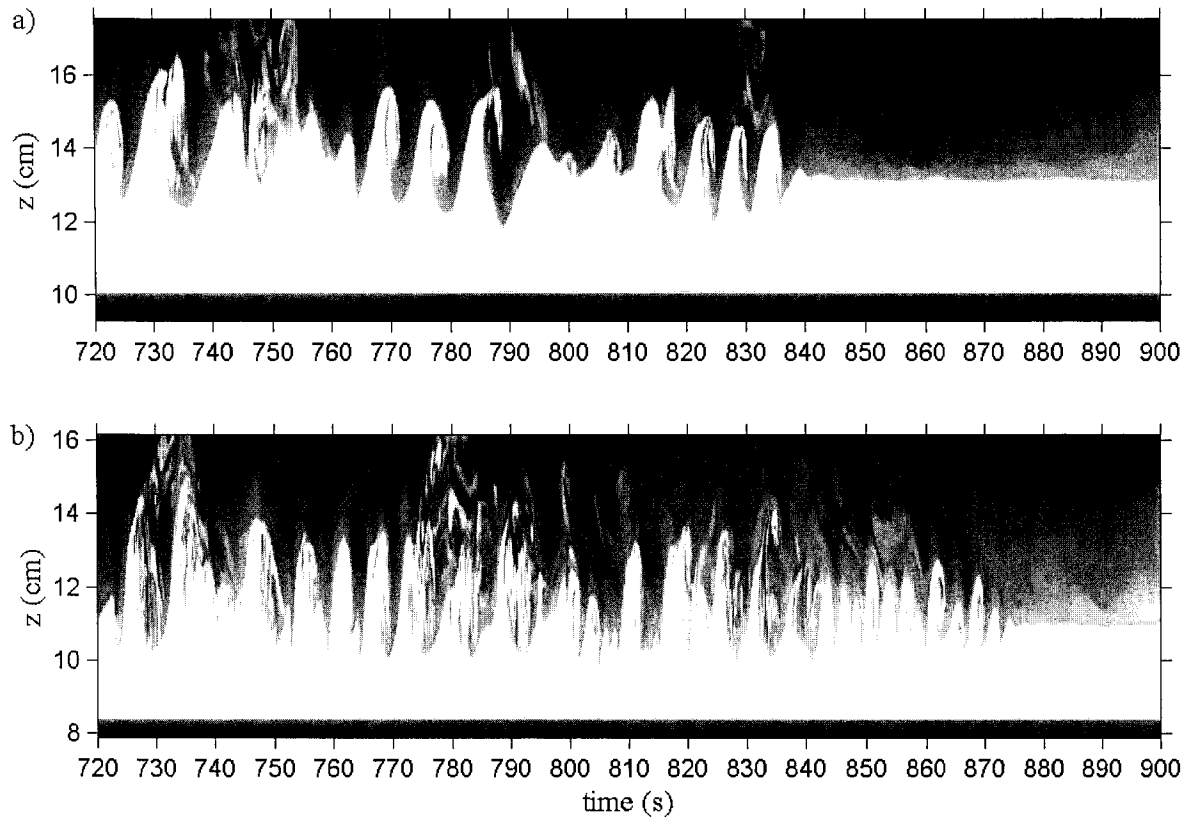
FIGURE 2-30. Two reconstructed images from Exp 1a: a) at $x = 8$ cm, and b) at $x = 15$ cm during the late periods of the sub-maximal regime. Clearly, the interface becomes stable at certain instant at one location and the point of generation of the K-H instabilities is shifted further downstream. The frequency becomes higher as x increases.

84
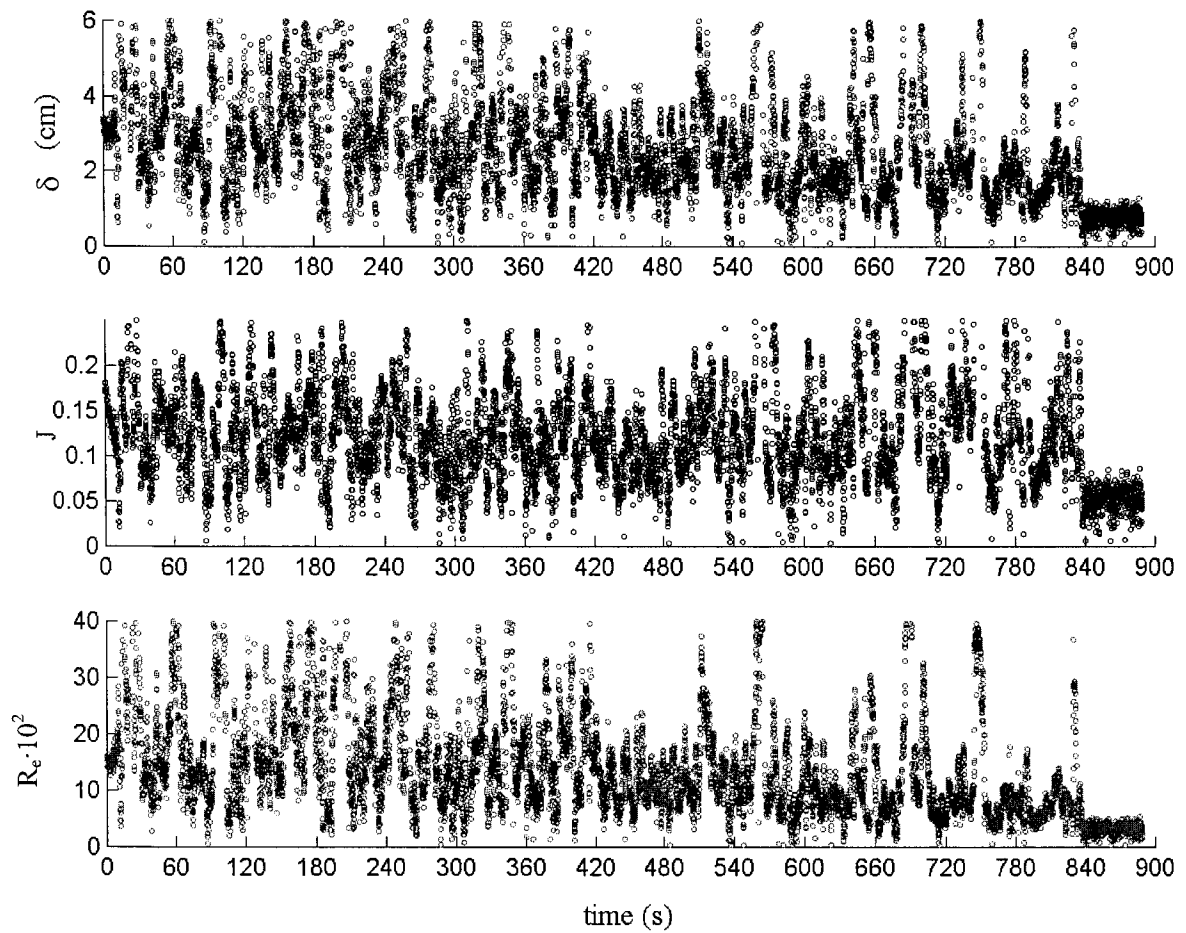
FIGURE 2-31. The temporal variation of the shear layer thickness, δ, the bulk Richardson number, J, and the shear layer Reynolds number, R_e, in Exp 1a at the $x = 8$ cm throughout the whole experiment.

85
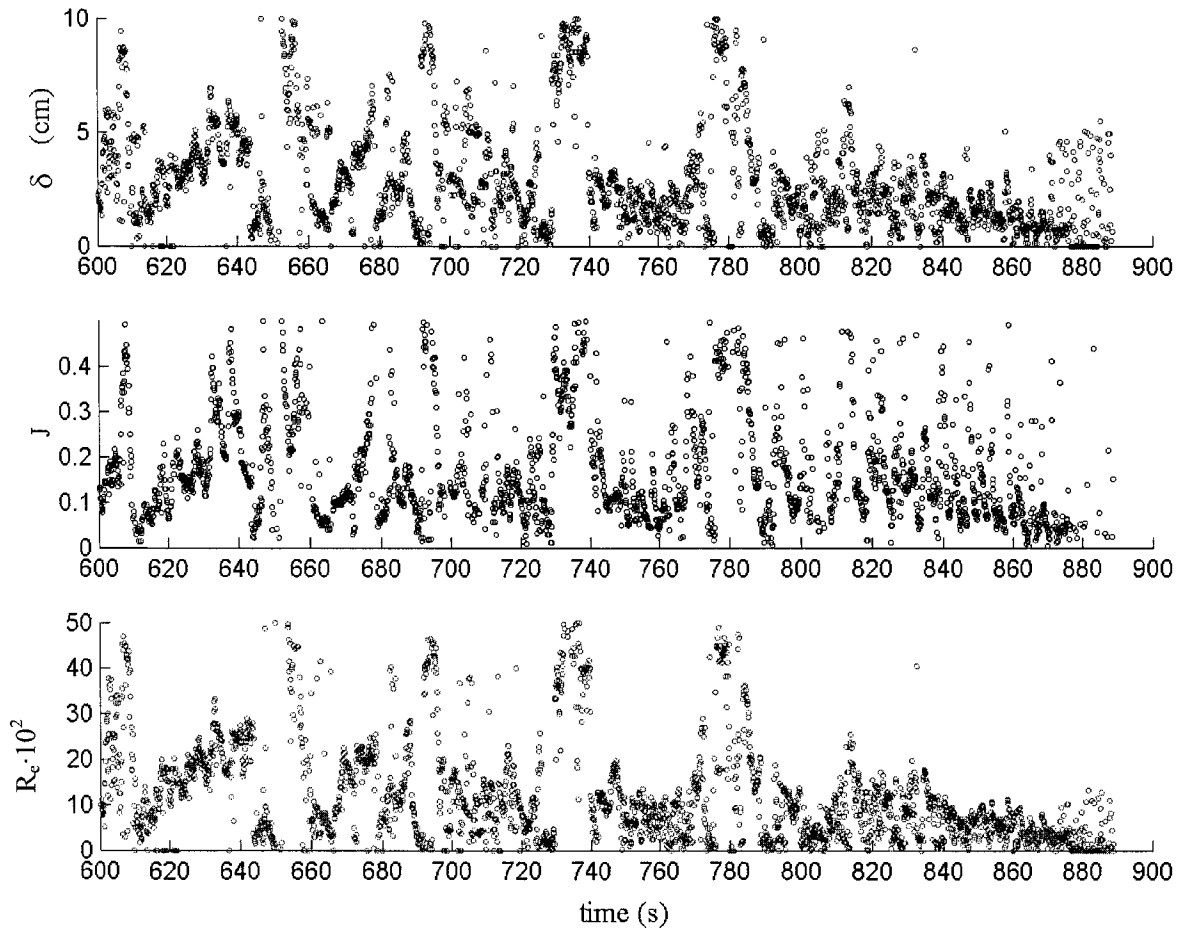
FIGURE 2-32. A zoomed-in plot showing the temporal variation of the shear layer thickness, δ, the bulk Richardson number, J, and the shear layer Reynolds number, R_e, in Exp 1a at $x = 15$ cm.
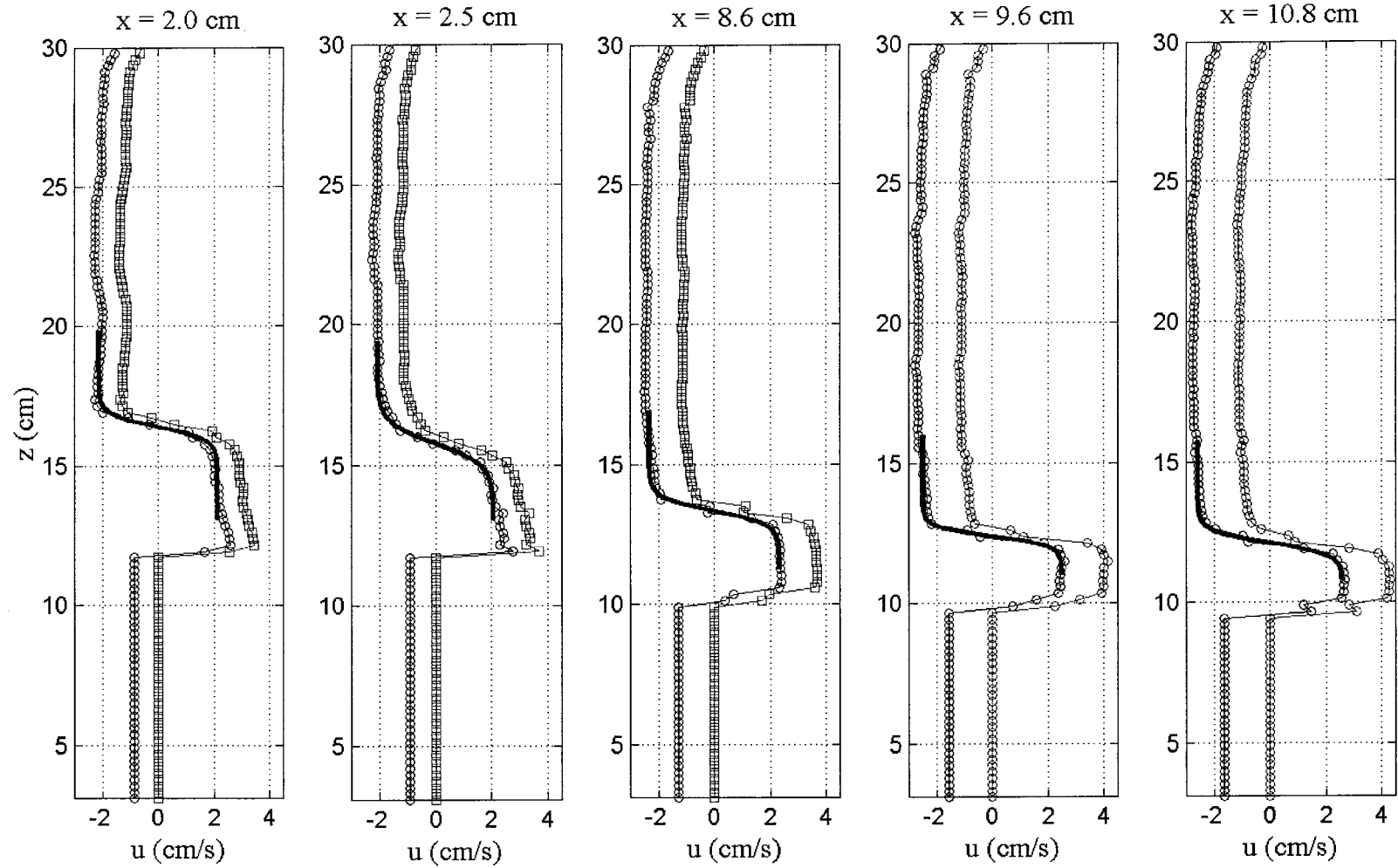
FIGURE 2-33. Sample velocity profiles at different locations prior to the generation of K-H instabilities down the slope (□: original profile; ○: shifted profile). An optimized hyperbolic tangent function was fitted to the data points around the shear layer of the shifted profile to define the shear layer center and eventually the vertical shift, d.
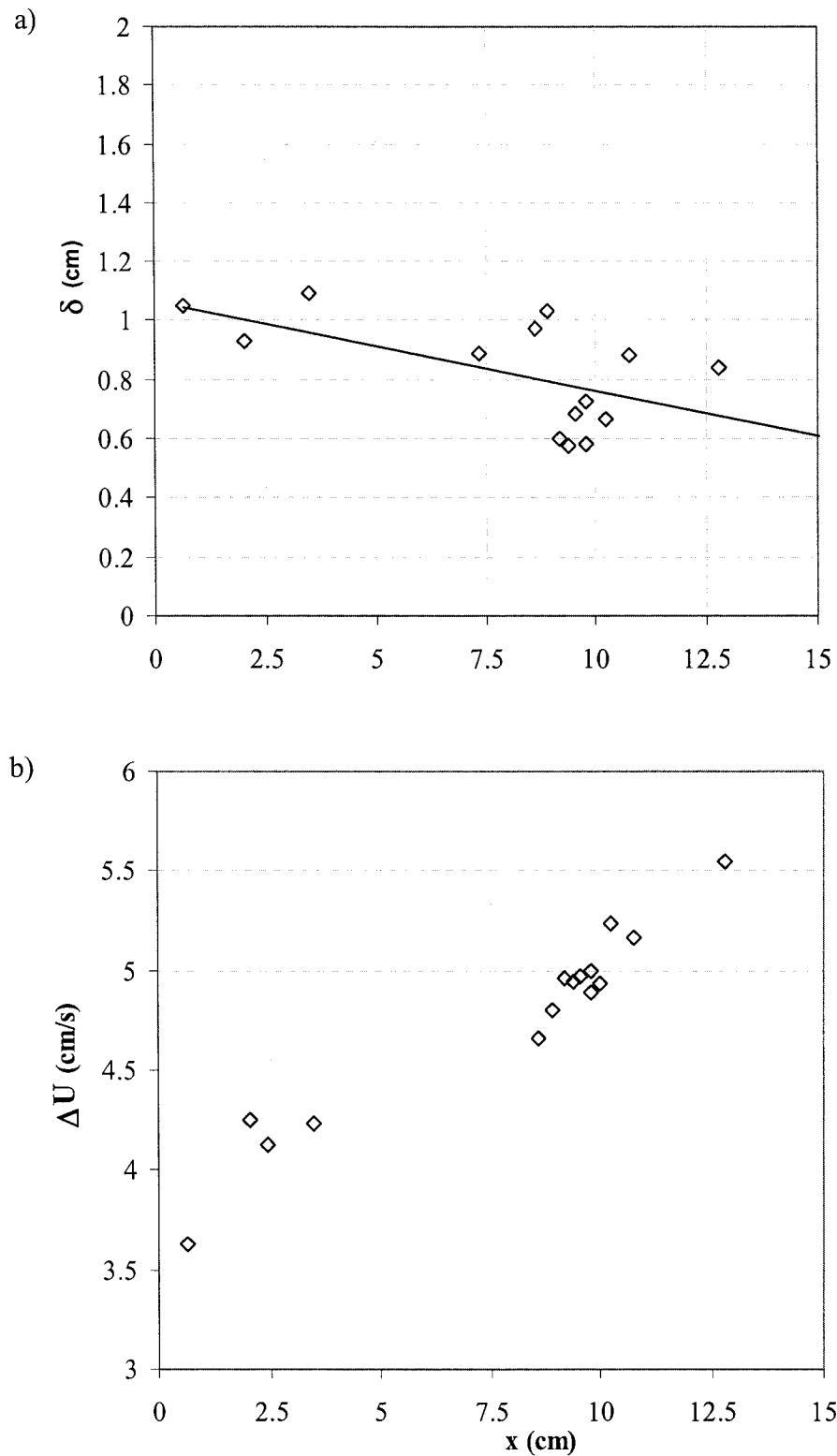
FIGURE 2-34. a) The spatial variation of the instantaneous shear layer thickness, δ, prior to the generation of individual K-H instabilities along with a linear best-fit trend, and b) the corresponding velocity shear, ΔU.
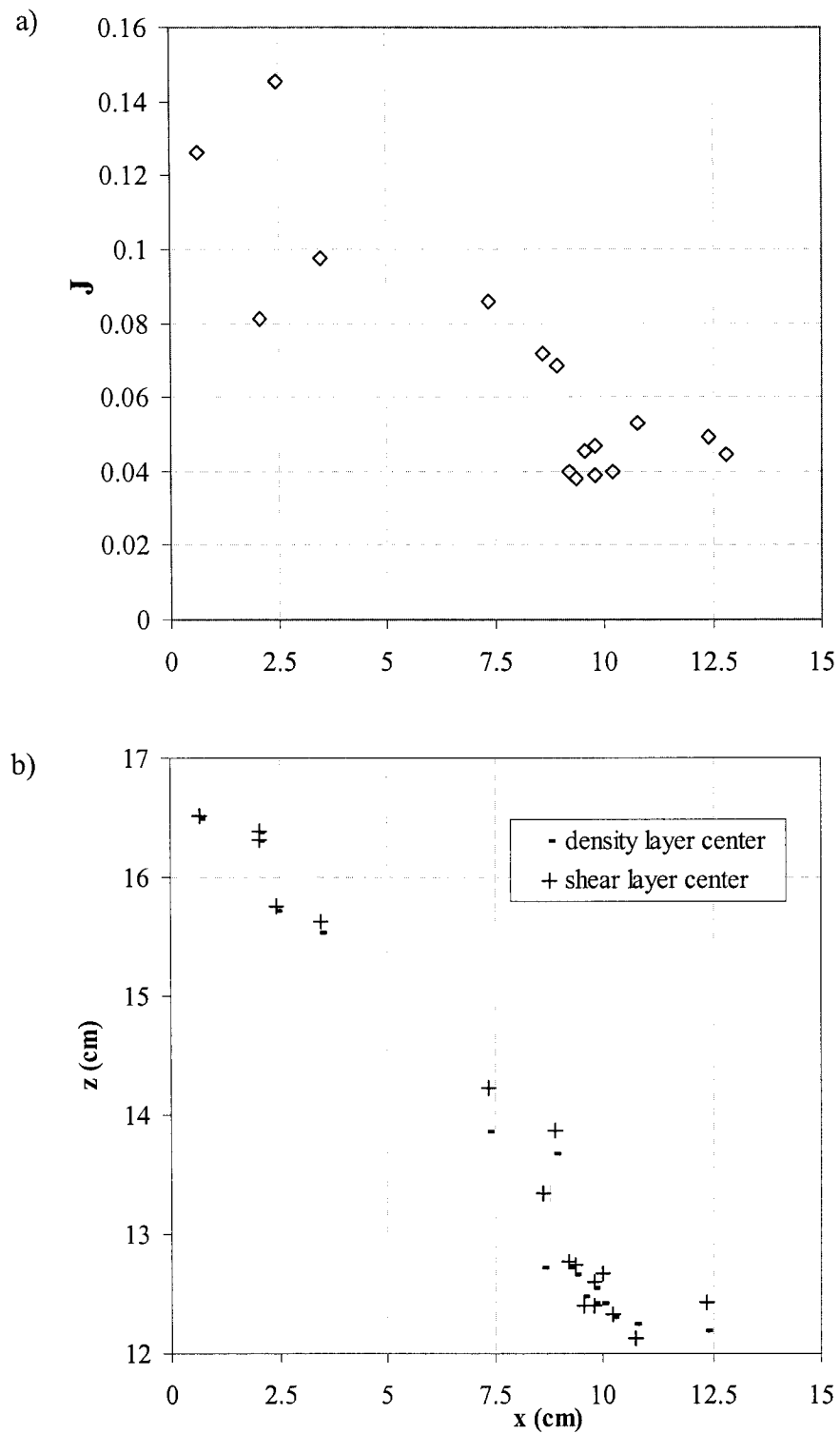
FIGURE 2-35. a) The instantaneous bulk Richardson number, J, prior to the generation of the late K-H instabilities, and b) the corresponding elevation of the density and shear layer centers used to calculate the vertical shift, $\mathcal{E}$.

89
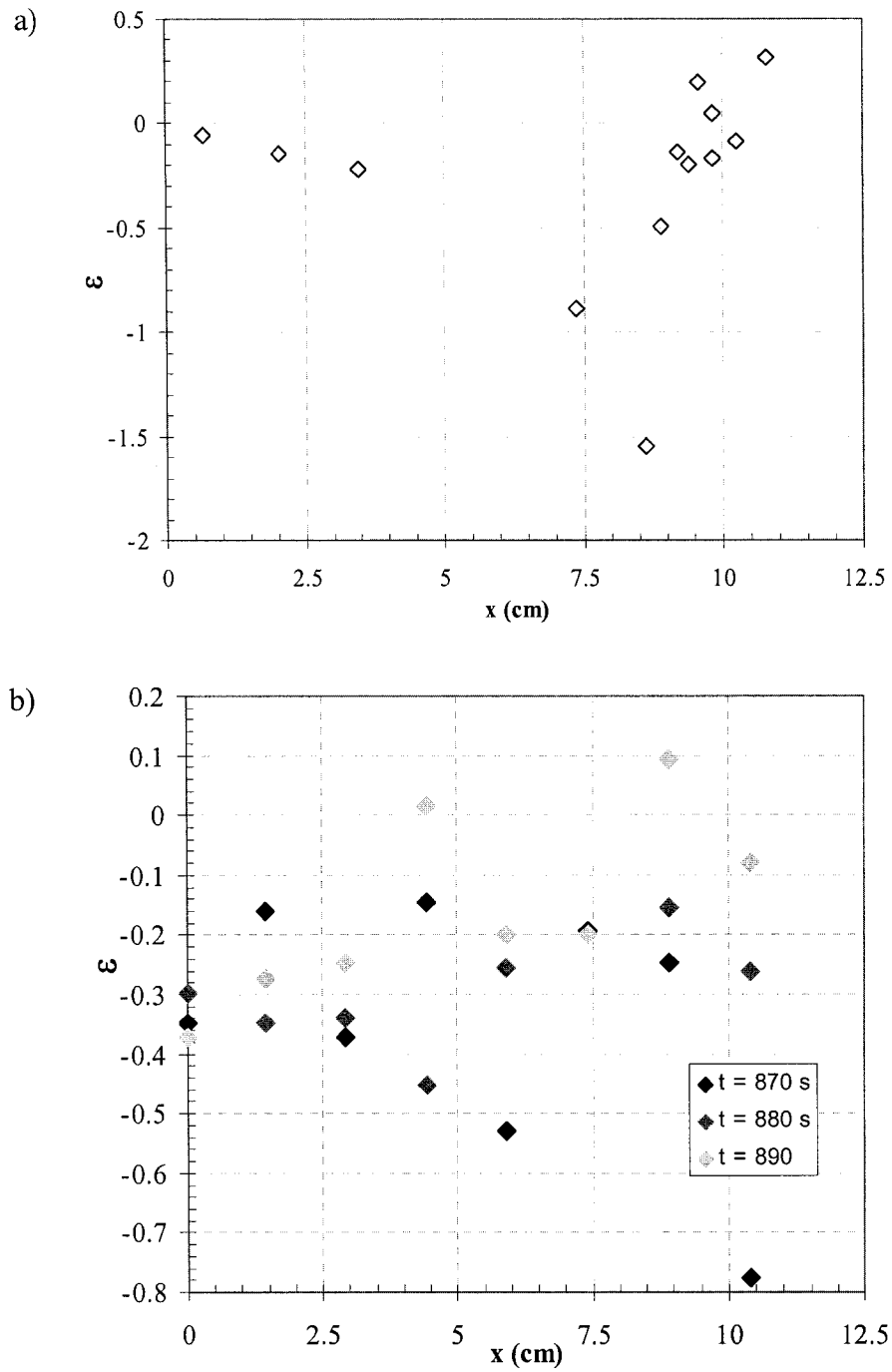
FIGURE 2-36. The spatial variation of the non-dimensional vertical shift, ε, of the density interface from the shear layer center: a) prior to the generation of K-H instabilities, and b) at times when the interface was stable and no more instabilities were observed to occur.

90
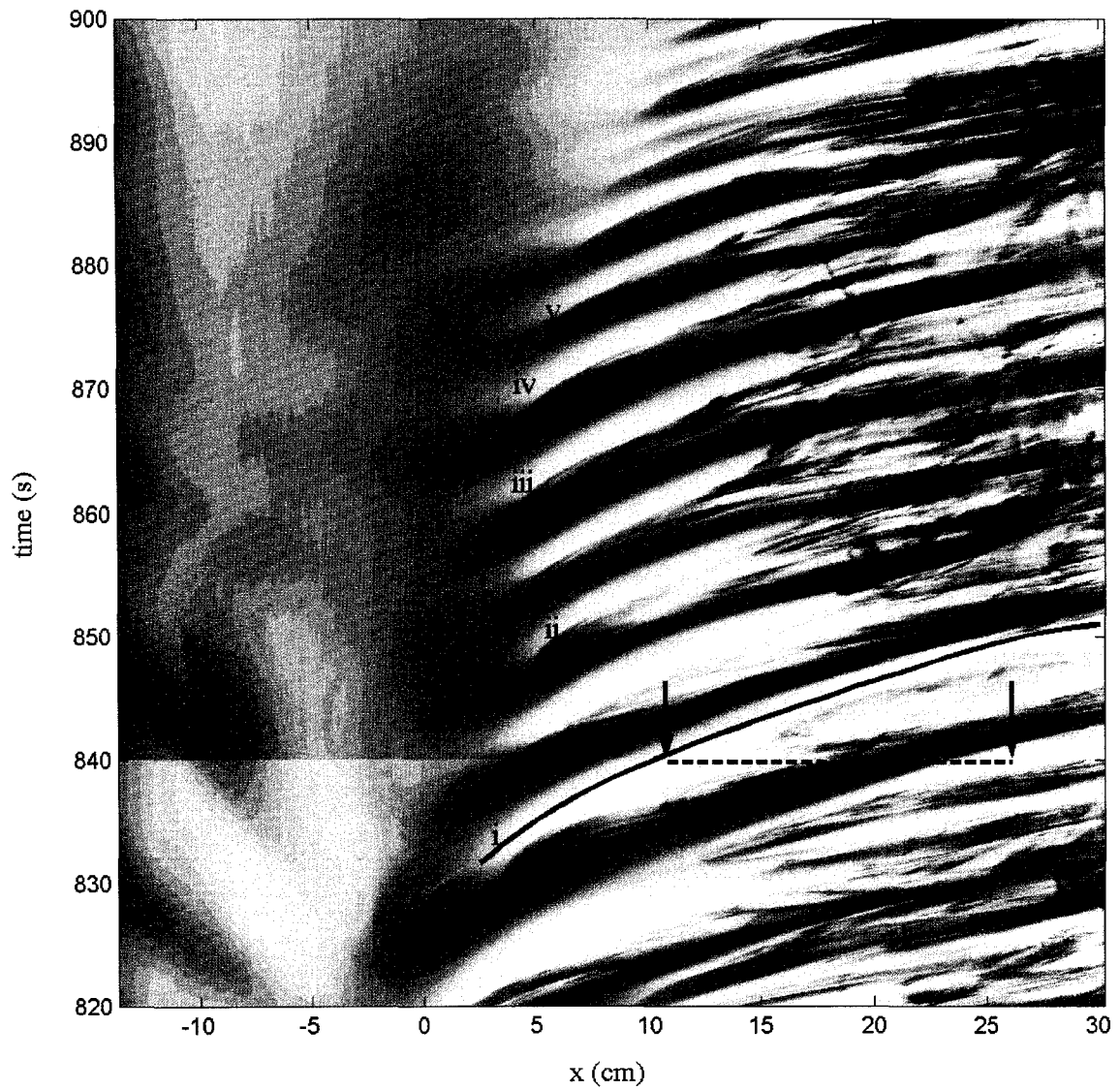
FIGURE 2-37. A zoomed-in view of the wave characteristics' plot in Exp 1 during the late sub-maximal exchange. The distance between the black arrows suggests λ of about 15 cm at t = 840s. The instabilities marked (i – v) were traced to investigate their growth rates and patterns as shown later in figures 2-39, 2-40.

91
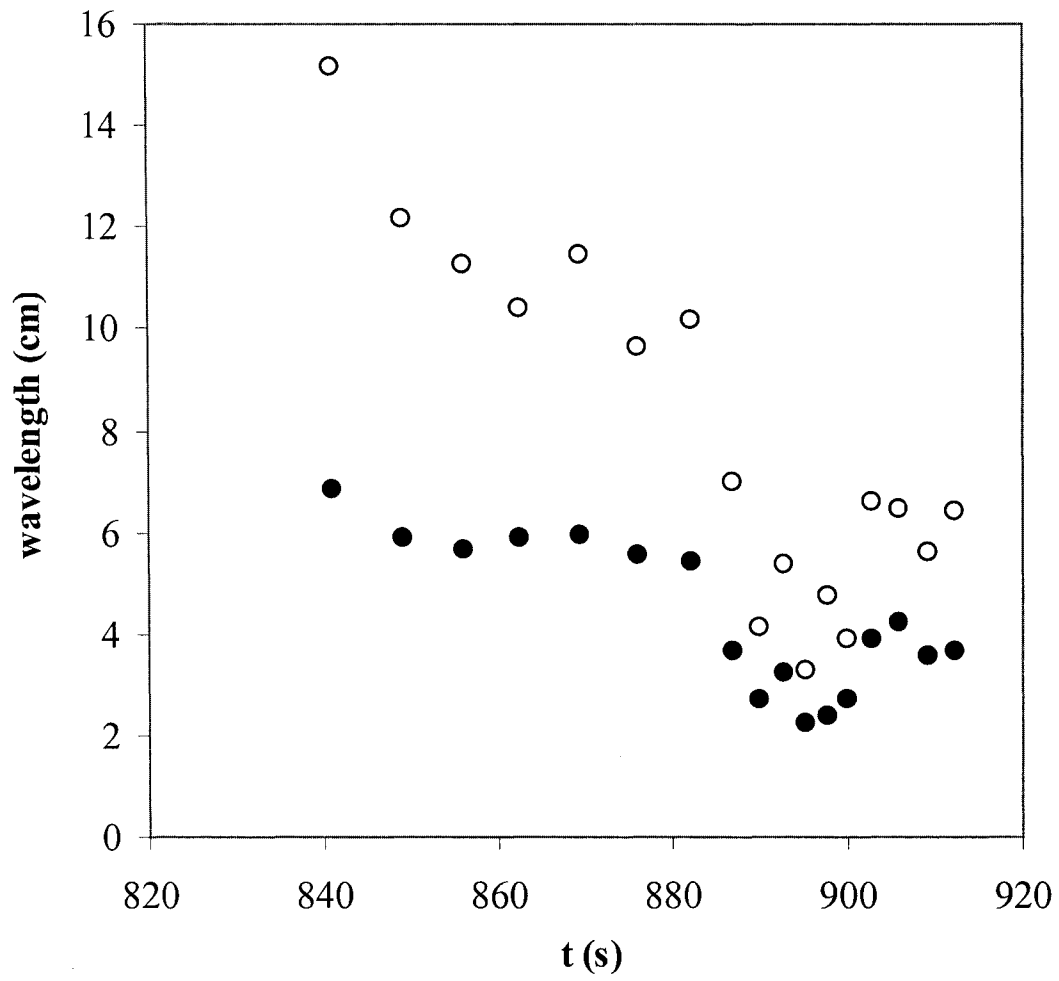
FIGURE 2-38. The temporal variation of the wavelength, λ, at x = 15 cm in Exp 1 showing a clear decay as time proceeds. (•) represents data based on depth-averaged flow velocities, while (o) reflects data based on interfacial wave speeds obtained from the wave characteristics' plot.

92
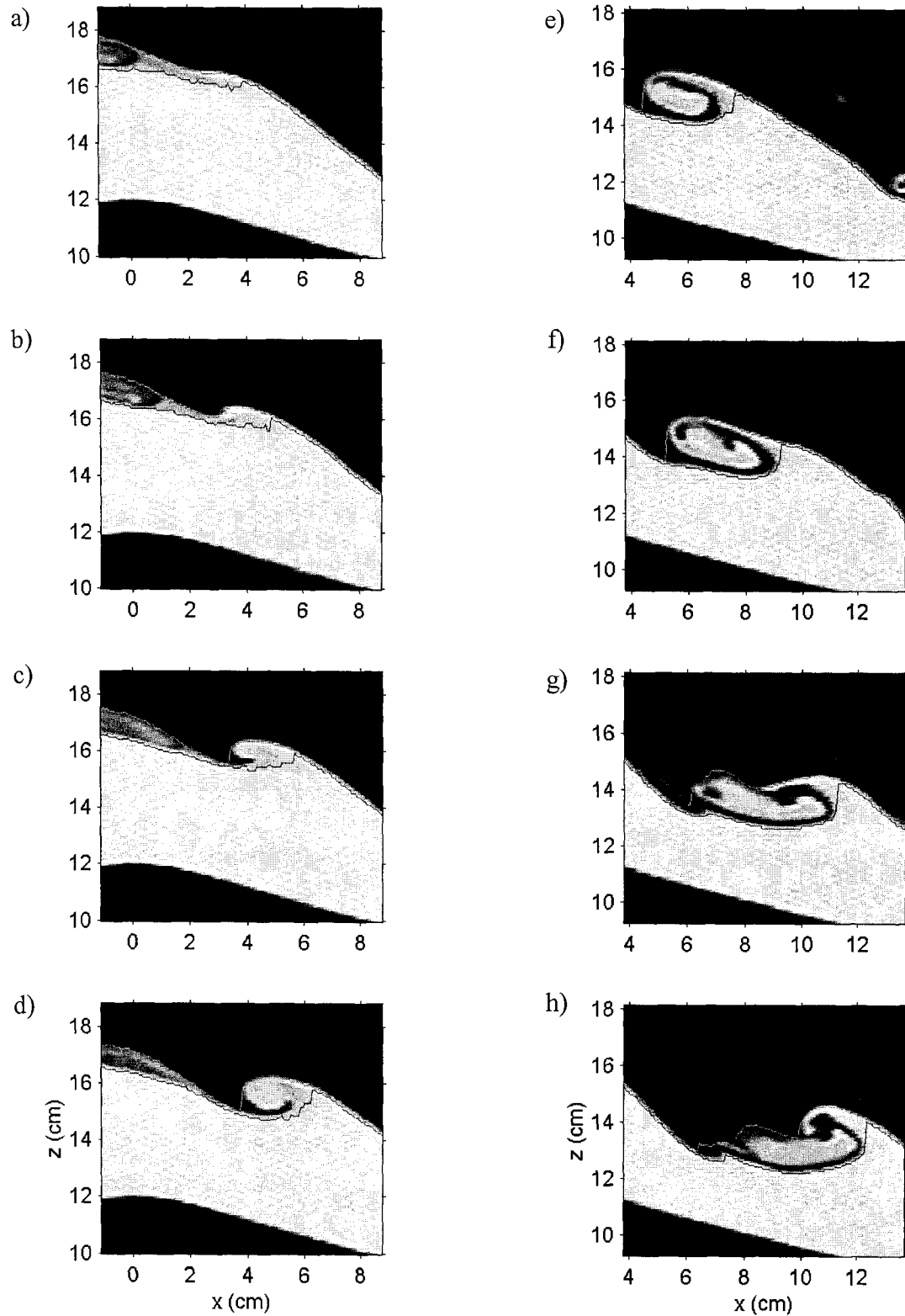
FIGURE 2-39i. Sequence of images showing the growth of the late K-H instability (i) in Exp. 1. Images (a – g) are one second apart starting at 13.82 min., while image (h) is at 0.6 s following image (g).
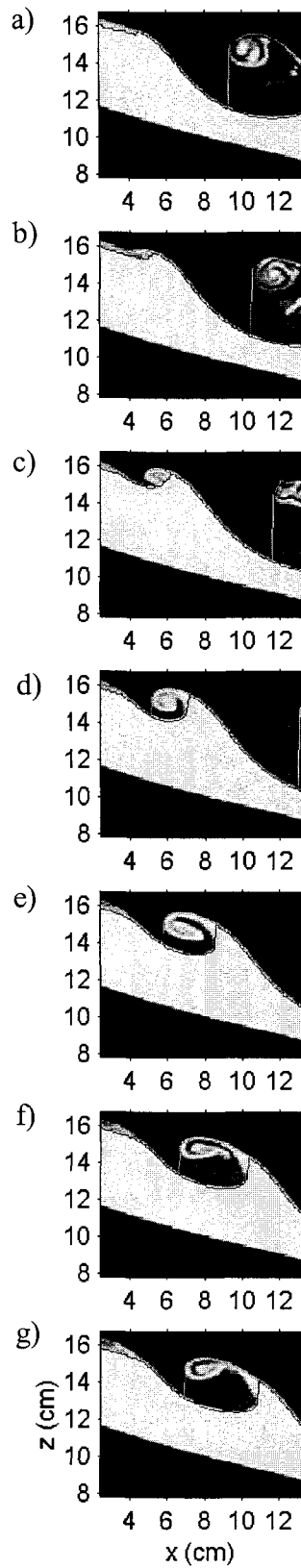
FIGURE 2-39ii. Sequence of images showing the growth of the late K-H instability (ii) in Exp 1. Images are one second apart starting at 14.1 min.

94
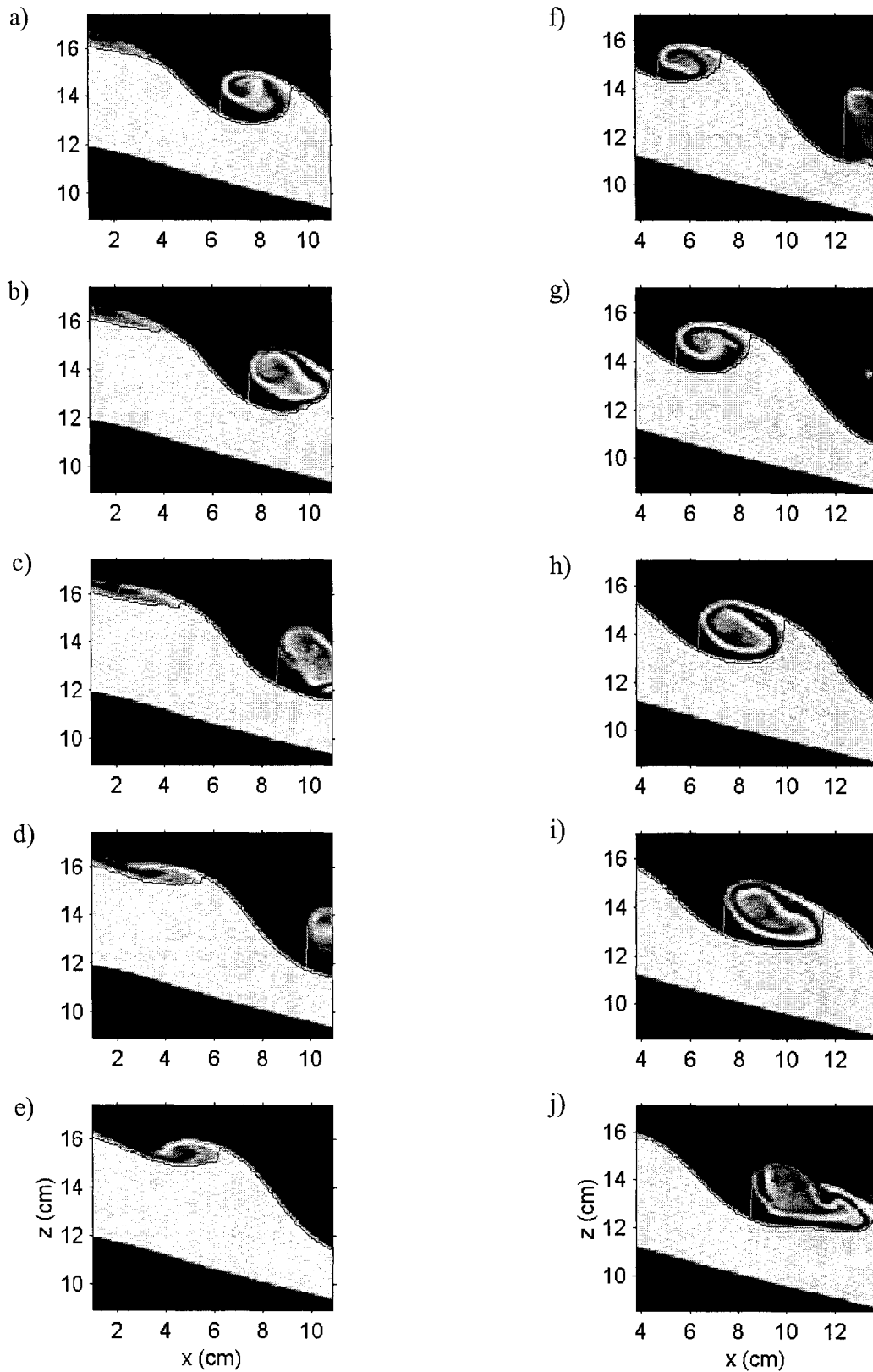
FIGURE 2-39iii. Sequence of images showing the growth of the late K-H instability (iii) in Exp 1. Images are one second apart starting at 14.28 min.

95
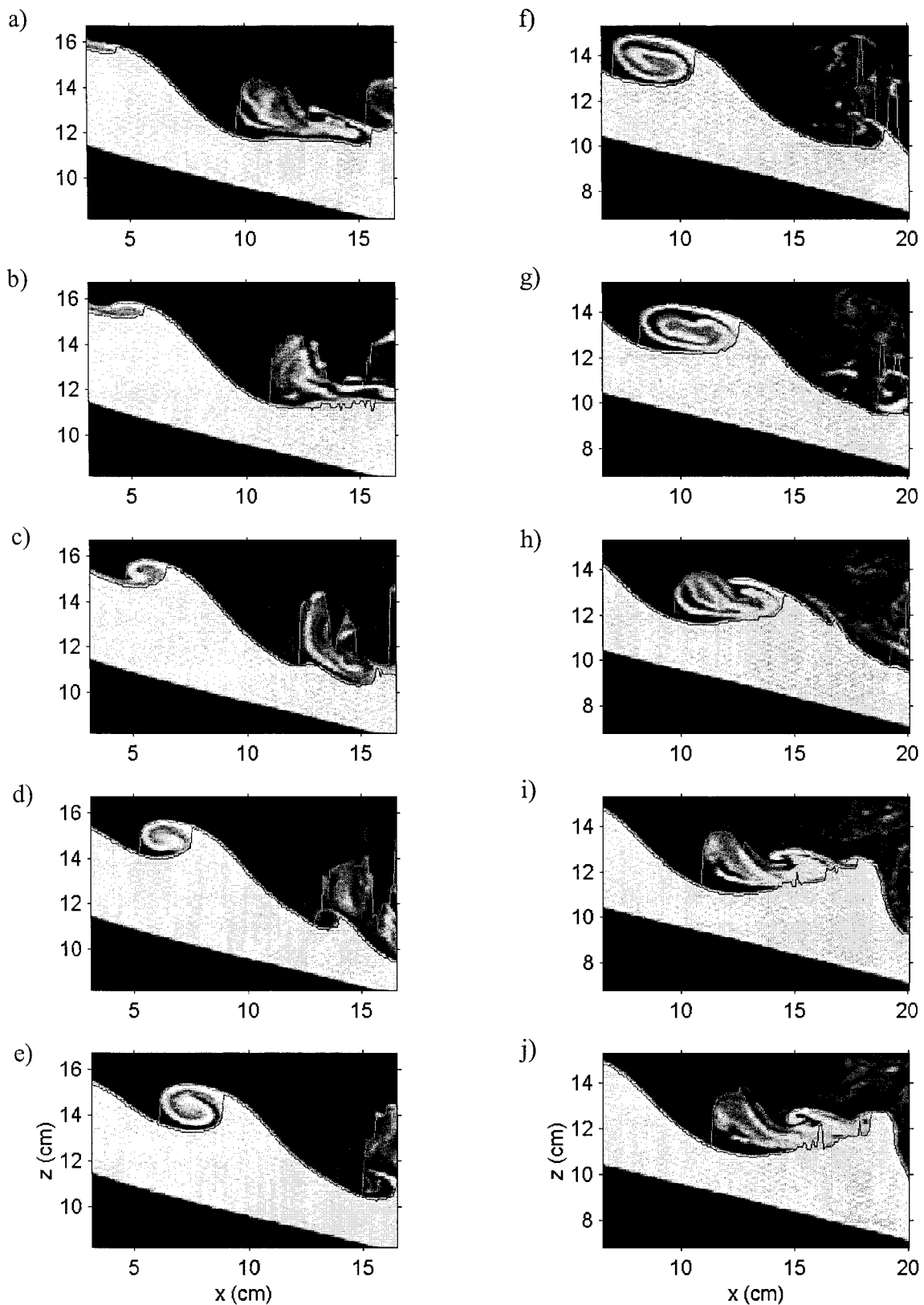
FIGURE 2-39iv. Sequence of images showing the growth of the late K-H instability (iv) in Exp. 1. Images (a – i) are one second apart starting at 14.45 min., except for image (j) which is 0.4 s following image (i) and at which time the instability got distorted.

96
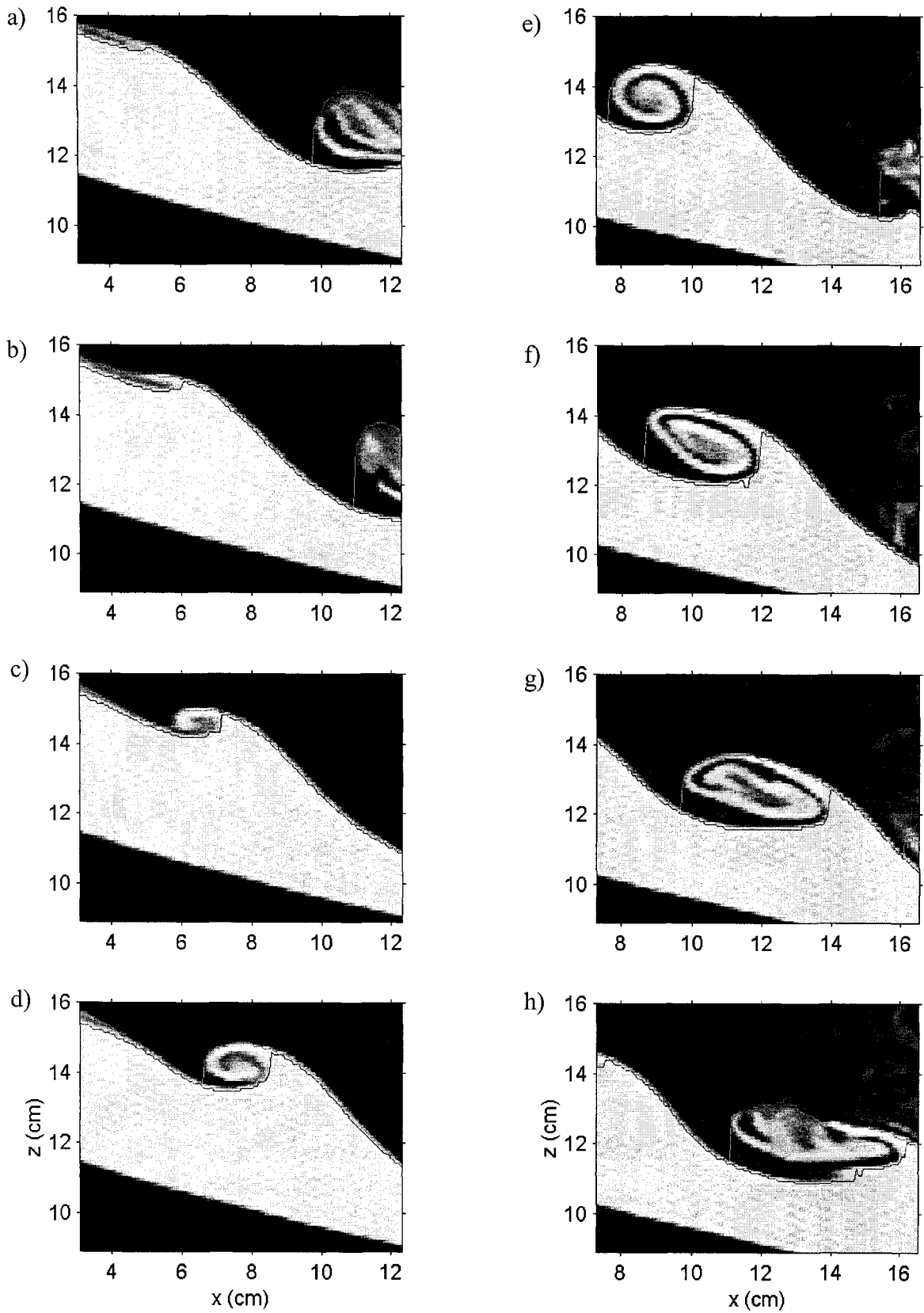
FIGURE 2-39v. Sequence of images showing the growth of the late K-H instability (v) in Exp. 1. Images are one second apart starting at 14.56 min.

97
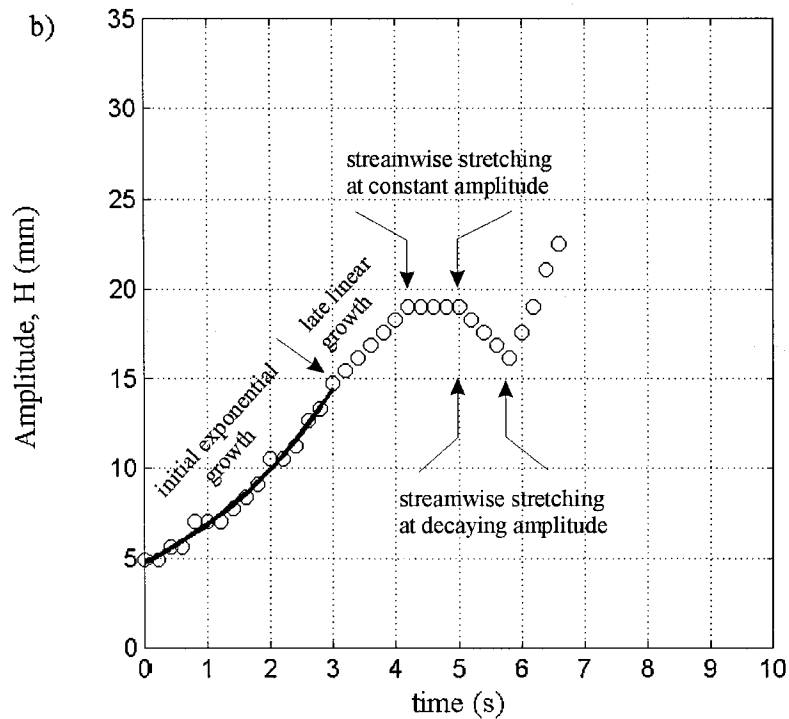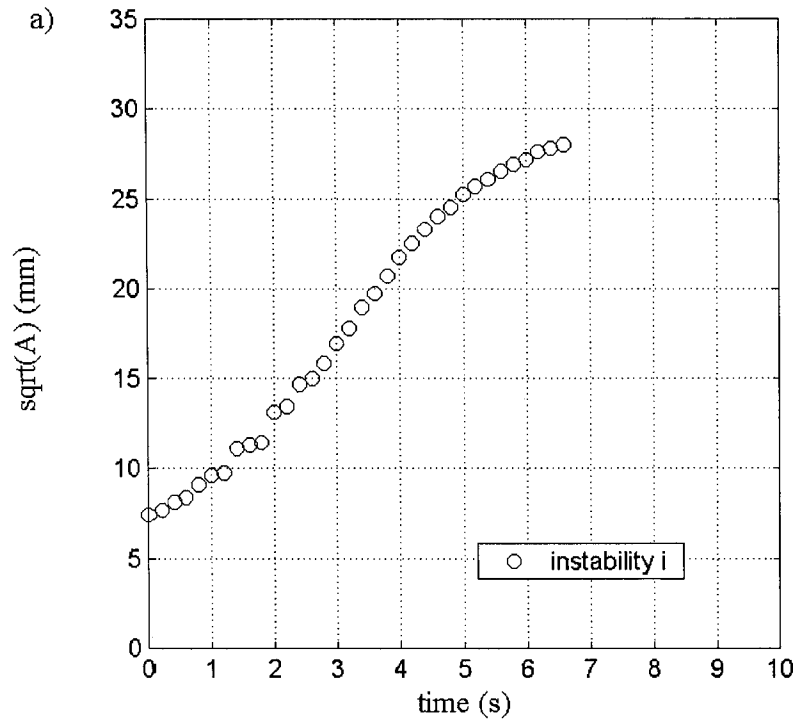
FIGURE 2-40i. a) the temporal growth of the size of instability (i) represented by the square root of its area; and b) the corresponding development of its amplitude, H. An exponential initial growth curve is over-plotted.

98
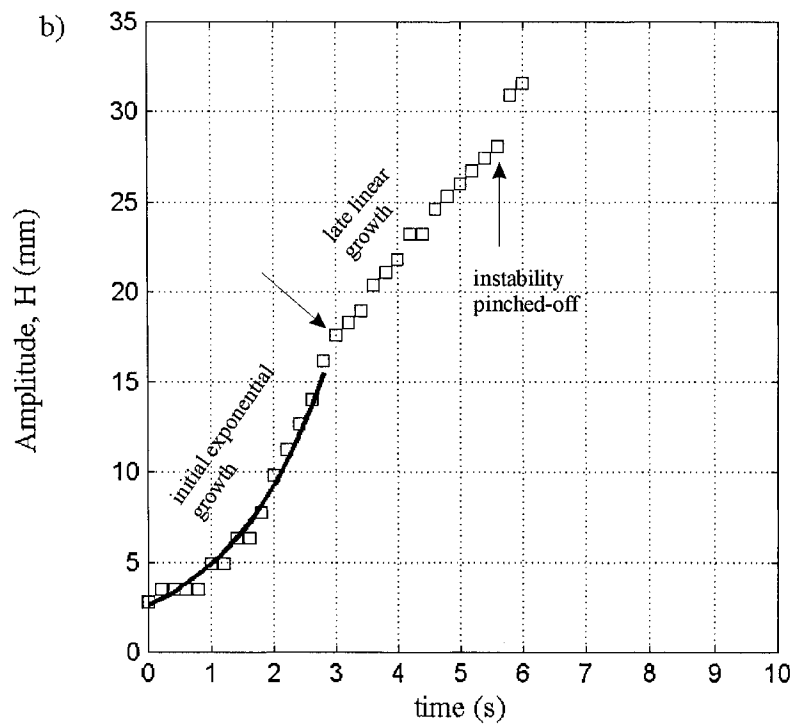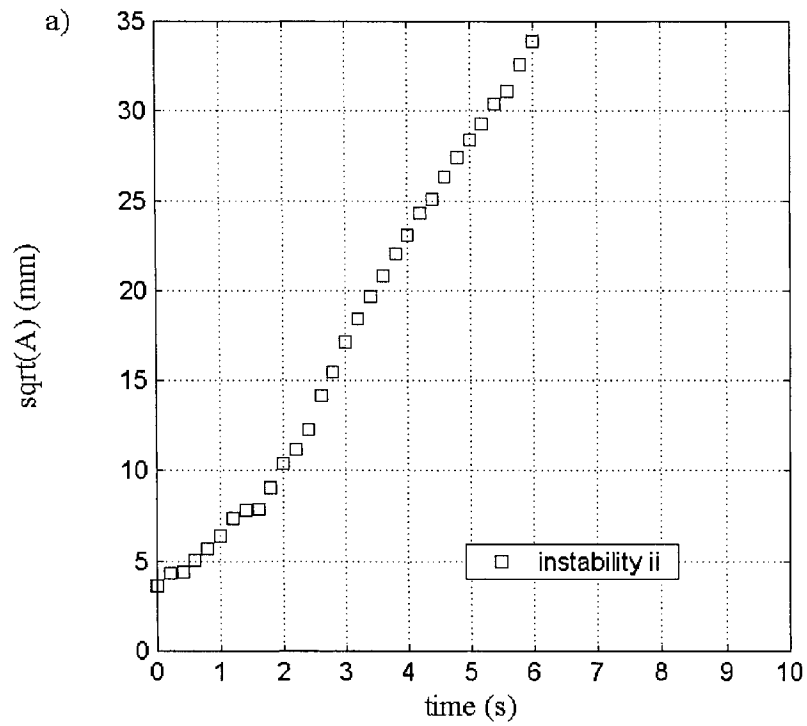
FIGURE 2-40ii. a) the temporal growth of the size of instability (ii) represented by the square root of its area; and b) the corresponding development of its amplitude, H. An exponential initial growth followed by a linear growth is observed.

99
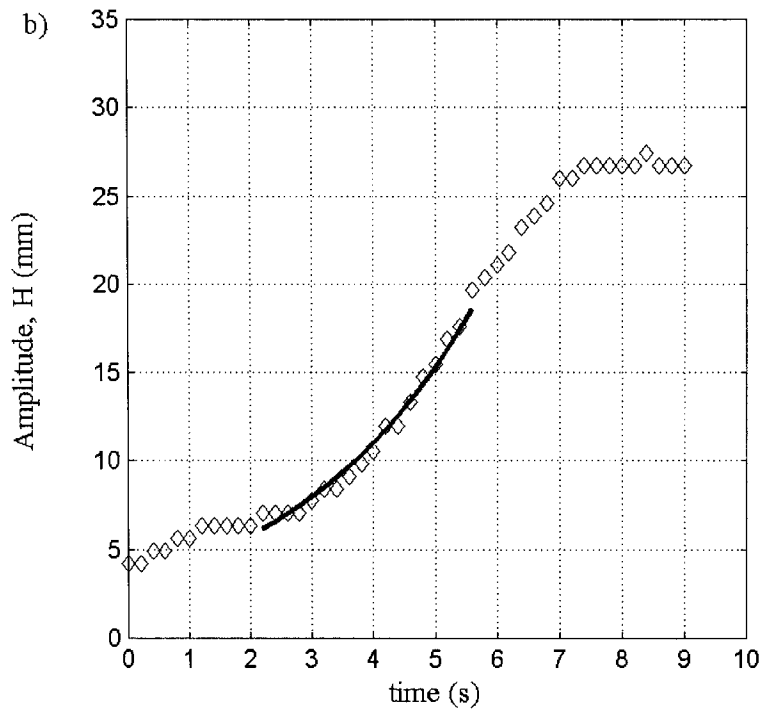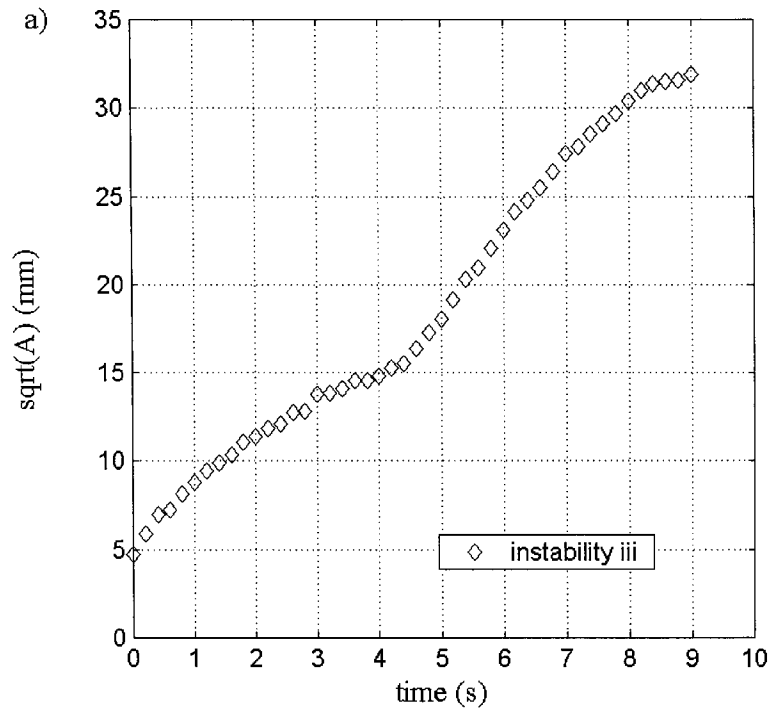
FIGURE 2-40iii. a) the temporal growth of the size of instability (iii) represented by the square root of its area; and b) the corresponding development of its amplitude, H. An exponential initial growth curve is over-plotted.

100
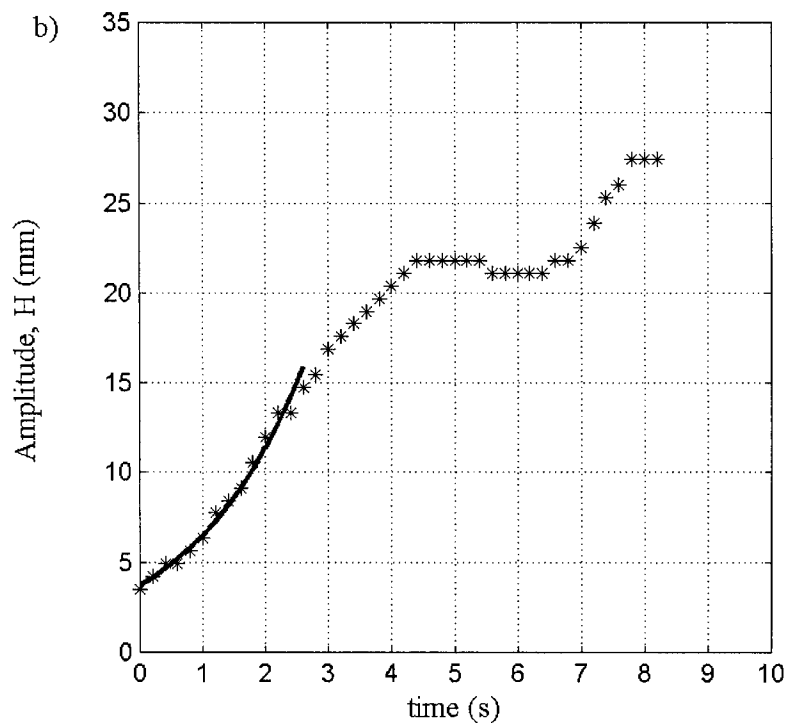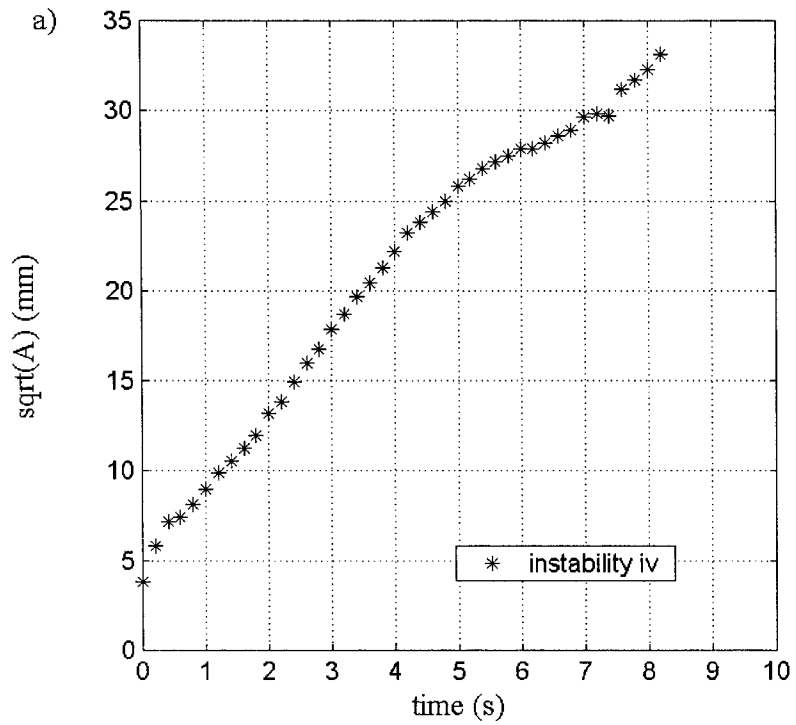
FIGURE 2-40iv. a) the temporal growth of the size of instability (iv) represented by the square root of its area; and b) the corresponding development of its amplitude, H. An exponential initial growth curve is over-plotted.

101
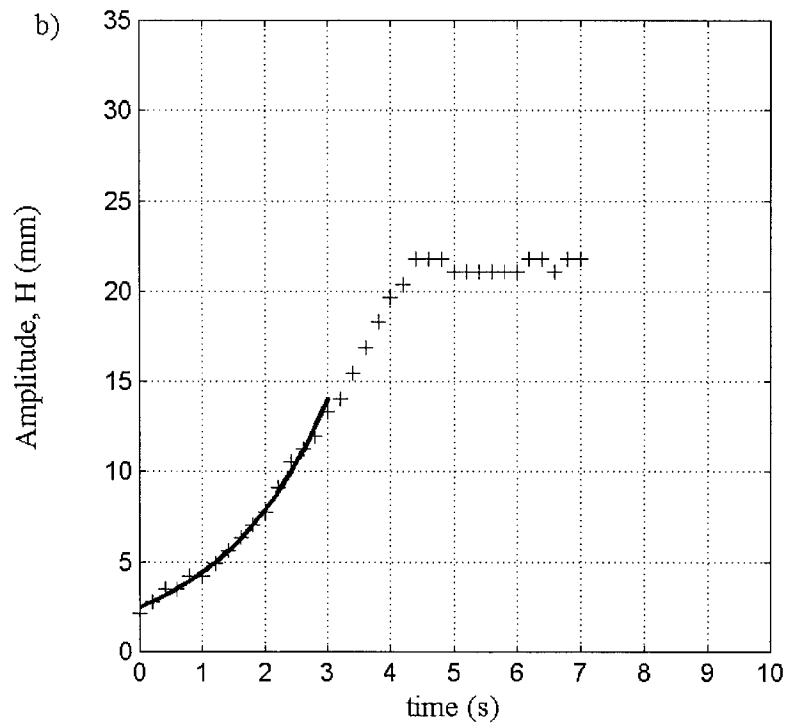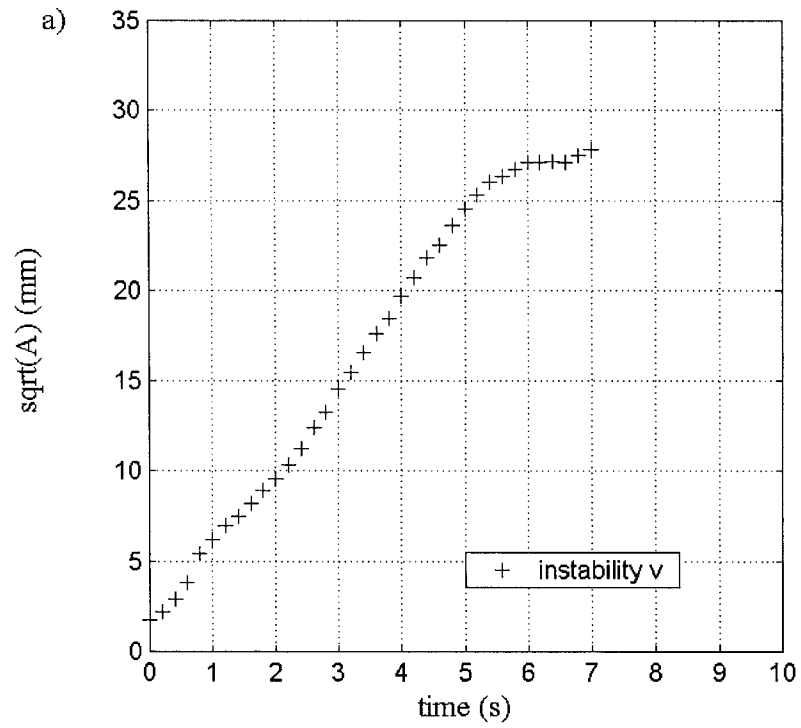
FIGURE 2-40v. a) the temporal growth of the size of instability (v) represented by the square root of its area; and b) the corresponding development of its amplitude, H. An exponential initial growth curve is over-plotted.

102

Table 2-1. List of experiments and their parameters. Fields of view are defined with reference to the sill crest being at x = 0.

Experiment	g' (cm/s^2)	Velocity data		Density data		Duration (min.)
		Resolution (cm/pixel)	Field of view (cm)	Resolution (cm/pixel)	Field of view (cm)	
1	1.62	0.0687	-12.60 : 31.36	0.0706	-14.47 : 30.71	18
1a	1.62	0.0286	-2.66 : 26.14	0.0602	-7.70 : 30.82	15
2	3.23	0.0534	-25.00 : 47.75	0.06	-26.22 : 34.26	15
3	6.47	0.0612	-14.41 : 23.43	0.0695	-14.59 : 29.88	4
4	18.03	---	---	---	-16 : 49	9

Table 2-2. The ratio of the standard deviation of the intrinsic mode functions, σ, to the total standard deviation of all modes, σ_{total}, during the maximal exchange as indicative to the relative power of each mode for the time series shown in figure 2-21.

mode	C1	C2	C3	C4	C5	C6	C7	C8	C9
% σ/σ_{total}	2.49	2.96	5.59	5.36	9.24	28.10	25.72	10.69	9.85

103

CHAPTER 3

EFFECT OF FLOW REGIME ON INTEFACIAL WAVES UPSTREAM TO A BOTTOM TOPOGRAPHY[2]

3.1 INTRODUCTION

When two water bodies at slightly different densities are brought in contact, exchange flow starts. Such flows are common in nature, for example, the exchange of more saline Mediterranean Sea water with less saline Atlantic Ocean water through the Strait of Gibraltar (Armi & Farmer, 1988; Bray et al., 1995) and the summertime exchange of warmer heavily polluted Hamilton Harbor water with cooler (more dense) Lake Ontario water through the Burlington ship canal (Hamblin & Lawrence, 1990; Lawrence et al., 2004). A narrow channel or strait usually connects the two water bodies and often the strait has topographic constrictions such as bottom sills, lateral contractions, or their combinations. For the case where only bottom topography exists, an internal hydraulic control is established around its crest. In two-layer flows, up to two controls can exist; hence the second control is around the channel exit where the channel connects to the reservoir. When both controls co-exist, the flow is said to be at maximal exchange. The loss of one of them causes the flow rate to decrease; hence it is termed sub-maximal (Farmer & Armi, 1986).

While there is ample literature on the mean hydraulics of exchange flows through topographic constrictions (see for example: Armi & Farmer, 1986; Lawrence, 1993; Helfrich, 1995; Zhu, 2002), little research has been published on the mechanisms of reservoir-strait interaction and how the latter may affect the exchange and the generated interfacial waves. Examples of recent studies include the exchange between Little Sodus Bay and Lake Ontario (Rueda & Cowen, 2005a, 2005b), and the exchange and circulation of a uniform basin separated from a large reservoir by a smooth sill (Finnigan & Ivey, 1999; Finnigan et al., 2001). The performance of aquatic systems is to a great extent dependent on the underlying hydrodynamic processes (Rueda & Cowen, 2005a). Our understanding of how such systems interact and behave has a crucial environmental and ecological impact on the aquatic systems and can improve our management

---

[2] The contents of this chapter in part have been presented in the 16th Canadian Hydrotechnical Conference, Canadian Society for Civil Engineering (CSCE), Burlington, Ontario, 2003.

104

and maintenance of the different environmental resources.

The existence of a bottom sill in the channel connecting the two water bodies results in accelerating flow field as a consequence of the internal hydraulic response to the topography (Pawlak & Armi, 1998). Equally important is the channel exit for not only around which an internal hydraulic transition occurs, but also because it is the gate through which the strait is connected to the reservoir. A key question in these flows is what causes the regime to change and whether the exchange is controlled by internal processes in the reservoir or it is channel-based. The dynamics of the outflow leaving the channel into the reservoir is another issue that is poorly understood and has not been well investigated. The present study contributes towards the understanding of these processes.

The interaction between stratification and geometrical boundary conditions is complicated and still requires comprehensive studies. A multitude of internal waves can be generated due to such interaction. For example, Pawlak and Armi (1998, 2000) observed Kelvin-Helmholtz (K-H) instabilities in hydraulically controlled wedge flow down a mild incline. Farmer and Armi (1999), Armi and Farmer (2002), and Cummins et al. (2003) described how internal solitary waves could be generated in the immediate vicinity of the sill crest at Knight Inlet due to internal hydraulic transition. Zhu and Lawrence (2001) observed Holmboe instabilities in their laboratory experiments on two-layer exchange flows over bottom sill within the sub-critical flow field. Morin et al. (2004) observed K-H instabilities in two-layer exchange flow over bottom sill within the super-critical flow reach. More recently, Nash and Moum (2005) observed plume-generated large-amplitude internal waves due to the discharge of the Columbia River into the Pacific Ocean. In the atmosphere, Zheng et al. (2004) presented results from true satellite images on the coexistence of upstream and downstream solitary wavetrains around Hainan Island in the South China Sea. In chapter 2 of this thesis, K-H instabilities were observed to be generated around the sill crest and propagated upstream where the flow is internally sub-critical.

All these instabilities and waves can generate turbulence that leads to mixing. Mixing is important in not only controlling the vertical transfer of heat, nutrients and mass; but also because it restricts the exchange between the two water bodies. These waves can also stimulate the stirring of sediments and may be of significant hazard to offshore structures. While K-H instabilities are known to have higher entrainment and mixing capacity over Holmboe instabilities, recently Smyth and Winters (2003) reported on numerical evidence of turbulent mixing generated through Holmboe waves. An understanding of the generation and characteristics of those instabilities and waves is required.

In the special case of exchange flows over bottom sills in a channel connecting two reservoirs,

105

the interaction between the reservoir and the channel is affected by the existence of internal controls. Internal controls not only affect the volume flux through the channel, but also have their impact on the waves generated along the channel and their properties. The dynamics of the outflow exiting the channel into the receiving basin has an obvious impact on the water quality of the system and is an important aspect which has not been explored in depth thus far. The whole processes of wave generation and reservoir-channel interaction appear to highly depend on the flow regime. A demanding need for studies that explore the development of those flows both qualitatively and quantitatively does exist.

This study is a preliminary step towards investigating the reservoir-channel interaction, and contributes into the understanding of how the change in flow regimes affects the generated wave activities along the channel and in the reservoir. Because of the nature of the topic that it relates to both the reservoir-channel interaction and internal waves in stratified flows over topography, Section 3.2 is devoted for a literature review on both areas. Section 3.3 then describes the experimental setup and techniques. In Section 3.4, an overview of the hydraulics of the flow is provided and coupled with experimental measurements for comparison and validation. The different flow regimes and the reservoir-channel interaction are assessed therein as well. Section 3.5 then discusses the evolution of the generated interfacial waves within the channel and the alongside part of the reservoir. In Section 3.6, the examination of a low-frequency long wave that was observed around the sill crest in chapter 2 and in previous similar studies (Zhu *et al.*, 2002; Morin *et al.*, 2004) is presented, and the paper is concluded in Section 3.7. While the current study focuses on the reservoir-channel interaction in two-layer exchange flow upstream to bottom topography, the results can be useful for other similar flows including river outflows into seas and oceans.

3.2 LITERATURE REVIEW

Exchange flow and circulation in a basin of uniform depth and width separated from an ocean by a smooth sill was modeled and studied by Finnigan and Ivey (1999). They investigated sub-maximal exchange over a bottom sill that connected a convectively forced basin and a large reservoir. They described two distinct unsteady regimes before the flow adjusted to a final steady state prescribed by the interior mixing within the basin and the hydraulic control at the sill crest. They showed that mixing conditions within the basin can determine how close the exchange is to maximal through the development of a theoretical model which included some coefficients that

106

were functions only of the interface level at the sill crest. Finnigan and Ivey (2000) re-investigated experimentally and theoretically the same problem, that is convectively driven exchange flow in a stratified sill-enclosed basin, based on a momentum balance approach. They showed that the magnitude of the exchange over the sill could be determined to a first order by the horizontal momentum balance within the basin. Their measurements indicated that inertia, buoyancy, friction and surface pressure gradient are all significant contributors in that balance. They illustrated that when the system is at steady state, the exchange is largely determined by the large-scale momentum balance. However, the exchange relative to the maximum limit is a result of the equilibrium between interior processes, such as mixing, recirculation and entrainment, and the hydraulic control at the sill crest, which confirmed their earlier result in 1999. The results indicated that increasing the surface buoyancy flux caused the recirculation and friction to increase, hence the reduction in the relative exchange across the sill. They envisaged that recirculation and turbulent entrainment would be insignificant in long basins.

Finnigan *et al.* (2001) conducted a series of numerical experiments to simulate the response characteristics of a buoyancy-driven sea to complement the studies of Finnigan and Ivey (1999, 2000). Through their numerical simulation they quantified the energetics of the flow within the basin. In the steady state limit, they showed that the rate of energy flux through the system is balanced by dissipation within the basin and advection of potential energy over the sill into the reservoir. They conducted a second set of numerical experiments to quantify the transient energetics prior to the steady state. They used the obtained results for the transient case to derive an expression describing the advection of potential energy across the sill for periodically forced systems.

Ivey (2004) discussed the interplay between topography, mixing and stratification in determining the exchange rate through relatively narrow straits connecting basins with different density fluids. He quantified the exchange using a dimensionless multiplex parameter of the aspect ratio of the strait and a turbulent Grashoff number, whereby a large value of such parameter indicates the exchange can be well estimated using internal hydraulic theory, otherwise the exchange drops below hydraulic predictions and could then be determined through diffusive controls when the parameter is small.

Lake-embayment exchange was studied by Rueda and Cowen (2005a) who analyzed the exchange between a weakly forced lacustrine embayment, Little Sodus Bay, and Lake Ontario through a long shallow channel. They differentiated between the exchange processes observed in lacustrine environment and those observed in large oceanic systems as that of the Strait of Gibraltar for instance. They emphasized different physical processes and forcing mechanisms as

107

determining the net exchange in their study. Among these are baroclinic and barotropic effects due to spatial thermal variations and oscillations in the water level, respectively, bottom friction, diffusion, wind and transient effects. They showed through a combination of scaling analysis, examination of field data and 3-dimensional simulations that bed stress, vertical turbulent diffusion, wind stress and transient effects all depart the exchange from predictions of the internal hydraulic theory. Their numerical simulations indicated that the exchange could be either maximal or sub-maximal depending on the phasing of the internal dynamics in the embayment with respect to the lake and the wind forcing.

Rueda and Cowen (2005b) used the concept of hydraulic residence time, the average time water remains within boundaries of an aquatic system, to describe the multiple complicated processes that generate the transport through the channel connecting Little Sodus Bay and Lake Ontario. Their analysis showed that the temporal variations of the mean hydraulic residence time occurred at interannual, seasonal and down to synoptic time scales which were closely related to the occurrence and frequency of upwelling events. Temperature gradients across the channel were due to differences in thermal inertia at the seasonal time scales, while due to differences in the internal dynamics of the two water bodies at shorter time scales. The exchange was an order of magnitude higher when episodic upwelling events during the stratified season in Lake Ontario caused the largest density gradients across the channel. Baroclinic effects were shown to be generally the dominant transport mechanism in the embayment.

The interaction between two different density water bodies, especially in the presence of geometrical boundary conditions, usually involves the generation of internal waves. Recently, Nash and Moum (2005) described the generation of internal waves due to the Columbia River plume discharging as a gravity current into the coastal Pacific Ocean. Their field measurements indicate that the amplitudes of those plume-generated internal waves are as big as those generated due to tide-topography interaction. Troy and Koseff (2005) investigated experimentally the generation of breaking interfacial waves in two-layer fluid in the absence of bathymetric variation. They demonstrated that breaking mechanisms can vary widely and distinguished between two types of breaking, namely: forcing wavetrains through lateral contraction in which the wave breaking mechanism is a shear instability produced solely through wave shear, and focusing of a dispersive wavetrain at a location when longer waves in the packet locally augment the shear experienced by a shorter wave causing the latter to break convectively. In both cases wave shear is the destabilizing force, but in the former wave breaks because of a modified K-H instability, whereas in the latter it breaks due to a convective instability.

With reference to long waves, their generation in stratified flows over topography has been

108

reported by many researchers particularly numerically through solving an internal Korteweg-de Vries (KdV) type equation. For example, Lee & Beardsley (1974) solved the equation numerically to demonstrate the relative importance of non-linearity and dispersion on the generation of large amplitude internal gravity waves from a local isolated internal disturbance or a front in a stratified shear flow. Their numerical results were in good agreement with laboratory experiments in which long internal waves were generated by moving a submarine ridge in a tank to create transient internal disturbances. Grimshaw and Smyth (1986) studied analytically and numerically near resonance flow of a continuously stratified fluid over topography in the long-wavelength weakly nonlinear limit using a forced KdV equation. Their results showed the possible existence of significant upstream disturbances, which they interpreted as either solitary waves or an oscillatory wavetrain produced by the topography. They indicated that the polarities of the disturbances and that of the topographic forcing would determine which upstream effect could appear. Likewise they predicted the generation of downstream wave packets as a result of perturbations of the topographic obstacle.

Funakoshi (1996) revisited the problem but for two-layer fluid flowing over localized bottom topography and examined the interaction and generation of waves in such a system. He discussed both the resonant interaction between a long internal mode and a wave packet of short surface mode, and the generation of long internal mode due to the resonant motion of the fluid with respect to the bottom topography. He reported that in the case of resonance, an incident soliton could be reflected at the topography and amplified or could pass through it with final deformation if it had sufficient energy. Another recent study by Hogg *et al.* (2001) investigated numerically the propagation characteristics of linear internal waves in exchange flows within a laterally gradually contracting channel, which connected two different density reservoirs. While their study was restricted to the steady exchange, they introduced diffusion into the governing equations and showed in their direct excitation numerical experiments that for an interfacial perturbation, upstream to the control point at the maximum contraction, which simulated a long wave traveling on the density interface, information propagated in both directions. That was unlike the hydraulic solution which predicted that a wave generated to the left of the contraction can not propagate information to the right end of the domain. They introduced a new notion of the hydraulic control in view of the propagation of information and reported on an upstream shift of the control point which increased as the barotropic flow rate increased.

The existence of a low frequency interfacial oscillation was observed upstream and at the sill crest in two layer exchange flows over a sill (Morin *et al.*, 2004). They attributed such long wave to the internal basin seiche and presumed that its energy, while continuously degrading downwind

109

the sill crest, got transferred into higher frequency waves that they related to the large-scale K-H instabilities. Similar low frequencies were observed earlier in a study of exchange flow through openings (Zhu et al., 2002) in the same facility. The phenomenon of the degeneration of long interfacial gravity waves into high frequency waves has been reported in other studies. For example, Horn et al. (2001) studied the degeneration of large-scale interfacial gravity waves in lakes. They assumed a simple two-layer model and introduced mechanisms for the transfer of energy from an initial basin-scale seiche to shorter waves that resulted in localized turbulent mixing and enhanced dissipation as they broke at the boundaries.

For the current flow setup, a schematic of which is presented in figure 1-2, two controls can occur at the sill crest and the channel left-hand exit (Morin et al., 2004). In this study, our interest is a three-fold one, namely: a) to examine how the change in flow regime affects the reservoir-channel interaction, b) to investigate the evolution and properties of interfacial waves within the channel and the alongside part of the adjacent reservoir, and c) to explore the low-frequency long-wave that was observed upstream and at the sill crest in Zhu et al. (2002) and Morin et al. (2004).

3.3 EXPERIMENTAL SETUP AND TECHNIQUES

Two-layer exchange flow over a smooth bottom sill in a 10 cm constant-width rectangular channel was modeled in the laboratory (figure 1-2: b, c). The sill had the shape: $h(x) = h_m cos^2(\pi x/L_s)$, with its maximum amplitude at the crest $h_m = 10$ cm, and its total length $L_s = 50$ cm, x being the horizontal distance measured from the crest. The crest is at about 84.5 cm from the left-hand side of the left reservoir. The axes are defined such that along the central plane within the channel, the crest is at $x = 0$, the positive x-axis points leftwards, the positive z-axis points upwards and the positive y-axis points into the tank normal to the channel walls. The channel exit is at $x = 37.5$ cm. The tank was first filled with fresh water to a total depth, H, of 30 cm. A vertical barrier was placed to the left of the sill at its toe to divide the tank into two reservoirs. NaCl salt was added into the left reservoir to create small density difference between the waters of the two reservoirs. Three experiments, namely Exp 1, 2, and 3 were conducted with $g' = 1.62$, 3.23, and 6.47 cm/s^2, respectively, where g' ($= \varepsilon\ g$) is the reduced gravity, with $\varepsilon = (\rho_2 - \rho_1)/\rho_2$, ρ_1 and ρ_2 being the density of the upper and lower layer, correspondingly. Exp 1 was repeated three times where two runs, hereafter referred to as Exp 1a and 1b, focused on the interfacial fluctuations within two different fields of view, namely the front view (A-A) within the

110

connecting channel and the side view (B-B) within the salt water reservoir (refer to figure 1-2c). The third run, referred to as Exp 1c, focused on the velocity fields for the front view (A-A). Exp 2 and 3 focused on the interfacial fluctuations within view (A-A) at g' of 3.23 and 6.47 cm/s^2, respectively. Table 3-1 lists all the experiments and their properties.

In using DPIV to measure the velocity fields, silver-coated spherical glass particles, with a mean diameter of 15 μm and a specific gravity of 1.65 (Potters Industries, Paoli, Pennsylvania), were seeded in both reservoirs and well mixed with the fresh water prior to placing the barrier and dissolving the salt. A small submersible pump circulated the water for long enough time to ensure efficient mixing of the particles and also avoid any temperature differences between the water in the two reservoirs. Fluorescein dye, which has excitation and emission wavelength peaks of 490 and 510 nm respectively, was well mixed with the salt water in the left reservoir to allow visualizing the lower layer. The use of the submersible pump in the left reservoir then ensured homogeneous distribution of dye and salt. A laser sheet was produced through a 5W argon-ion laser (Stabilite 2017, Spectra-Physics Lasers) operating at a wavelength of 514 nm, and a fiber optical cable (OZ Optics Ltd.) transmitted the light then to a top-located lens that produced a laser sheet of 2 mm width. The laser sheet was at the center of the connecting channel for view (A-A), while 10 cm away from the left-hand wall for view (B-B). Two cameras were used during the measurements: a progressive scan full frame shutter CCD camera (Pulnix TM-1040, Pulnix America Inc.) with a resolution of 1008x1008 pixels and a 10-bit dynamic range for recording PIV images, and a digital Hi8 Sony video camera for density fields' images.

The field of view for the PIV images was initially about 56x56 cm. The images were cropped a little above the free surface and below the bed to allow a field of view of 55 cm (horizontal) x36 cm (vertical) with pixel resolution of 0.06 cm/pixel. The PIV camera was connected to a personal computer which had image acquisition software (Video Savant, I.O. Industries Inc.) and a frame grabber (Road Runner, Bitflow), both of which allowed capturing and streaming the PIV images at a rate of 30 Hz. The raw velocity fields were computed using a standard cross-correlation PIV algorithm (Marxen, 1998). The interrogation window size was set to 32 by 32 pixels and the size of the search window was set to 64 by 64 pixels. A 50% window overlap was used in order to increase the nominal resolution of the velocity field to 16 by 16 pixels. After removing the velocity vectors below the channel bed and above the free surface, a scheme based on a local median test was used to correct for the erroneous vectors within the flow field (Morin, 2002). Then, all the vectors were interpolated onto regular grid points using Adaptive Gaussian Window (AGW) interpolation (Agüí & Jiménez, 1987).

111

The interface position images were 640x480 pixels. They covered a field of view of approximately 80 cm (horizontal) x 32 cm (vertical) for view (A-A) at a resolution of about 0.14 cm/pix, and 75 cm (horizontal) x 32 cm (vertical) for view (B-B) at a resolution of about 0.17cm/pix. They were digitized at the rate of 5 Hz. An algorithm based on the differing gray scale values of the upper and lower layers was used to estimate the interface position. Because of the existence of rolling interfacial K-H instabilities (figure 3-1: image a), a base interface level, which would border the lower part of the instability, is first determined at all locations through a bottom-top scheme. To account for the rolls, the pixels above the base interface having bright gray scale values as part of the lower layer are integrated across depth to provide an excess equivalent depth. The true interface position is estimated as the base interface level plus the excess depth. The scheme is similar to that used previously in chapter 2 and is described therein in more detail. Within the reservoir (view B-B) though (see figure 3-1: image b), and because of the intensive mixing filling the upper layer most of the times, the true interface position was considered as the base interface only. The interface positions were obtained as a time series at all locations for the two views (A-A) and (B-B). The fluctuations of the interface defined in this way are expected to provide information on the different wave activities, but can not indicate the height of the K-H billows. To have an estimate of the height of those billows, an upper interface is detected in a similar fashion to the base interface previously introduced. The difference between the two interfaces, the upper and base, would give the wave height as will be shown later.

3.4 FLOW REGIMES AND RESERVOIR-CHANNEL INTERACTION

3.4.1 Overview of the hydraulics and flow regimes

The hydraulics of two-layer steady exchange flow over smooth bottom sill in a constant-width channel (see figure 1-2c) has been studied by Morin et al. (2004) using the internal hydraulic theory. In what follows a brief account of the theory is given. The energy head (or Bernoulli constant) for layer i (i = 1, 2 for the upper and lower layers, respectively) is:

$$E_i = p + \rho_i g z + \tfrac{1}{2} \rho_i U_i^2 \qquad (3.1)$$

where p, ρ_i, g, z, are the pressure, density, gravitational acceleration, vertical coordinate and U_i

112

$(U_i = q_i/z_i)$ is the horizontal velocity, in which q is the flow rate per unit width and z_i is the layer depth. In studying two-layer flows, the internal energy, E, is commonly used. It is defined as:

$$E \equiv (E_2 - E_1)/(\rho_2 - \rho_1)g \qquad (3.2)$$

Assuming hydrostatic pressure distribution, the internal energy becomes:

$$E = z_2 + h + (U_2^2 - U_1^2)/2g' \qquad (3.3)$$

where h is the sill height. This study considers flows with small density differences for which the relative density difference $\varepsilon \ll 1$.

The internal Froude number, G, describes the criticality of two-layer flows to interfacial waves and is defined as:

$$G^2 = F_1^2 + F_2^2 \qquad (3.4)$$

where F is the densimetric Froude number ($F_i^2 = U_i^2/g'z_i$). Locations where $G = 1$ are called internal controls. G is similar in its significance to the traditional Froude number in single-layer flows and can be used to determine whether the flow is internally super- ($G > 1$) or sub-critical ($G < 1$). Two-layer exchange flows can have up to two controls. With two controls, the flow is at maximal exchange and could be considered steady; whereas with one control only it is sub-maximal and unsteady. For the exchange flow shown in figure 1-2b, the maximal exchange flow has two controls located roughly at the sill crest and the channel left-hand exit. Recent studies of hydraulically driven stratified sill flows indicated that mixing and entrainment could cause an upstream or downstream shift in the location of the hydraulic control depending on the direction of flow and strength of the upper layer (Nielsen et al., 2004). The exchange flow is sub-critical in the region bounded by the controls, but super-critical immediately outside. Thus, the flow is steady and not affected by variations in reservoir conditions.

The solution to the maximal exchange flows can be obtained in a simple way graphically using the control curve approach (Zhu, 2002). The control curves at the sill crest and the channel exit are shown in figure 3-2a for $h = 10$ cm and $g' = 1.62$ cm/s^2, which applies to the current Exp 1. For maximal exchange flows, the flow rate is predicted at the intersection of the two control curves, which gives a predicted flow rate of ≈ 24.46 cm^2/s at an internal energy of about 19.59 cm. Within the maximal exchange regime where both controls at the channel exit and the sill

113

crest exist, the variation of the internal energy, E, with the lower layer depth, z_2, at both locations can be obtained and is shown in figure 3-2b for the same values of h and g' stated earlier. At the predicted energy obtained from figure 3-2a, the internal hydraulic theory estimates the lower layer depths at the crest and the exit as 7.73 and 22.75 cm, respectively. These values will be compared shortly with our experimental measurements of the flow rate and layer depths. In addition, the control curves will be used to predict the flow rates, to a first order, in the sub-maximal regime as will be presented in what follows.

To assess the flow regimes, it is necessary to trace the interfacial fluctuations at the sill crest and the channel exit being the two viable hydraulic controls in the experiments. The time series of the interface positions', as defined in Section 3.3, were extracted at both locations in Exp 1a, 2, and 3 (figure 3-3). The fluctuations in the interface, mainly because of K-H instabilities as reported in chapter 2, are remarkably bigger in amplitude but less frequent at the sill crest than at the channel exit. The vertical scale range in figure 3-3 is kept constant for comparison. As mentioned earlier, there is an initial unsteady period before the interface attains a quasi-steady position. This initial adjustment lasts longer at the crest than at the exit and its duration seems to be in inverse proportion with g'. The loss of the control is marked by the continuous gradual drop in the level of the interface. It can be seen that the interface starts to drop at the exit earlier than at the crest. Because of the lag of the interface at the crest to attain the quasi-steady value and its prior drop at the exit than at the crest, the steady maximal exchange is valid only in the overlap when the interface is at the quasi-steady level at both locations. During this time, the two controls co-exist. This time is estimated as 120 s, 80s, and 65s for Exp. 1a, 2, and 3, respectively (note that this time of steady maximal exchange is in close inverse proportion with $\sqrt{g'}$).

The time-averaged interface position at the exit during the quasi-steady period in the three experiments is about 23.5 ± 0.2 cm. The corresponding value at the sill crest is approximately 18.5 ± 0.4 cm ($z_2 = 8.5 \pm 0.4$ cm). Recalling the predictions of the internal hydraulic theory for the lower layer depth of 22.75 cm at the exit and 7.73 cm at the crest, our measurements are in close agreement with theory with an error of about 4% at the exit and 15% at the crest. Note that the internal hydraulic theory does not account for the significant streamline curvature in the neighborhood of the crest, nor does it account for interfacial friction, entrainment and viscous effects. Nielsen $et\ al.$ (2004) indicated theoretically that entrainment can affect the interface height, and Morin $et\ al.$ (2004) provided experimental measurements that showed similar effect as compared to predictions of internal hydraulic theory. If the lower layer depth, z_2, is scaled with the total flow depth, (z_1+z_2), the non-dimensional lower layer depth would decrease from about 0.78 at the exit to approximately 0.43 at the crest. Similarly, the non-dimensional upper layer

114

depth would decrease on the average from about 0.57 at the crest to 0.22 at the exit; hence both layers accelerate each in its direction of flow.

Reconstructed images of the two layers at the exit in the three experiments are shown in figure 3-4. Although they are similar to figures 3-3: a, b and c, they show in addition that at the moment the sub-maximal regime begins, an intermediate layer of medium density starts to form. This intermediate layer thickens with time and its thickness is directly proportional to g'. It is quite interesting to observe in all three experiments a remarkable interfacial dip down, which marks the moments at which the loss of the exit hydraulic control occurs. This generic feature could be a consequence of the relaxation of the hydraulic control (Farmer & Armi, 1999) and is also similar to the large downward displacement of near surface waters reported by Nash and Moum (2005) in their study of the Columbia River plume discharging into the Pacific Ocean. A closer look towards the end of the experiments reveals the existence of relatively larger less frequent K-H rolls than during the maximal regime. The frequency and amplitude of fluctuations get bigger as g' increases and the temporal growth of the intermediate layer is clear. During the maximal regime, the interfacial mixing is flushed away due to the accelerating flow field within the two layers. The mixing that occurs due to the finite-amplitude K-H instabilities upon their break is intermittent and a sharp interface is usually attained in the wake of the instabilities.

The instantaneous velocity fields were obtained for view (A-A) in Exp 1c and corrected for as stated previously in Section 3.3. At any location, the horizontal velocity, u, was integrated across depth in each layer to obtain the flow rate per unit width, q, at that location. The instantaneous variation and temporal development of the lower layer flow rate, q_2, at the sill crest as an example is shown in figure 3-5 for a duration of about 11 minutes from the start of the experiment. The flow rate initially increases through an unsteady phase until it reaches a steady maximal exchange whose mean is approximately 23.78 cm^2/s. This is in very close agreement to the prediction of the internal hydraulic theory (figure 3-2a) with a relative error of about 2.8 %. We estimate the unsteady period at the sill crest to be about 2 minutes as was shown earlier in figure 3-3d for the interface position at the crest in Exp 1a. The flow becomes sub-maximal afterwards as shown by the decay of the time series in figure 3-5 although as mentioned previously with the leading loss of the hydraulic control at the channel exit, the sub-maximal regime has already started. The fluctuations in q_2 follow a similar pattern to those of the interface positions presented earlier in figure 3-3, except that the time series for q_2 lasts a little longer.

While the time series of both of the interface position and flow rate at the channel exit and the sill crest would indicate the different regimes, yet it is the value of the internal Froude number, G, that determines when the hydraulic control is lost. The time series of the instantaneous flow rates

115

per unit width of the upper and lower layers were used along with the interface position to obtain the temporal variation of G at these two locations. Although we do not have actual simultaneous measurements of the flow rates and the layer depths, we consider the results good enough for at least a qualitative description of the processes. Figure 3-6 shows these results which confirm the loss of the exit control after about 200 s from the start of the experiment. The value of G dips down abruptly by the end of the maximal regime as was noted earlier in figure 3-4. The crest control seems to last longer for up to about 6 minutes matching with the measurements of the interface data (figure 3-3d). The fluctuations in G at the crest are larger and less frequent than at the exit as it was reflected as well in the interface positions' time series.

The horizontal velocity, u, was time-averaged over the steady maximal exchange. Sample vertical profiles of the time-averaged horizontal velocities at five locations, namely: $x = 0$ (crest), 9.86, 18.82, 27.79, and 37.5 (exit) cm were selected. These profiles were integrated across depth to obtain the flow rate per unit width, q ($q = Q/b$), along the channel reach. The mean variation of the discharge intensity in the upper and lower layers, q_1 and q_2 respectively, as well as the internal Froude number, G, is presented in figure 3-7. The solution to the maximal exchange flows as presented earlier in this Section can be predicted using the control curve approach. A predicted theoretical flow rate of ≈ 24.46 cm^2/s was obtained at the crest. This is in very close agreement with the measured values at the crest ($q_{1-crest} = 22.76$ cm^2/s and $q_{2-crest} = 23.78$ cm^2/s) with a deviation of 6.9 % and 2.8 % considering the upper and lower layer flow rates, respectively.

Starting at the crest ($x = 0$), while q appears to be almost constant until $x = 10$ cm, we observe a remarkable deviation between q_1 and q_2 as the exit is approached. We anticipate that flow separation within the lower layer as it enters the channel reduces the flow width; hence q_2 increases. An increase of about 34% in q_2 at $x = 28$ cm is measured compared to its value at the crest. While this may be valid for the lower layer, the upper layer experiences no separation as it leaves the channel; hence it appears fairly constant. Zhu (1996) reported such separation in the lower layer. He observed it through a horizontal laser sheet, but reported no data on its effect on the flow rate along the channel. His experiment where he observed separation had H of 28 cm, g' of 1.56 cm/s^2, h_{sill} of 8 cm, $L_{channel}$ (between the crest and the exit) of 103 cm, and q_{crest} of 20.91 cm^2/s, which are relatively close to our Exp 1c. With these values, he could observe a maximum separation thickness of about 3 cm. Although his setup is different from the current and the latter has curved ends, assuming the same thickness to be valid in our experiments would produce an increase in the flow rate, q, of about 43% with respect to $q_{2-crest}$. Definitely the curved ends act to reduce flow separation, yet the measured flow rate increase of about 34% is unexpected given that the estimated errors in the flow rate measurements are within 5%. More detailed

116

experiments, perhaps focusing on smaller field of view around the channel exit and also examining horizontal plans within the lower layer, can be performed to investigate flow separation.

The development of a boundary layer along the side walls of the channel could be another factor that could affect the flow rate, q. The boundary layer will act to reduce the effective width of the flow along the channel; hence higher q values would be achieved. The boundary layer thickness, δ_{BL}, can be roughly estimated in a similar way to that used for a uniform flow along a flat plate. The flow field along the channel in our case is more complicated, however, due to its accelerating nature. Neglecting the curved end parts of the inner wall and considering it as a flat plat whose start is at the channel exit, δ_{BL} would depend on the development length from the exit into the channel, s, and Reynolds number, Re_x ($=U_2 \cdot s/v$) in which U_2 is the depth-averaged velocity along the central laser plane, and v is the kinematic viscosity of the salt water. Table 3-2 shows that Re_x increases from 1168 at s = 9.71 cm to roughly 9180 at the sill crest in Exp 1. These values are much less than 10^5 above which the boundary layer is considered turbulent; therefore the boundary layer is laminar and δ_{BL} is estimated as: $\delta_{BL} \approx 5 \cdot s/\sqrt{Re_x}$ (White, 1999). As seen from table 3-2, δ_{BL} at one side was about 1.4 cm when g' was 1.62 cm/s^2. It kept on increasing to about 2 cm as the flow reached the left toe of the topography. Along the upstream side of the topography and due to the spatial acceleration of the lower layer, δ_{BL} started to decrease slowly as the increase in U_2 overrode that of s. In the experiments with larger g', the velocities were estimated in proportion with $\sqrt{g'}$ and as can be seen δ_{BL} was smaller. Clearly because the channel is narrow (b = 10 cm), δ_{BL} can reduce the width to only 6 cm at some locations.

The variation of G within the reach confirms that the flow is sub-critical ($G < 1$) between the crest and the exit controls, at which G approaches unity. The measurements indicate that the hydraulic control at the crest might be shifted downstream. This seems to agree with Nielsen *et al.* (2004) who reported on possible downstream movement of the control section in response to increasing reverse velocities in the overlying fluid. It is also noteworthy here mentioning that upon observing few sections across width in the channel (refer to chapter 4 for more details), lateral oscillations and interfacial instabilities were observed. The lateral oscillations were biased towards the outer wall of the channel and were referred to the horizontal curvature effect as the lower layer enters into the channel. This provides evidence of different three-dimensional effects that can affect both the flow rates and the composite Froude number, G.

117

3.4.2 Reservoir-channel interaction

Once the barrier separating the fresh and salt water bodies is removed (see figure 3-8: image a), the exchange flow starts with an initial unsteady period before it attains the maximal exchange as stated previously. The interfacial wave activities differ during the course of the experiment and depend on the flow regime. During the initial unsteady exchange, interfacial mixing occurs within the channel (figure 3-8: images a, b). This initial mixing is soon flushed away upon the formation of a two-layer accelerating shear flow structure, and a sharp interface is then established (figure 3-8: images c – e) along which small-amplitude K-H instabilities are being constantly generated in the immediate upstream proximity of the sill crest. These instabilities get quenched in amplitude as they approach the channel exit and in many times they die out and stabilize.

Observations of the video stream of the experiment reveal, however, that sometimes these instabilities would make their way through the channel exit beyond which they remarkably grow into large K-H billows that eventually break causing extensive intermittent mixing (figure 3-9: image f). On the other hand, other instabilities are generated within the channel close to the exit or more frequently right upstream to the exit as the upper layer leaves the channel. The latter is more regular and dominant during the steady maximal regime with both hydraulic controls at the sill crest and the channel left exit established. A possible mechanism for their generation is the rapid internal hydraulic transition as the flow exists the channel (Farmer & Armi, 1999).

During the steady maximal regime, both layers accelerate each in its direction of flow and the pattern of the large amplitude K-H billows, be them of instabilities that started in the channel or right as the upper layer passed the exit, is persistent. Some time later, while the flow is still at maximal exchange within the channel, it appears that the strength of the flow in the basin to the left of the exit weakens enough for interfacial waves reflected at the wall to bounce back and counter-flow against outgoing instabilities (figure 3-9: images g, h); meanwhile the height of those outgoing instabilities decreases. The interface is still relatively sharp at this stage and any mixing which occurs whether within or outside the channel is intermittent and gets flushed away due to the accelerating shear flow. The maximum height of the large K-H instabilities that form outside the channel within the maximal regime as can be seen from figure 3-9 (image f) and the continuous video stream of the experiment is roughly about 5 cm. Note that the level of the interface gradually drops in the reservoir due to the continuous fresh water inflow while its level in the channel is maintained during the maximal regime (compare images f, g).

Eventually the exit control is flooded due to the accumulation of the fresh water in the salt water tank, and the flow becomes sub-maximal. The sub-maximal regime is characterized by the

118

absence of the large K-H instabilities that grew upstream to the channel exit and by the formation of a thin intermediate layer around the exit location (figure 3-9: images i, j). The decaying shear at the interface is no longer flushing the interfacial mixing. As time proceeds, the intermediate layer expands horizontally and the flow is more parallel than accelerating. Eventually, the crest control is lost due to the reduction in the flow rates further below the maximal since the volume of the tank is confined. While very subtle wave activities are observed upstream to the sill crest, a sharp interface along which K-H instabilities are generated is still maintained downstream to the sill crest. It is noticeable as well that the intermediate layer does not expand leftwards towards the wall (figure 3-9: image j). It is the accumulative effect of the small-scale interfacial processes (namely the pairing of instabilities and their collision, and eddy impingement on the interface) that caused the mixing. Such mixing mechanisms were reported previously in a study of turbulence and waves at shear-free density interfaces by McGrath *et al.* (1997).

To observe the flow field in the reservoir, snapshots of view (B-B) at different times during the experiment, Exp 1b at the same g' of 1.62 cm/s^2 as for Exp 1a, are shown in figure 3-9. The fresh water spreads into the left tank and causes mixing, which occupies the upper layer depth within the reservoir. Within the maximal regime, big blobs of fresh water at a frequency of about 25 s, observed visually from the video stream of the experiment, emerge from the channel into the reservoir. These events of outflow cause remarkable erosion of the interface as shown in figure 3-10 (images a, c). They occupy the top right part of the images and as seen cause erosion of the lower layer. In between two events, various interfacial waves that are highly three-dimensional are generated and cause mixing that fills the upper layer depth (image b). Predominantly interfacial K-H instabilities are generated and move into the reservoir. It is noteworthy here mentioning that this period of 25 s matches with that of the large scale down slope breaking interfacial waves reported in chapter 2 for the same g' due to the frequent pilling and release of the interface at the sill crest. Within the sub-maximal regime (figure 3-9: images e, f), signatures of interfacial K-H instabilities almost vanish and the formation of an intermediate layer at medium density is observed as a wedge (see image e) overlaying the lower layer. The region of the outflow from the channel, $y < 10$ cm, has relatively sharp interface since the mixed fluid is continuously flushed away by the incoming fresh water inflow. The wave activities perish and the intensity of mixing decays subsequently (image f).

Within the salt water reservoir (view B-B), the interface positions' time series were extracted at different locations starting at $t = 120$ s when both hydraulic controls were valid within the channel in Exp 1a. Figure 3-10 shows the fluctuations of the interface at four sample locations into the tank. As it is observed, there is a continuous drop in the interface position due to the

119

fresh water flux into the reservoir regardless of the flow regime in the channel. It appears that there is a higher wave activity as we move further from the channel axis ($y = 0$) into the basin. The vertical scale range is kept constant in each plot to facilitate comparing the data. The data shows as well that the rate at which the interface drops is faster as we move away from the channel. However, the amplitude of fluctuations does not vary much with distance or time. In the following, the interaction between the reservoir and the channel will be explained in view of figures (3-3, 3-10) and the visual observation of the experiment from an energy point of view.

Equation 3.3 can be used to describe the temporal evolution of the reservoir-channel interaction as a first order approximation. Away from the sill within the channel and in the reservoir, the topography is flat and the equation reduces to:

$$E = z_2 + (U_2^2 - U_1^2)/2g' \qquad (3.5)$$

During the maximal regime and through the control curves shown in figure (3-2), values of 19.59 and 22.75 cm were obtained for E and z_2, respectively. Within the channel, the interface changes gradually and energy sinks can be assumed absent that E may be considered constant, hereafter referred to as E_{exit}. Losses due to interfacial friction and entrainment can be neglected especially that the sub-critical region has relatively short span. That z_{2exit} is greater than E_{exit} requires that the differential velocity head be negative, which is natural given the shallowness of the upper layer.

Within the reservoir, velocities can be neglected compared to their magnitudes in the channel. Consequently, the energy in the reservoir, E_{res}, approximately equals the lower layer depth therein, z_{2res}, using equation 3.5. From figure (3-7), the upper layer flow rate at the exit, q_{1exit}, measures ≈ 24 cm^2/s during the maximal regime. Prior to the establishment of the two controls, the flow rates are on average lower in magnitude. However, even while considering the magnitude of q_{1exit}, the dimensions of the reservoir and an elapsed time of about 2 minutes until both controls were established, an estimate for the upper layer depth in the reservoir would be about 2 cm presuming uniform distribution of the fresh water. The images in figure (3-9) show though that the flow into the reservoir takes the shape of a wedge resulting in higher depths at the channel side. Rough measurements of the upper layer depth within the reservoir in the early maximal regime are less than 5 cm, which results in E_{res} greater than E_{exit}. The two energies can be related using the following equation through which the reservoir-channel interaction is explained below:

$$E_{res} = E_{exit} + \Delta E \tag{3.6}$$

in which ΔE is the energy head loss.

In the early times during the maximal regime and under the assumption that E_{exit} is fixed then, z_{2res} is large and consequently ΔE is relatively high. The frequent large amplitude K-H instabilities that form in the basin upstream to the exit dissipate the energy until it matches E_{exit}. As time proceeds, more fresh water flows into the reservoir and causes gradual drop in z_{2res} (refer to figure 3-10). ΔE becomes smaller; hence the outgoing K-H billows decay in amplitude (figure 3-8: image g, h). The continuous fresh water inflow causes z_{2res} to drop further until the conditions are no longer favorable to maintain the hydraulic control at the exit. At this stage, the exit control is lost and z_{2exit} starts to drop; hence the sub-maximal regime starts. The interface becomes almost leveled along the channel and the flow is almost parallel (figure 3-8: images i, j).

We will now use figure 3-2 to predict the sub-maximal exchange. Under the same assumption stated previously that the velocities are negligible within the basin, $E \approx z_2$. Here we assume that the energy loss from the channel left hand exit to the reservoir due to flow expansion is minor. From figure 3-10 at $y = 0$ (channel axis), the interface position drops on average gradually from about 19.55 cm at $t = 370$ s to about 18.65 cm at $t = 480$ s. Using these values for E into the sill control curve of figure 3-2 shows that the flow rate would drop from about 23 to 21 cm^2/s, respectively. These predicted flows are over-plotted in figure 3-5 and are in close agreement to the measured sub-maximal flow rates. Few more points were selected at $t \approx 420$ s and 440 s and they also seem to match with the measurements.

Within the left reservoir of the tank (view B-B of Exp 1b: refer to figure 3-9), different wave activities were observed at different times of the experiment. With the fresh water entering into the left reservoir and replacing the salt water, the flow is unsteady during the whole course of the experiment. Due to the more complexity and multitude of the interfacial wave activities which led to extensive mixing in the reservoir, it was not easy to define the interface. Therefore, it was estimated as that which defined the lower layer only while not accounting for the waves on top (see figure 3-1b). The fluctuations of this interface should still retain the basin seiche, which is a main long wave activity in the tank and is discussed later in this chapter, but also reflect the high frequency fluctuations not too much different from the real interface. The interface positions' time series were used to generate a wave characteristics' plot that describes the wave activities in the x-t domain. Figure 3-11 portrays such a plot and reflects the high frequency waves within the field of view (B-B).

It appears that the big blobs of fresh water outflow from the channel and the large scale K-H

instabilities observed in view (A-A) approaching the boundary wall act to generate two sets of waves that propagate in two opposite directions within the reservoir. These waves are reflected in figure 3-11. The left propagating waves are interfacial gravity waves atop of which a train of small amplitude K-H instabilities would continuously form due to the interfacial shear produced by the continuous influx of fresh water into the reservoir (figure 3-9: image b). The generated interfacial gravity waves seem to have constant speeds as reflected in the left panel of figure 3-11. The other set of waves bounded by the inner and outer walls of the channel is merely of vertical oscillations of the interface against the right wall in view (B-B). By tracing the individual left propagating gravity waves each represented by a characteristic line; both the speeds and the frequencies can be estimated. At the location $y = 50$ cm for example, it is clear that there are waves whose periodic times are about $8 - 10$ s within the time frame 120:180 s (these have frequencies of roughly $0.1 - 0.125$ Hz and match with those reflected later in figure 3-25 when discussing the spectral analysis within the basin). The range of their speeds of propagation is between 1.5 and 3 cm/s. On the assumption that they can be approximated to linear interfacial waves, their speeds can be predicted using equation (1) in Farmer and Armi (1999) which describes the dispersion relation of linear interfacial waves in terms of their wavenumber, k, and the parameter R_i ($R_i = \rho_i \cdot \text{cotanh}(k \cdot z_i)$), in which $i = 1, 2$ for the upper and lower layers, respectively. The equation, after simplifications presuming there is no mean flow in the basin, reads:

$$C(k) = \frac{\sqrt{(R_1 + R_2)\rho_2 g' k}}{k(R_1 + R_2)} \qquad (3.7)$$

in which $C(k)$ is the wave speed as a function of the wavenumber, k. From figure 3-10, z_2 decreases gradually from about 24 to 18 cm within the salt water reservoir. The wavelength, λ, can be estimated from figure (3-11) as about 30 cm; hence k ($=2\pi/\lambda$) is ≈ 0.21. For such values, equation (3.7) predicts average speeds ranging from about 1.88 to 1.96 cm/s, which is comparable with the measured speeds from figure (3-11). As the experiment proceeds in time, the frequencies of the waves become smaller and the periodic times are longer as reflected in the second and third rightmost panel of figure 3-11. Times of about 10 and 18 s are observed for example at $320 - 340$ s and $380 - 400$ s, respectively.

The time-averaged interface over the steady maximal exchange period for view (B-B) in Exp 1b was obtained and is shown in figure 3-12. The fresh water as it leaves the channel and spreads into the reservoir within the maximal regime could be simulated to a surface buoyant jet or plume

122

(figure 3-9: images a – d). A rough estimate for the fresh water depth in the reservoir can be obtained using the predicted flow rate of 24.46 cm^2/s (review Section 3.4.1) and the time elapsed before the exit control was lost ($t \approx 190s$). The volume of fresh water entering into the salt water reservoir can be estimated and divided by the surface area to obtain an average depth of the upper layer. A depth of about 3 cm is obtained. This value is not far from the depth in the middle of the reservoir at about $y = 60$ cm in figure 3-12. The mean interface has a slope of about 8% into the reservoir, while a milder slope in the opposite direction at about 2.8%. The discharge of the upper layer into the reservoir could resemble the disposal of effluents into lakes or oceans. It could behave as a surface buoyant jet or plume depending on how much momentum it possesses compared to buoyancy. A good indicator for that is the densimetric Froude number at the source,

F_o ($F_o = \dfrac{U_o}{\sqrt{g' \cdot b_o}}$), in which U_o is the average velocity and b_o is the depth or thickness of flow at the source. From figure 3-10 (at $y = 10$ cm) and within the steady maximal regime, b_o can be estimated at about 8 cm, and assuming the predicted flow rate of 24.46 cm/s^2 at the sill crest remains constant, these produce F_o of about 0.24 which is an indicator of a plume rather than a jet. The fresh water flow into the salt water reservoir may resemble the plumes found at the mouths of rivers and estuaries.

3.5 EVOULTION OF WAVES ALONG THE CHANNEL

3.5.1 Overview of the wave field

The analysis of the interface positions' time series is expected to reflect the wave activities observed in both views (A-A) and (B-B). Before we analyze and discuss the results though, an overview of how the interface changes temporally and spatially along the channel at various locations is provided in what follows. As mentioned previously, different wave activities were observed along the channel and in the reservoir during the course of an experiment. The frequency as well as the amplitude of those waves varied both in time and space within the different flow regimes. Figure 3-13 shows the interface positions' time series at 15 different locations in Exp 1a. The locations within the channel are designated the labels 'CH-i', while those within the basin upstream to the channel exit are labeled 'B-i', i being the location number starting from the sill crest (CH-1) in a sequential order outwards. The locations are generally spaced at 5-cm intervals except for the channel exit (CH-9) which is at 2.5 cm from the two

123

locations at its either side, namely CH-8 and B-1.

It can be clearly seen that there is a dominant low frequency wave, with overriding higher frequency components, in the proximity of the sill crest (CH-1 : CH-4). As we move away further upstream from the sill crest, it is quite obvious that the higher frequency components overtake and the lower frequency mode fades and may even barely be detected visually. Within the flat-bed reach inside the channel (CH-6 : CH-9), it is also noticeable that the amplitude of the fluctuations, be it of the high or low frequency modes, is relatively much smaller than in the neighborhood of the sill crest. The amplitude especially that of the higher frequency mode and within the maximal exchange regime, however, grows larger as we move further upstream outside the channel and the upper layer departs the exit location. This is in agreement with the visual observation presented previously in figure 3-8. A remarkable interfacial dip down propagating outside the channel can be seen in the time series of CH8 - B2, which was also observed in the reconstructed images of figure 3-4. It appears that this dip down is generated within the channel rather than at the channel exit as one might intuitively think. This generic feature seems to mark the end of the maximal regime and might have been generated due to the relaxation of the exit hydraulic control as stated earlier.

Within the sub-maximal regime, both the frequencies and amplitudes of fluctuations become generally smaller than within the maximal regime. This is somehow expected if we think globally of the temporal development of the available energy in such a confined system of two different density reservoirs. Initially, the salt water reservoir has a higher energy than the fresh less dense reservoir. Within the maximal regime, this energy potential is continuously being used up to generate the different wave activities in the system. As the time proceeds and the salt water slowly occupies the lower part in the whole tank, the available energy potential decreases and there exists no more large enough horizontal energy gradients to maintain the generation of the waves at the higher frequency and amplitude levels that were available within the maximal exchange. Although the transfer of potential energy into kinetic energy results into establishing the mean flow and that instabilities have their own generation mechanism, yet the higher initial kinetic energy available within the maximal regime produces higher interfacial shear that would allow for instabilities to form.

The interface positions detected as described in Section 3.3 were used to generate wave characteristics' plots, which portray the temporal and spatial evolution of the whole flow field during the course of an experiment. A sample wave characteristics' plot was generated from the lower (base) interface positions' time series in Exp 2 and is shown in figure 3-14 for view (A-A). From the figure, it is clear that there are two sets of waves being generated a little upstream to the

124

sill crest ($x \approx 5 - 10$ cm), then propagate in two different directions (the downstream to the crest propagating waves were discussed in chapter 2). It is also obvious that some waves are generated within the channel at about $x = 20$ cm. On a closer look at the plot and by tracing the individual waves, it appears that those uni-directional high frequency waves propagate to the left through the channel then die out as they approach the exit; although some may find their way through the exit and grow remarkably big beyond. A regular set of large amplitude K-H instabilities are generated upstream to the channel exit. They are very regular in pattern, especially within the maximal regime (shown in the leftmost panel of figure 3-14). The origins of these instabilities are either in the basin right upstream to the exit, or of an instability that was generated within the channel and found its way through the exit. A careful look into the plot close to the left boundary reveals that there are signatures of waves traveling rightwards towards the exit. Those waves are due to the reflection at the left wall of the tank and as seen are able to advance further as time elapses and the upper layer flux becomes weaker not to block their propagation.

It is also noticeable that once the hydraulic control at the exit is lost and the sub-maximal regime started at $t \approx 140$ s (recall figure 3-4: image b), the location of the generation of the two sets of waves is observed to have shifted further upstream from the sill crest (figure 3-14: mid-panel). As the experiment proceeds further into the sub-maximal regime, the amplitudes of the waves decay as can be seen by the more homogeneous color in the third panel of figure 3-14. This matches with the observations where the interfacial fluctuations faded after the steady state was over.

Figure 3-15 portrays such effects in images where the sprout growth of the outgoing K-H instabilities during the maximal regime (images a – f) and the occasional pairing of two successive instabilities (images e, f) is clear. Typical propagation speeds obtained from these images in this regime were $0.9 - 1.15$ cm/s with $g' = 1.62$ cm/s^2. During the sub-maximal regime (right column) the reflected instabilities at the wall are able to counter-flow and may cause erosion of the interface. To observe the effect of g' on the interfacial activities, figure 3-16 shows a sequence of images from Exp 3 within the steady maximal regime where g' was four times larger than that of Exp 1a. The increase in g' resulted in higher velocities in each layer, hence stronger interfacial shear. As a consequence, the generation of K-H instabilities along the channel became more frequent and led to a rougher interface compared to the sharp interface we observed earlier in Exp 1a. In some instants, the interface attained a horizontal level within the channel (image e) or even had a slightly adverse slope (image f), a feature that was not observed earlier in Exp 1, 2. As the upper layer flow escapes the exit, the interface sometimes had an upward steeper inclination (images e, f). The instabilities formed upstream to the channel exit

125

grew larger than when g' was 1.62 cm/s^2, yet their pairing was still observed as in Exp 1a. Their maximum height had values of roughly about 8 cm as they approached the wall (almost 1.6 – 2 times that height with g' of 1.62 cm/s^2 in Exp 1a). Typical propagation speeds were about 4.6 cm/s as obtained from figure 3-16. Events of pairing and propagation of reflected waves at the wall towards the channel were also observed. Within the sub-maximal regime, similar to Exp 1a, the interfacial shear weakened and as a result we did not observe the large scale K-H instabilities outside the channel. The formation of an intermediate layer which expanded horizontally into the channel was also observed. In the following sub-sections we explore some of the characteristics of those high-frequency K-H instabilities along the channel.

3.5.2 Wave speeds

The wave characteristics' plots of the different experiments were used to compute the propagation speeds of the generated K-H instabilities within the channel and upstream to the channel exit. By following any characteristic line, the tangent to the path line of the wave provides a measure for the wave speed at that location in space and time. As shown in the wave characteristics' plot (figure 3-14) and per visual observation, it is obvious that the waves accelerate initially as they are generated within the channel until they attain almost constant speed. Outside the channel, they appear to maintain their speeds although close to the wall they decelerate due to the reflected waves at the boundary and pairing events. To gain a global view of the wave speeds, the interface positions' time series at many adjacent locations along the channel were cross correlated and the time lag between each pair of signals was used to obtain an estimate of the wave speeds. The results are shown for the three experiments in figure 3-17 where the speeds were made non-dimensional using the velocity scale $\sqrt{(g'\cdot H)}$, H being the total water depth. The data indicate that along the topography there is acceleration in the flow field and that along the flat bed reach along the channel the speeds were constant. This is in line with observations and the wave characteristics' plots. While this may be true in a time-averaged and global sense, the real flow field is fluctuating and the waves may propagate at different speeds in space and time. To assess the scatter of the data, individual waves form the wave characteristics' plot were traced and their speeds were determined within the channel. Figure 3-18 shows the wave speeds of a number of waves during the course of the experiments. Although there is an obvious scatter in the data due to the oscillatory flow fields, there is a clear acceleration on the average due to the convergence of each layer in the direction of the flow. The speeds appear to be generally in direct proportion to $\sqrt{g'}$.

126

Because the waves appear to maintain almost constant speeds outside the channel and before approaching the left boundary wall, it would be adequate to choose one representative location and investigate how the speed changes with time as the flow regime changes. The location B-3 (x = 50 cm) was selected in all three experiments and the wave speeds were measured in time. Figure 3-19 presents the results from the three experiments. It is quite obvious that there is some scatter in the data especially initially during the maximal exchange, which is then followed by a decaying trend within the sub-maximal regime. During the maximal regime, the data is concentrated on the average around 2.5, 3.5, and 5.3 cm/s in Exp 1, 2, and 3, respectively. These values are again in direct proportion with $\sqrt{g'}$. It is also noticeable that the times around which the decaying trend starts, thereby marking the beginning of the sub-maximal regime, are in match with those obtained earlier from the interface positions' time series at the exit.

3.5.3 Wave height and Reynolds number effect

The interface data presented earlier were for an estimate of the density interface. Their fluctuations reflected the different wave activities which were generated during the course of the experiment. However, the magnitude of those fluctuations does not provide information on the height of the instabilities themselves. To obtain an estimate of the height of the generated interfacial instabilities, both the upper and lower density interfaces that would envelope the instabilities were detected based on an optimized threshold gray scale value that matched the images at different times. During the maximal regime, it was observed that instabilities were generated within the channel, then grew and collapsed without leaving remarkable mixing since the maximal exchange and the accelerating flow field assisted in flushing the mixing continuously. Sharp interfaces were observed in the wake of the instabilities, although in Exp3 the interface was rougher and some mixing was observed due to the higher shear associated with higher density difference between the two reservoirs. It is important to see if Reynolds number may have an effect on the wave height. In what follows, data from the three experiments are compared for such investigation.

The time series of both the upper and lower interfaces were obtained and time-averaged over the maximal exchange period to estimate a mean height for the instabilities along the channel. Figure 3-20 shows both interfaces in the three experiments. As shown from the figure, it appears there are two locations at which the mean height experiences "necking": the first is a little upstream to the sill crest where the instabilities are first generated, then grow spatially in both directions, and the second is at the channel exit where the instabilities generated within the

127

channel would fade in amplitude as they pass through the hydraulic control and new larger amplitude instabilities are generated right upstream to the exit. The outgoing instabilities grow gradually further as they travel away from the exit until they reach the location $x \approx 55$ cm when they start to grow abruptly to larger amplitudes. The results are consistent among the three experiments although there is a little shift of the point of generation towards upstream as g' increases. This has been also reflected in the wave characteristics' plot of the different experiments. Although there seems a small increase in the mean wave height as g' increases, it is not that remarkable, which indicates that the effect of the shear layer Reynolds number, is minimal on the amplitude of the generated instabilities. The shear layer Reynolds number, R_e, is defined as: $R_e = \delta.\Delta U/v$, in which δ is the shear layer thickness, ΔU is the velocity shear between the upper and lower layer and v is the kinematic viscosity. Its value at the sill crest was in the order of 1000, 1600, and 2100 in Exp 1, 2, and 3 respectively.

3.5.4 Frequency analysis and wavelength of the recurrent K-H billows

Both the individual time series of the interface positions in figure 3-13 and the wave characteristics' plot in figure 3-14 showed that during the maximal regime, especially within the basin, very organized and repetitive large-scale K-H instabilities are formed. Their remarkable growth as they travel away from the channel exit and their eventual breaking, which would contribute significantly into mixing, deems it interesting and necessary to further investigate their characteristics. In this section we try to examine them in the frequency domain. Because they seem to experience a sprout growth only beyond some distance away from the channel exit, the locations B-2 – B-6 were selected and spectral analysis of the interface positions' time series at those locations was performed using both Fast Fourier Transform (FFT) and Hilbert-Huang Transform (HHT). While the former provides global idea on the frequencies contained in a signal, the latter isolates the different frequency components and shows how each vary in time.

In the Hilbert analysis, the data are decomposed according to their intrinsic characteristic scales into a number of intrinsic mode function components (IMFs), later will be denoted by C. This is done using the method of empirical mode decomposition (EMD), which aims at expanding the data in a basis derived from the data itself. Hilbert transform is then applied to those components with the result that the time localities of events are preserved. The empirical mode decomposition method is necessary to deal with both non-stationary and nonlinear data (Huang *et al.*, 1996, 1998). For a complete description of the Hilbert technique and its application, the reader is referred to Huang *et al.* (1998). Because our data are both non-

128

stationary and nonlinear, we believe the Hilbert-Huang transform is rather more appropriate than the Fourier transform. However, both are used herein to complement one another as will be shown shortly.

To begin with, a sample time series of the interface positions' at the location B-4 in Exp 1a is chosen and analyzed using HHT. The choice of that location is mainly due to the fact that the signal seems most regular and far enough from the channel exit for the fluctuations to have developed, yet adequately away from the left wall of the tank to avoid interactions with the wall as a boundary (at least within the maximal regime when the strong upper layer outflow blocked the reflected waves) and the breaking of the instabilities that occurs further upstream. Both the individual fluctuations in figure 3-13 and the wave characteristics' plots in the three experiments helped in picking that location. The generated IMFs of the signal are presented in figure 3-21 at no intermittency. Intermittency is an option that allows isolating certain frequencies and will be explained later when investigating the long wave mode in the channel. By comparing the original signal (refer to figure 3-10) and the components of figure 3-21, it is obvious that both modes C3 and C4 are the major contributors of the processes embedded within the time series. C1 and C2 are very high frequency components that most likely reflect the noise in the signal; C7 corresponds to a low frequency mode that will be discussed in a later section. The residual, R, clearly represents the trend, and modes C5 and C6 seem to have lower frequencies to the observed repeated K-H instabilities that they would not relate to them. Note also that C5 and C6 have smaller amplitudes of fluctuations than C3 and C4.

A closer look at C3 reveals that it reflects the strong sinusoidal pattern of the signal within the maximal regime at the highest energy among all other modes. It is about $t \approx 180$ s, when the hydraulic control at the exit is lost and the sub-maximal regime starts, that the amplitude drops significantly and becomes minimal. The mode C4 on the other hand, although at lower energy than C3 within the maximal regime, seems to mimic the sub-maximal regime part of the original signal. From the time series of C3 and C4, it appears as well that they experience some sort of '*beating*' effect, a well-known phenomenon in physics in which a reference wave may be combined with a second wave whose frequency can be studied through investigating the time variations in the amplitude of the combination. For that both modes, C3 and C4, were selected in all three experiments at that location, B-4, and their frequency evolution in time was studied.

Figure 3-22 shows the instantaneous frequency of the modes C3 and C4 at the location B-4 in all three experiments as a function of time along with the spectral power reflected through the associated color coding. As it is clear the frequency is highly fluctuating in time although the peak power seems to exist in relatively limited band and is concentrated at certain times. The

129

maximum power of mode C3 is concentrated within the maximal regime in Exp 1 and 2 in agreement with figure 3-21, while it extends into the sub-maximal regime in Exp 3 possibly due to the high frequency fluctuations that persisted even at later times (refer to figure 3-4: image C for the exit location as indicative). The lower and relatively less fluctuating frequency of mode C4 is also shown and seems to exist at all times in all experiments at not much variation. Because of the high fluctuations in the frequency with time, we perform FFT for the time series at the rest of the locations (B-2 – B-6) to attain a global idea on how the frequencies may change with g'.

In performing FFT, only the maximal regime part of the time series at those locations was used since it has both components as indicated earlier through the decomposition shown in figure 3-21 and the spectra of figure 3-22. The initial transient was excluded as well so that the signal retains only the regular pattern that prevailed within the maximal regime outside the channel. Figure 3-23 shows the Fourier power spectra of the time series at the five locations in the three experiments. In all spectra it is obvious that there are some distinguished peaks that are persistent at all locations in one experiment. For example in Exp 1 at locations B-2 and B-3 there is a single dominant peak at about 0.156 Hz ($\approx$ 6.4 s). At the locations B-4 and B-5 the same peak exists but a second peak at 0.195 Hz ($\approx$ 5.1 s) emerges in the spectra. These two peaks now are likely to correspond to modes C4 and C3, respectively, in the HHT spectra of figure 3-23. Although the energy of the first peak in the Fourier spectra is higher than that of the second, which seems contradicting to the HHT spectra, yet the mean values of the HHT spectra match with the Fourier-based peaks. The Fourier spectrum is after all a global time-averaged indicator, but it helps with the HHT spectrum in describing the processes.

Based on the results of both spectra for the location B-4, it is likely that during the maximal regime in Exp 1 the large scale high frequency K-H instabilities that form outside the channel appears to occur at a frequency of 0.195 Hz ($\approx$ 5.1 s). This is in very good agreement as well with the zoomed-in wave characteristics' plot of Exp 1 within the maximal regime (see figure 3-24) where it can clearly be seen that at the location B-4 ($x = 55$ cm) there is a regular pattern of waves at about 5 s. As time passes and the experiment is into the sub-maximal regime, the second peak starts to become more dominant (refer to the decomposition of figure 3-21) and due to the weakened interfacial shear, the instabilities start to form at lower frequencies. Note that the lower frequency peak of about 0.156 Hz in the Fourier spectra is shifted at the location B-6 to 0.117 Hz possibly due to the interaction with the wall boundary.

An estimate for the wavelength, λ, of the K-H instabilities can be obtained either from the wave characteristics' plot as an average over different times or through an appropriate velocity scale and the frequency of the wave ($\lambda = U/f$). Different velocity scales could be used to estimate

λ. While Pawlak and Armi (2000) assumed a convective velocity for their interfacial K-H instabilities of $\Delta U/2$, we choose the interfacial wave speeds obtained from our wave characteristics' plot and combine them with the frequencies obtained through the spectral analysis. Zhu and Lawrence (2001) obtained λ directly from their characteristic plot since they had no frequency analysis of their interface positions' fluctuations. From figure 3-24, the average speed of the instabilities at about $x = 55$ cm in Exp 1 is roughly 2.4 cm/s. The K-H instabilities were observed at the frequency of about 5 s at that location; hence the wavelength would be estimated at about 12 cm. Wavelengths were also obtained from the wave characteristics' plot of Exp 1a and seem to be in fairly good agreement with this estimate. Measured wavelengths varied between 10 and 15 cm within the steady maximal regime (figure 3-24).

Similar results are shown for Exp 2 in figure 3-23 where the first peak of about 0.195 – 0.215 Hz (4.7 – 5.1 s) seem to be persist at all locations. The second peak of about 0.332 Hz (3.0 s) is also there and increases in energy at locations B-4 and B-5. Likewise the wave characteristics' plot of Exp 2 reveals a clear 3-second period for the large scale K-H instabilities during the maximal regime. In Exp 3, there seems a little shift in the peaks along the locations although it is obvious that the two peaks of 0.234 and 0.349 Hz (2.9 and 4.3 s) are persistent at the locations B-4 to B-6. Table 3-3 summarizes the results of the three experiments. Unlike low frequency gravity waves, for example the internal basin seiche, which is in proportion to $\sqrt{g'}$, the generation of instabilities is not known to have such relation and rather depends on the local shear and buoyancy conditions. However, from the results in table 3-3, it is obvious that within the maximal regime the frequency increases as g' increases. The dependence of the generation frequency on g' alone is crude and may not likely have constant proportion.

3.6 THE LONG WAVE ALONG THE CHANNEL

3.6.1 The basin wave activities

If we consider the left reservoir as a three-dimensional basin with lengths L_x and L_y equals to 122.5 and 123.5 cm, respectively, then the resonant period of the internal basin oscillation at a particular mode NM can be given, as in homogeneous flows (Sorensen, 1997), by:

$$T_{NM} = \frac{1}{C_i}\left[\left(\frac{N}{L_x}\right)^2 + \left(\frac{M}{L_y}\right)^2\right]^{\frac{-1}{2}} \tag{3.8}$$

131

where N and M can each have values of 0.5, 1.0, 1.5, etc. C_i is the speed of shallow water waves propagating along the interface of two fluids and can be approximated by $\sqrt{(g' \cdot z_1 \cdot z_2/(z_1+z_2))}$. If we roughly choose z_1 and z_2 as equal to 10 and 20 cm, respectively, and taking $N = M = 0.5$ as the fundamental oscillation mode, we get T_o of about 53 s for g' of 1.62 cm/s^2. To check for the internal basin seiche frequency and other wave periods and their development with time, FFT and HHT are both used in what follows. Five sample locations within the tank including those whose time series were presented previously in figure 3-10 were selected to assess the frequencies embedded in their interface positions' signals. The Fourier power spectra of those signals are shown in figure 3-25 in which it is clear that there is a dominant low frequency of about 0.0166 Hz ($T \approx 60$ s) which persists at all locations. This frequency is in line with the earlier prediction of equation (3-8) and would reflect the basin oscillation. It is also obvious that it takes up considerable energy component in the spectra, thereby a major wave activity in the signals. Other higher frequencies exist in the spectra although varying with location. They vary between 0.055 – 0.20 Hz ($\approx 5 - 18$ s) and would reflect the multitude of gravity waves and K-H instabilities generated along the interface (recall figure 3-11).

The interface positions' time series at $y = 50$ cm as an intermediate location within the field of view was chosen and analyzed using HHT. The data was extracted from about 50 s into the experiment when the upper fresh water layer extended along the view (B-B) until about 9 minutes. The time series was analyzed at no intermittency and the generated IMFs were obtained as shown in figure 3-26. The original time series is displayed in the top panel. Modes C1 and C2 are high frequency noise. The modes C3 – C10 and the residual were used to reconstruct the signal. The reconstructed signal is shown in the bottommost panel and in very good agreement with the original signal. The residual, R, is almost a montonic linear function which reflects the continual drop in the interface position with time. The trend composed of the mode C10 and R is over plotted onto the reconstructed signal and shows the decaying trend in the data. Clearly the mode C7 is the closest to the internal basin seiche and has a period of about 60 s. It in interesting to see that internal seiching existed from the very beginning of the experiment. Although it has almost uniform amplitude until about 300 s, the amplitude almost doubled between 350 – 500 s. Similar to the high frequencies we obtained in FFT, the modes C3 – C6 correspond to K-H instabilities and other interfacial gravity waves. The average frequencies of these modes are approximately 0.25, 0.15, 0.08, and 0.05 Hz, respectively. These correspond to periodic times of about 4, 6.7, 12.5, and 20 s. Although the instantaneous frequency variation with time was highly fluctuating, yet these average values are not far from those obtained in the FFT analysis and the visual observation.

132

The internal basin seiche frequency was referred to in explanation of a low frequency mode that was observed at and upstream to the sill crest in previous studies. For example, Zhu *et al.* (2001) and Veronique *et al.* (2004)) observed in experiments performed in the same tank such low mode that was in match with the basin seiching. While the former study dealt with flow through openings, the latter had the same setup described herein. In chapter 2 of this thesis, a close frequency to the internal seiching was also observed upstream and at the crest of different geometry bottom sill. In the following, an attempt is made using HHT to trace this low frequency mode along the channel.

3.6.2 The low frequency mode along the channel

Due to the non-linear and transient complexity of the interface time series at the different locations along the channel (refer to figure 3-13), we attempt to analyze them using Hilbert-Huang Transform (HHT). In this section, we try to examine particularly the low frequency mode that was observed at and upstream the sill crest in this and previous studies. Such low frequency component has been reported earlier in studies that were performed in the same tank (Zhu *et al.* (2001); Veronique *et al.* (2004)). In those studies, it was suggested that the low frequency mode was that of the internal basin oscillation which would propagate from the salt water reservoir into the connecting channel through the exit hydraulic control. The analysis of the interface time series in those studies was performed though using Fast Fourier Transform (FFT) which lacks the temporal evolution of the frequencies and amplitudes.

To start with we perform FFT for the 15 time series that were shown in figure 3-13. FFT helps attain global view of the available frequencies and their mean power distribution. Additionally, it complements the HHT analysis as will be shown afterwards especially when we have multiple modes and a high possibility of mode mixing. The FFT power spectra results are shown in figure 3-27. As it can be seen, a low frequency peak, f_o, of approximately 0.01495 Hz (with periodic time $T_o \approx 67s$) is dominant at the sill crest ($x = 0$). A second peak, f_1, with a frequency of about 0.02939 Hz (periodic time $T_1 \approx 34s$) is also distinguishable in the spectrum. Although f_1 could be thought of as sub-harmonic to f_o ($f_1 \approx 2 f_o$), f_1 has been referred to in chapter 2 as that of the release events which caused the large scale down slope interfacial breaking waves.

By tracing the low peak f_o along the channel upstream to the sill crest, it seems that it exists almost everywhere, although at some locations (for example CH-3, CH-6, and CH-7) it increases to about 0.01942 Hz (or 51s). It is interesting to note though that the magnitude of the spectral energy of this low frequency seems to be at a minimum at locations CH-5 and CH-6 within the

133

channel and increases in both directions towards the crest and the exit with a much remarkable increase towards the former. This is in line with how the amplitude of fluctuations changes spatially as discussed earlier when looking at the time series in figure 3-13. Likewise it is also noticeable that gradually as we move away from the sill crest, higher frequency peaks start to emerge and slowly overtake in terms of energy indicating that new higher frequency waves evolve within the channel. With the upper layer flow departing the channel into the left reservoir, high frequency K-H instabilities grow big and become dominant as reflected in the spectra of stations B-1 – B-6. Note the match in the spectra of figure 3-27 and that of 3-23 at the corresponding locations; keeping in mind that in figure 3-23 only part of the signal within the maximal regime was considered. In what follows we implement HHT to obtain more details particularly on the long wave that seems to exist almost everywhere.

Before applying HHT, we first briefly introduce the notion of intermittency. It is basically a tool that is used within HHT to avoid mode mixing and allow the isolation of the different modes embedded into the time series. One may look at intermittency as a variation of a low-pass filter that assists in removing the high frequency events and retain the lower frequency modes. Intermittency acts on the time separation between the upper and lower extrema within the signal and thus may correspond to ½ of the wave period. By setting a certain threshold for intermittency that depends upon the signal, it could be possible to isolate the high frequency events. In what follows, an example that demonstrates HHT with intermittency is provided for the time series of the interfacial fluctuations at the sill crest, CH-1. For more details on intermittency and its application, the reader is advised to refer to Huang $et\ al.$ (2003).

From the FFT power spectra shown in figure 3-12 for CH-1, it is obvious that we can choose the frequencies 0.055 and 0.025 Hz (corresponding to periodic times of 18 and 40s) as our cutoff frequencies in performing the intermittency to isolate the two dominant peaks in the spectrum. We will follow the nomenclature of Huang $et\ al.$ (2003) to designate the results; thereby CEI (M, S; n_1, n_2, ...) will correspond to Components from Extrema with Intermittency testing, while n_1, n_2, ... indicates the level of intermittency (i.e. ½ the wave period for each component). When the same intermittency criterion is repeatedly used for k times, it is indicated by n^k. M and S stands for the maximum number of sifting steps allowed and the sifting stopping criterion, respectively. The process of sifting is detailed in Huang $et\ al.$ (1998, 2003) and in brief is a systematic way to generate the IMFs based on local extrema that are connected by a cubic spline envelope. As such S indicates that the data must be sifted and pass the stopping criterion this number of times before it can be considered an IMF. Upon personal communication with N. Huang, an upper limit for S was set to 5. M is a criterion that is applied to each IMF and is meant to protect against possible

134

infinite sifting of the data. It is therefore higher than S and was set to 100 in our analysis.

In applying HHT, it is necessary to predict some data points outside the boundaries. Few endpoint predictions such as linear, pattern, and mean predictions can be applied. There is no perfect solution for the end point effects and the best would be to try different approaches until one reaches the one that makes more sense to the original data (personal communication with N. Huang). In our analysis, we used both the pattern and linear predictions among the different time series. A last indicator of the linear statistical independence for the generated IMFs is the orthogonal index, O.I., which should be below a certain preset limit, 0.1 say (Huang *et al.*, 2003).

The time series of CH-1 at the sill crest was decomposed using HHT with the following scheme: CEI $(100, 5; 18^8, 0, 40, 0^4)$. A value of 0 indicates that no intermittency was used at that level for the following IMF. From this combination we generated 13 IMF components and a residual, R, which represents the trend of the data. The decomposition had an O.I. of -0.00813 << 0.1, which says the components were orthogonal and uncorrelated. Figure 3-28 shows the different components along with the residual and the reconstructed signal of the components C4, C9, C11 – C13 and R. It is clear that the two modes C9 and C11 were successfully isolated representing the two peaks that we observed earlier in the Fourier spectrum. It is also obvious that the reconstructed signal compares well to the original data and maintains both the main high and low frequencies in the signal.The process was carried out for all of the time series that were shown in figure 3-13 previously. However, for stations CH-4 – CH-9 and those within the basin outside the channel where the high frequency waves dominate the time series, it was very difficult to isolate the long wave. The data has very sharp extrema as for shocks and earthquakes' signals which made the direct application of intermittency to the original data series much more difficult than for CH-1 – CH-3. For that we used a low-pass 8th order Butterworth filter prior to performing the HHT decomposition. The long wave mode that corresponds to the low frequency peak found in the Fourier power spectra was obtained at the different stations first using the filter and then decomposed using HHT to isolate it in an attempt to trace its direction of propagation. Few more stations were added around the channel exit and the sill crest, where the hydraulic controls would be, to better track the wave. These are stations CH-1A, CH-2A, CH-6A, and CH-7A with CH-1A between CH-1 and CH-2, and so on.

The long wave modes at the different locations were collected and over plotted onto the original time series as shown in figure 3-29. By closely looking at each signal, it can be seen that the long wave modes in most of the signals are in line with the long fluctuations embedded within the signals. A thorough investigation of the original time series at some locations revealed that sometimes the high frequency waves may be propagating in an opposite direction to the long

135

wave as a carrier structure. This may be observed for example by tracing the second crests in the signals at locations CH-2 – CH-3. While the higher peak in the original time series seems to be propagating outwards from the sill crest, the global long wave whole structure as a carrier, whether in the original data or the HHT reconstructed signal, is traveling inwards to the crest. The same can be seen in the same signals for the crests shortly after 360 s.

To better view the long modes and trace their directions of propagation, they were re-plotted in figure 3-30 along with path lines tracing the crests of individual waves. From the figure a few interesting observations can be deduced. The origin of each wave propagating in one direction is indicated by a circle and assigned an identity character for easier reference. Firstly, it appears that the waves are not generated right at the sill crest, but rather within the sub-critical reach between the two hydraulic controls in the channel. The reach between the locations CH-2A ($x =$ 7.5 cm) and CH-6A ($x = 27.5$ cm) seems to have the sources of most of the waves which are generated within the channel. Recall that in the Fourier power spectra of figure 3-27, it was shown that the location of minimum energy for the long mode, f_o, was that of CH-5 and CH-6 ($x = 20$ and 25 cm, respectively). This agrees with the notion that the long waves are generated due to interfacial perturbations that occur probably due to the topography in the approach flow of the lower layer within the channel.

Within the maximal regime, those waves denoted by A – I would propagate in both directions with the flow being internally sub-critical. Secondly, waves like K – M are traveling towards the channel but are blocked by the hydraulic control at the exit then. Only after the hydraulic control at the exit is lost that we see some waves able to travel into the channel through the exit (see waves O – Q). It is difficult to decide whether waves like N, P, and Q could be extended into the channel and connected to those like J, R, and S since in the sub-maximal regime the long wave modes were hard to extract especially that the whole signal faded and the fluctuations became subtle as indicated earlier from the original time series of figure 3-13.

The results suggest that such long wave could have possibly started within the channel due to the topography and propagated in both directions owing to the fact that the flow is internally sub-critical upstream to the sill. The buoyancy frequency, N ($N = \sqrt{\dfrac{-g}{\rho} \dfrac{\partial \rho}{\partial z}}$), was estimated and ranged from 2 to 5 s^{-1}. This is based on a density layer thickness of about 2-3 mm as measured from vertical density profiles along the channel. The period corresponding to this range is $2\pi/N$ and would be between 1 and 3 s, which is much shorter than the long wave oscillation in question. The notion that such a long wave could be related to the internal basin seiche could be valid probably only within the sub-maximal regime after the hydraulic control at the exit was lost

136

and the flow has been internally sub-critical everywhere. Many studies support the opinion that interfacial level changes in the two reservoirs can not propagate through the connecting channel within the maximal regime (see for example: Hogg *et al.* (2001); Tedford *et al.* (2005)). In other terms, the hydraulic controls, with the flow being internally super-critical in their outer regions, would be expected to isolate their inter-region and block the transfer of information from either side into the domain bounded by the controls. In the following, however, different opinions are suggested and discussed regarding the source of this long wave.

To begin with, it is worth referring to figures 3-26 and 3-30 both of which indicating that the long mode at the matching frequency of the internal basin seiche exists right from the start of the experiment whether in the tank or along the channel. Three notions could now be presented regarding the existence of such low frequency along the channel. The first opinion, we will later refer to as opinion A, is that the internal basin seiche is able to propagate through the channel against the hydraulic control at the channel exit. This opinion might be justified with reference to figures 3-6 and 3-7, which show that the composite Froude number, G, on the average is below unity and as such the exit is not a perfect hydraulic control point. Even if the time-averaged G at the exit may be unity during the maximal regime, figure 3-6 and the fluctuating characteristic of the flow field as observed suggest that there would be times at which the flow will be internally sub-critical ($G < 1$) and others when it will be super-critical ($G > 1$). During the times when the flow is sub-critical, there is a chance of leakage of the energy from the tank and possible propagation of the internal seiche through the control point into the channel.

The second notion, opinion B, would be in line with opinion A in that we would still assume that the internal seiche would propagate from the tank into the channel but only initially during the unsteady phase and prior to the establishment of the hydraulic control at the exit. This opinion is supported by looking at figures 3-3a and 3-3d, which reveal a time lag of about 90 seconds between the establishment of the controls at the exit and the crest, respectively. It could be possible that an initial long wave of the internal basin seiche could have traveled along the channel until it hit the right boundary wall and bounced back before the hydraulic control at the crest is established. This reflected wave could have gotten trapped within the sub-critical region bounded by the two controls. The assumption can be shown through the following calculation. An estimate of the interfacial long waves' propagation speed with respect to an observer at the bank is expressed after Schijf and Schonfeld (1953) as follows:

$$\lambda_{\pm} = \frac{U_1 z_2 + U_2 z_1}{z_1 + z_2} \pm \sqrt{\frac{g' z_1 z_2}{z_1 + z_2}(1 - F_{\Delta}^2)}$$

(3.9)

137

where F_Δ is the stability Froude number and is given by:

$$F_\Delta^2 = \frac{(U_2 - U_1)^2}{g'(z_1 + z_2)}$$ (3.10)

Assuming roughly that z_1 and z_2 = 22 and 8 cm, respectively, and using the predicted flow rate of 24.46 cm^2/s in Exp 1c, λ_+ would be about 4.4 cm/s. The distance between the sill crest and the right wall is 159 cm. The time a long interfacial wave would take to return to the crest would be about 72 seconds which is shorter than the time elapsed for the crest control to form. On the assumption of a shallow-water or long-wave approximation, the phase velocity could also be estimated as $\sqrt{g' \cdot z_2}$ (Kundu and Cohen, 2002). If z_2 = 8 cm roughly, then the phase velocity would be 3.6 cm/s. The time taken by the wave to travel through the channel from the crest to the right wall and to bounce back to the crest would be 88 seconds, which is close to the previous estimate and still shorter than the elapsed time for the crest control to form. The existence of the low frequency wave within the sub-critical reach between the sill crest and the exit during the maximal regime could then be explained as being an initial trapped reflected wave at the right wall of the tank. The internal seiche would still exist, however, outside the channel until later when the exit control is lost and it becomes able to pass through. This opinion hinges on the idea that the hydraulic control at the exit would block the transfer of energy during the maximal exchange and it is only initially prior to its establishment that the seiche could propagate. It could be argued though that such trapped long wave within the two controls would decay with time due to viscous dissipation.

It is noteworthy mentioning here that the recent study by Tedford *et al.* (2005) on interfacial waves in laboratory exchange flows supports the notion that hydraulic controls block disturbances which form outside the channel from entering the channel. Their study was performed in a similar tank with the exception that the connecting channel did not have any bottom topography. They used 2D FFT in their analysis but their results reflected the behavior within the steady maximal exchange and did not include the initial unsteady phase. They had *g'* of about 1.45 cm/s^2, which is fairly close to Exp 1 herein, but their full water depth was 10.8 cm, which might affect the wave behavior.

The last of those ideas, opinion C, relies on the assumption that HHT will efficiently preserve the phases in the empirical mode decomposition process. With reference to figure 3-30, it appears that the mode corresponding to the internal seiche is excited within the sub-critical

138

domain between the two controls along the channel. The long interfacial waves are initiated in the lower layer approach flow prior to reaching the topography and propagate in both directions. Signatures of long waves propagating into the channel are not seen during the maximal exchange, which supports the idea that the exit hydraulic control would block their passing through. Only after the exit control is lost that we see signs of long waves intruding into the channel (waves O, P, Q in figure 3-30).

The measured low frequency oscillations at the sill crest were extracted in different experiments with different g' and geometry of the obstacle. Table 3-4 presents the periodic times of those low frequency modes. A comparison between the values indicates that they scale with $\sqrt{g'}$ within 20% differences even when the obstacle was significantly different as that of the middle opening in the vertical barrier (refer to appendix A). This might support the notion of internal basin seiching. Further analytical and experimental studies can focus on this issue in more detail so as to decide whether such low frequencies are due to internal basin seiching or attributed to the topography. Although the aforementioned HHT analysis suggests that the low frequency mode is because of the topography, the result in inconclusive and still needs more thorough investigation. One suggestion is to design experiments in a long channel with re-circulating flow over bottom topography to see if the long oscillation still persists. The approach lengths upstream of the topography as well as the height of the topography are important parameters and should be investigated.

3.7 SUMMARY AND CONCLUSIONS

An experimental study on two-layer exchange flow upstream to a smooth bottom sill placed in a channel which connected two large reservoirs at slightly different densities has been conducted. Digital particle image velocimetry (DPIV) was used to obtain the velocity fields. Fluorescein dye was mixed with the salt water which when illuminated using Argon-ion laser fluoresced and allowed visualizing the concentration fields; hence the interface position was detected. The experiments lend a unique study on the reservoir-channel interaction of two-layer salinity stratified flows over bottom topography in a channel connecting two reservoirs. The study is also a pioneer one in experimentally providing a proof of the coexistence of upstream and downstream interfacial waves that are likely generated due to topographic effects in straits. The role of the hydraulic controls at the sill crest and the channel exit has been clearly demonstrated and their effect on the interfacial waves was discussed. The discharge of the upper fresh water layer into

the reservoir has proven to behave more like a surface buoyant plume than a jet with a densimetric Froude number, F_o, of about 0.24.

The reservoir-channel interaction has been explained in view of the internal hydraulic theory. During the early stages within the maximal regime, the internal energy, E, in the reservoir was shown to be higher than that within the channel. The energy loss appears to happen through the generation of frequent large amplitude K-H instabilities along the interface. This process is a rapidly varying internal flow phenomenon and could be similar in nature to the traditional hydraulic jump as an efficient energy dissipater. The role of the hydraulic controls at the channel exit and the sill crest has been to maintain constant energy, and consequently steady interface positions within the channel. A possible mechanism for the generation of the frequent K-H instabilities is the rapid internal hydraulic transition around the exit. The continuous fresh water inflow into the salt water reservoir caused the interface and energy levels therein to drop with time. As such the energy deficit between the channel and the reservoir decreased with time; hence the K-H instabilities started to decay in amplitude. The ongoing fresh water inflow into the reservoir caused further drop in the energy below its fixed value within the channel. At that stage, that fixed energy within the channel could not be maintained any more and the hydraulic control first at the exit was lost. Once the hydraulic control at the exit was lost, the flow became sub-maximal. Both the interface levels and the flow rates dropped down gradually along the channel and at a later time the crest control vanished.

The wave characteristics' plot and visual observation of video streams of the experiments revealed that the large amplitude K-H instabilities which formed within the basin along the channel were mainly generated due to disturbances that started as the upper layer flow left the channel. Although some of those large billows could be traced to instabilities that started within the channel and could pass through the exit, it appears they are predominantly generated outside the channel. The expansion in the flow as it leaves the channel causes the shear to drop; hence the conditions of generation of K-H instabilities become more favorable. Their generation frequencies did not seem to have explicit relation with g', yet the higher g' was, the more frequent they were generated. The mean height of those high frequency interfacial instabilities along the channel did not seem to change as the shear layer Reynolds number at the sill crest increased from about 1000 to 2100 in the different experiments.

The application of Hilbert-Huang Transform (HHT) enabled exploring different notions regarding the observation of a low frequency wave along the channel, a frequency that has been attributed to internal seiche in pervious studies (Zhu *et al.* (2002), Morin *et al.* (2004)). In the present study, however, HHT analysis of many time series of the interface positions along the

140

channel indicated that this long wave is probably generated along the upstream face of the topography and propagate outwards. The results indicate that the long wave could only propagate into the channel in the sub-maximal regime once the exit hydraulic control was lost. That the period of this long wave is close to the internal seiche is not yet clear and requires further studies. Further related studies could focus as well on investigating the fate of the outflow into the reservoir. Studies can aim at quantifying interfacial mixing within the basin. Analytical or numerical studies are needed to investigate the long topographically generated waves.

141

REFERENCES

AGÜÍ, J. C. & JIMÉNEZ, J. 1987 On the performance of particle tracking. *J. Fluid Mech.* **185**, 447-468.

ARMI, L. and FARMER, D. M. 1986 Maximal two-layer exchange through a contraction with barotropic net flow. *J. of Fluid Mech.* **164**, 27-51.

ARMI, L. and FARMER, D.M. 1988 The flow of Mediterranean water through the Strait of Gibraltar. *Progress in Oceanography*, **21**, 1-105.

ARMI, L. and FARMER, D.M. 2002 Stratified flow over topography: bifurcation fronts and transition to the uncontrolled state. *Proc Roy. Soc. London*, A **458**, 513-538.

BRAY, N. A., OCHOA, J. & KINDER, T. H. 1995 The role of the interface in exchange through the Strait of Gibraltar. *J. Geophys. Research* **100** (C6), 10,755-10,776.

CUMMINS, P. F., VAGLE, S., LAURENCE, A. & FARMER, D. M. 2003 Stratified flow over topography: upstream influence and generation of non-linear internal waves. *Proc. R. Soc. Lond.* A **459**, 1467-1487.

FARMER, D. & ARMI, L. 1986 Maximal two-layer exchange over a sill and through a combination of a sill and contraction with barotropic flow. *J. Fluid Mech.* **164**, 53.

FARMER, D. & ARMI, L. 1999 The generation and trapping of solitary waves over topography. *Science* **283**, 188-190.

FINNIGAN, T. D. & IVEY, G. N. 1999 Submaximal exchange between a convectively forced basin and a large reservoir. *J. Fluid Mech.* **378**, 357-378.

FINNIGAN, T. D. & IVEY, G. N. 2000 Convectively driven exchange flow in a stratified sill-enclosed basin. *J. Fluid Mech.* **418**, 313-338.

FINNIGAN, T. D., WINTERS, K. B. & IVEY, G. N. 2001 Response characteristics of a buoyancy-driven sea. *J. Physical Ocean.* **31**, 2721-2736.

FUNAKOSHI, M. 1996 Interaction and generation of waves in a two-layer fluid flowing over localized bottom topography. *Dyn. Atmos. Ocean* **23**, 267-277.

GRIMSHAW, R. H. J. & SMYTH, N. 1986 Resonant flow of a stratified fluid over topography. *J. of Fluid Mech.* **169**, 429-464.

HAMBLIN, P. F. & LAWRENCE G. A. 1990 Exchange flows between Hamilton Harbour and Lake Ontario. In *Proc. of 1990 Annual Conf. of Canadian Society for Civil Eng.* **V**, 140-148.

HILFRICH, K. R. 1995 Time-dependent two-layer hydraulic exchange flows. *J. of Physical Oceanogr.* **25**, 359-373.

HOGG, A. McC., WINTERS, K. B. & IVEY, G. N. 2001 Linear internal waves and the control of stratified exchange flows. *J. of Fluid Mech.* **447**, 357-375.

HOLMBOE, J. 1962 On the behaviour of symmetric waves in stratified shear layer. *Geofysike Publikasjoner*, **24**, 67-113.

HORN, D. A., IMBERGER, J. & IVEY, G. N. 2001 The degeneration of large-scale interfacial gravity waves in lakes. *J. of Fluid Mech.* **434**, 181-207.

HUANG, N. E., LONG, S. R. & SHEN, Z. 1996 The mechanism for frequency downshift in non-linear wave evolution. *Adv. Appl. Mech.* **32**, 59-111.

HUANG, N. E., SHEN, Z. & LONG, S. R. 1999 A new view of nonlinear water waves: The Hilbert spectrum. *Annu. Rev. Fluid Mech.* **31**, 417-457.

HUANG, N. E., SHEN, Z., LONG, S. R., WU, M. C., SHIH, H. H. et al. 1998 The empirical mode decomposition and the Hilbert spectrum for non-linear and non-stationary time series analysis. *Proc. R. Soc. London Ser. A* **454**, 903-995.

HUANG, N. E., WU, M. C., LONG, S. R., SHEN, S. S. P., QU, W. et al. 2003 A confidence limit for the empirical mode decomposition and the Hilbert spectral analysis. *Proc. R. Soc. London Ser. A* **459**, 2317-2345.

IVEY, G. N. 2004 Stratification and mixing in sea straits. *Deep-Sea Res. II* **51**, 441-453.

KUNDU, P.K. and COHEN, I.M. 2002 Fluid Mechanics, 2nd Edition. Academic Press.

LAWRENCE, G. 1993 The hydraulics of steady two-layer flow over a fixed obstacle. *J. Fluid Mech.* **254**, 605-633.

LAWRENCE, G., PIETERS, R., ZAREMBA, L., TEDFORD, T., GU, L., GRECO, S. & HAMBLIN, P. 2004 Summer exchange between Hamilton Harbour and Lake Ontario. *Deep-Sea Research II* **51**, 475-487.

LEE, C.-Y. & BEARDSLEY, R. C. 1974 The generation of long nonlinear internal waves in a weakly stratified shear flow. *J. of Geophys. Res.* **97**, 453-462.

MARXEN, M. 1998 Particle Image Velocimetry in Stromugen mit staken Geschwindigkeitsgradienten, *Diplom Thesis*, Fakultat fur Physik und Astronomie, Ruprecht-Karls-Universitat Heidelberg, Germany.

MCGRATH, J. L., FERNANDO, H. J. S., and HUNT, J. C. R. 1997 Turbulence, waves and mixing at shear-free density interfaces. Part 2. Laboratory experiments. *J. of Fluid Mech.* **347**, 235-261.

143

MORIN, V. M. 2002 An Experimental Investigation of Interfacial Instabilities and Entrainment in Exchange Flow over a Smooth Sill. M.Sc. thesis, University of Alberta.

MORIN, V. M., ZHU, D. Z., and LOEWEN, M. R. 2004 Super Critical Exchange Flow Down a Sill. *J. Hydraulic Engineering* **130** (6), 521-531.

NASH, J. D. & MOUM, J. N. 2005 River plumes as a source of large-amplitude internal waves in the coastal ocean. *Nature* **437**, 400-403.

NIELSEN, M. H., PRATT, L. & HELFRICH, K. 2004 Mixing and entrainment in hydraulically driven stratified flows. *J. Fluid Mech.* **515**, 415-443.

PAWLAK, G. & ARMI, L. 1998 Vortex dynamics in a spatially accelerating shear layer. *J. Fluid Mech.* **376**, 1-35.

PAWLAK G. & ARMI L. 2000 Mixing and entrainment in developing stratified currents. *J. Fluid Mech.* **424**, 45-73.

RUEDA, F. G. & COWEN, E. A. 2005a Exchange between a freshwater embayment and a large lake through a long, shallow channel. *Limnil. Oceanogr.* **50** (1), 169-183.

RUEDA, F. G. & COWEN, E. A. 2005b Residence time of a freshwater embayment connected to a large lake. *Limnil. Oceanogr.* **50** (5), 1638-1653.

SCHIJF, J. B. & SCHONFELD, J. C. 1953 The practical considerations on the motion of salt and fresh water. *Proceedings of Minn. Int. Hydr. Conv. Joint Meeting of the IAHR and Hydr. Div.*, ASCE, New York, 321.

SMYTH, W. D. & WINTERS, K. B. 2003 Turbulence and mixing in Holmboe waves. *J. Phys. Oceanog.* **33**, 694-711.

SORENSON, R. M. 1997 Basic Coastal Engineering, 2nd edition. Chapman & Hall, ITP International Thompson Publishing, New York, USA.

TEDFORD, E. W., LAWRENCE, G., and PIETERS, R. 2005 Interfacial Waves in a Laboratory Exchange Flow. *Proceedings of the 17th Canadian Hydrotechnical Conference*, CSCE, Edmonton, Canada.

TORY, C. D. & KOSEFF, J. R. 2005 The generation and quantitative visualization of breaking internal waves. *Experiments in Fluids* **38**, 549-562.

WHITE, F. M. 1999 Fluid Mechanis, 4th edition. McGraw-Hill series in mechanical engineering.

ZHENG, Q., SHEN, S. S. P., YUAN, Y., HUANG, N. E., KLEMAS, V. et al. 2004. Evidence of the coexistence of upstream and downstream solitary wavetrains in the real atmosphere. *Int. J. Remote Sensing* **25** (21), 4433-4440.

ZHU, D. Z. & LAWRENCE, G. A. 2000 Hydraulics of exchange flows. *J. of Hydraulic Engineering*, ASCE, **126**(12), 921-928.

ZHU, D. Z. & LAWRENCE, G. A. 2001 Holmboe's instability in exchange flows. *J. Fluid Mech.* **429**, 391-409.

ZHU, D. Z., FOULI H. & OKYERE, Y. A. 2002 Exchange flow through an opening. *J. Hydraulic Research*, **40** (3), 341-350.

ZHU, D. Z. 2002 Control curves for two-layer flows. *J. of Hydraulic Engineering*, ASCE, **128**(1), 113-116.
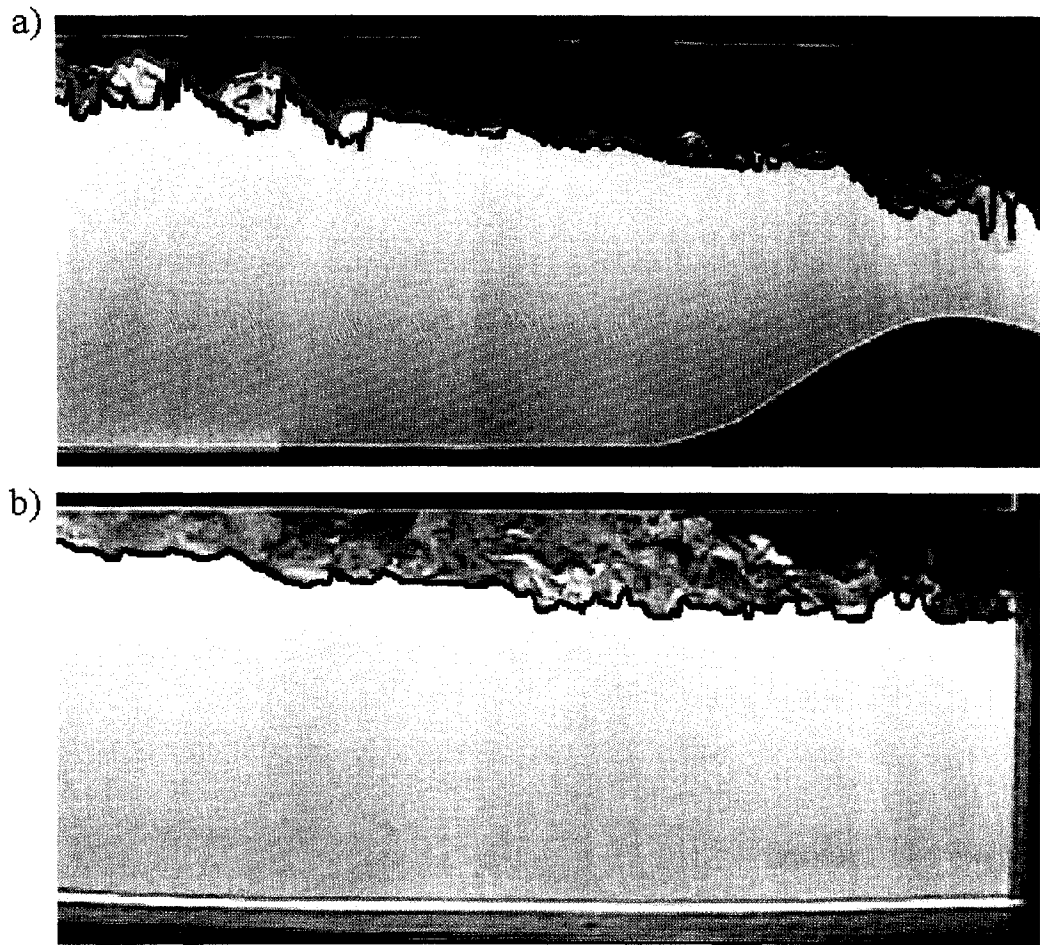
FIGURE 3-1. Instantaneous images of the density fields in: a) Exp 1a, along the channel (view A-A), and b) Exp 1b, within the salt water reservoir (view B-B) with the interface over plotted.

146
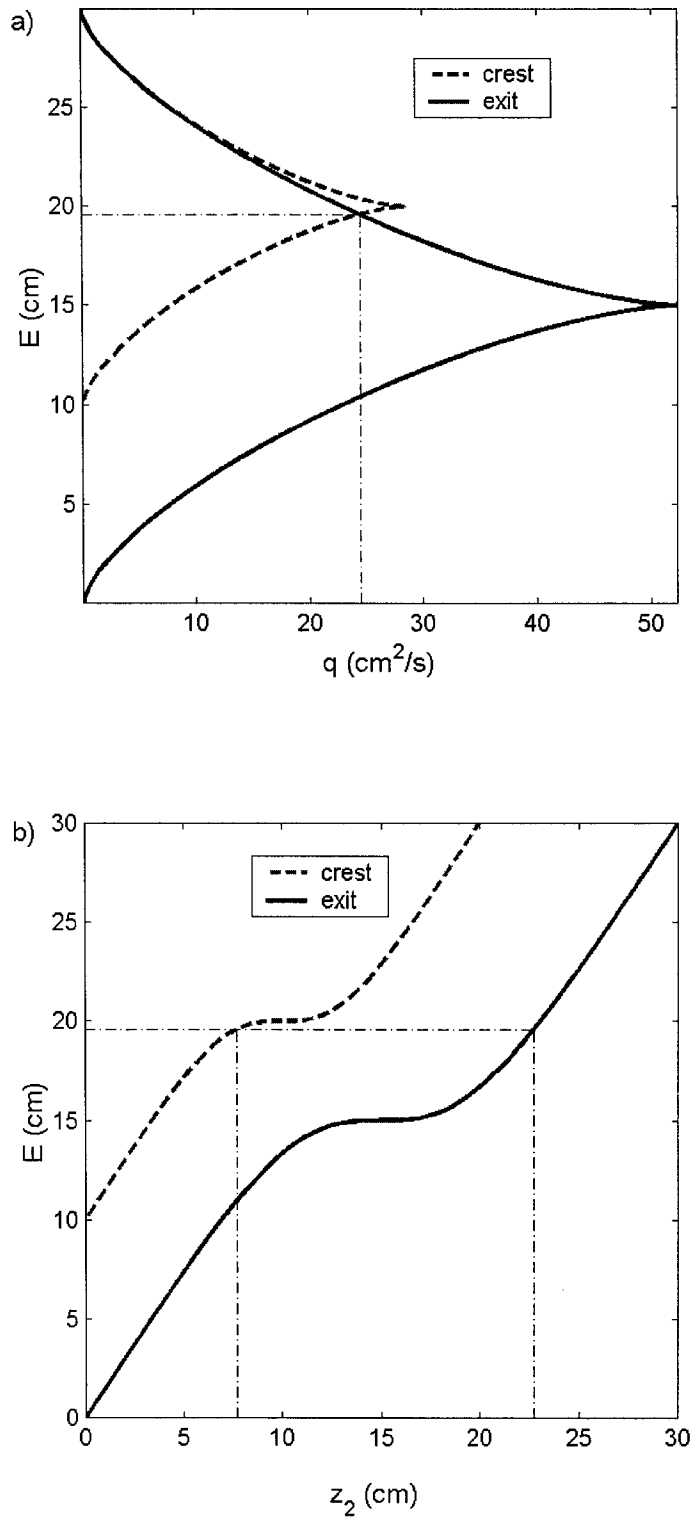
FIGURE 3-2. a) control curves at the sill crest ($h = 10$ cm) and the channel exit ($h = 0$) with $g' = 1.62$ cm/s² simulating Exp 1; b) the corresponding variation of the internal energy, E, with the lower layer depth, z_2, within the maximal steady exchange for the same parameters.

147
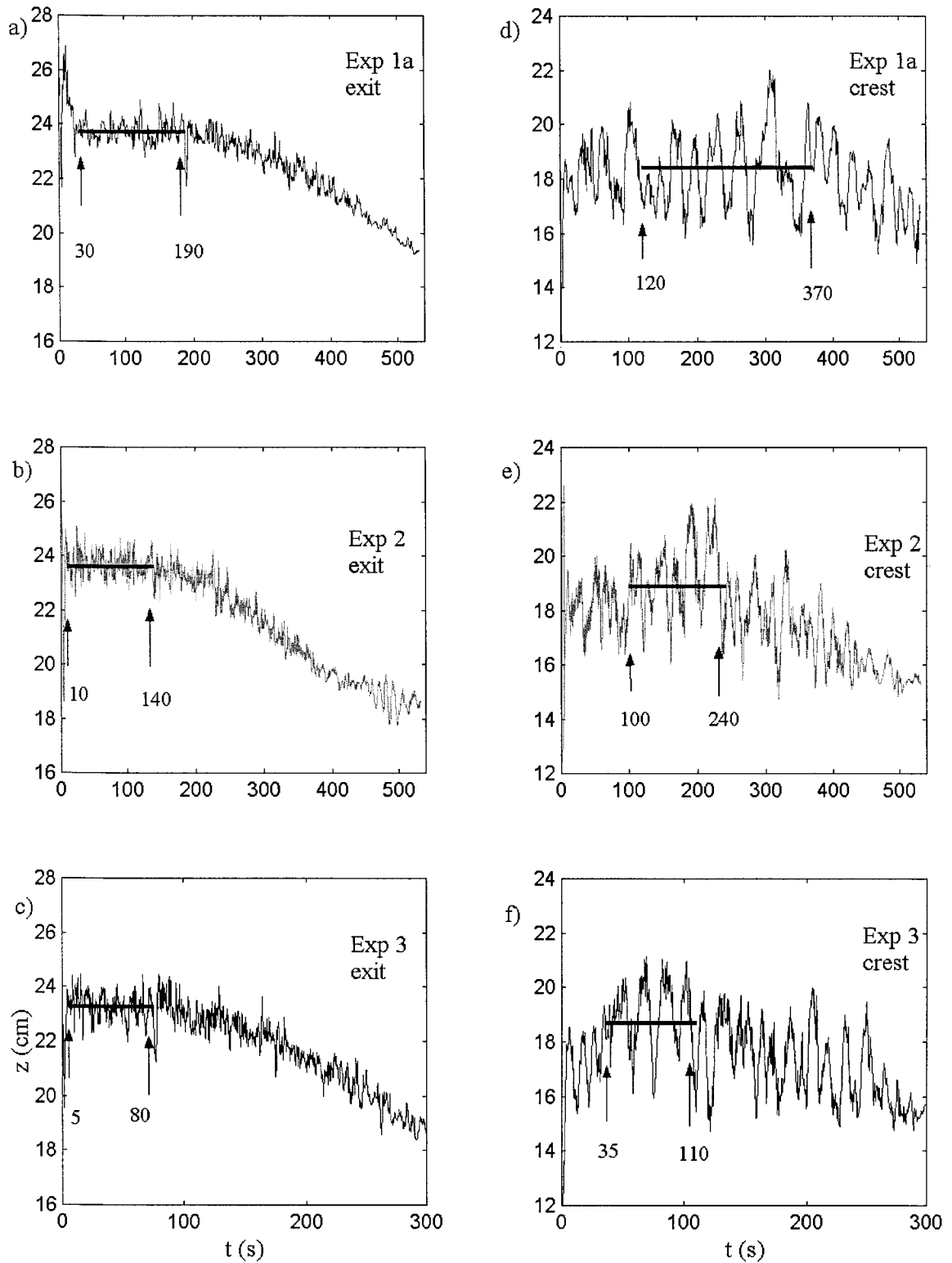
FIGURE 3-3. Interface positions' time series at the exit (left) and the crest (right) in Exp. 1a, 2, and 3. The arrows mark the start and end of the quasi-steady period when the interface attains a constant level.

148
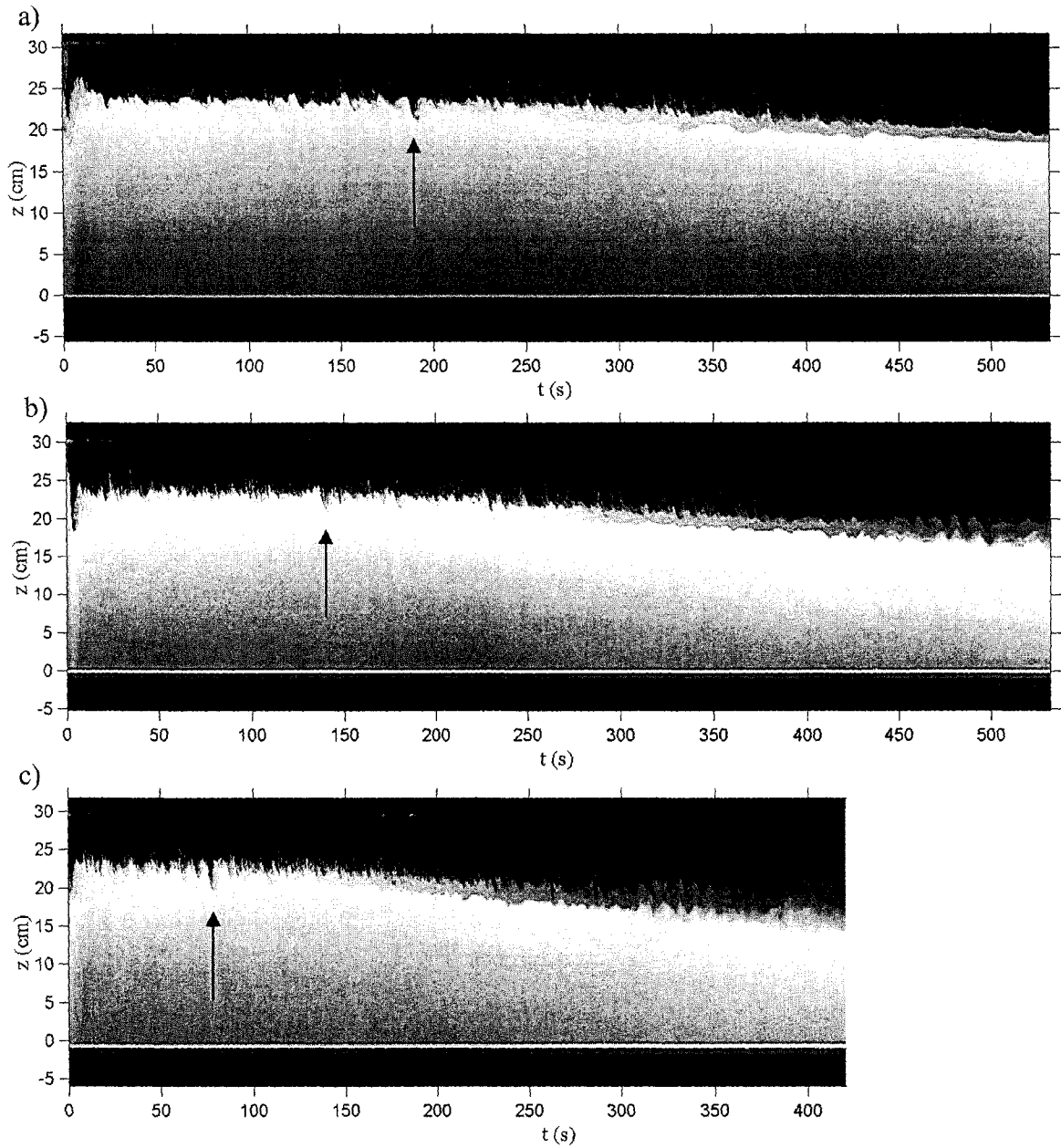
FIGURE 3-4. Reconstructed images for the interfacial fluctuations at the channel exit in: a) Exp 1a, b) Exp 2, and c) Exp 3. A clear dip down of the interface (indicated by the arrows) is consistent in the three experiments.

149
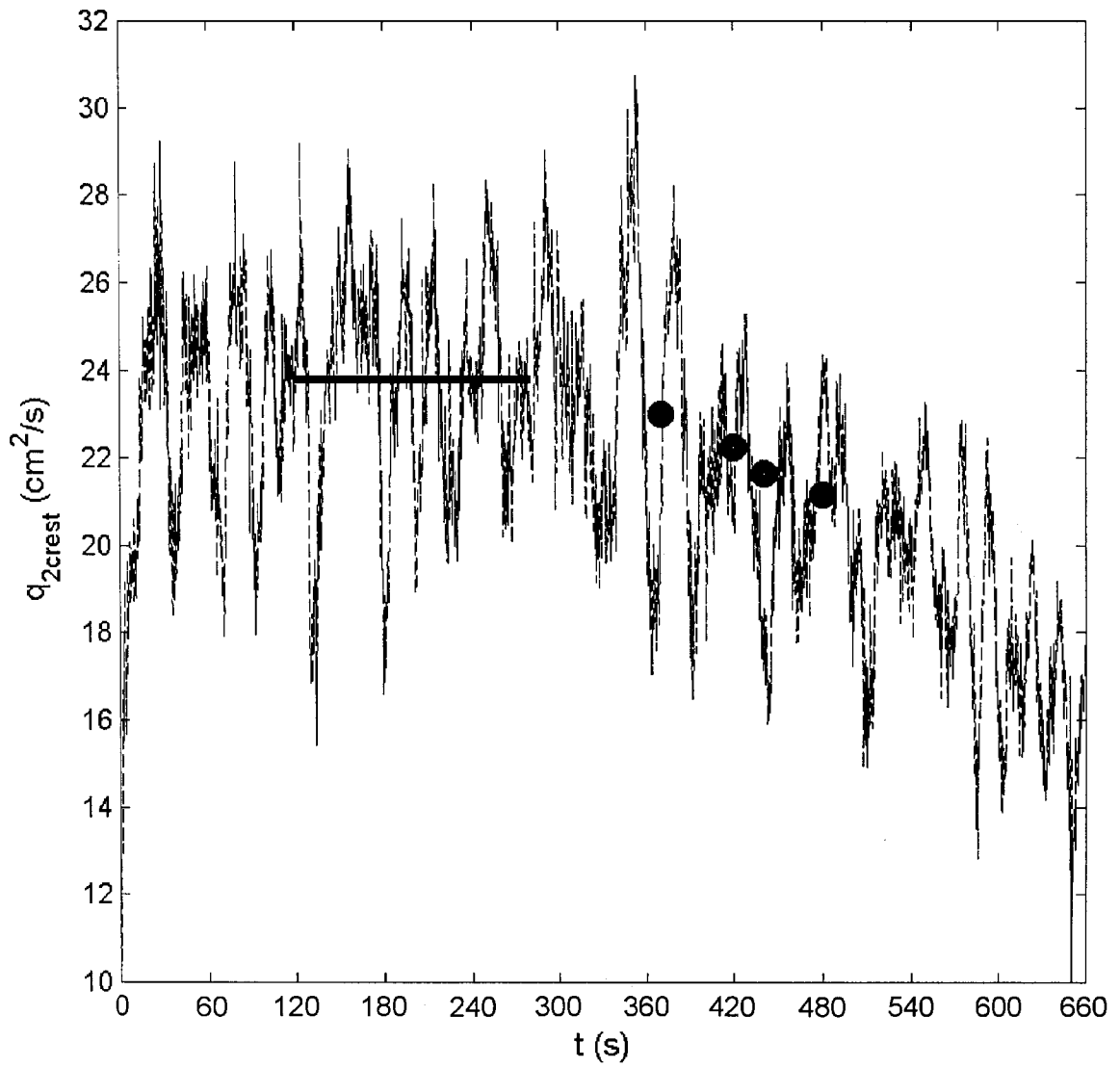
FIGURE 3-5. Time series of q_2 at the sill crest from the start of the experiment and up to about 11 minutes. The solid line shows the mean maximal exchange of 23.78 cm^2/s and the circles represent selective sub-maximal values at $t = 370, 420, 440$ and 480 s.

150
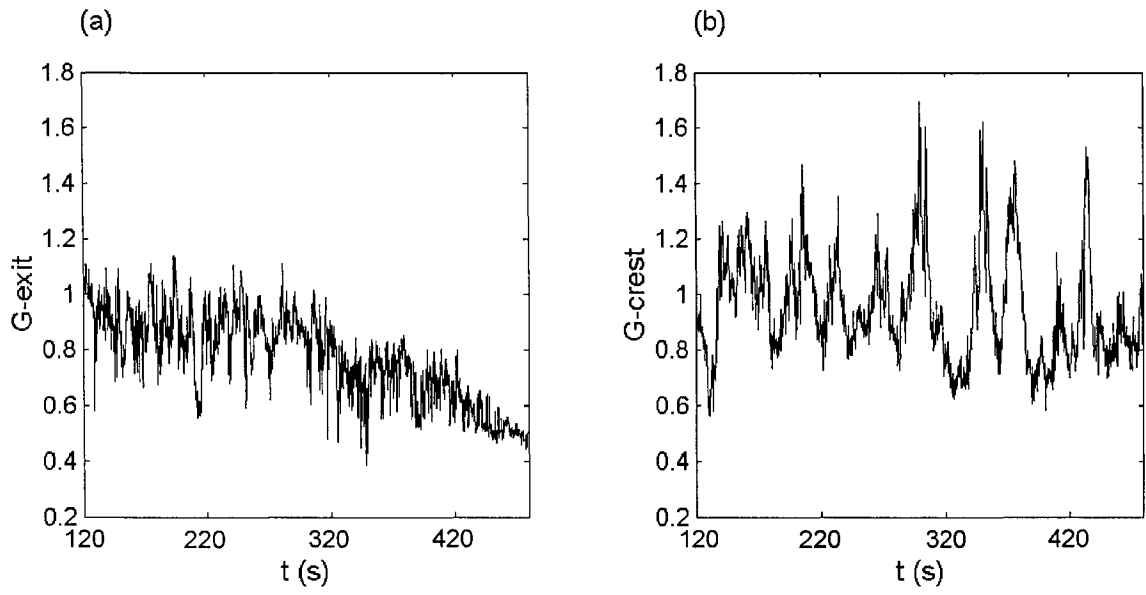
FIGURE 3-6. The temporal evolution of the composite Froude number, G: (a) at the channel exit; and (b) at the sill crest.

151
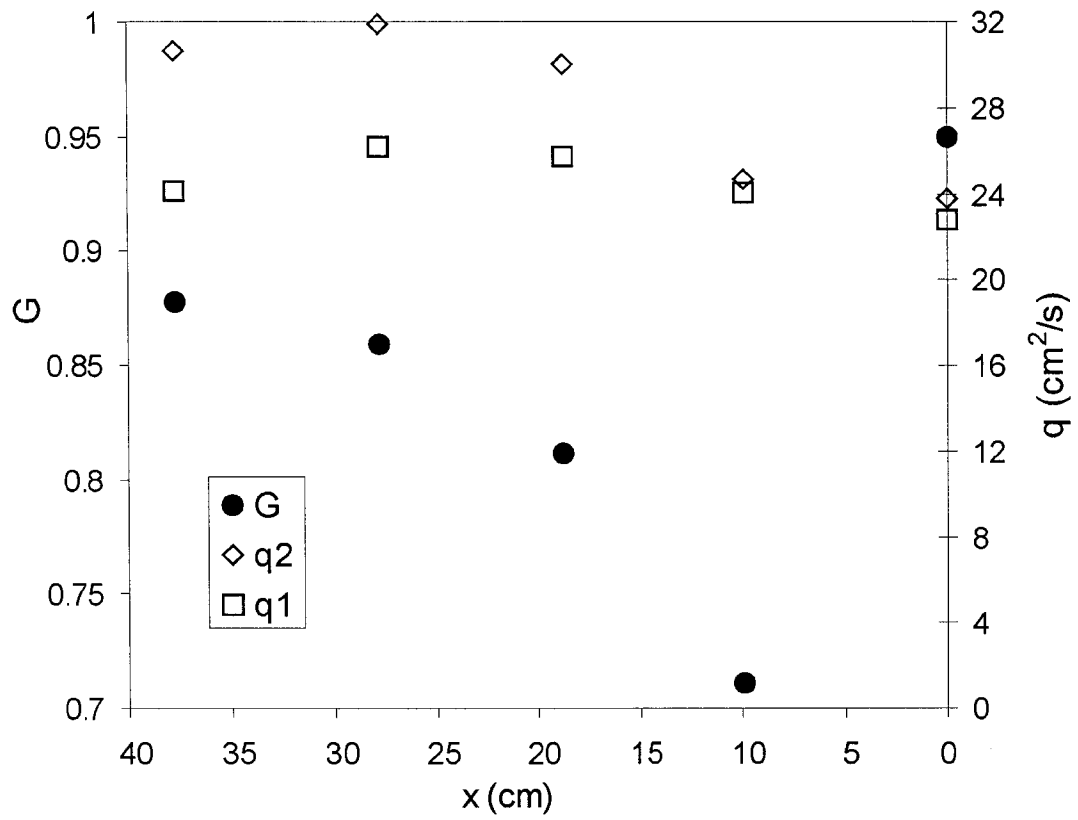
FIGURE 3-7. The variation of the time-averaged composite Froude number, G, and the flow rate per unit width, q, in the upper and lower layers along the channel measured within the steady maximal exchange in Exp 1c. Locations are at $x = 0$ (crest), 9.86, 18.82, 27.79, and -37.5 (exit) cm.

152
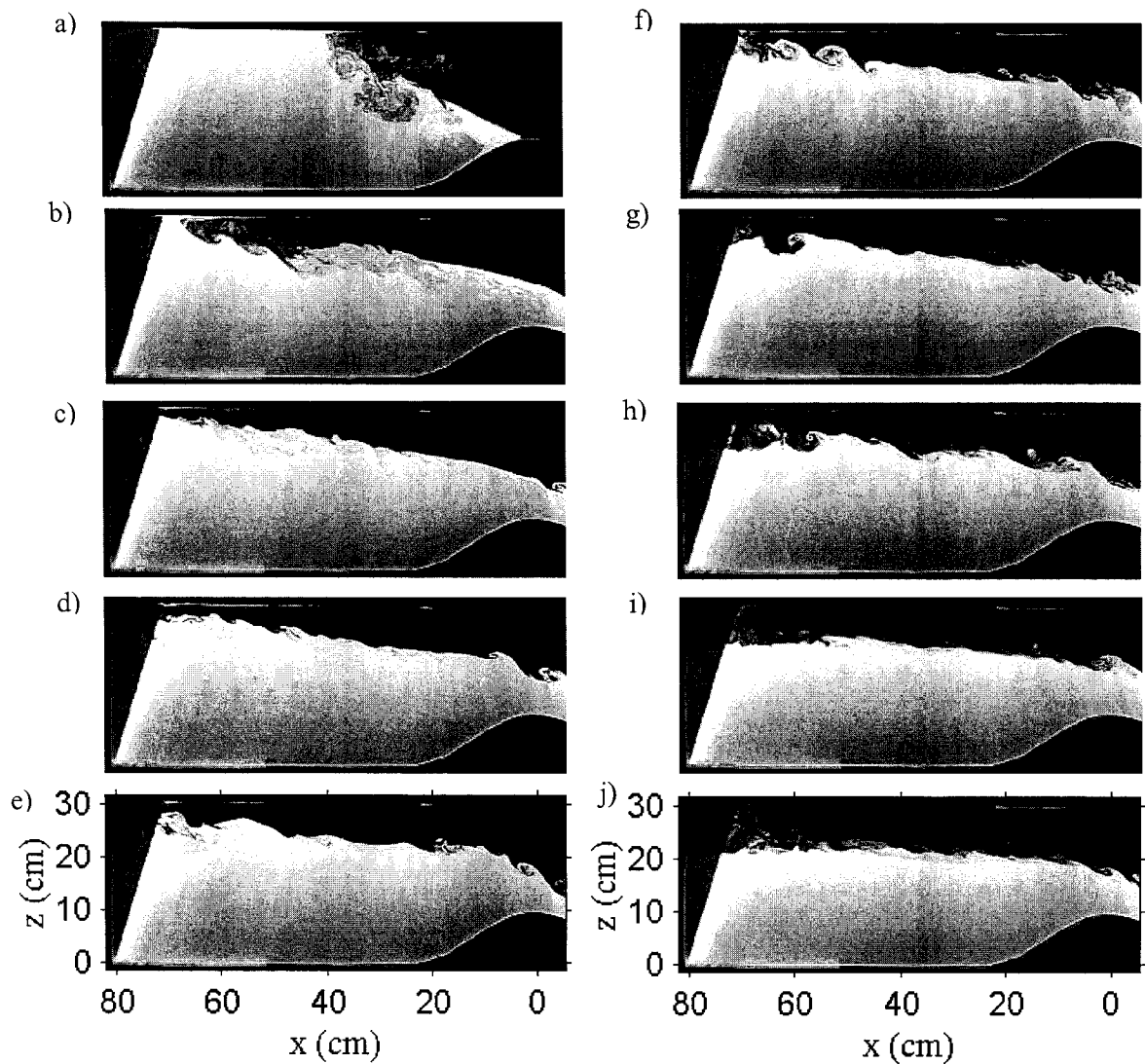
FIGURE 3-8. Selective images from Exp 1a showing the development of the flow field with time. To the left: images are 7 s apart from the beginning of the experiment to almost when the exit hydraulic control was established ($t \approx 30$ s). To the right: images are 40 s into the experiment and are 75 s apart.

153
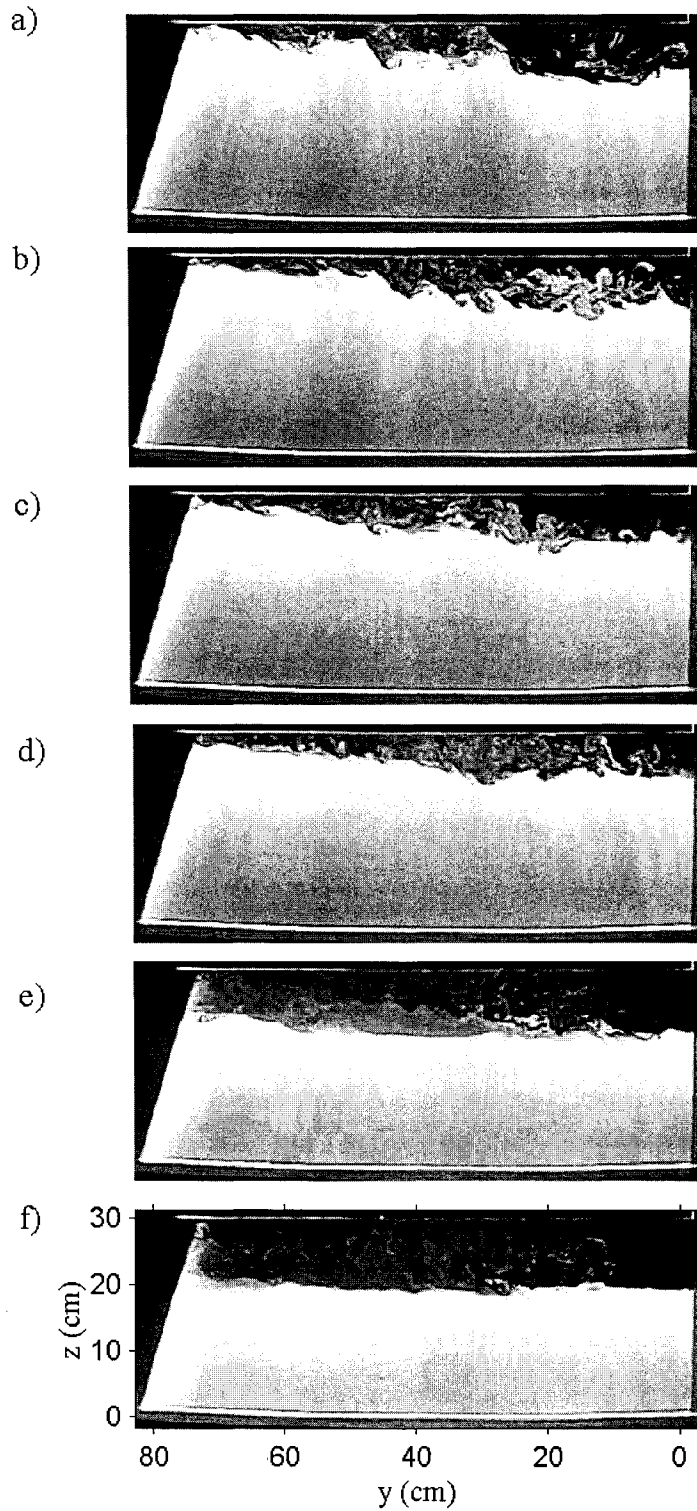
FIGURE 3-9. Selective images of view (B-B) in Exp 1b at 142, 150, 166, 171, 371, and 471 s from the start, successively from top to bottom. Images a - d are within the maximal regime, while images e and f are in the sub-maximal regime.

154
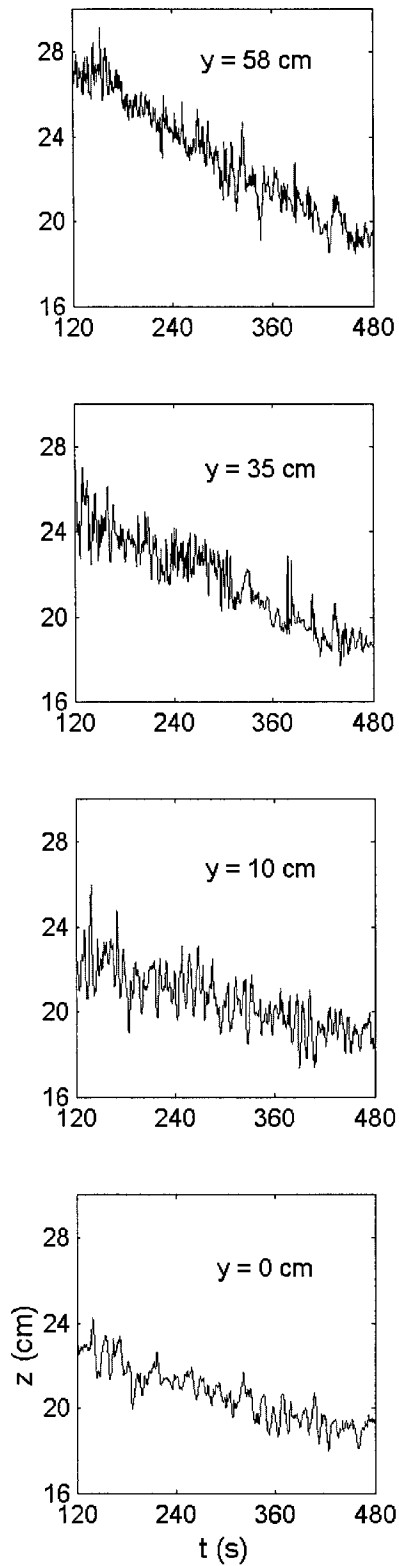
FIGURE 3-10. The interface positions' time series at different locations within the reservoir after the maximal regime has started in Exp 1b.

155
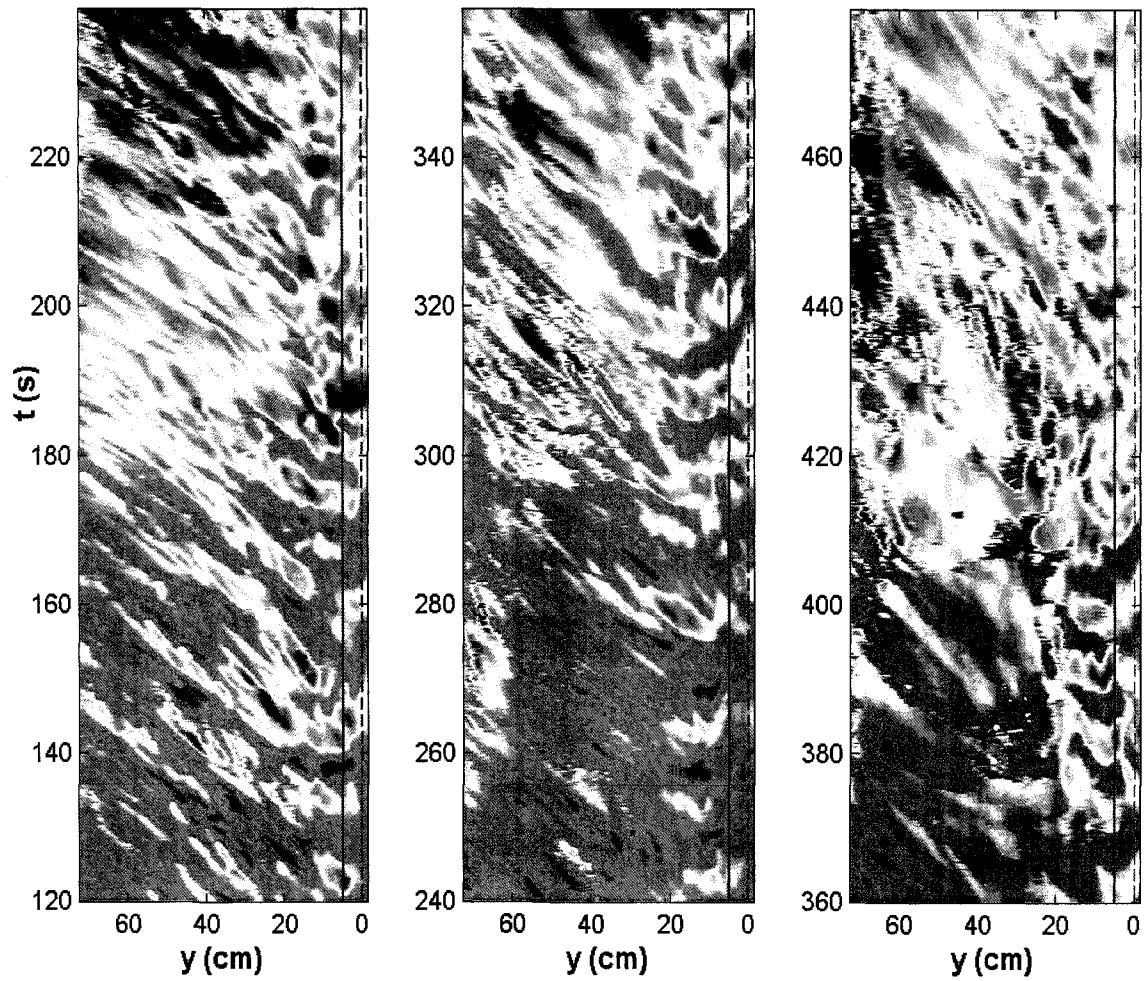
FIGURE 3-11. The wave characteristics' plot in Exp 1b for the view (B-B) into the tank. The channel centerline is shown in dashed line and the left boundary of the channel is in solid.

156
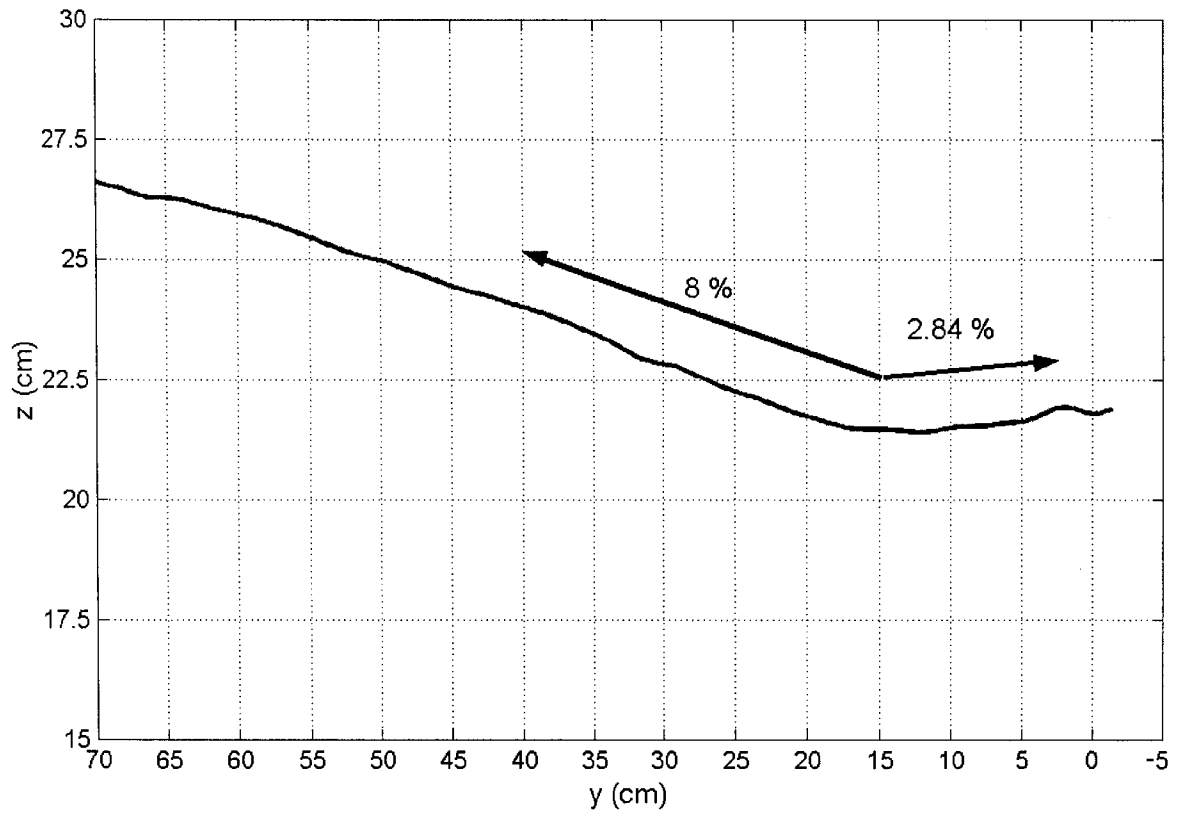
FIGURE 3-12. The time-averaged interface over the maximal exchange in Exp 1b within the field of view (B-B). The channel axis is at $y = 0$.

157
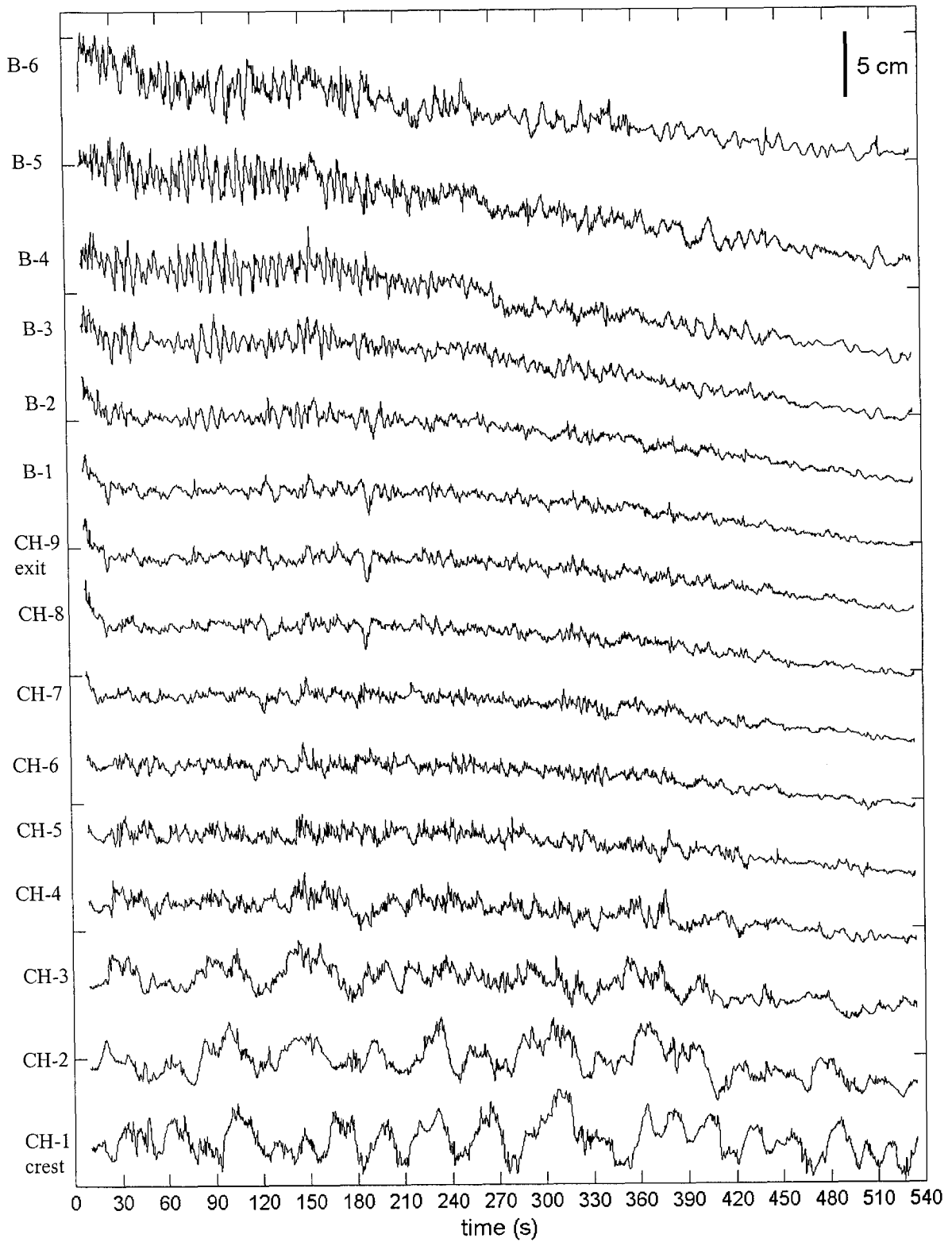
FIGURE 3-13. The interface positions' time series at 15 different locations upstream to and including the sill crest in Exp 1.

158
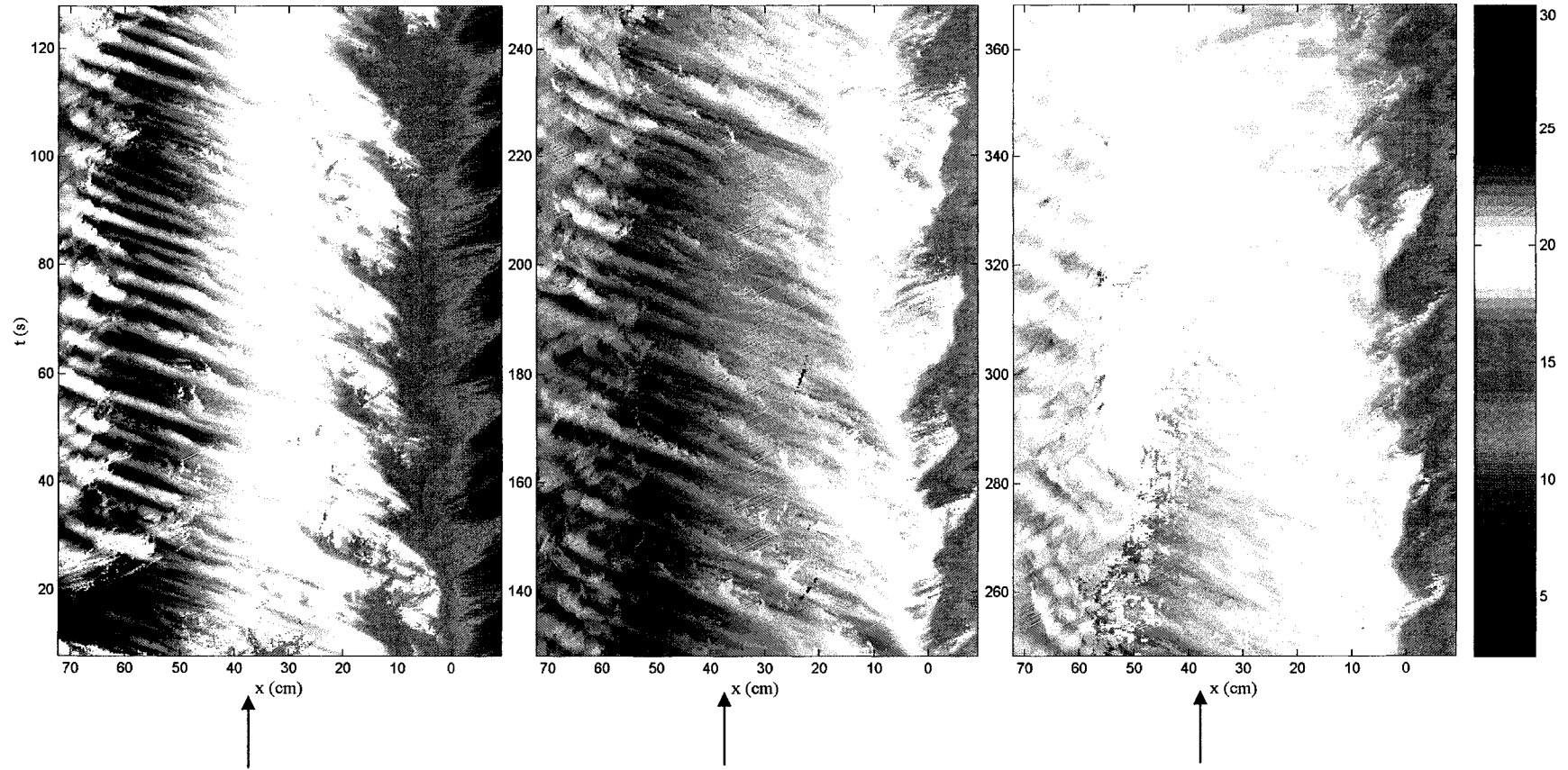
FIGURE 3-14. The wave characteristics' plot of the lower interface positions' time series for over 6 minutes in Exp 2. Two sets of waves are observed simultaneously to be generated around $x \approx 5$ cm. The arrows indicate the channel exit ($x = 37.5$ cm), while the crest is at $x = 0$. The color bar reflects the interface height above the channel bed in centimeters. Signatures of frequent large-scale K-H instabilities are obvious outside the channel in the left panel.
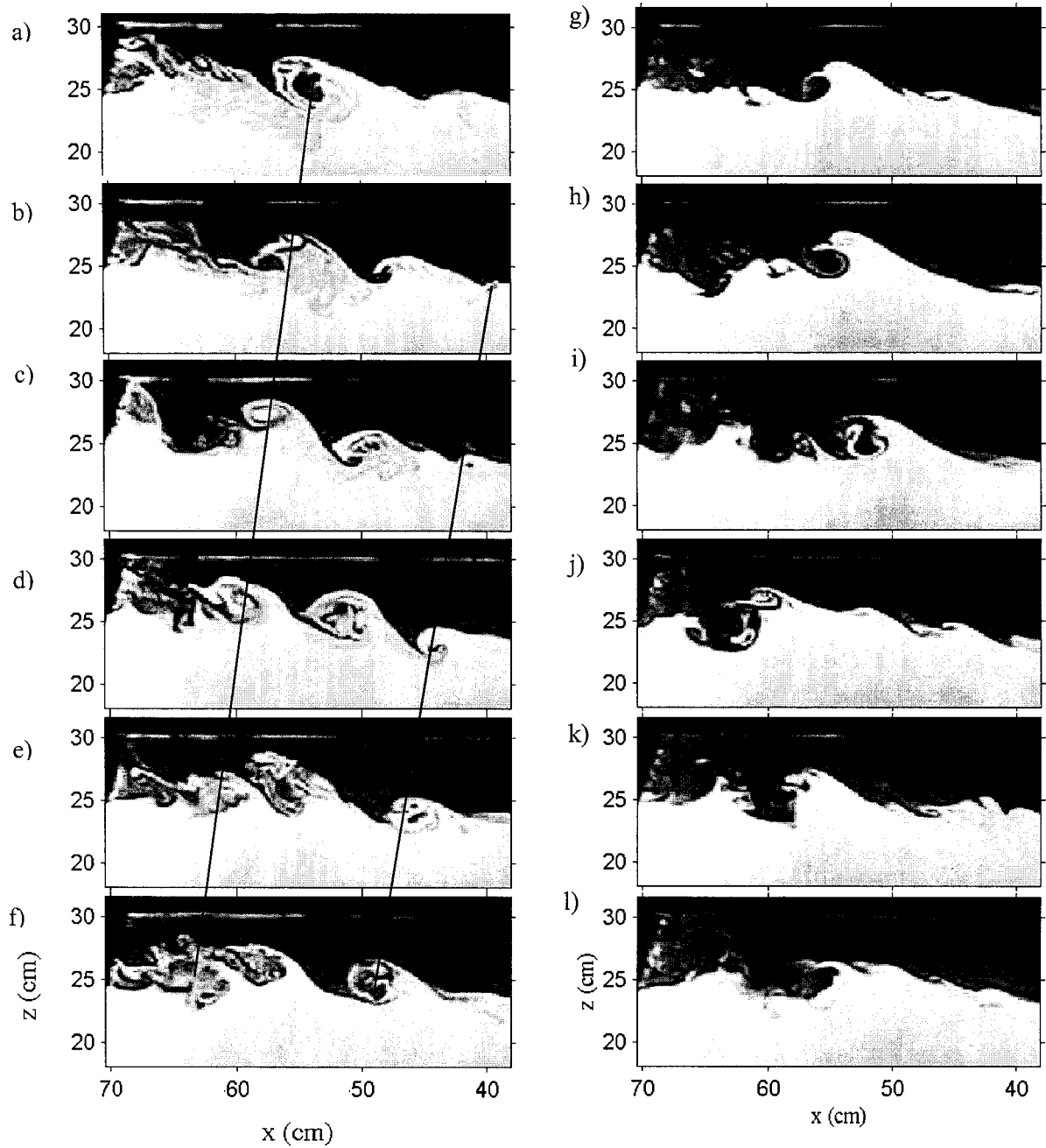
FIGURE 3-15. To the left: series of images showing pairing of large scale K-H instabilities outside the channel in Exp1. Images are 34 s into the experiment and are 2 s apart. To the right: selective images showing collision of two counter-flowing K-H instabilities (images g, h), and the erosion of the interface due to counter-rotating instabilities (images i - l). The images (from top to bottom) are at about 80, 89, 102, 117, 128, and 142 s into the experiment.

160
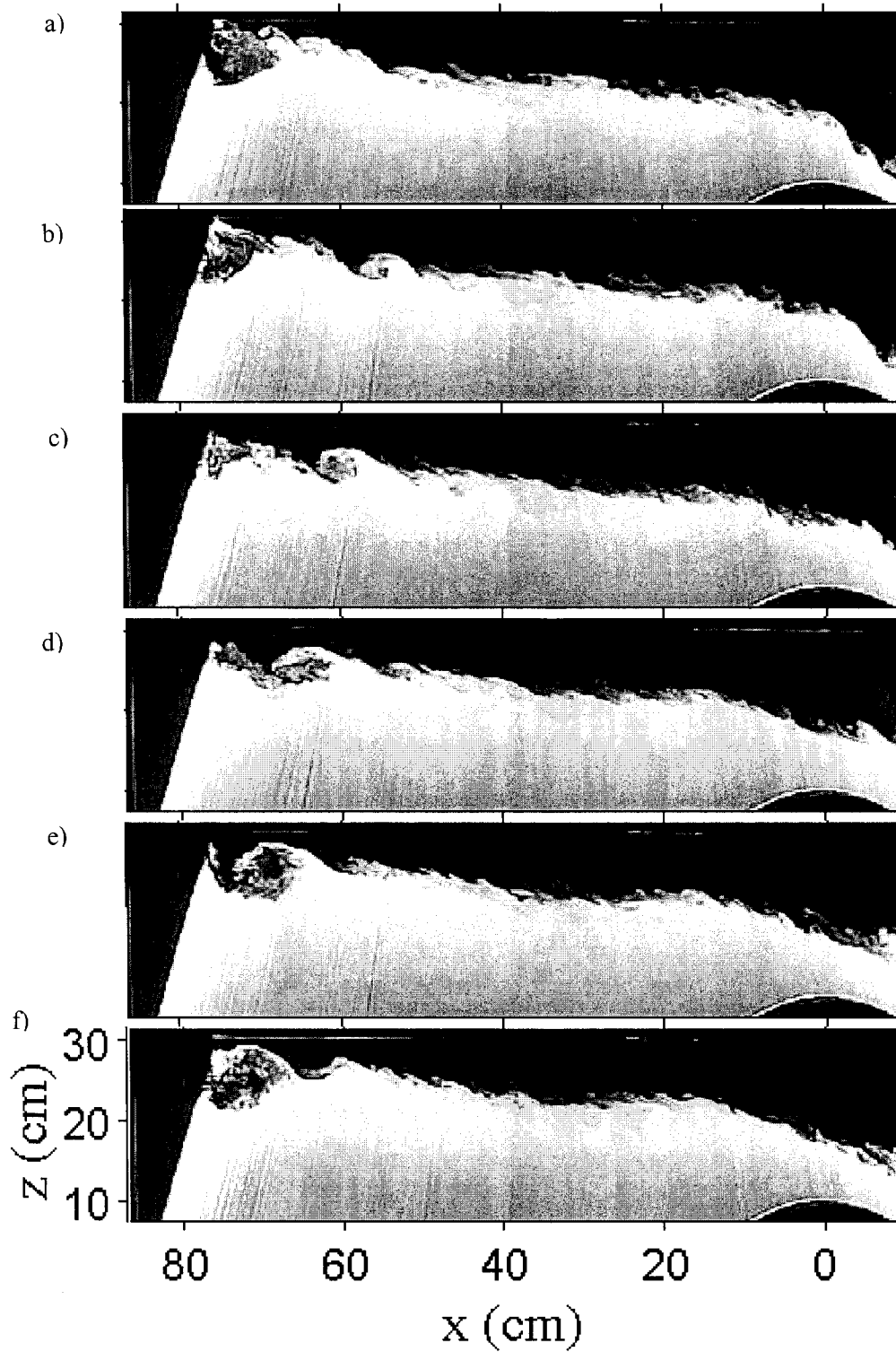
FIGURE 3-16. Series of images from Exp3 during the maximal regime. The images are at about 26 s into the experiment and are one second apart starting from top.

161
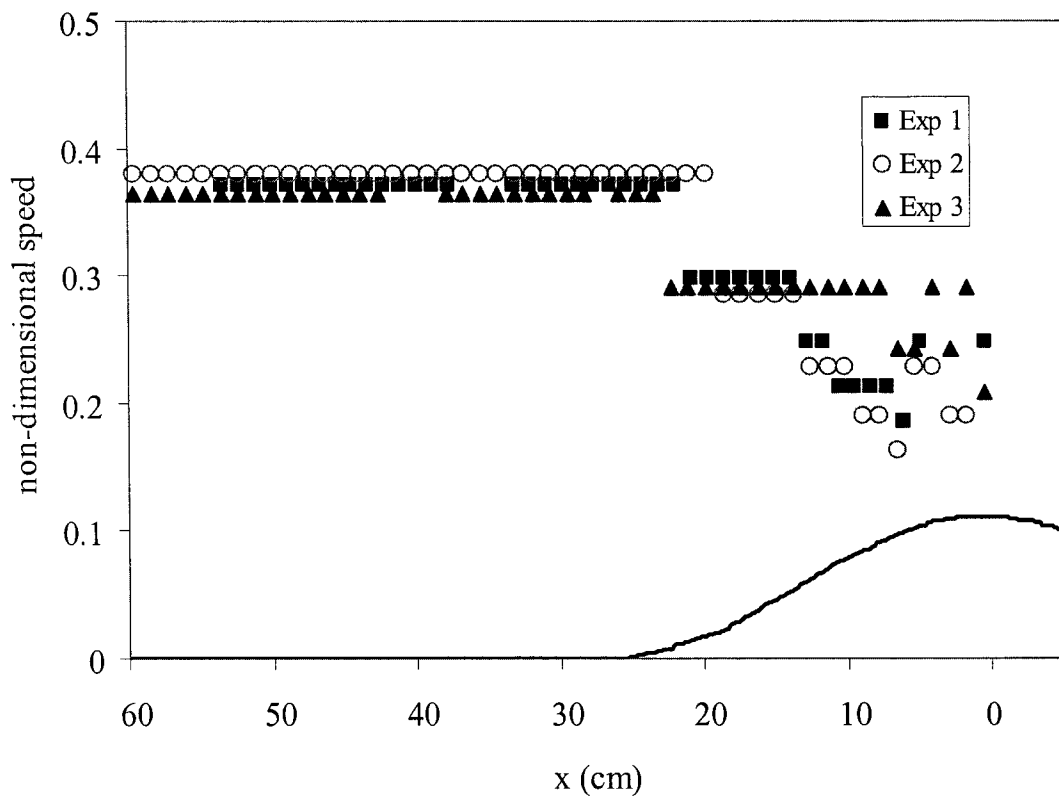
FIGURE 3-17. The spatial variation of the non-dimensional wave speeds obtained through cross-correlation of adjacent times series of the interface positions in the three experiments.

FIGURE 3-18. Speeds of propagation of individual K-H instabilities within the channel in the three experiments and their mean.

163
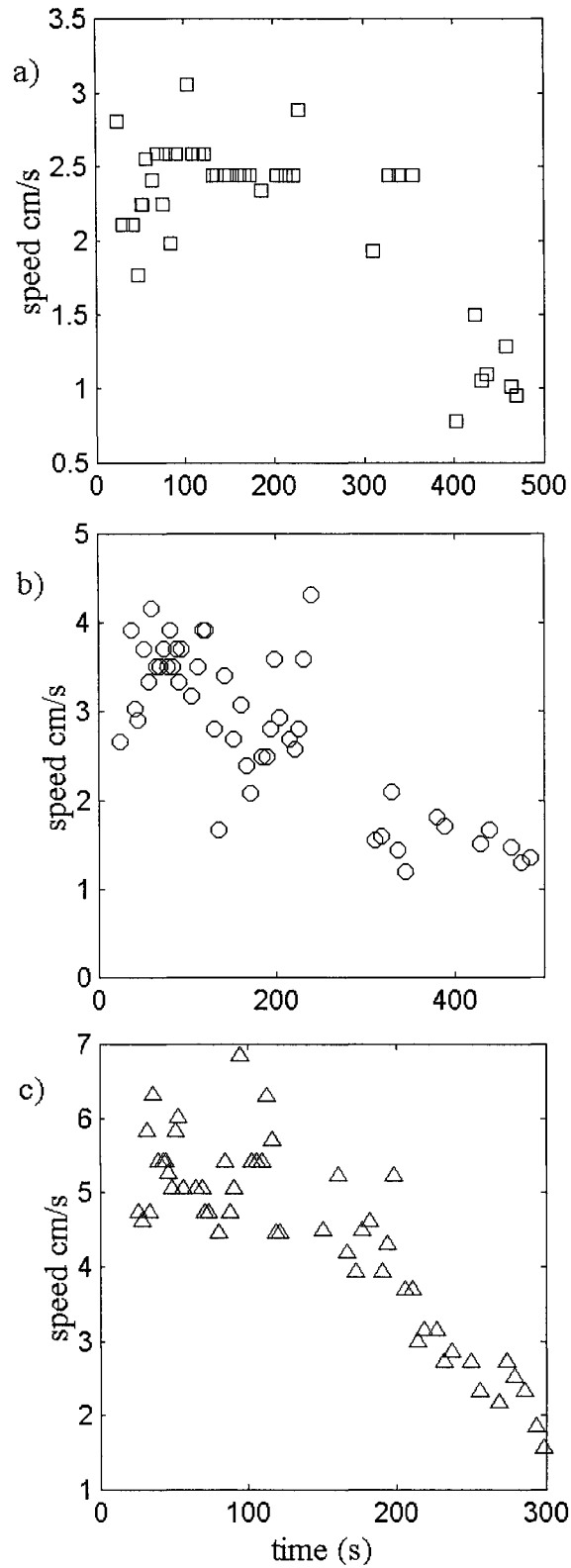
FIGURE 3-19. The temporal variation of the wave speed at the location B-3 (x = 50 cm) in: a) Exp 1, □; b) Exp 2, ○; and c) Exp 3, △.

164
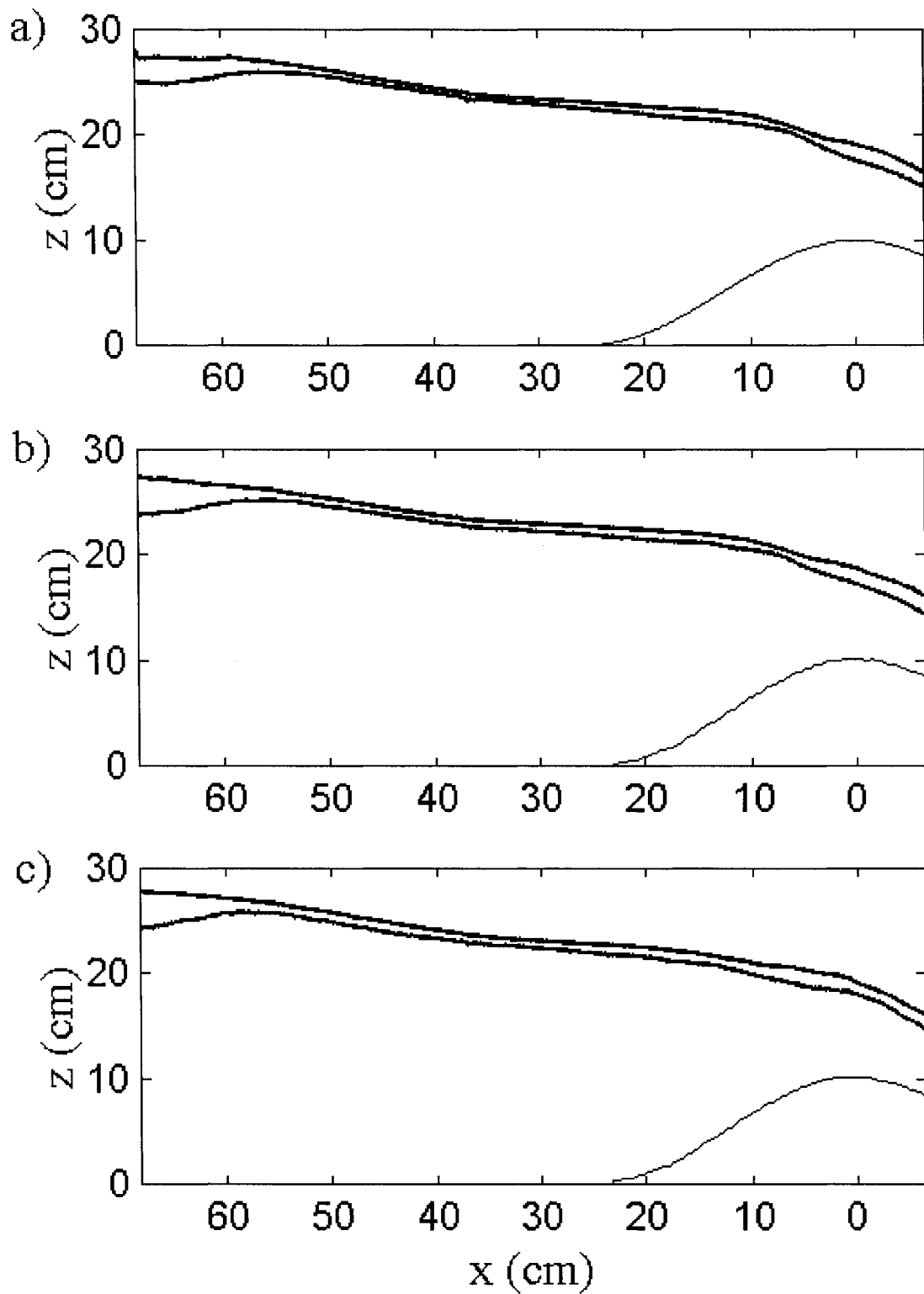
FIGURE 3-20. The time-averaged upper and lower interfaces over the maximal regime in: a) Exp1, b) Exp 2, and c) Exp 3.
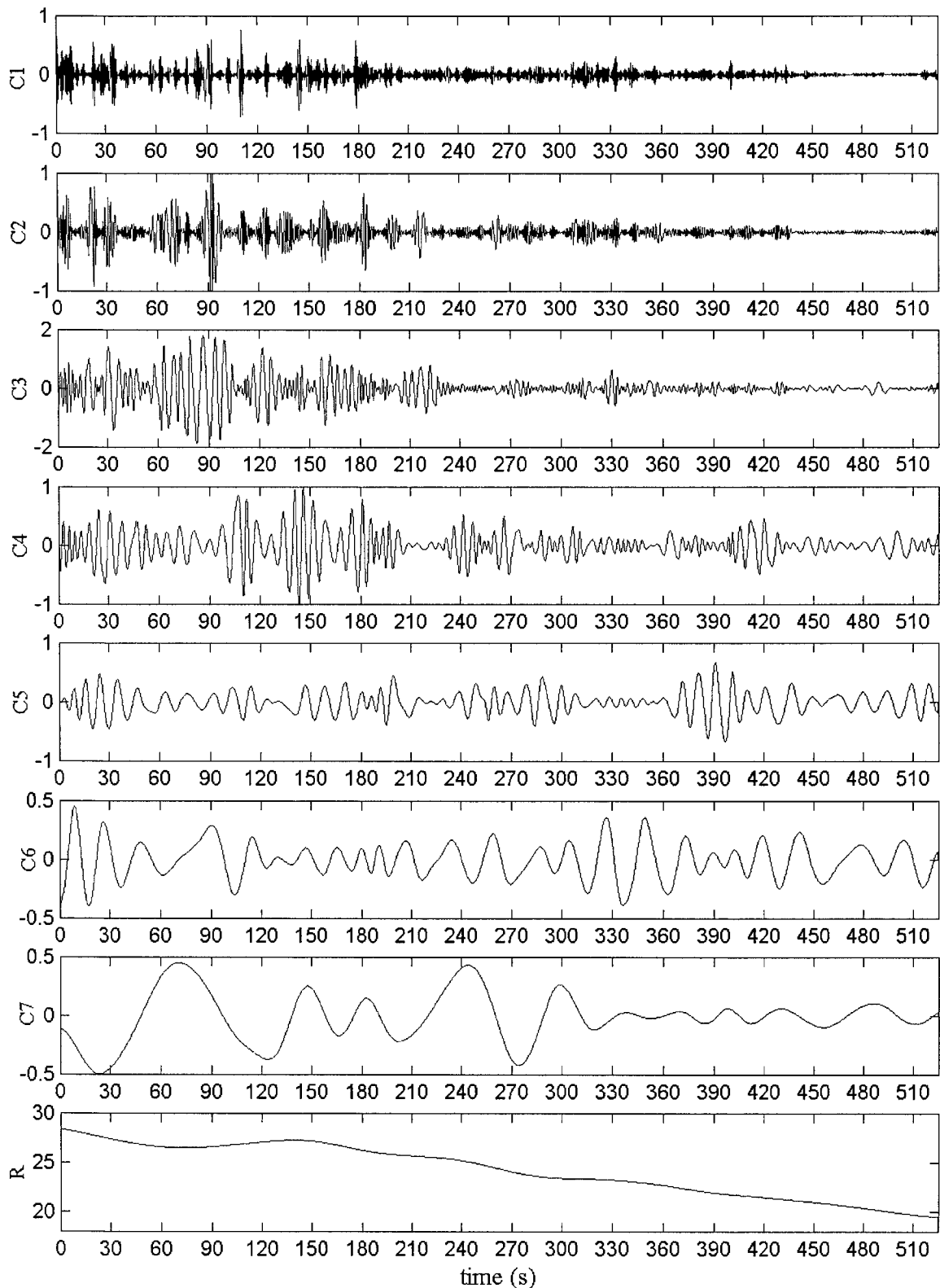
FIGURE 3-21. The IMFs generated through the empirical mode decomposition of the interface positions' time series using HHT at the location B-4 in Exp 1a. Modes C3 and C4 are the relevant modes for the observed high frequency K-H instabilities.

166
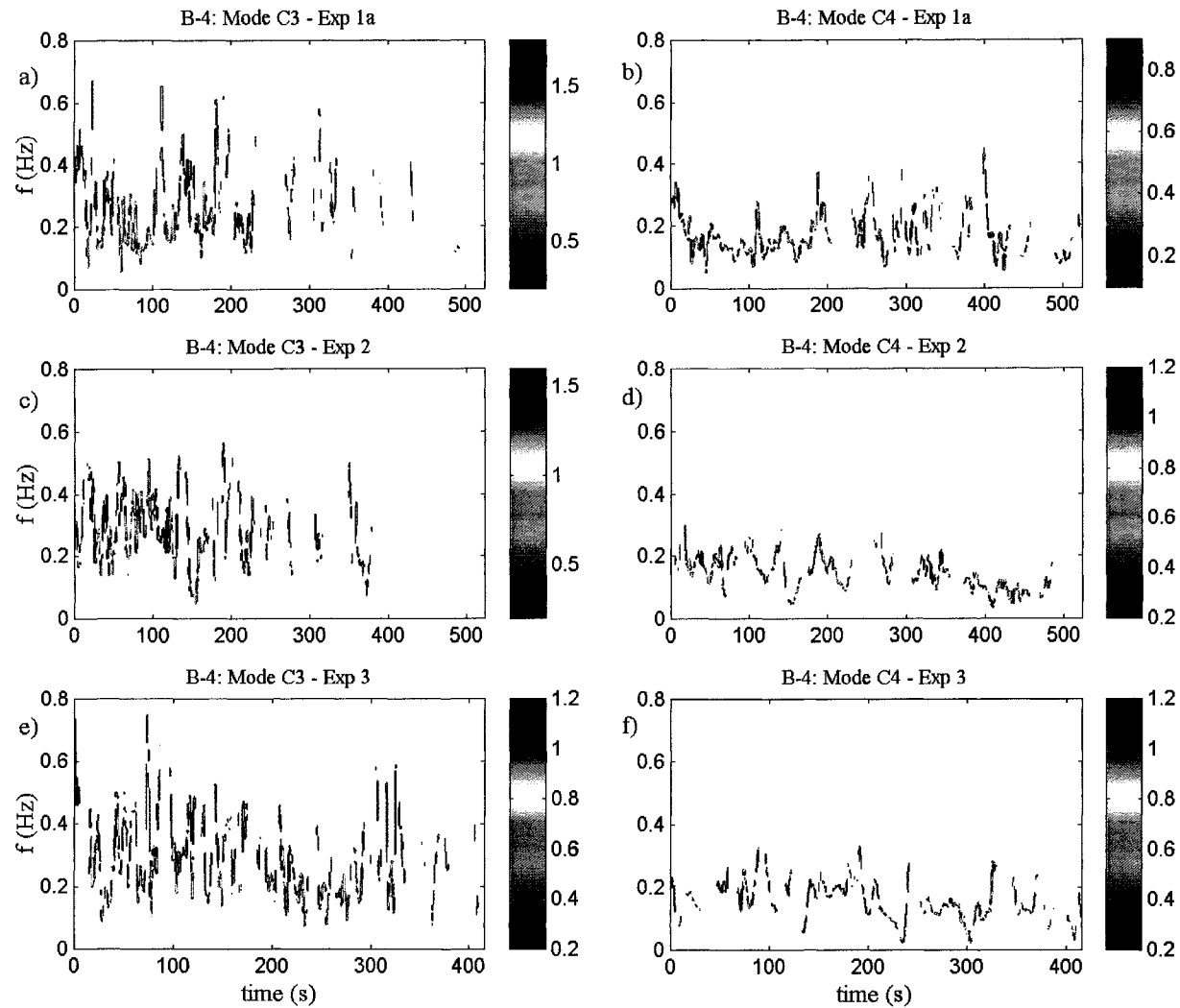
FIGURE 3-22. The temporal variation of frequency for mode C3 at the location B-4 in the three experiments. HHT was performed at no intermittency.
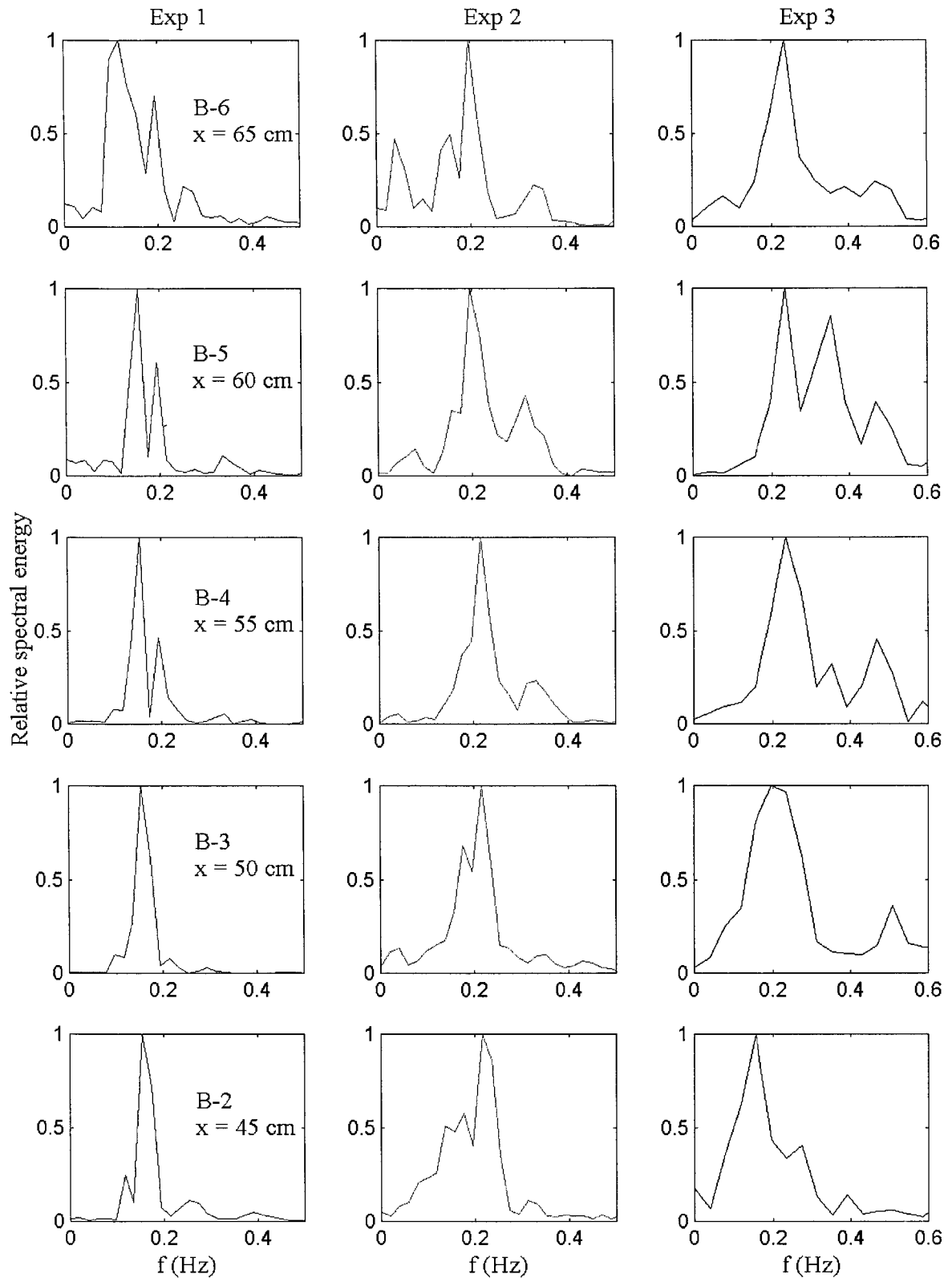
FIGURE 3-23. The Fourier power spectra of the interface positions' time series at five sample locations in the basin upstream to the channel exit (view A-A) in the three experiments. Locations are indicated in the left column.

168
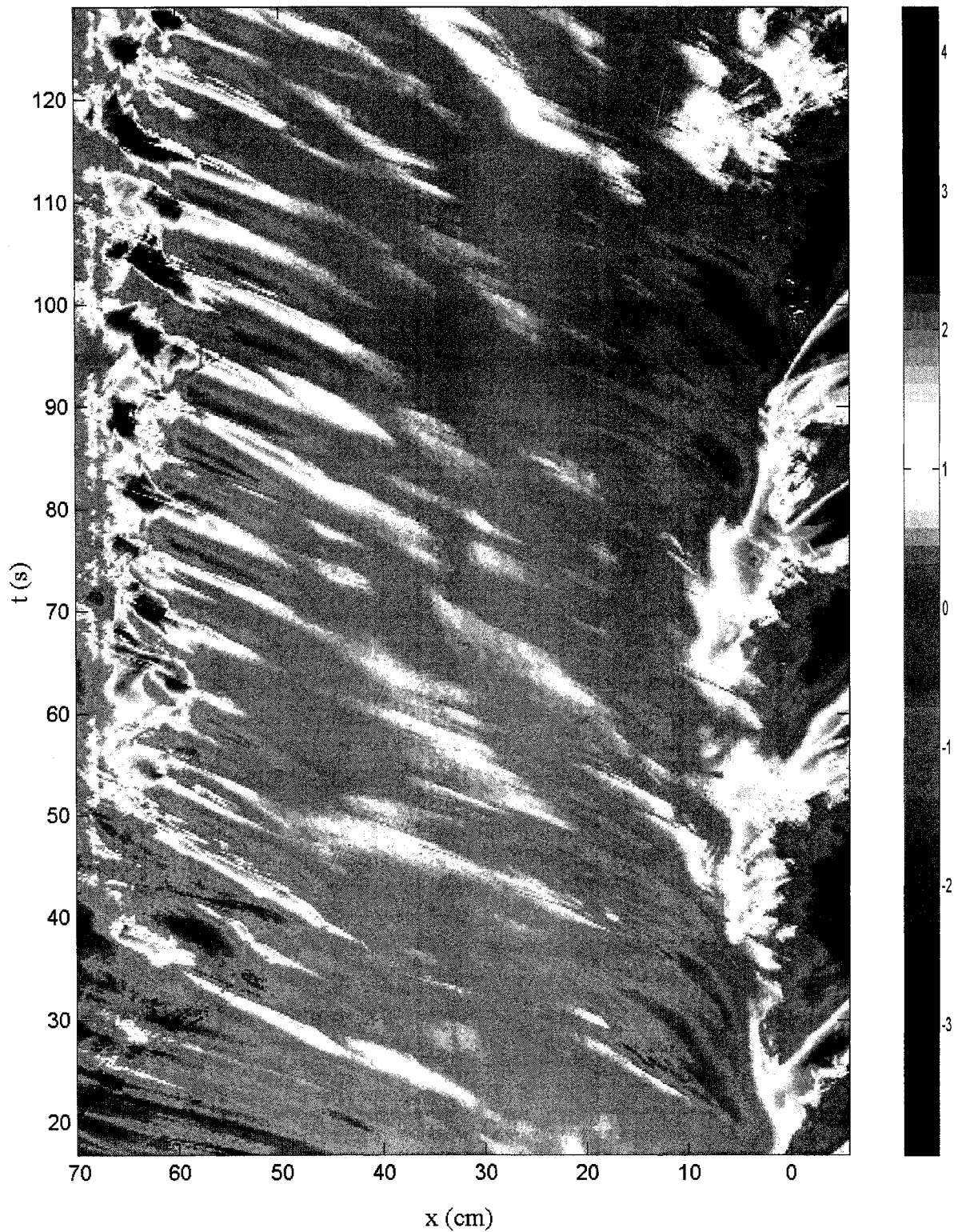
FIGURE 3-24. Wave characteristics' plot for Exp 1 - tile A ($t = 17\text{-}129\text{s}$), color bar reflects the difference in cm between the instantaneous and the 2-minute-mean interface.

169
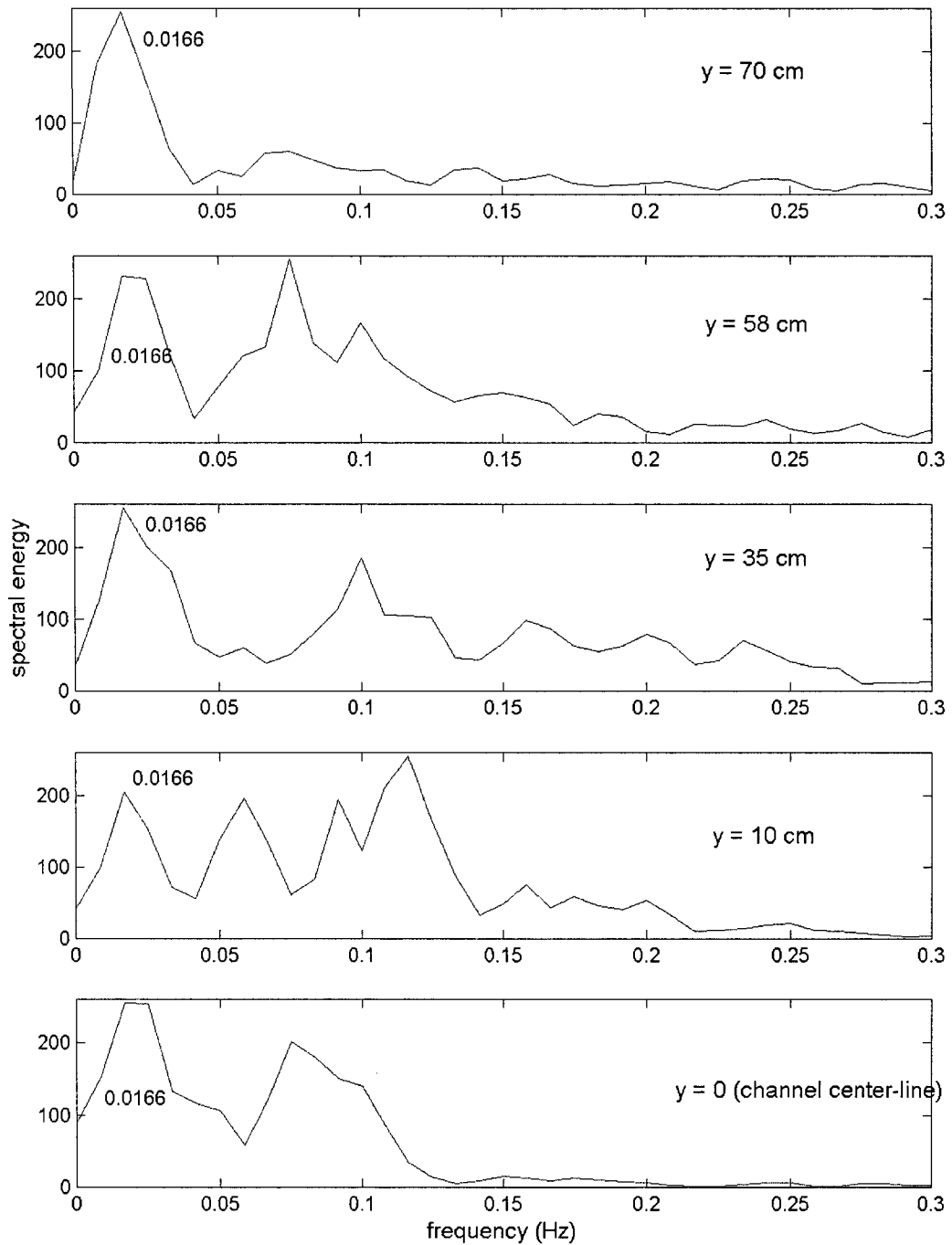
FIGURE 3-25. The Fourier power spectra of sample interface positions' time series within the tank in Exp 1b. The persistence of the low frequency of 0.0166 Hz is obvious at the different locations.

170
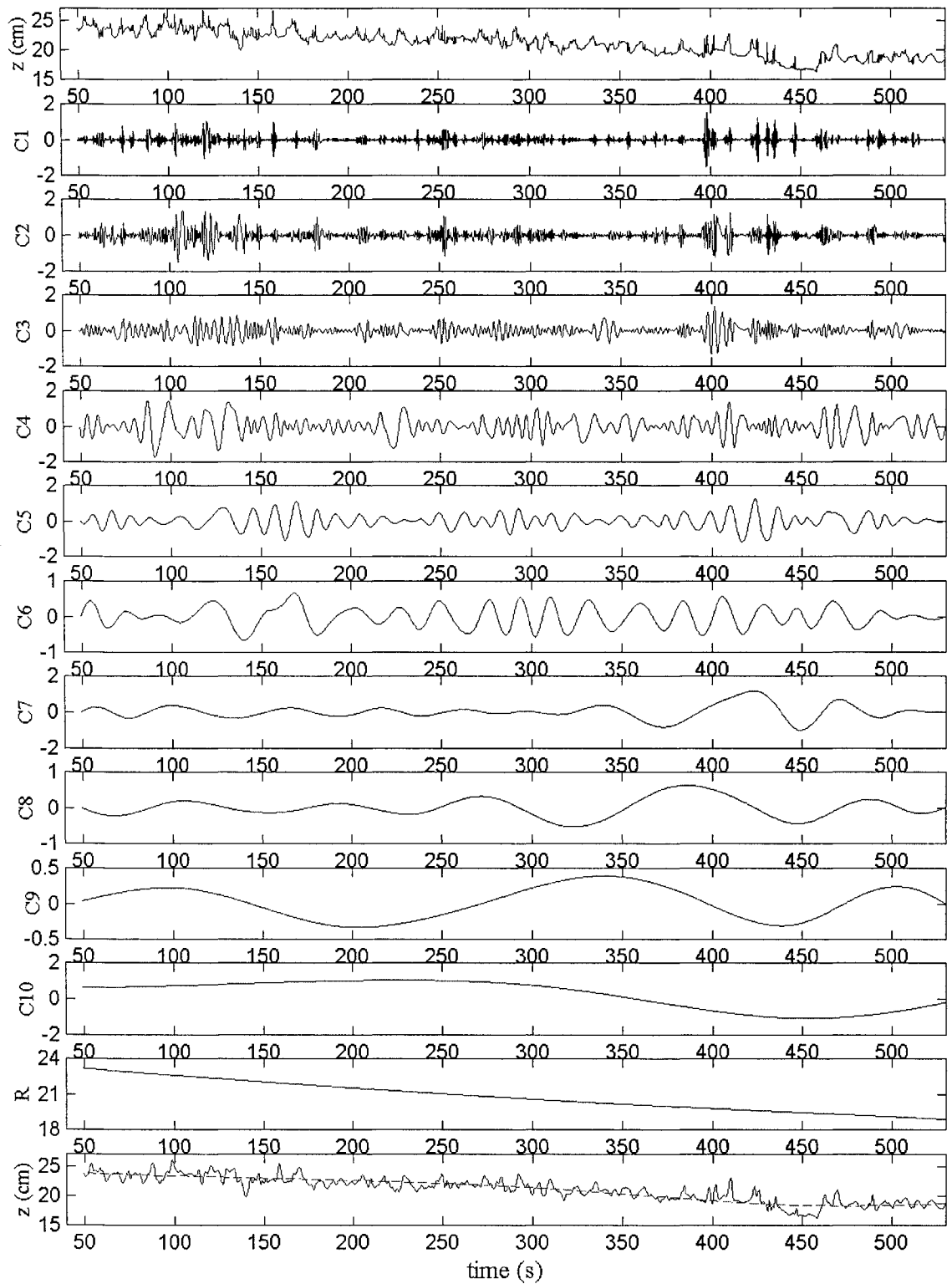
FIGURE 3-26. The IMFs generated using the empirical mode decomposition of the interface positions' time series for the location $y = 50$ cm into the tank using HHT at no intermittency. The reconstructed signal of (C3:C10 + R) is shown at the bottommost panel along with the trend composed of (C10+R) over-plotted.

171
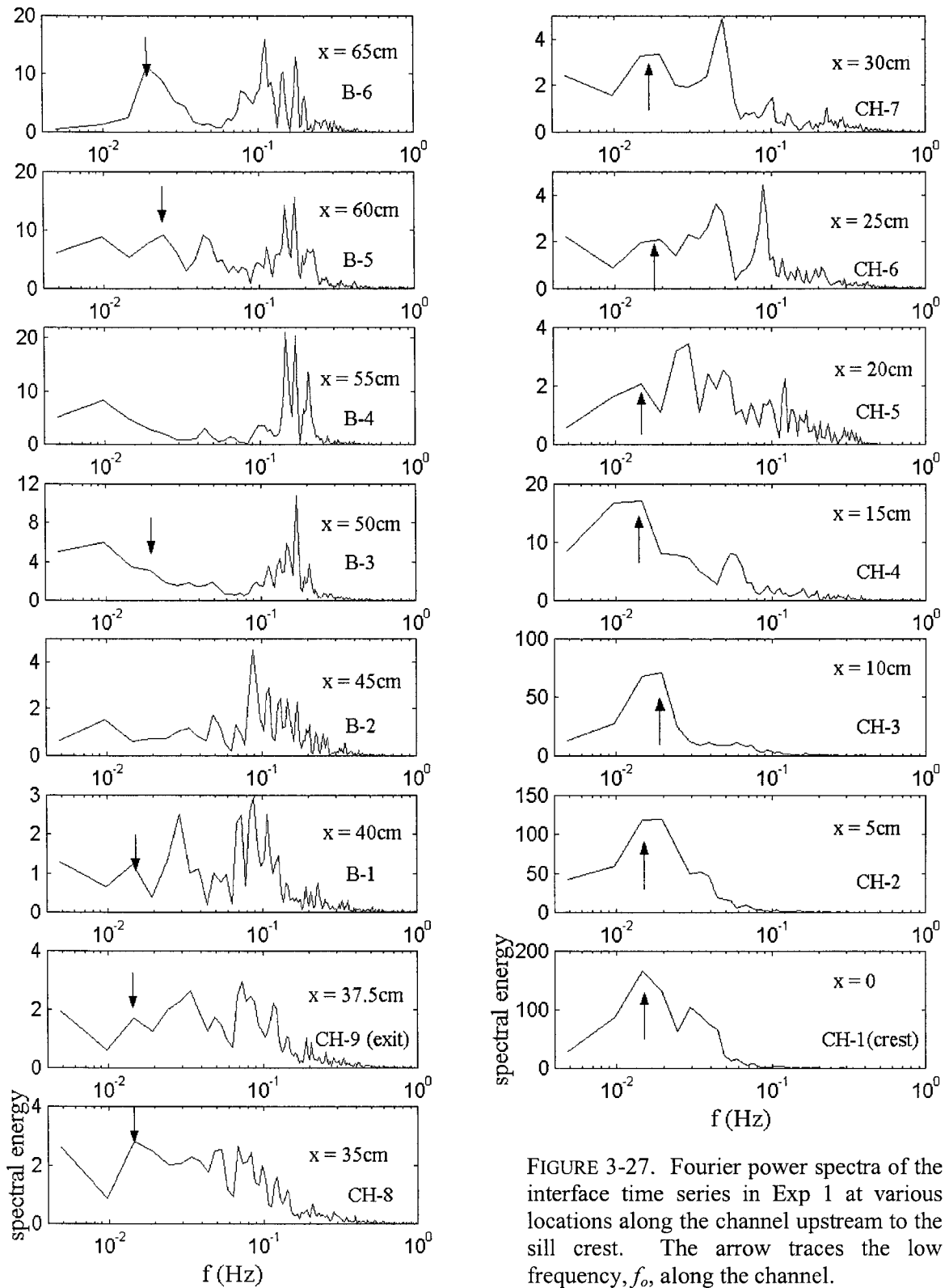
FIGURE 3-27. Fourier power spectra of the interface time series in Exp 1 at various locations along the channel upstream to the sill crest. The arrow traces the low frequency, f_o, along the channel.

172
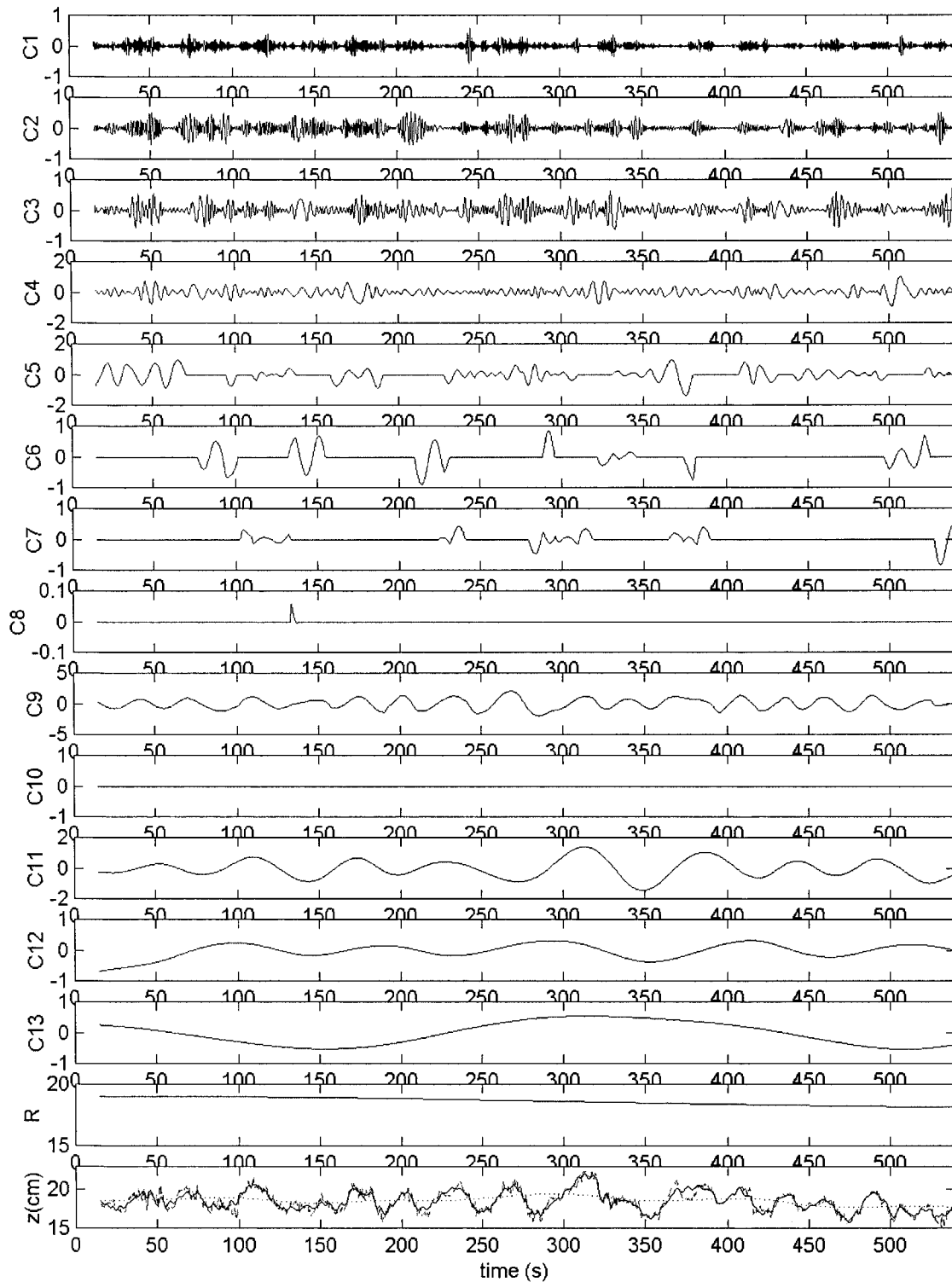
FIGURE 3-28. The EMD of the interface positions' time series at the sill crest using HHT with intermittency. The lowermost panel shows the original time series (...) with the reconstructed signal of C4, C9, C11-C14 (solid) and the trend (C13+R) over plotted (dashed).

173
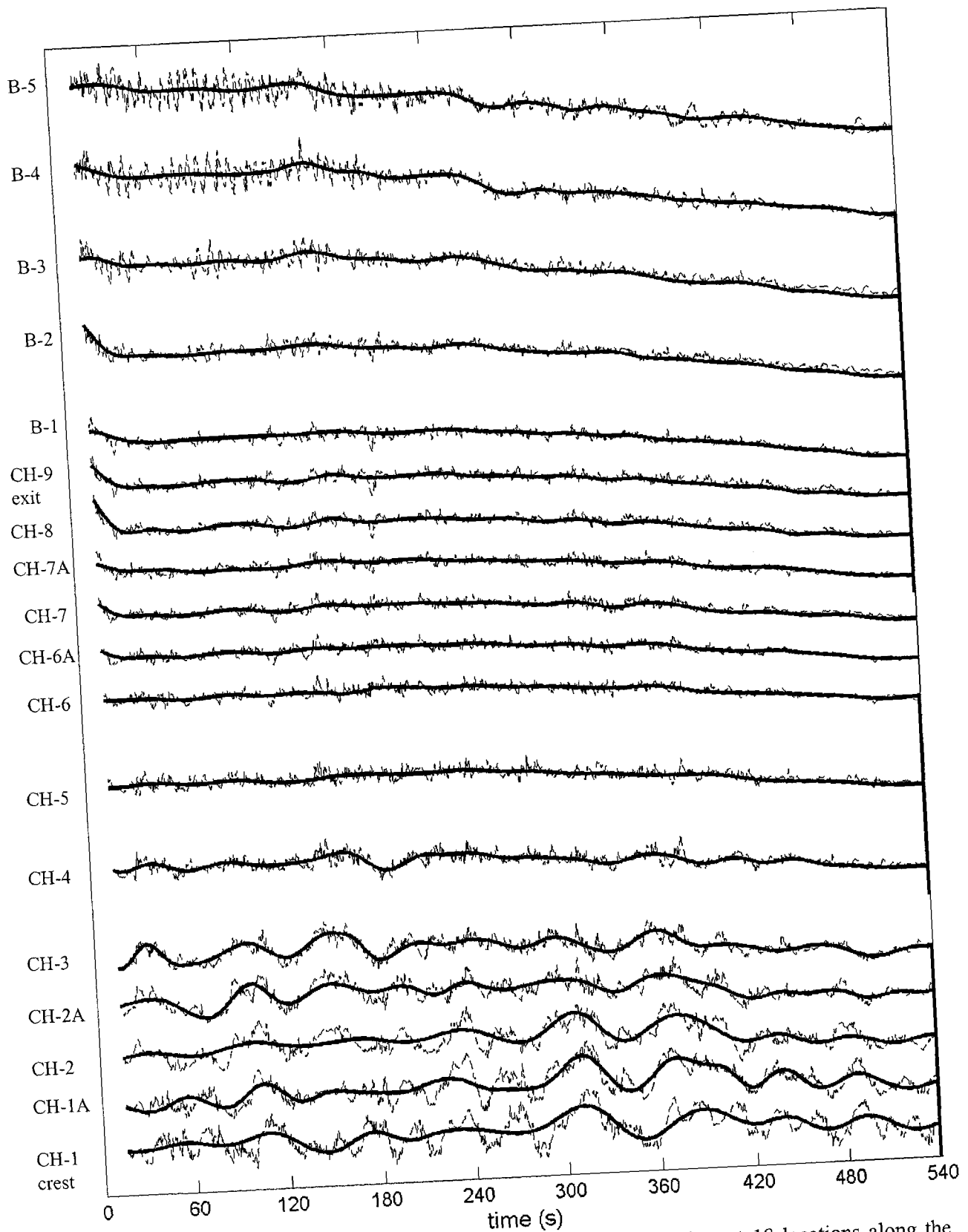
FIGURE 3-29. The original time series of the interface position data at 18 locations along the channel with the long wave mode obtained via HHT over plotted.

174
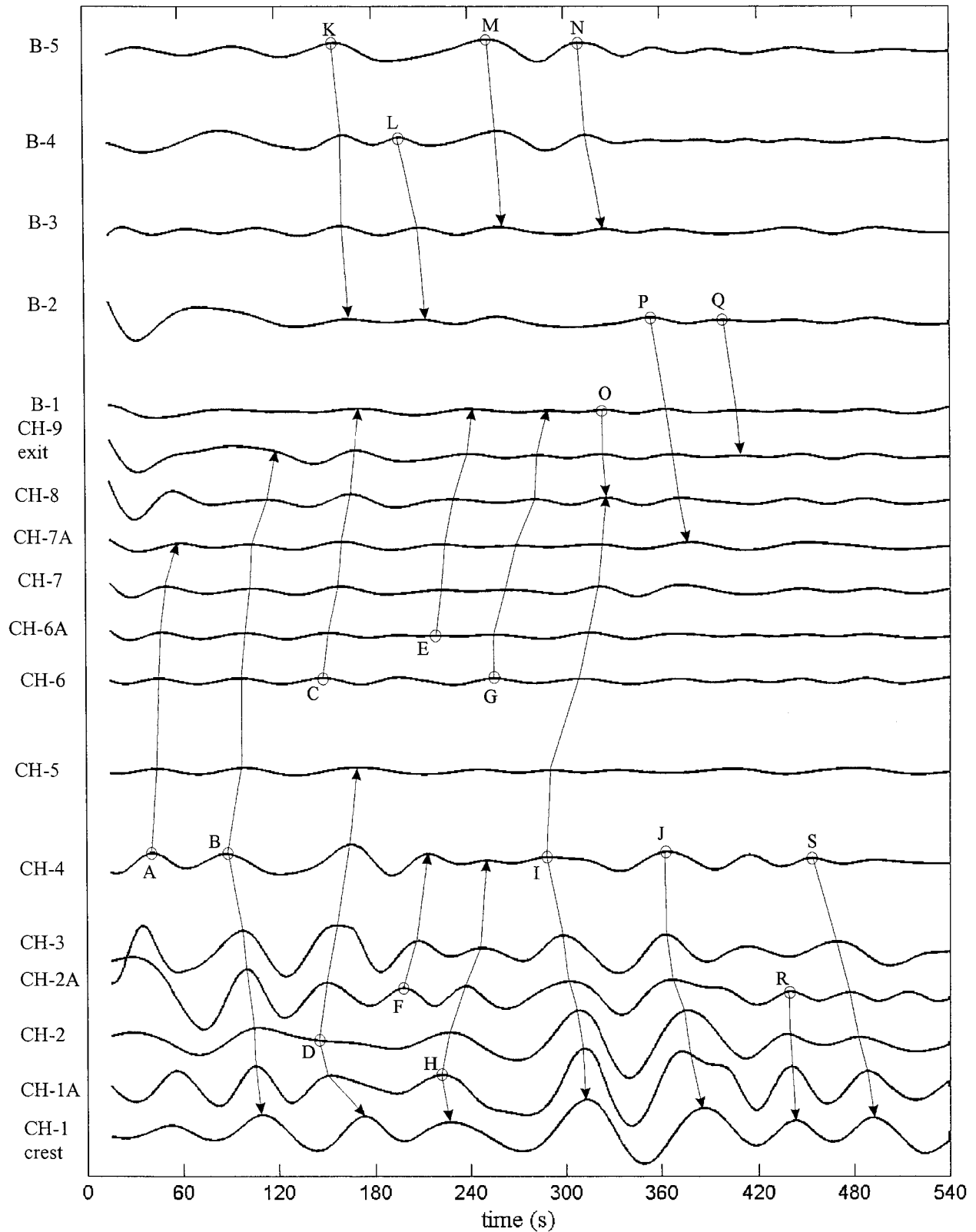
FIGURE 3-30. The long wave modes obtained from the HHT analysis at the different locations along the channel. The nodes indicate the source of the waves being traced by the path lines with the arrows indicating the direction of propagation.

175

Table 3-1. List of experiments and their parameters.

Experiment	g' (cm/s^2)	Field of view	H (cm)	Objective
1a	1.62	(A-A)	30	Interface
1b	1.62	(B-B)	30	Interface
1c	1.62	(A-A)	30	Velocity
2	3.23	(A-A)	30	Interface
3	6.47	(A-A)	30	interface

Table 3-2. Boundary layer thickness along the channel upstream to the sill crest.

	Distance from exit, s (cm)	9.71	18.68	27.64	37.50
	q_2 (cm^2/s)	31.82	30.07	24.62	23.74
	z_2 (cm)	23.10	20.58	14.40	8.40
	U_2 (cm/s)	1.39	1.46	1.71	2.83
Exp 1	Re_x	1168	2359	4089	9180
	δ_{BL} (cm)	1.4	1.9	2.2	2.0
Exp 2	Re_x	1649	3331	5773	12963
	δ_{BL} (cm)	1.2	1.6	1.8	1.7
Exp 3	Re_x	2335	4718	8177	18360
	δ_{BL} (cm)	1.0	1.4	1.5	1.4

176

Table 3-3. The variation of the frequencies of the large scale K-H instabilities that form outside the channel with g'. Frequencies are in Hz and the periodic times in seconds are in brackets.

g' (cm/s^2)	1.62	3.23	6.47
Maximal regime	0.195 (5.1)	0.332 (3.0)	0.349 (2.9)
Sub-maximal regime	0.156 (6.4)	0.195 – 0.215 (4.7 – 5.1)	0.159 – 0.273 (3.7 - 6.3)

Table 3-4. Comparison between the periods of the low frequency oscillation observed at the sill crest in different experiments. All periods are in seconds.

g' (cm/s^2)	Periods of the low frequency oscillation at the sill crest		
	h_{sill} = 10 cm	h_{sill} = 12 cm	Opening
1.64	60	68	
3.23	45	41.5	
6.47	36	32.8	
2.50*			62.5

* In this experiment, the sill was replaced by a vertical barrier that had a middle opening whose details are included in Appendix A.

177

CHAPTER 4

ENTRAINMENT AND MIXING IN TWO-LAYER EXCHANGE FLOW IN THE LEE OF BOTTOM TOPOGRAPHY

4.1 INTRODUCTION AND BACKGROUND

Entrainment and mixing of stably stratified fluids are important components in many air and water flows. Examples of such natural flows in which entrainment and mixing are core elements include: air flow over mountain ridges (Worthington, 2002), gravity currents (Alavian et al., 1992), flow of cold river water into lakes, and exchange flow through straits (Bray et al., 1995). These buoyancy-driven flows are typically highly turbulent flows in which the generated mixing changes the density of the flowing layers and controls the transfer of heat, mass and nutrients across the interface between the two concerned layers. Likewise entrainment can affect the volumetric flow rate and may change the density interface height of the flowing layers in such flows (Nielsen et al., 2004; Morin et al., 2004). A distinguishing property in these flows is that they feature processes that combine vertical mixing and horizontal advection.

Because many of these flows occur over sloping terrain, which increases the driving buoyancy force, various recent experimental and theoretical studies focused on mixing and entrainment in stratified down slope flows (Pawlak & Armi, 2000; Baines, 2001). In the context of two-layer exchange flow down an incline, however, the experiments presented in chapter 2 of the current study and those of Morin et al. (2004) revealed that the accelerating flow field washed out any mixing due to the breaking of interfacial waves along the slope. On the other hand, in the late times of the experiments, an intermediate mixing layer which originated in the lee of the topography was seen to slowly propagate up the slope. Such intermediate layer was reported in earlier studies (for example: Wilkison & Wood, 1983; Farmer & Armi, 1998), and discussed mainly from the hydraulics point of view. The mechanism through which such layer interacts with the flowing layers is yet inadequately understood. The effect of density difference on the thickness of such layer and the concentration distribution in such flow field are important issues that need to be investigated. The purpose of the current study is to examine the bulk

178

characteristics of the velocity and concentration fields in two-layer exchange flow in the lee of bottom topography.

In the lee of topography, different mechanisms and phenomena could occur depending on a variety of factors like the head and tail water conditions for the lower layer, the height of the sill, the strength of the approach flow and the nature of existing stratification (Staquet and Sommeria, 1996). Among those mechanisms are: internal hydraulic jumps (Rajaratnam $et\ al.$, 1991), wall jets, lee waves (Sutherland, 2002), separation and subsequent recirculation zone, turbulent wakes and internal waves. In most of those flow phenomena, an intermediate layer of medium density usually forms due to the interfacial shear at the interface. Quite often interfacial mixing and entrainment are major concerns in such physical flows.

Ellison and Turner (1959) studied turbulent entrainment, α_e, in stratified flows by conducting experiments related to surface jets and down slope heavier inclined plumes. They presented a theory that related α_e to an overall layer Richardson number, R_i. They reported that stable density gradients inhibited turbulent mixing and found that α_e was almost negligible when R_i equaled 0.8. Wilkinson and Wood (1971) studied entrainment in internal density jumps with the upper layer being stagnant. They observed that entrainment was generally considerable within an initial entrainment zone, after which a roller region exhibited negligible entrainment. They varied the tail water conditions and studied their effects on the entrainment capacity of the jump. Wilkinson and Wood (1983) described a mechanism through which continuous mixing from shear-flow instabilities in two-layer flow over a bottom sill could be maintained. In their experiments, they observed a turbulent intermediate layer in which mixing, due to highly rotational fluid that entered through, made it homogeneous and separated it by sharp interfaces from the upper and lower layers. They found that the density of the intermediate layer was closer to the denser lower layer in fluid parts' ratio of one in three from the upper and lower layers, respectively. When the density stratification of the 2 layers was very strong, the intermediate layer was extremely thin.

In their field measurements of the dominant cyclic tidal flow, Farmer and Armi (1998) observed an intermediate layer downstream to Knight Inlet Sill, B.C. They related it to an oscillating internal jump and reported on separation at the lee side of the topography with subsequent generation of lee waves. According to their analysis, small scale shear instabilities caused entrainment that thickened the intermediate layer and undulation of jet stream started to follow. As time proceeded, the thickened mixed layer suppressed separation while pronounced oscillations of the downstream flow field were still remarkable. Surprisingly, they found the entrainment to be upward from the down slope flow into the weakly stratified layer. More recently, Sutherland (2002) observed boundary-trapped lee waves, characterized by an undular

179

shear layer downstream of the base of a step over which uniformly stratified fluid flew. He found out that the frequency of those waves was an approximately constant fraction of the buoyancy frequency.

In the current study, the focus in only on the mean flow and concentration properties within the maximal exchange regime when both hydraulic controls at the sill crest and the channel left exit co-exist. However, few results describing the effect of remarkably increasing the density difference and the end conditions of the experiments within the sub-maximal regime are also included. The aim is to describe the physics of the flow and explore some global characteristics through simultaneous measurements of both velocity and concentration fields using digital particle image velocimetry (DPIV) and planar laser-induced fluorescence (PLIF). In Section 4.2, the experimental setup and techniques are presented. The evolution of the flow field is illustrated in Section 4.3. Section 4.4 details the image pre-processing and the PLIF calibration procedure. The results and discussion are included in Section 4.5 and the conclusions in Section 4.6.

4.2 EXPERIMENTAL SETUP AND TECHNIQUES

The experimental setup for this study is exactly the same as that used previously to study the super-critical reach along the downstream sloping side of the topography (refer to figure 1-2: a, c). In this study, however, the focus is on the field of view including the end part of the downstream slope and further downwind to capture the lee part of the topography for a distance of about 60 cm down the right toe of the sill. A side compartment was appended to the fresh water reservoir to allow for longer times in the experiments, yet it was far enough from the right exit of the channel to maintain the downstream conditions. The axes are such that the origin is at the sill crest with the positive x-axis pointing rightwards, the positive y-axis is into the tank, and the positive z-axis points upwards in a right-hand co-ordinate system. Three experiments were carried out at different density variations between the two reservoirs. Two experiments were at relatively low g', namely: Exp 1 and 2 at g' of 1.64 and 6.47 cm/s^2, respectively. The third experiment was at much higher density difference, Exp 3, and had g' of about 18 cm/s^2 to explore such effect on the behavior of the flow.

Digital particle image velocimetry (DPIV) and planar laser induced fluorescence (PLIF) were used to acquire the velocity and concentration fields, respectively. The advantages of both techniques are clear in that they are non-intrusive and provide field measurements rather than the classic point-measurement techniques. They both depend on image processing and therefore can

180

provide adequately accurate and high frequency results that mainly depend on the capturing and recording devices. However, with the on-going fast developments in the computer powers, CCD cameras and image capturing/processing software, it has become relatively easy to use both techniques simultaneously to perform thorough analysis of many flows. The use of both techniques is relatively new though in the areas of experimental environmental hydraulics and fluid mechanics. For example, Cowen *et al.* (2001) used a single camera that provided coupled particle tracking velocimetry (PTV) and LIF measurements to study neutrally buoyant turbulent round jet. Roberts *et al.* (2001) used LIF and conductivity probes to study mixing in stratified jets. Webster *et al.* (2003) used LIF to study a neutrally buoyant chemical plume in turbulent open channel flow.

While DPIV has been introduced in the previous two chapters, the details of PLIF are presented in the following sections. Two high resolution 10-bit JAI-Pulnix CCD cameras (1392x1040 pixels) were used to simultaneously capture the PIV and LIF images. The sampling frequency for the PIV images was set to 30 Hz in all three experiments, while that for LIF was set to 15 Hz in Exp 1, 2 and to 10 Hz in Exp 3. Rhodamine 6G was mixed with the salt water to allow visualizing the salt water layer during the experiment. A light sheet generated through a 5-Watt Argon ion laser allowed viewing both the PIV tracer particles and the dye, hence the need to use optical filters. The laser setting and the optical filters' characteristics have been described earlier in the chapter discussing the super-critical flow down the sill. Experiments 1 and 2 were identical in terms of the field of view and the camera setting, while in Exp 3 larger field of view was captured through the LIF camera to examine the behavior of the flow along the sill at such higher *g'*. Table 4-1 provides information on some properties and sampling frequencies in the three experiments.

4.3 EVOLUTION OF THE FLOW

Figure 4-1 presents a sequence of images describing the initial motion of the two layers until the flow established a clear two layer steady exchange. Upon the removal of the barrier separating the two reservoirs, two nose like structures of each layer form into the other (image a) with the free surface almost constant hence acting as a rigid lid. Small amplitude interfacial K-H instabilities are generated in the wake of the nose and quickly break resulting in the formation of an early intermediate layer at medium density. The flow initially has relatively thick depths of up to about 10 cm in the lower layer (images b, c, d) and then attains shallower depths as it

181

establishes the two-layer steady structure (images e, f). Down the incline, interfacial instabilities are generated and may break along the slope but the resulting mixing is flushed away through the accelerating lower layer and the interface retains its sharpness. Some instability though would travel further downstream into the lee of the topography before they break. The lower dynamically active layer sometimes attains very shallow depths in the order of a centimeter (image g). It may be noticeable from those images that there is a horizontal non-uniformity in the laser intensity where alternation between bright and dim spots is observed, a defect due to the fiber optics that is corrected for as discussed later in the PLIF calibration section.

Once the two hydraulic controls at the sill crest and the left hand exit are established, the maximal exchange regime starts. The lower layer accelerates down the incline and frequent interfacial instabilities as well as lumps of released lower layer fluid are observed. The details of this phenomenon have been discussed in more depth previously in Chapter 2. Figure 4-2 shows a cycle of sequential images within the maximal regime in which two successive large scale interfacial waves are formed due to release of lumps of lower layer fluid. The period between these two events is roughly 45s. Note that this period is almost the same as that observed previously in chapter 2 (figures 2-17b, 2-18) and is reflected later as well in the wave characteristics' plot (figure 4-9). The periods of those large-scale down slope waves were variable especially with small values of g'. In the wake of those large scale events smaller more frequent K-H instabilities are formed along the interface. The same pattern of such interfacial waves was observed in chapter 2.

By tracing the large scale wave (images a, b, c) as it travels down the slope, it can be seen that it stretches in the longitudinal direction with the result that its amplitude reduces. By the time it reaches the toe, it breaks and a dominant vertical eruption motion takes place that contributes into the development of the intermediate layer. The rest of the wave flattens underneath the intermediate layer and flows as a lower layer at a depth of about 3–5 cm. The process goes on until the hydraulic control at the exit is lost and the sub-maximal regime starts. During the maximal regime, the intermediate layer was limited to an elevation of about 12 cm above the bed. As can be seen in figure (4-2), the intermediate layer is almost stagnant and dynamically inactive. The side color bar, with a dynamic range from 0 to 255, indicates roughly that the concentration of the intermediate layer is at 20% or less of the lower layer concentration. More details though on the concentration distribution, subsequent to the LIF calibration, are presented later.

To explore the end conditions of the experiment and how g' affects the development of the intermediate mixing layer, a characteristic time scale, T, is chosen such that: $T = L/\sqrt{g' \cdot H}$, in

182

which L is the total length of the sill ($L = 72.7$ cm) and H is the full flow depth of 30 cm while g' is the reduced gravitational acceleration. The non-dimensional time t^* is defined as ($t^* = t/T$) where t is the real elapsed time since the removal of the barrier. Exp 1 lasted for about 14 minutes at which time $t^* \approx 81.21$. The corresponding times in Exp 2 and 3 were obtained ($t = 7.6$, 5.4 min, respectively) and the matching images are shown in figure 4-3. The images in figure 4-3 as well as the visual observation of the real experiments show that the intermediate layer becomes more homogenous as g' increases. This could be attributed to the higher momentum and mass fluxes in the vertical direction when g' increases. It also appears that the higher acceleration in Exp 3 along the topography acts to flush the interfacial mixing further downstream and delays the progression of the intermediate layer up the slope. Note that in figure 4-3 the level of the intermediate layer at the same non-dimensional time is almost the same and at about 14 cm.

An interesting phenomenon was observed additionally in Exp 3 at a later time ($t = 7.85$ min) when the experiment was almost to an end and the flow rate was minimal. Figure 4-4 shows such phenomenon in which a vertically uprising plume at the front of the intermediate layer up the slope was observed. This is different from the traditional vertical plumes in which less dense fluids ascend upwards due to buoyancy difference with the ambient fluid. The observed plume-like structure here is part of the intermediate layer, which is at higher density than the fresh upper layer. Its rising up is presumably attributed to the convective transport of the mean upper layer velocity. Note that the images show that it lies at an elevation higher than the zero-velocity point. The plume has a mushroom-like front and stratification clearly inhibited its vertical spreading into the upper fresh water layer. As the plume further developed, inverted interfacial K-H instabilities were observed within the body of the intermediate layer (image f). By that time, the intermediate layer submerged the sill crest and extended along the whole channel to an elevation of about 20 cm above the bed (image a). In Exp 1 and 2, on the other hand, the upper level of the intermediate layer was limited to about 15 cm above the bed when the experiments were to an end. It appears that the higher value of g' in Exp 3 caused significantly higher level of turbulence, and vertical mass and momentum transfer that led to thicker intermediate layer.

4.4 IMAGE PROCESSING FOR INTERFACE DETECTION AND LIF CALIBRATION

4.4.1 Correction for the horizontal non-uniformity in laser intensity

Plane laser is acquired with the aid of fiber optics, and therefore the distribution of the output energy is not homogeneous. As noted previously in Section 4.3, measurements of gray scale (which is an indicator of the strength of laser light) made along the laser sheet show this difference apparently. This non-uniformity was also observed in stagnant homogeneous water in the tank used for LIF calibration as will be detailed later, and in other experiments as well. The effect becomes more obvious when the field of view gets larger as it is the case with the experiments in this chapter. Such spatial non-uniformity made it initially difficult to detect the interface positions accurately from the images. To correct for such non-uniformity, a time-averaged image over the maximal exchange in the real experiment was used to create a background correction image. The time-averaged image had the advantage that it avoided the effect of physical interfacial waves on the horizontal distribution of the light intensity. In that time-averaged image, the mean of each column within the illuminated lower layer was used to generate a horizontal profile that would represent the variation of the light intensity along the image. A background correction image identical in size to the real experimental images was then created using that profile.

Next, the real images were subtracted from the correction image and the mean of the correction profile was added to offset the real images to their normal mean gray scale, a process similar to removing and adding the direct current (DC) component in an alternating current (AC) signal. Figure 4-5 shows such a process in which the real image is shown suffering from the horizontal non-uniformity in the light intensity clearly (image a). In image b, this defect is remarkably removed and the lower flowing layer appears more homogeneous than before; hence the detection of the interface became relatively easier and more accurate. The interface position was detected based on the differing gray scale values between the upper and lower layers and a vertical gradient condition pretty much similar to how it was detected in the previous two chapters. Errors of about 3 pixels ($\approx$ 2 mm) were estimated in obtaining the interface. The time series of the interface detected in this way can provide good measurement of the interfacial wave activities as will be discussed later in the results' section. Nevertheless, the time-averaged interface over the steady maximal regime is shown in figure 4-5c. It is obvious that the lower layer accelerates down the slope until the toe of the topography after which it maintains an almost uniform depth

184

of about 4 cm although shallow fluctuation seems to exist at $x \approx 60$ and 90 cm. In the following section, the PLIF technique is briefly introduced, while more details can be found in the appendix.

4.4.2 Planar Laser Induced Fluorescence (PLIF)

PLIF is a relatively recent non-intrusive technique which is based on image processing. It is sufficient to inject a fluorescent dye, which will fluoresce with the laser, to visualize the flow field and any mixing that may occur. The experiment can be recorded using a CCD camera and the obtained images can then be treated numerically afterwards. We have chosen the dye Rhodamine 6G for few reasons. It is easily soluble in water and therefore can be considered a passive tracer. Secondly, its excitation (526 nm) and emission (555 nm) wavelengths are adequately different. Thirdly, it has a range of linear response for the luminescence intensity to reflect the dye concentration at every pixel. To achieve this relation though, it is necessary to perform essential verifications concerning the sensitivity of the camera, the homogeneity of the laser, and the domain in which the concentration measurements are valid at acceptable marginal errors (Grazzini, 1999). The first step in such process is the image acquisition device, the CCD of the camera.

4.4.2.1 Correction for the CCD camera

For this correction, we use an optical filter, a CCD camera and an acquisition card. The procedure is to expose uniform gray color KODAK (or DELTA 1) sensitive paper (reflectance of 18% in the range of the visible light 410-690 nm) to normal light and capture few images at each aperture opening. In this step we correct for the non-linearity and non-uniformity of the CCD response to the incident light. It is not necessary to have the distance between the camera and the KODAK paper equal to that between the camera and the object while running the true experiment. Yet, the camera has to be in focus with each aperture opening. The intensity, or CCD, will vary with the aperture opening as:

$$CCD = A\left(\frac{1}{f^2}\right)^{\gamma} \tag{4.1}$$

185

in which γ is the camera correction factor ($\gamma < 1$) and A is a constant. Figure 4-6 shows the dependence of the measured intensity on the aperture opening and its logarithmic representation through which γ was estimated at ≈ 0.4467. By normalizing the bright intensities over the dynamic range [0-255], it is then possible to adjust the transfer function to correct for any image as follows:

$$CCD_c = 255\left(\frac{CCD_i}{255}\right)^{\frac{1}{\gamma}} \qquad (4.2)$$

in which CCD_i is the initial gray scale intensity, CCD_c is its corrected value.

4.4.2.2 Correction for the attenuation of the laser plane

It is necessary to take into account the variation of light intensity due to the attenuation of the laser power in the vertical direction if it is desired to restore concentration properly. Otherwise, different fluorescence will be obtained for identical concentration in a homogeneous image. To correct for this problem, it is enough to have a reference image filmed under the same conditions of the camera during the real experiment (Grazzini, 1999). By same conditions it is meant that the height of the laser source, the focal length of the lens as well as how far the camera is from the object, and the aperture opening should all be the same for this reference image and the real experiment. On the assumption that the concentrations will be within the linear range of the luminescence-concentration function, this reference image would be of the maximum concentration used in the experiment. The reference image is of a container (calibration tank) filled with a homogeneous concentration of the dye. Once this image is acquired it is adequate to calculate the mean value, and to normalize then every pixel of the image and correct for attenuation as follows:

$$IC(i, j) = IC_o \frac{CCD_c(i, j)}{CCD_{c_o}(i, j)} \qquad (4.3)$$

in which $IC(i,j)$ is the corrected gray scale of pixel (i,j), IC_o is the mean value of the reference image CCD_{Co} and CCD_C is the γ-corrected image of the real experiment.

186

4.4.2.3 Fluorescence as function in concentration

To ensure that the maximum concentration in the experiment is within the linear range of the luminescence-concentration function, various concentrations of the dye were used in a calibration tank that was at the same conditions for the real experiment. The calibration tank was approximately 100x7x40 cm and was placed within the channel. The consequence of double-walled glass was tested and found of minor effect (see the appendix). A mini-submersible pump was used to ensure good mixing and homogenous medium. To account for the effect of salt and PIV particles, the same salt and particles' concentrations of the real experiment were maintained. It is commendable to start at high concentration then dilute using fresh water and compensate for the salt. More than ten concentrations starting at C of 64 g/m^3 were used. A concentration of 1 g/m^3, C_o, was used to normalize the results shown in figure 4-7a. While Pawlak and Armi (1998) mention that the concentration should be kept below 0.5 g/m^3, our measurements indicate an upper bound of ≈ 0.1 g/m^3. The reference concentration in the experiment was chosen as 0.086 g/m^3 and the intercept in figure 7a is an estimate of the background noise which would contribute into an error of about 1%. The concentration images were γ-corrected and the results are plotted in figure 4-7b along with the prediction of equation (4.2). Clearly there is close agreement between both. However, as it is obvious from the figure the error depends on the concentration. The maximum error occurred at an initial gray scale of about 218 and reads about 0.4 %. We estimate the combined error to be within 2%.

The different correction processes were carried out on many images and a sample image is shown in figure 4-8. The second image from top reflects the correction for the horizontal non-uniformity in the laser sheet and was used to detect the interfacial wave activities. The bottommost image is the final corrected image and shows that the layer of maximum concentration is shallower than the flowing layer; hence the contribution of the interfacial waves into mixing that would dilute the concentration in the vertical column is obvious.

4.5 RESULTS AND DISCUSSION

4.5.1 Frequency of the interfacial waves and mean concentration field

The instantaneous interface positions detected in Section 4.3 were subtracted from the time-averaged mean interface previously presented in figure 4-5c to reflect the wave amplitudes around the mean interface during the maximal regime. The differences were scaled and plotted in

187

the x-t domain to generate the wave characteristics' plot shown in figure 4-9. From the figure, it is clear that the waves accelerate as they travel down the incline until they reach its toe, beyond which they seem to attain constant speed. Frequent large scale waves appear to dominate initially with a period of about 45 s (see those for example at $t \approx$ 75, 120, 145 s). Their maximum amplitudes reach about 7 cm as they travel down the slope then fade to about 4 cm as they pass underneath the intermediate layer past the toe of the sill. In the wake of those large scale waves, more frequent smaller amplitude waves are observed. It is difficult though to decide upon their frequencies through the wave characteristics' plot. However, periods of about 10 – 25s can be roughly estimated. Beyond the toe of the sill, as might be inferred from figure 4-9, the large scale waves deform and become similar in amplitude to the K-H instabilities that happen in between. This leads to spatial modifications of the frequencies of the interfacial wave activities. To better resolve that, the time series are analyzed in the frequency domain in what follows.

Sample time series were extracted at 9 different locations and are plotted in figure 4-10. The plot shows that the frequencies increase as we move downstream due to the breaking of the interfacial waves and the subsequent chaotic motions. It can be seen that some of the peaks in the signals can be traced along the whole spatial domain. Those peaks are of the highest amplitude and their period match with the above estimated time of about 45s (see the time series at x = 20, 30 cm). As mentioned previously though, beyond the toe of the sill the amplitude of fluctuations for those waves starts to decay and match the rest of the other smaller scale wave activities (see for example the time series at x = 50, 60 cm). The signal becomes almost uniform in amplitude as the waves travel further downwind (see those signals at x = 80, 90, 100 cm). The nine time series were analyzed in the frequency domain using Fast Fourier Transform (FFT) and the results are shown in figure 4-11. It is clear that there is a dominant single peak at all locations at about 0.059 Hz (17s). The spectra broaden with distance due to the chaotic fluctuations and the energy drops gradually as the amplitudes fade with distance. This measured frequency (of a period $\approx$ 17s) was also obvious in chapter 2 for the stations down the slope (refer to figure 2-17b). In chapter 2, a dominant peak of about 17 s overrode the other peaks at $x \approx$ 30 cm (refer to figure 2-17b). It appears from figure 4-11 that the waves interact and merge with one another resulting in single dominant events at a frequency whose period is about 17s. As stated in chapter 2, at higher values of g', a single peak that overtook most of the energy was quite distinguished even along the slope (refer to figure 2-19b).

The instantaneous corrected LIF images were time-averaged over the steady maximal regime to obtain the mean concentration field within the field of view. Figure 4-12 shows the mean concentration field along with sample profiles at 8 different locations. Self similarity of the

188

profiles can be observed along the channel. Although in figure 4-5c the flowing lower layer appears to be at a mean depth of approximately 4 cm, the mean concentration image in figure 4-12 indicates that the concentration drops to about 15–20 % of the maximum concentration at that depth level. No undulations in concentration appear to be obvious in the lee of the topography as the case with the interface position was. A shallow layer of approximately one cm appears to be uniform along the channel at concentration levels above 75 % of the maximum concentration. The quasi-uniform concentration within the lowermost layer away from the interfacial mixing layer has also been reported in the study done by Pawlak and Armi (2000) (refer to their figure 9). It appears that the interaction between the lower and intermediate layers is only limited to the upper part in the lower layer. A shallow layer adhering to the bed within the lower stream seems not to be affected by mixing and experiences no dilution with distance as it is the case with turbulent jets where the concentration decays spatially due to entrainment of ambient fluid. Figure 4-12 indicates as well that the intermediate layer, observed earlier in figure 4-2 to extend up to about 12 cm above the bed, has concentrations as low as 5% or less of the maximum concentration. This indicates that stable stratification suppresses turbulence and inhibits it within the lower flowing layer.

4.5.2 Velocity field and variation of discharge intensity

The instantaneous PIV images were cross-correlated to obtain the displacement vectors. An iterative multi-grid cross-correlation PIV algorithm (Scarano and Riethmuller, 1999) was used for this purpose to generate velocity fields at 15 Hz. The search and interrogation windows were initially set to 64 and 32 pixels respectively at a 50 % overlap. Three iterations were carried out so that the final resolution had a grid spacing of 8 pixels allowing a velocity measurement almost every 4 mm. Velocity vectors were post-processed to remove any spurious vectors using a local median test. The test compares the vector in question to a percentage of the median value of its 8 neighboring vectors both in terms of magnitude and phase. Vectors were corrected and interpolated onto uniform grid points using Adaptive Gaussian Window (AGW) interpolation.

The instantaneous velocity fields were time-averaged over the steady maximal exchange regime. Figure 4-13 shows sample velocity profiles of the u-component at 14 different locations along the channel. It is obvious that the upper layer is uniform across depth as expected. The lower layer, on the other hand, seems to spread vertically in the lee of the topography similar to a wall jet. Likewise with the concentration profiles, self similarity is observed and the existence of an intermediate layer that experiences circulation could also be seen in the plot. The profiles

189

were integrated across depth to obtain the flow rate per unit width, q, in each layer. Predictions of the internal hydraulic theory for the flow rate at the sill crest can be graphically obtained through the control curve approach assuming the co-existence of two hydraulic controls at the sill crest and the channel left exit (the reader is to refer to Zhu (2002) for more details on the approach). In the following, a comparison between the flow rates down the slope is presented.

For the current topography and g' of Exp 1, the predicted flow rate is around 20.71 cm^2/s. In chapter 2 for the same topography and g' (Exp 4 therein), an increase in the upper layer flow rate of about 40% with respect to its value at the sill crest was reported due to interfacial entrainment and streamline curvature. That increase occurred over a distance of about 25 cm down the incline at which q measured ≈ 29 cm^2/s. The spatial variation of the discharge intensity with distance in the current Exp 1 is presented in figure 4-14. The flow rate at $x = 30$ cm measures about the same value as that reported in chapter 2 for Exp 4. The upper layer flow rate continues to increase gradually down the incline until the toe of the sill, beyond which it attained a fairly constant value of ≈ 31 cm^2/s along the flat bed. The upper layer flow rate increase along the topography has been reported in earlier studies as well. For example, Morin *et al.* (2004) reported an increase in the upper layer flow rate down a 25-cm curved sill of about 20% compared to that at the sill crest. They referred it to the entrainment caused by interfacial K-H instabilities. In an earlier study by Zhu *et al.* (2002) for flow through openings in the same reservoir, they reported an increase of up to about 50% in the measured flow rate compared to the prediction of the internal hydraulic theory. Their measured flow rates were halfway between the opening and the channel right hand exit where the flow was almost parallel. They referred such increase to the strong streamline curvature and the interfacial entrainment.

The results in figure 4-14 indicate as well a remarkable difference between the flow rates in both the upper and lower layers. While the upper layer flow rate varies as stated above, the lower layer flow rate increases from about 17 cm^2/s at $x = 30$ cm to approximately 28 cm^2/s at $x = 95$ cm. The discrepancy between the upper and lower layer flow rates is surprising since the confined volume of the tank would necessitate the conservation of the volume flow rate in both layers. For that, the PIV images were re-processed such that successive image pairs at 30 Hz were cross-correlated to generate 30-Hz velocity fields. The velocity profiles were integrated across depth and the results are over-plotted in figure 4-14. Very close agreement with the 15-Hz data can be seen, yet the discrepancy between the upper and lower layer flow rates persists. On investigating few sections across the channel in a repeat of the experiment, more details of which is described in the following section, significant fluctuations and three dimensional highly turbulent motions were observed. It appears that the highly turbulent motion within the lower

190

layer causes significant out-of-plane motion for the tracer particles, hence the difficulty in capturing the lower layer velocities. This may be the reason for such discrepancies in the flow rates.

4.5.3 Flow field across the channel

To gain some idea about the flow field across the channel, seven cross sections were selected with the first at the sill crest ($x = 0$) and the rest at 15-cm intervals downstream along the channel. Figure 4-15 shows sample images for three of those cross sections in Exp 1. To capture the full depth of flow, the focal length was kept constant; hence the images are smaller the further they are from the lens. At the sill crest, regular transverse oscillations were observed at periods of about 15 s. Interestingly, those oscillations were more obvious at the outer wall of the channel than at the inner side, a possible effect of the horizontal curvature as the lower layer flow enters into the channel. A sample cycle of this oscillation is shown in the leftmost column of figure 4-15. A differential elevation of the interface positions at both sides was approximately 2.5 cm at the maximum inclination. Gradually the interface became leveled then inclined again to the maximum lateral slope. Although the channel is narrow ($b = 10$ cm), high frequency and irregular disturbances at the density interface were observed, which indicates the flow is highly three-dimensional.

As we move further downstream to the sill crest, two effects start to interfere. Firstly, the flow becomes super-critical; hence the transverse oscillation with its relatively long period of about 15s is no longer as obvious. The super-critical lower stream would wash out any lateral long oscillations and the transverse interface would be fluctuating chaotically. Secondly, stratification has its clear effect in restraining the highly turbulent motion within the bottom layer only. In addition, the depth of the upper layer becomes larger and it becomes dynamically less active than the lower layer. These effects result in relatively uniform motion in the upper layer along the longitudinal direction, and highly turbulent motions in the lower layer. As we move further downstream, the interfacial instabilities in the x-direction break generating highly turbulent motion that would dominate and the lower layer flow would be highly three-dimensional. Beyond the toe of the sill (as seen in the middle column of figure 4-15), the intermediate layer would isolate the upper and lower layers and acts as turbulence absorber that would allow the upper layer to become more uniform. The lower layer, on becoming shallower then, would experience very high random turbulent motions that are more vigorous than along the slope, an

191

effect that could be clearly seen through the motion of the tracer particles when a low-pass filter was mounted in front of the lens.

Although the rightmost column in figure 4-15 shows images at late times of the experiment that accumulative mixing would have caused the lower and intermediate layers to be more homogenous then, the longitudinal velocity field downstream to the toe (see figure 4-13) shows the vertical expansion of the lower layer, and that by $x \approx 1$ m the two-layer structure seems to be retained even within the steady regime. The intermediate layer, while exhibiting signs of extended weak circulation, seems to exist within the domain $30 < x < 100$ cm during the steady maximal regime. Afterwards, it expands further up the slope until it eventually submerges the sill crest. The high turbulence activities and chaotic motion within the lower layer, especially in the lee of the topography apparently causes significant out-of-plane motion for the tracer particles. Additionally, the random interfacial fluctuations in the lower layer across the channel void the assumption of two-dimensional flow, hence the difficulty in capturing the lower layer velocities. It is to be noted that another set of sections across the channel at the same locations was captured in a second repeat of the experiment but in the reverse order to overcome the temporal evolution effects. In this latter set, only tracer particles were used and the recorded video stream showed the same effects described above.

4.5.4 Baroclinic generation of vorticity along the channel

The time-averaged total velocity profiles were plotted along with the density interface obtained previously and shown in figure 4-5c. Figure 4-16 shows such plot and the results can be explained in view of the vorticity equation, which reads in a simple form:

$$\frac{D\bar{\omega}}{Dt} = (\bar{\omega} \cdot \nabla)\bar{V} + \frac{1}{\rho^2}|\nabla\rho \times \nabla p| \qquad (4.4)$$

where ω, V, ρ, and p are the vorticity, total velocity, density and pressure, respectively. The second term on the right hand side of equation (4.4) expresses the baroclinic generation of the vorticity component ω_y in the plane of the laser sheet. On the assumption that the pressure is hydrostatic, the directions of the gradients of the density and the pressure are as shown in figure 4-16. Down the slope, the direction of ω_y is such that it elevates the density interface counterclockwise. With the interface now sloping upwards, ω_y changes its direction to clockwise

192

rotation which makes the interface retains the downward slope and hence an undulation is formed. The process goes on and leads to a series of lee waves two of which are seen in figure 4-16.

By closely looking at the velocity field, it can be seen that the magnitudes of the u- and w-components are almost comparable within the lower layer down the incline. The down-sloping jet hits the flat bed and renounces creating an undulation in the velocity field very close to the bed. The lowermost 2 cm within the lower layer downstream to the toe of the sill experiences clear undulation in the velocities of which once cycle is seen within the field of view. These undulations appear to be at a phase shift with the density field undulations. A more detailed study focusing on smaller field of view is required to resolve the interaction between the two layers. Undular waves in the lee of bottom topography have been reported earlier in Baines (1995) and Sutherland (2002).

4.6 SUMMARY AND CONCLUSIONS

The present study provides bulk properties of two-layer exchange flow over bottom topography at its lee side during steady maximal exchange. Three experiments: Exp 1, 2 and 3 were carried out at g' of 1.64, 6.42 and 18 cm/s^2, respectively. DPIV and PLIF were used simultaneously to obtain velocity and concentration fields, respectively. The results showed the formation of an intermediate layer of medium density between the upper and lower layers. The intermediate layer extended from $x \approx 30$ cm to almost one meter down the sill crest ($x = 0$) within the steady maximal regime. The velocity fields were integrated to obtain the flow rate in the domain, and the LIF images were corrected for different effects including the CCD camera response, the horizontal non-uniformity in the laser sheet due to the fiber optical cable, and the laser attenuation due to the dye absorption to obtain the concentration field. The following results were obtained.

The results revealed a gradual increase in the upper layer flow rate down the incline until its toe, beyond which the flow rate seemed constant at a value almost 50% higher than the predicted flow rate at the sill crest using internal hydraulic theory. The increase in the flow rate is referred to interfacial entrainment due to the generation of large scale breaking waves and streamlines' curvature. On the other hand, it was difficult capturing the velocities in the lower layer which resulted in the lower layer flow rate showing a deficit of about 40% compared to the upper layer around the toe of the sill. However, it constantly increased with distance until it matched the

193

upper layer flow rate over a distance of about 60 cm down the toe where the intermediate layer ended. Cross sections at different stations along the channel revealed highly turbulent motions within the lower layer especially in the lee of the topography where the waves' breaking was dominant. Such turbulence and non-uniformities in the interface across width are probably the cause of such discrepancy in the flow rate within the lower layer in the laser sheet. The cross section at the sill crest revealed as well interesting lateral periodic fluctuations of about 15 s for g' of 1.64 cm/s^2. Those fluctuations were biased towards the channel outer wall and caused a differential elevation between the interface level at the inner and outside walls of the channel of about 2.5 cm over a flow depth of 18 cm. This is likely due to the horizontal curvature effect as the lower layer enters the channel.

In the lee of the topography, periodic undulations in both the density interface and boundary velocity fields were observed in concurrence although there appeared a little phase shift with the density interface wave leading towards upstream. Those lee waves could be explained in view of the vorticity equation due to the baroclinic vorticity generation term. Spectral analysis of the density interfacial fluctuations of the lower moving layer showed a dominant single frequency for the repetitive breaking waves of about 17 s everywhere. This frequency was previously measured in chapter 2 and seemed to have overridden other frequencies close to the toe of the sill. The instantaneous interfacial fluctuations were used to generate a wave characteristics' plot which showed the wave amplitudes are at maximum of about 7 cm down the incline then fade to about 4 cm as they break and flow underneath the intermediate layer. Large scale breaking waves were observed at a period of about 45 s. This period match with events of release of lower layer fluid lumps that were also reported earlier in chapter 2.

PLIF was used to obtain the concentration fields. Both the concentration and velocity profiles maintained self similarity with distance. The mean concentration field indicated that the lowermost one centimeter layer has 75% and up of the maximum concentration. It appeared that the interfacial mixing was limited only to the shear layer and caused no dilution of the shallowest one cm layer. This is in line with previous study by Pawlak and Armi (2000) for wedge flow down an incline of the same slope. The flowing lower layer though had an average depth of about 4 cm, at which level the concentration dropped to about 15-20% of its maximum value. The intermediate layer above the lower flowing layer, although extended to depths up to about 12 cm, had concentrations as low as 5% and less of the maximum concentration level. This indicates that stable stratification suppresses turbulence efficiently.

In Exp 3 with g' of 18 cm/s^2, large-scale interfacial waves were still being generated down the incline during the steady maximal exchange. Those waves caused the intermediate layer in the

194

lee of the topography to remarkably thicken (2/3 of the total depth) at the end of the experiment and to become more homogenous than with g' of 1.64 and 6.42 cm/s^2. An uprising plume-like structure was observed as well along the slope when the intermediate layer overtopped it at the late times of the experiment. This plume is different from the traditional plume and is presumably carried convectively by the mean velocity of the upper layer flow.

195

REFERENCES

ALAVIAN, V., JIRKA, G. H., DENTON, R. A., JOHNSON, M. C. & STEFAN, H. G. 1992 Density currents entering lakes and reservoirs. *Journal of Hydraulic Engineering* **118**, 1464.

BAINES, P. G. 2001 Mixing in flows down gentle slopes into stratified enviroenments. *J. Fluid Mech.* **443**, 237-270.

BRAY, N. A., OCHOA, J. & KINDER, T. H. 1995 The role of the interface in exchange through the Strait of Gibraltar. *J. Geophys. Research* **100** (C6), 10,755-10,776.

COWEN, E. A., CHANG, K.-A. & LIAO, Q. 2001 A single-camera coupled PTV-LIF technique. *Exps. in Fluids* **31**, 63-73.

ELLISON, T. H. & TURNER, J. S. 1959 Turbulent entrainment in stratified flows. *J. Fluid Mech.* **6**, 423-448.

FARMER, D. & ARMI, L. 1998 Stratified flow over topography: the role of small-scale entrainment and mixing in flow establishment. *Proc. Royal Society of London, series* A **455**, 3221.

GRAZZINI, F. 1999 Etude expérimentale de la dispersion de polluants en présence d'obstacles. Doctoral thesis no. 1559 at the L'Institut National Polytechnique de Toulouse, France. Spécialité: Physique et Chimie de l'Environnement (in French).

MORIN, V. M., ZHU, D. Z. & LOEWEN, M. R. 2004 Super Critical Exchange Flow Down a Sill. *J. Hydraulic Engineering* **130** (6), 521-531.

NIELSEN, M. H., PRATT, L. & HELFRICH, K. 2004 Mixing and entrainment in hydraulically driven stratified flows. *J. Fluid Mech.* **515**, 415-443.

PAWLAK G. & ARMI L. 1998 Vortex dynamics in a spatially accelerating shear layer. *J. Fluid Mech.* **376**, 1-35.

PAWLAK G. & ARMI L. 2000 Mixing and entrainment in developing stratified currents. *J. Fluid Mech.* **424**, 45-73.

RAJARATNAM, N., TOVELL, D. & LOEWEN, M. 1991 Internal jumps in two moving layers. *J. of Hydraulic Res*, **29**, 91-106.

ROBERTS, P. J. W., MAILE, K. & DAVIERO, G. 2001 Mixing in Stratified Jets. *J. of Hydraulic Engineering*, ASCE, **127**, 194-200.

SCARANO, F. & RIETHMULLER, M. L. 1999 Iterative multigrid approach in PIV image processing with discrete window offset. *Experiments in Fluids* **26**, 513-523.

STAQUET, C. & SOMMERIA, J. 1996 Internal waves, turbulence and mixing in stratified flows: A report on Euromech Colloquium 339. *J. Fluid Mech.* **314**, 349-371.

SUTHERLAND, B. R. 2002 Large-amplitude internal wave generation in the lee of step-shaped topography. *Geophysical Research Letters* **29** (16), art. no. 1769.

WEBSTER, D. R., RAHMAN, S. & DASI, L. P. 2003 Laser-induced fluorescence measurements of a turbulent plume. *J. of Engrg. Mech.*, ASCE, **129**, 1130-1137.

WILKINSON, D. L. & WOOD, I. R. 1971 A rapidly varied phenomenon in a two-layer flow. *J. Fluid Mech.* **47**, 241-256.

WILKINSON, D. L. & WOOD, I. R. 1983 The formation of an intermediate layer by horizontal convection in a two-layered shear flow. *J. Fluid Mech.* 136.

WORTHINGTON, R. M. 2002 Mountain waves launched by convective activity within the boundary layer above mountains. *Boundary-Layer Meteorology* **103**, 469-491.

ZHU, D. Z. 2002 Control curves for two-layer flows. *J. of Hydraulic Engineering*, ASCE, **128**(1), 113-116.

ZHU, D. Z., FOULI H. & OKYERE, Y. A. 2002 Exchange flow through an opening. *J. Hydraulic Research*, **40** (3), 341-350.
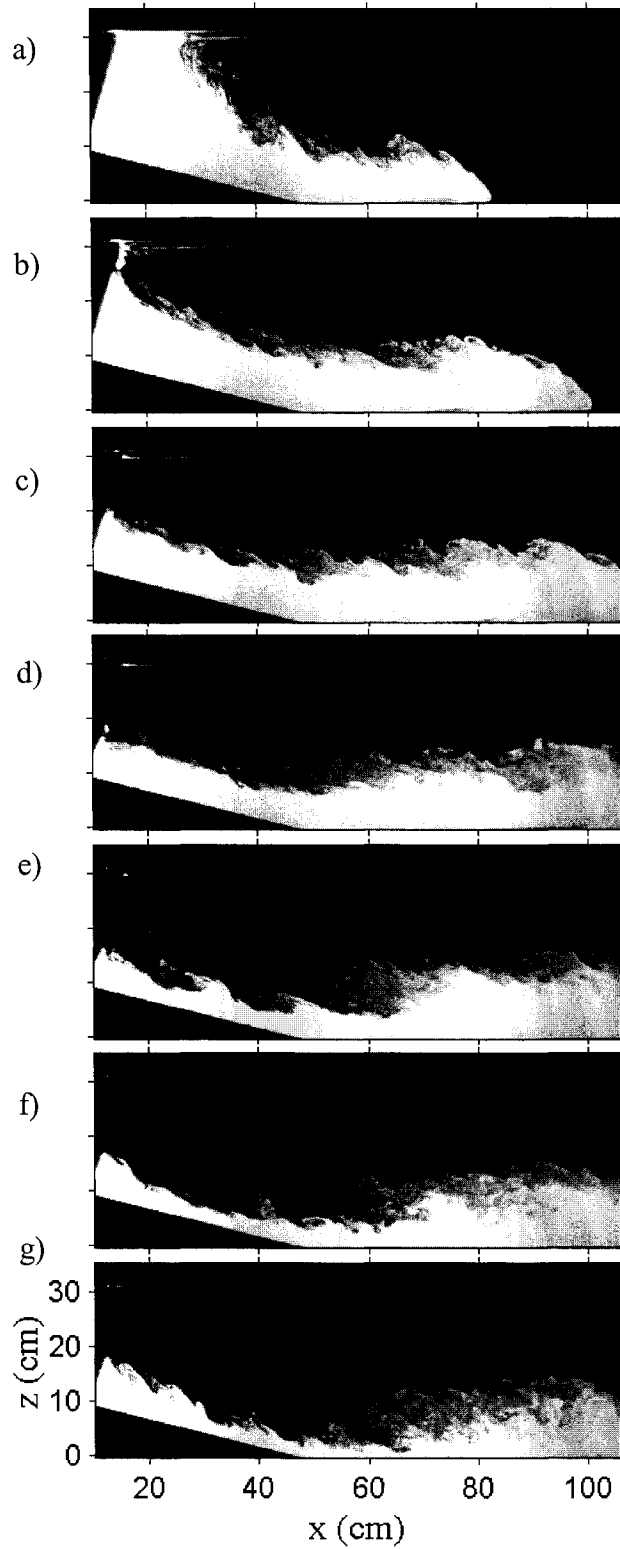
FIGURE 4-1. Series of images from Exp 1 about 10 seconds into the experiment from the moment the barrier was removed. Images are 5 seconds apart.

198
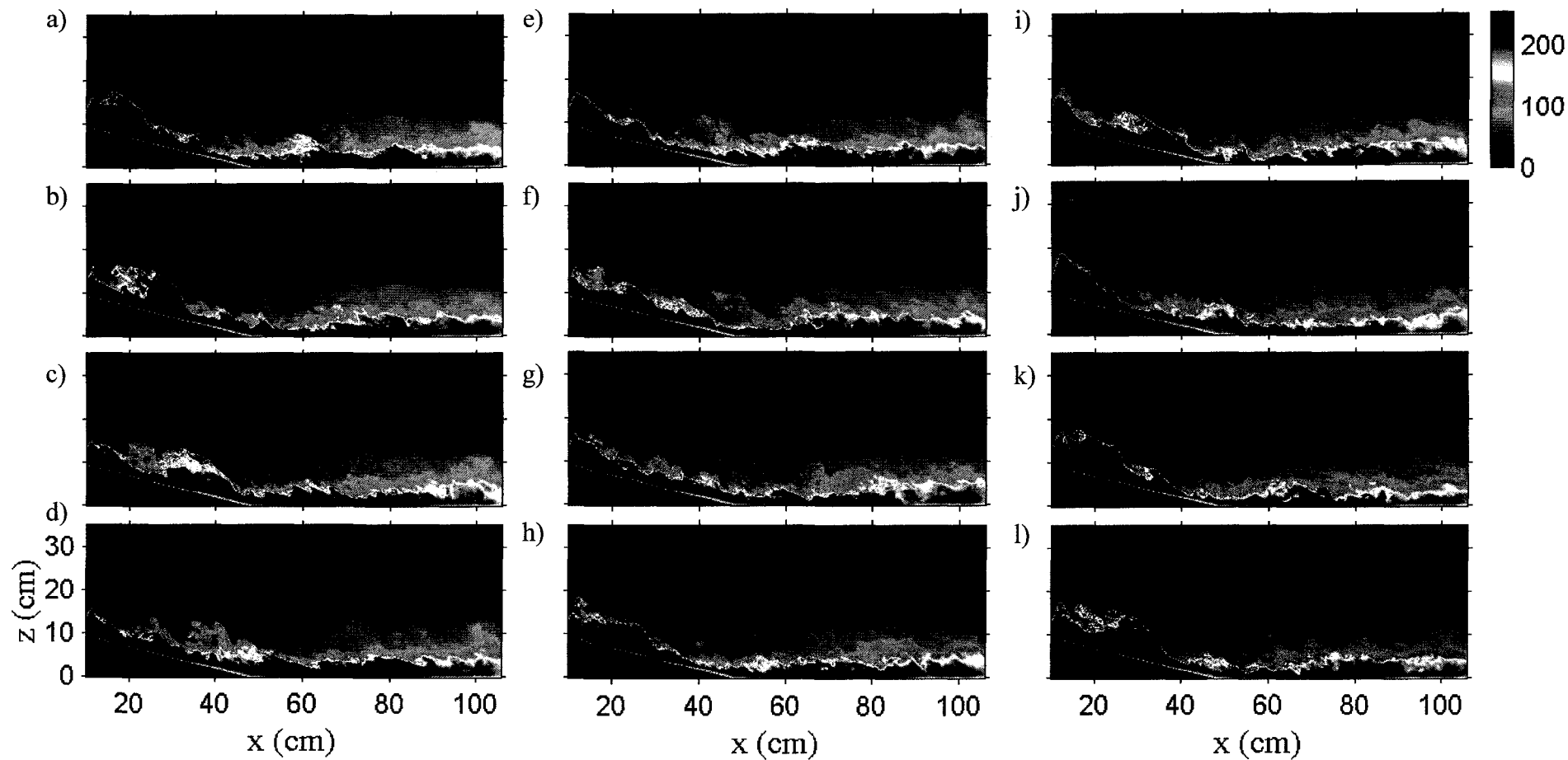
FIGURE 4-2. Series of images from Exp 1 within the steady maximal regime at about 129 s into the experiment. Images are 4 seconds apart covering duration of 44 seconds.
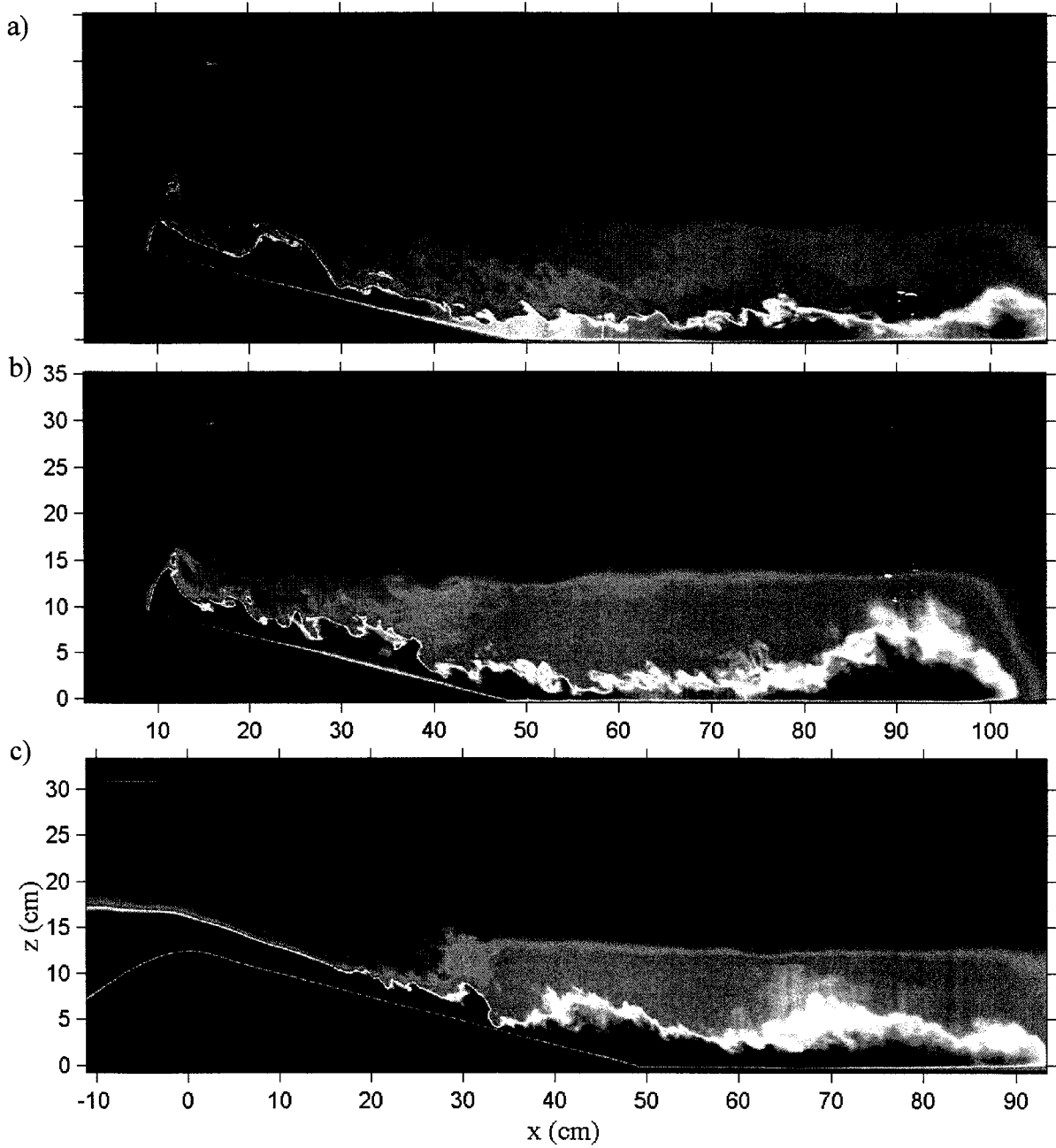
FIGURE 4-3. Instantaneous images at the same non-dimensional time, t^* of 81.21, from: a) Exp 1; b) Exp 2; and c) Exp 3. Note that the vertical and horizontal scales for Exp 1 and 2 are identical.

200
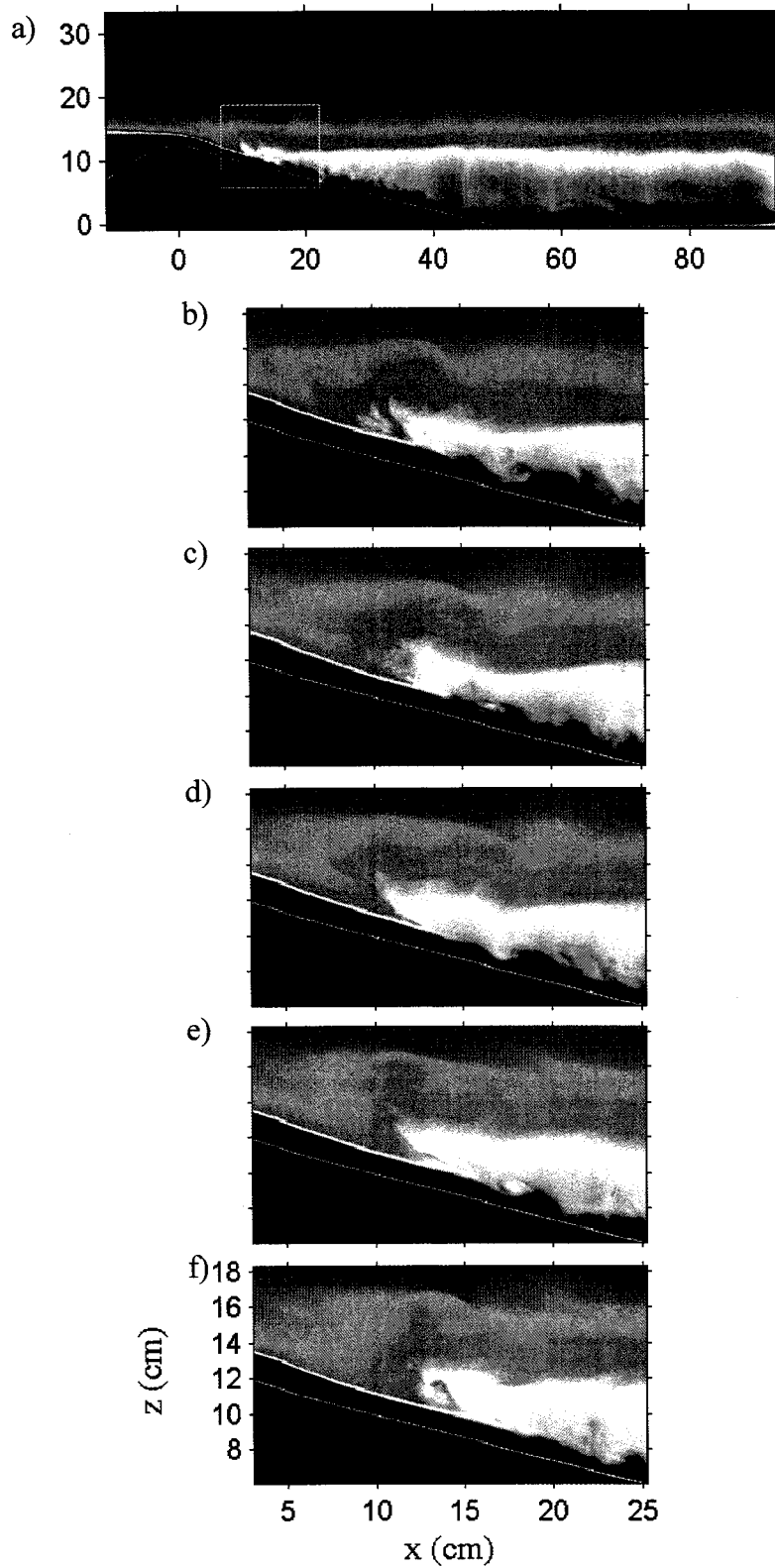
FIGURE 4-4. a) A snap shot from Exp 3 at the end of the experiment ($t \approx 7.85$ min); b-f) series of zoomed-in images showing the development of an uprising plume up the slope. Images are 2 seconds apart.

201
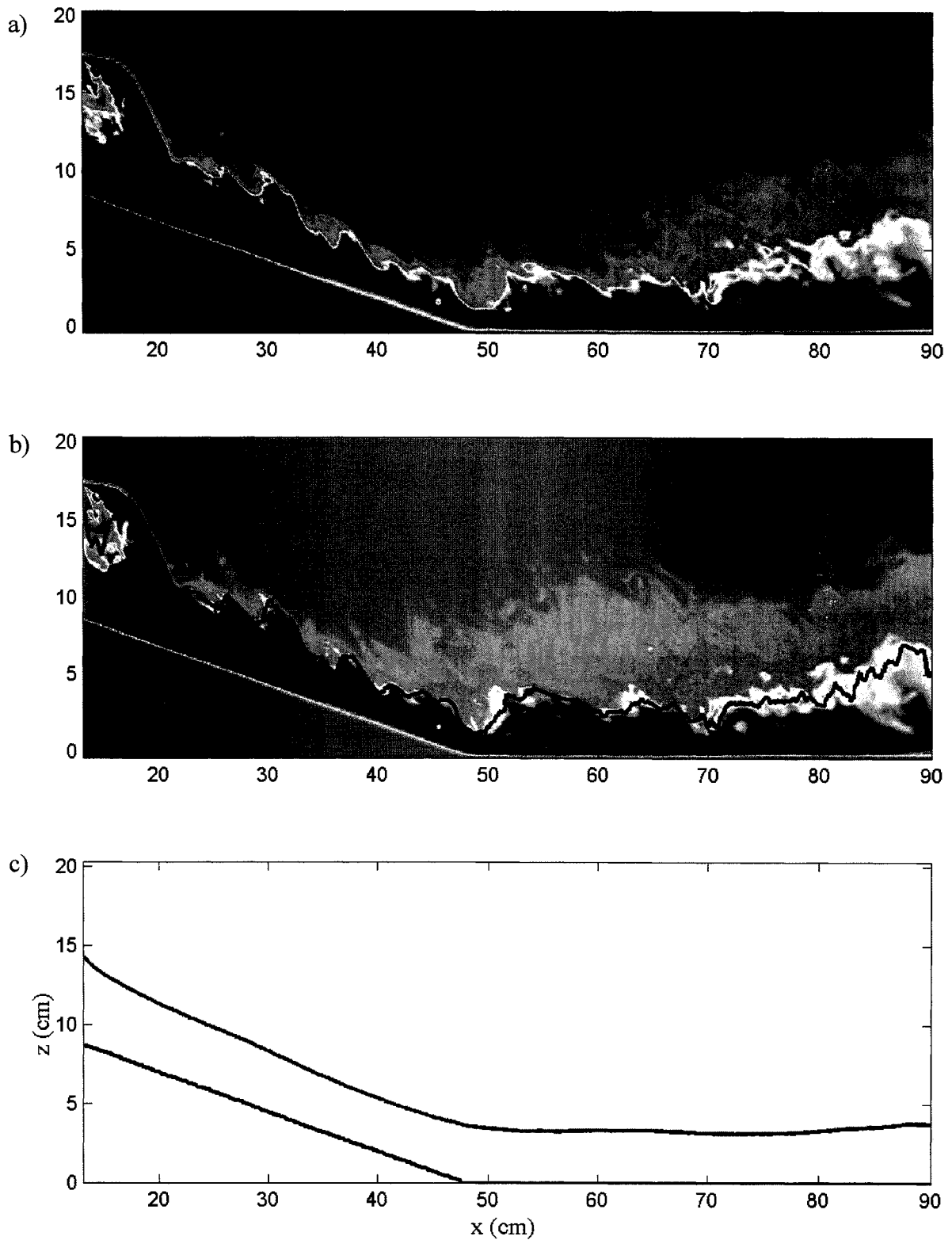
FIGURE 4-5. a) A raw image from Exp 1 during the steady maximal regime; b) The corrected image for the non-uniformity of the laser sheet in the horizontal direction and the instantaneous interface over-plotted; c) The time-averaged interface position over the maximal regime.

202
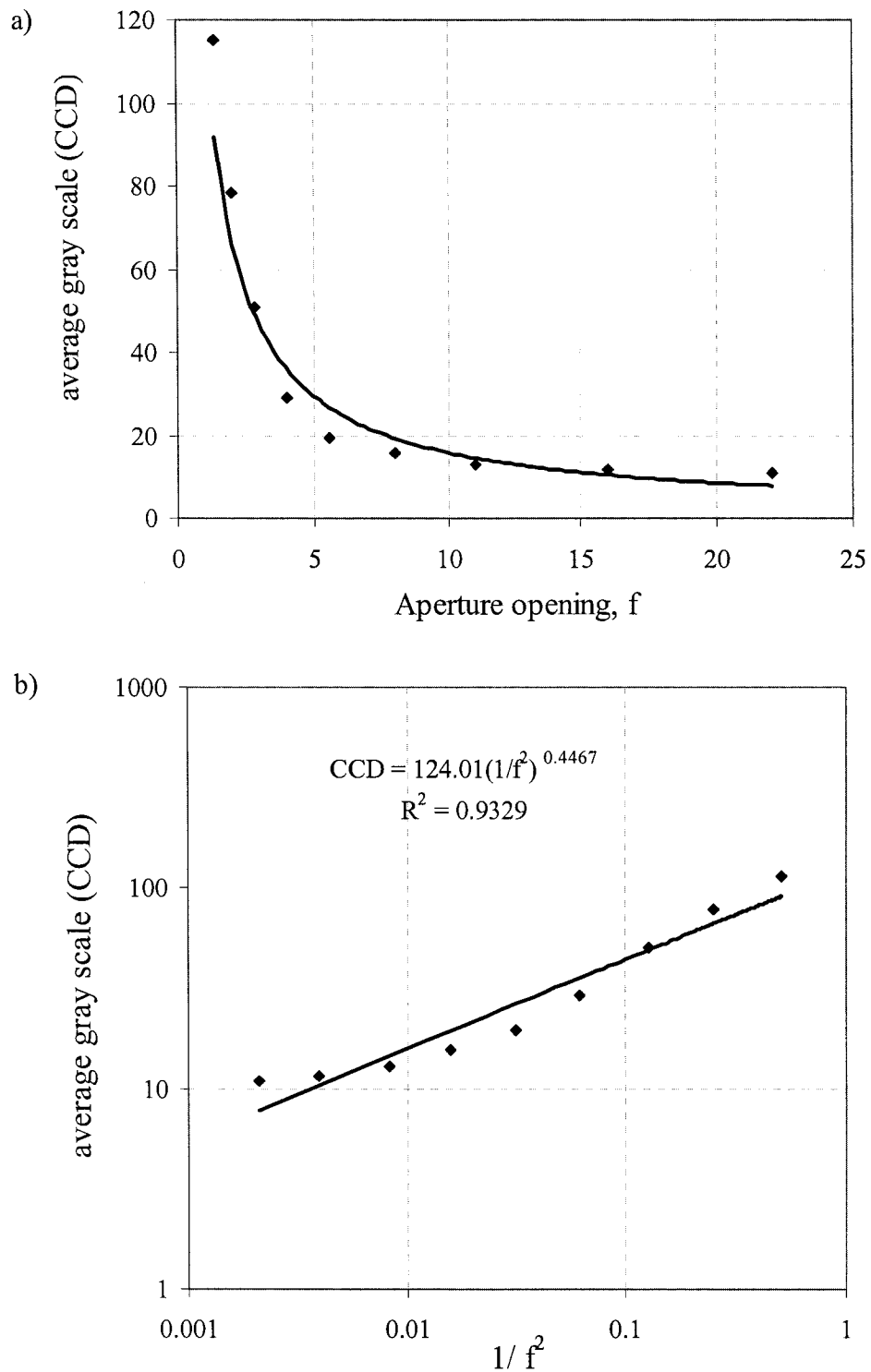
FIGURE 4-6. a) Variation of the luminous intensity arriving at the CCD of the camera as a function of the aperture opening, f; and b) logarithmic representation of the data showing the γ correction of the CCD.

203

a) $CCD_i = 1726.3(C/C_o) + 32.252$

$R^2 = 0.986$
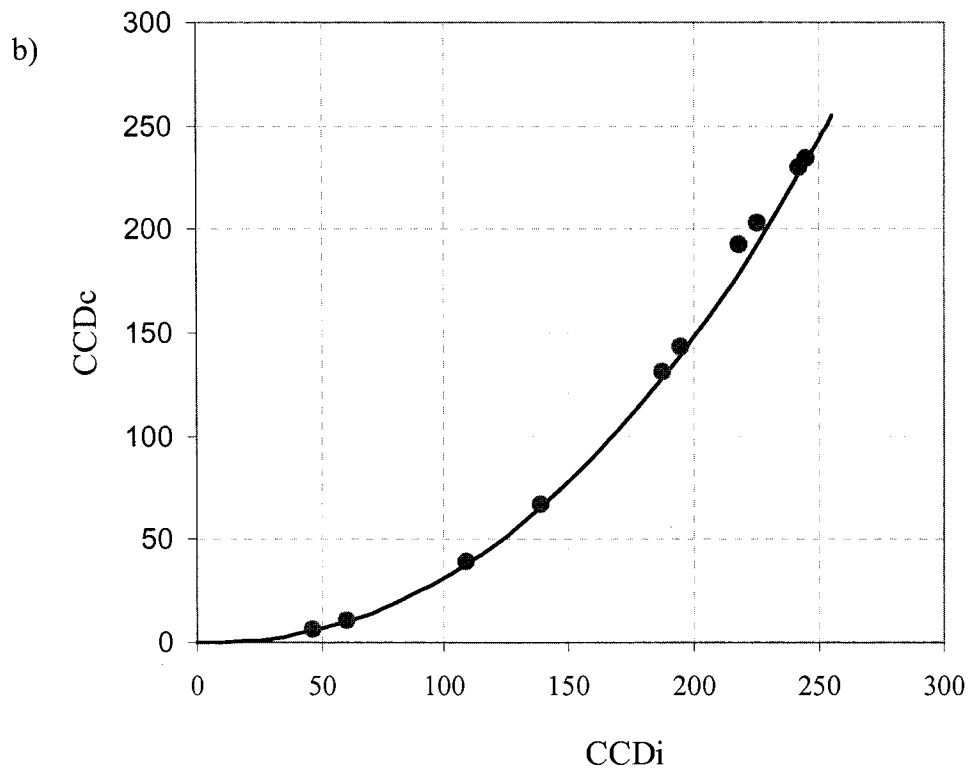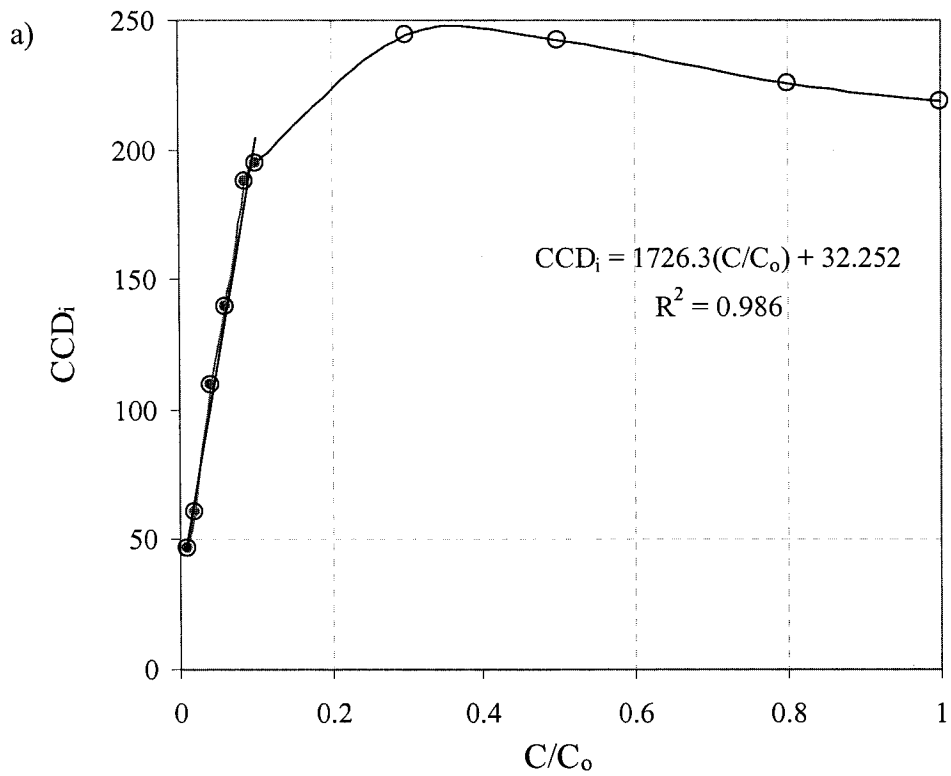
FIGURE 4-7. a) Variation of fluorescence as a function in concentration C/C_o, with $C_o = 1$ g/m3; and b) the transfer function of the camera for the different concentrations.

204
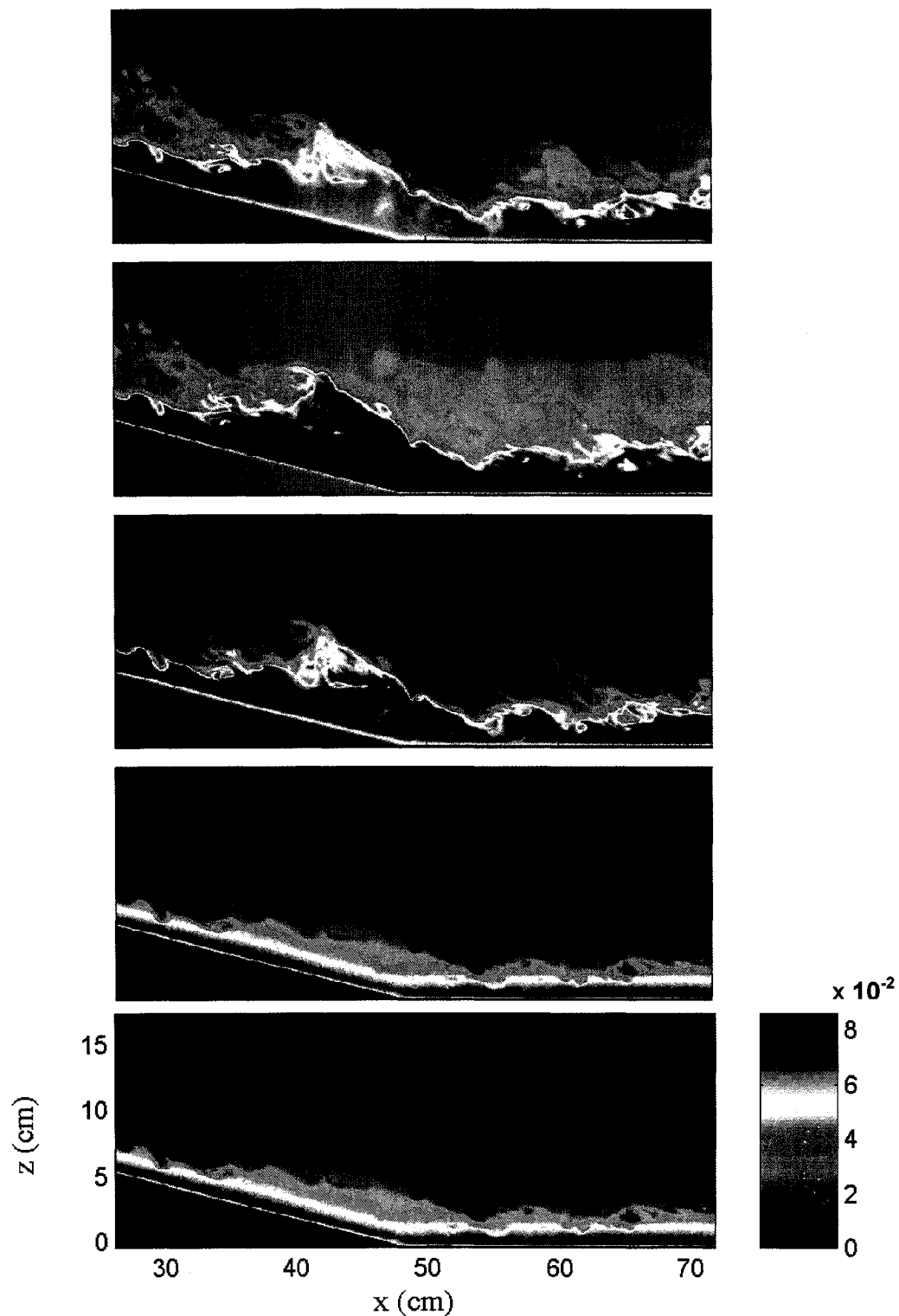
FIGURE 4-8. Sample instantaneous LIF image at about 4 min. into Exp 1. The raw image is at the top followed by: correction for horizontal non-uniformity in the laser sheet, γ-correction for the camera, and the laser vertical attenuation. At the bottom is the corrected image in real units for concentration indicated by the colorbar aside (C_{max} = 0.086 g/m3).
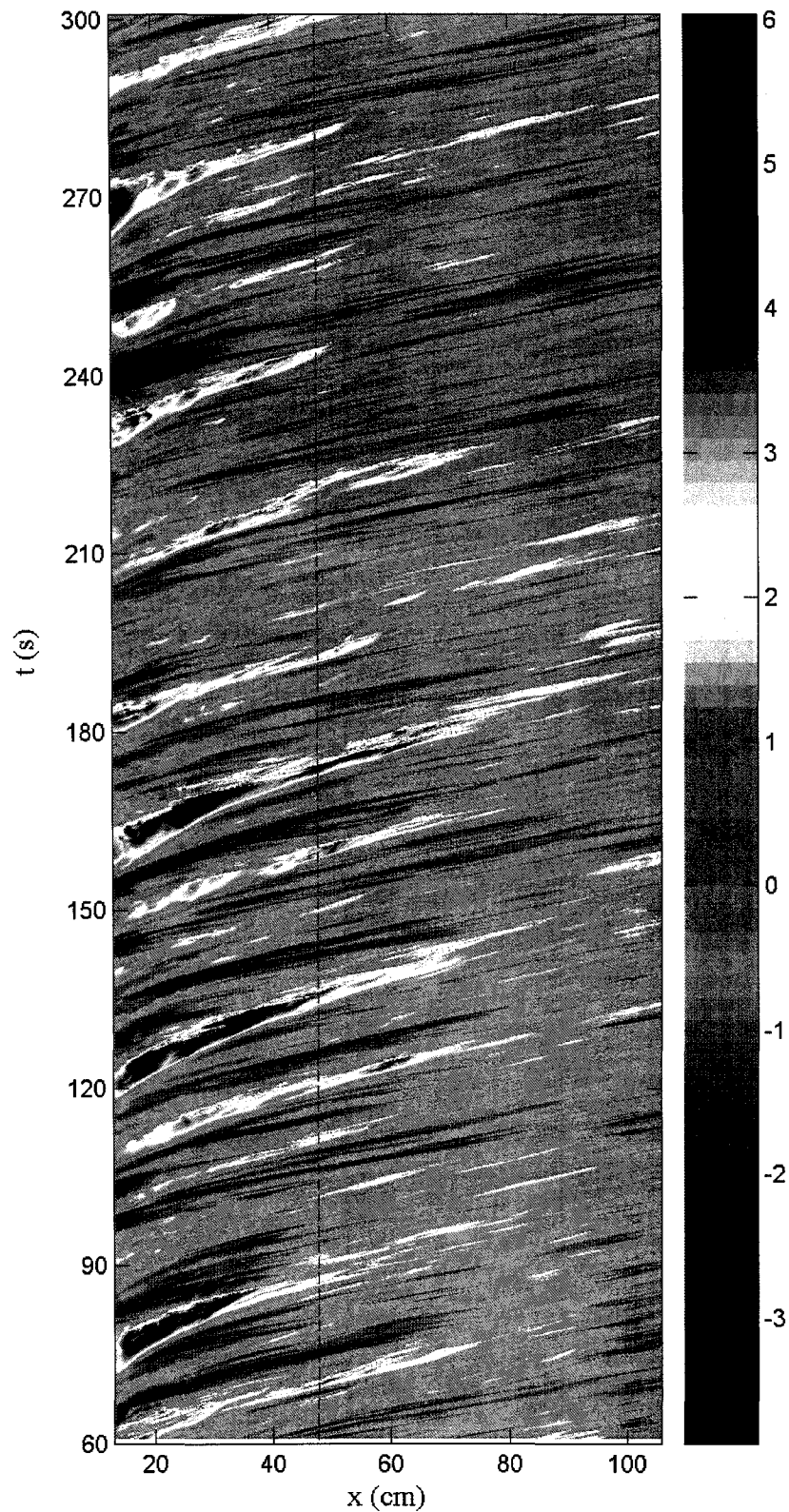
FIGURE 4-9. The wave characteristics' plot in Exp 1 during the maximal regime. The dashed line points to the right toe of the sill and the color bar reflects the instantaneous wave amplitude in cm with respect to the time-averaged mean interface.

206
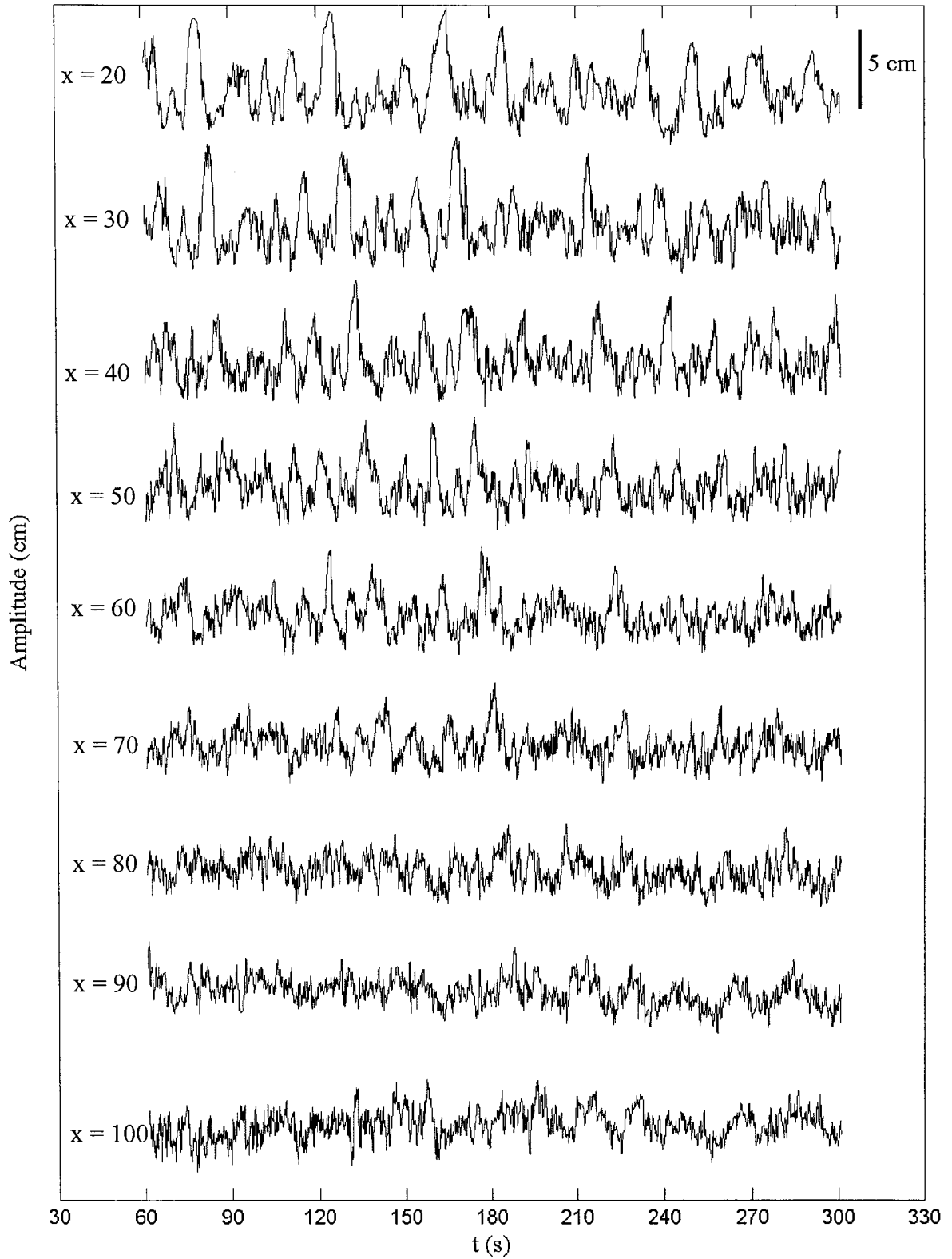
FIGURE 4-10. The interface positions' time series in Exp 1 during the maximal regime at 9 different stations. Locations of stations are indicated to the left in centimeters.
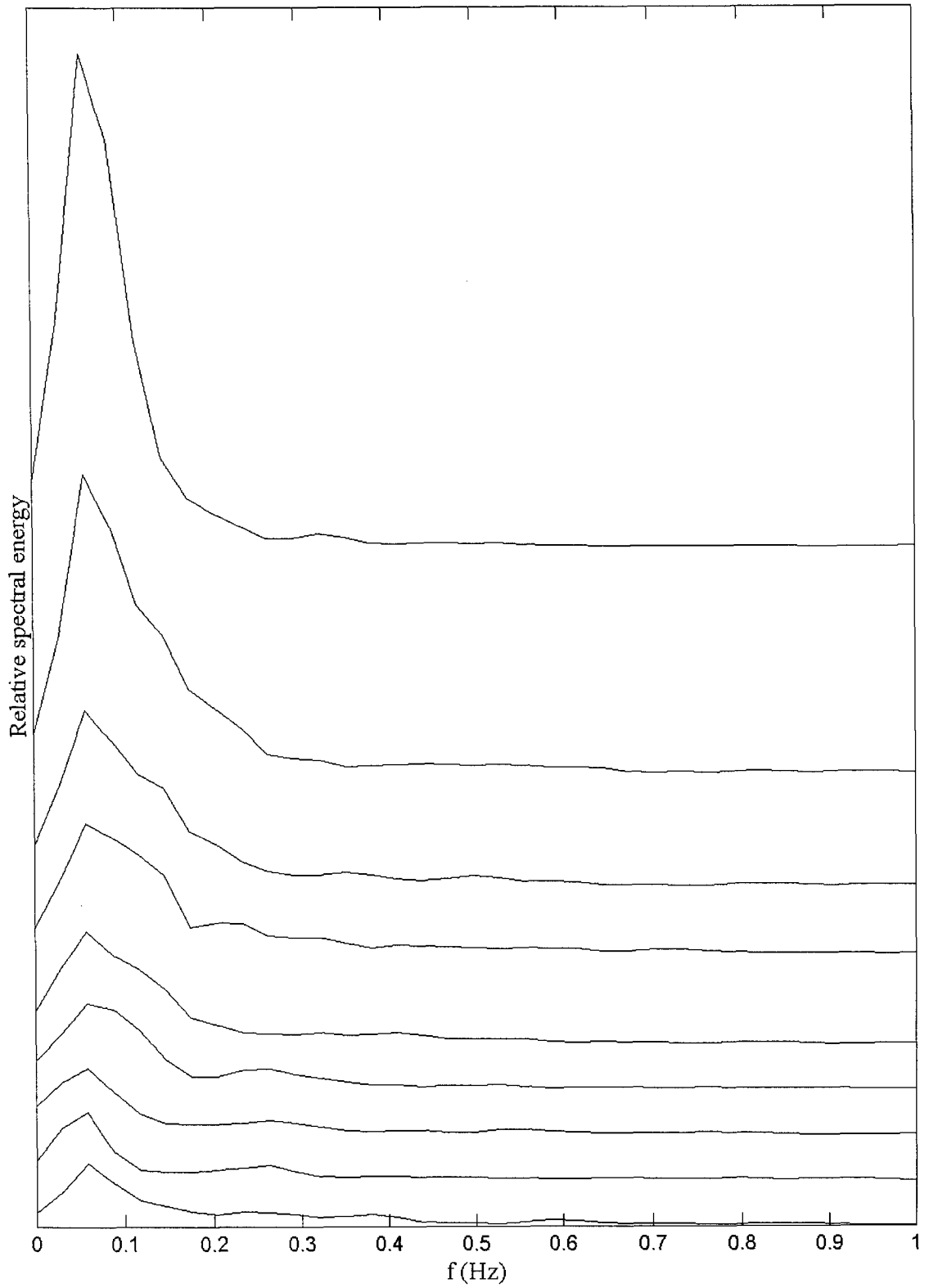
FIGURE 4-11. The FFT power spectra of the interface positions' time series shown in figure 4-10.

208
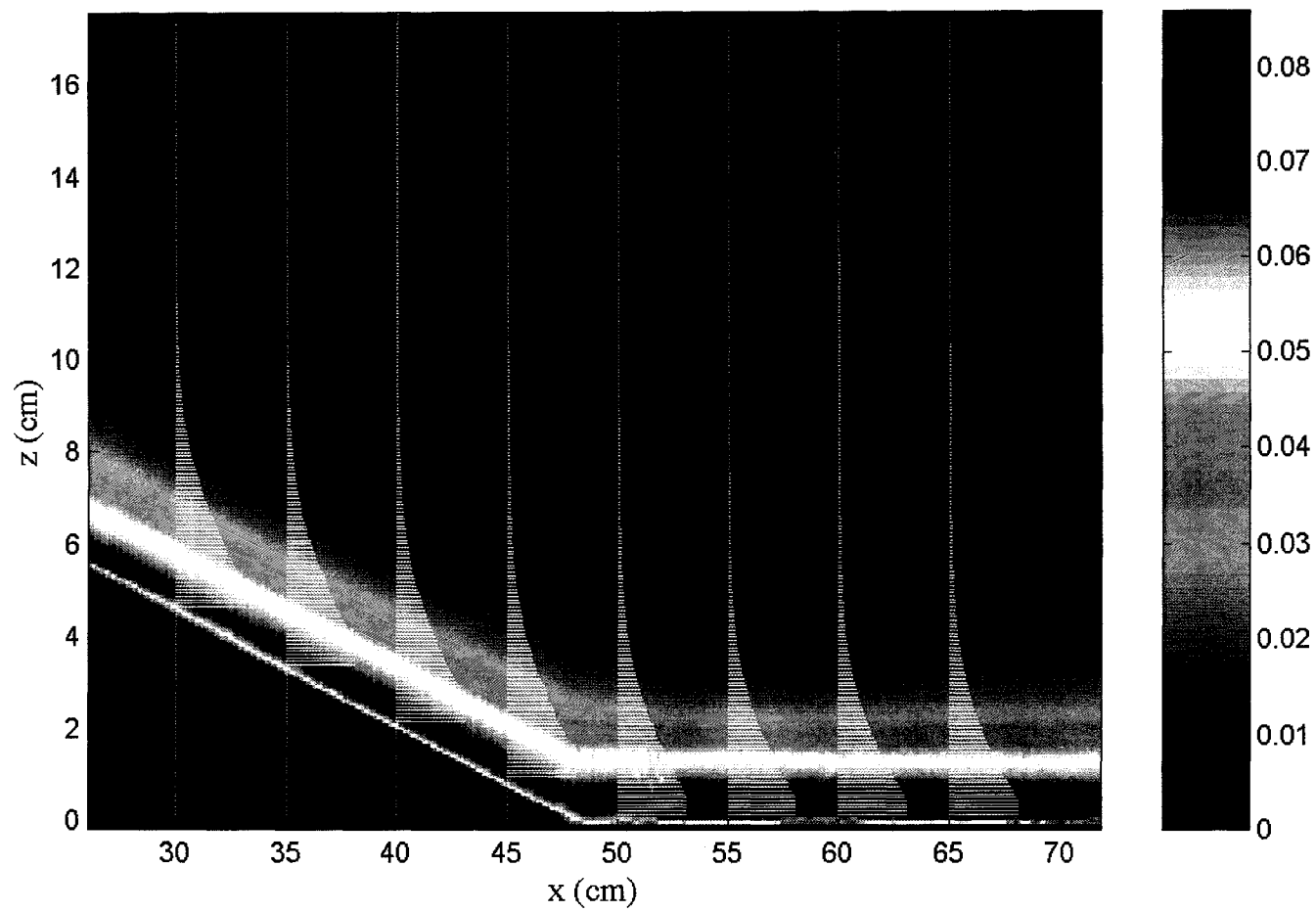
FIGURE 4-12. Time-averaged concentration image and sample profiles over the maximal exchange regime in Exp 1. The colorbar indicates concentration levels in g/m3.
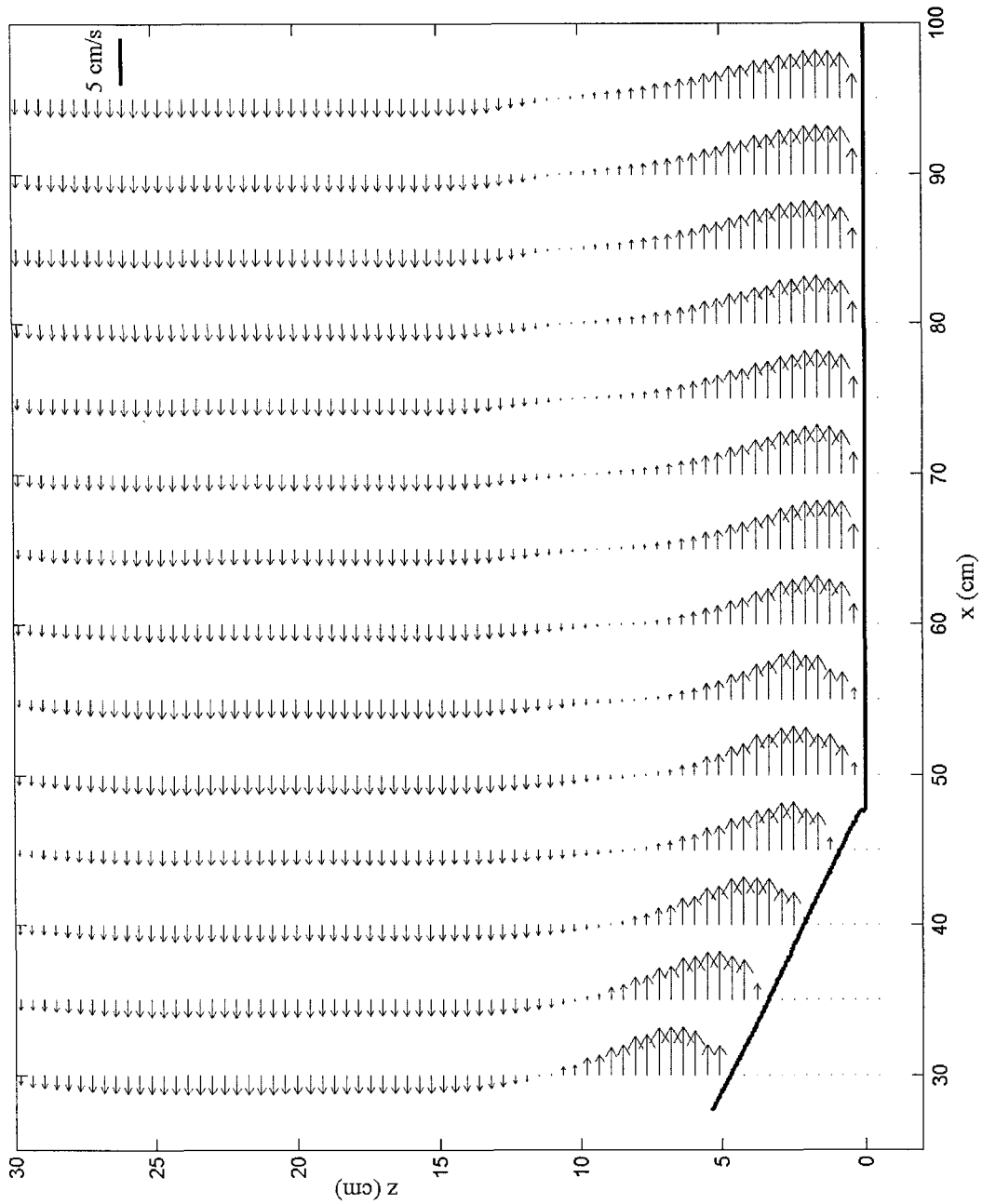
FIGURE 4-13. Sample horizontal velocity profiles at 14 locations time-averaged over the maximal exchange regime in Exp 1.

210
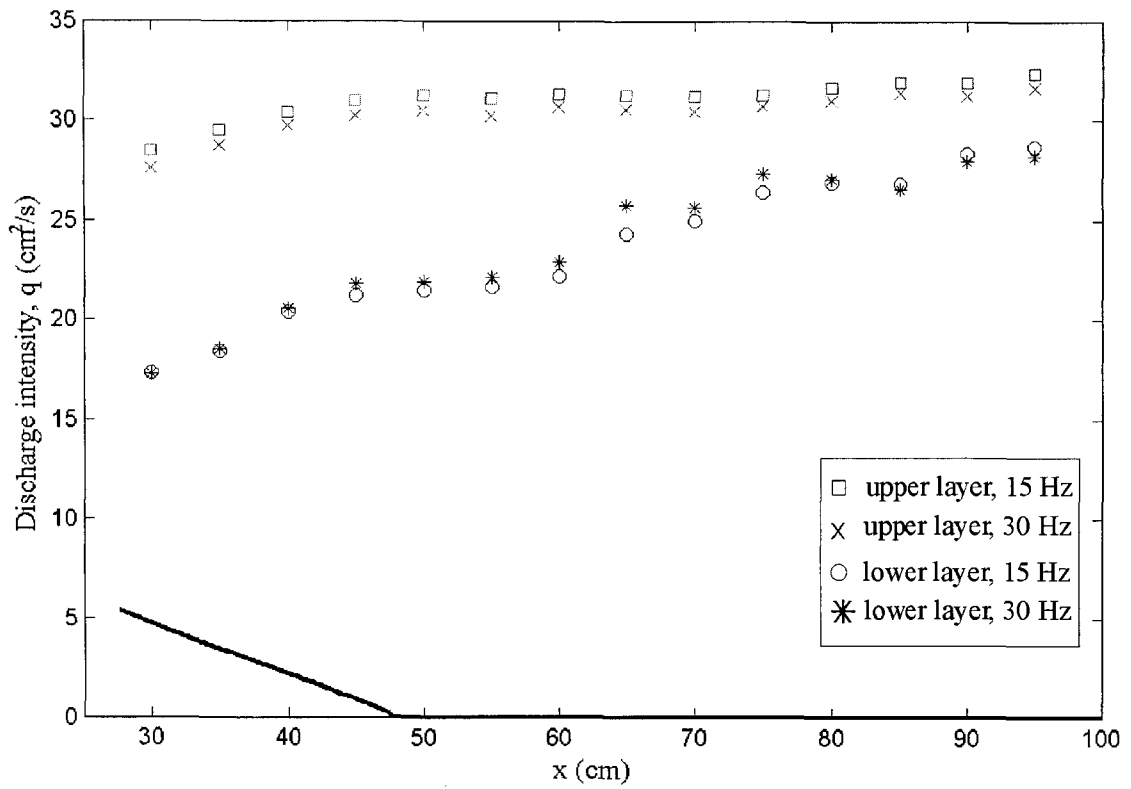
FIGURE 4-14. The flow rate per unit width, q, time-averaged over the maximal exchange regime in Exp1 both at 15 and 30 Hz.

211
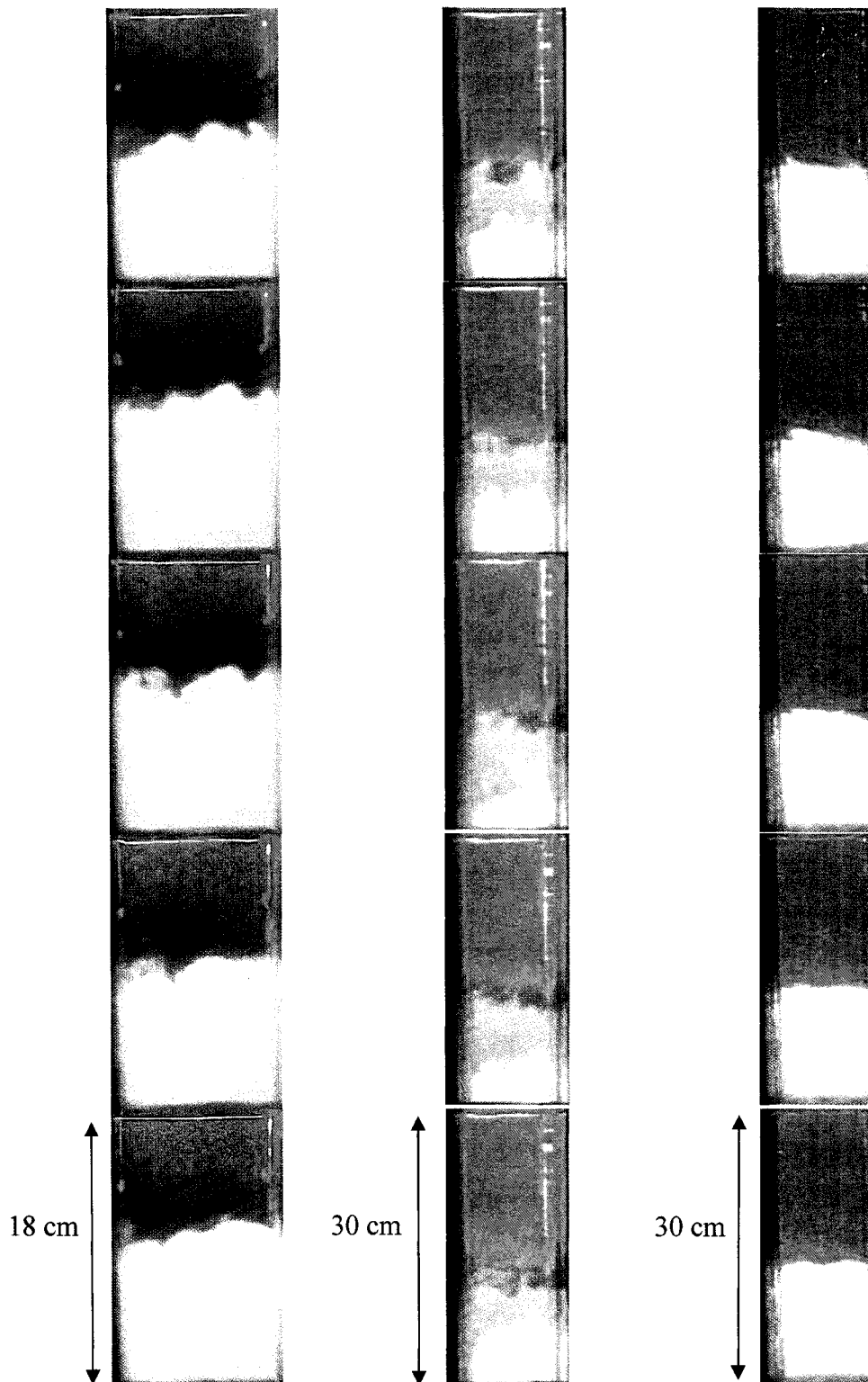
FIGURE 4-15. Sample sequential images from top to bottom at three different sections in Exp 1. The leftmost column is for the sill crest ($x = 0$) at about 30 s into the experiment; the middle for x = 75 cm after around 7 min., and the rightmost for x = 105 cm at 2 min. later. All images are 3.6 s apart and the flow width is 10 cm.

212
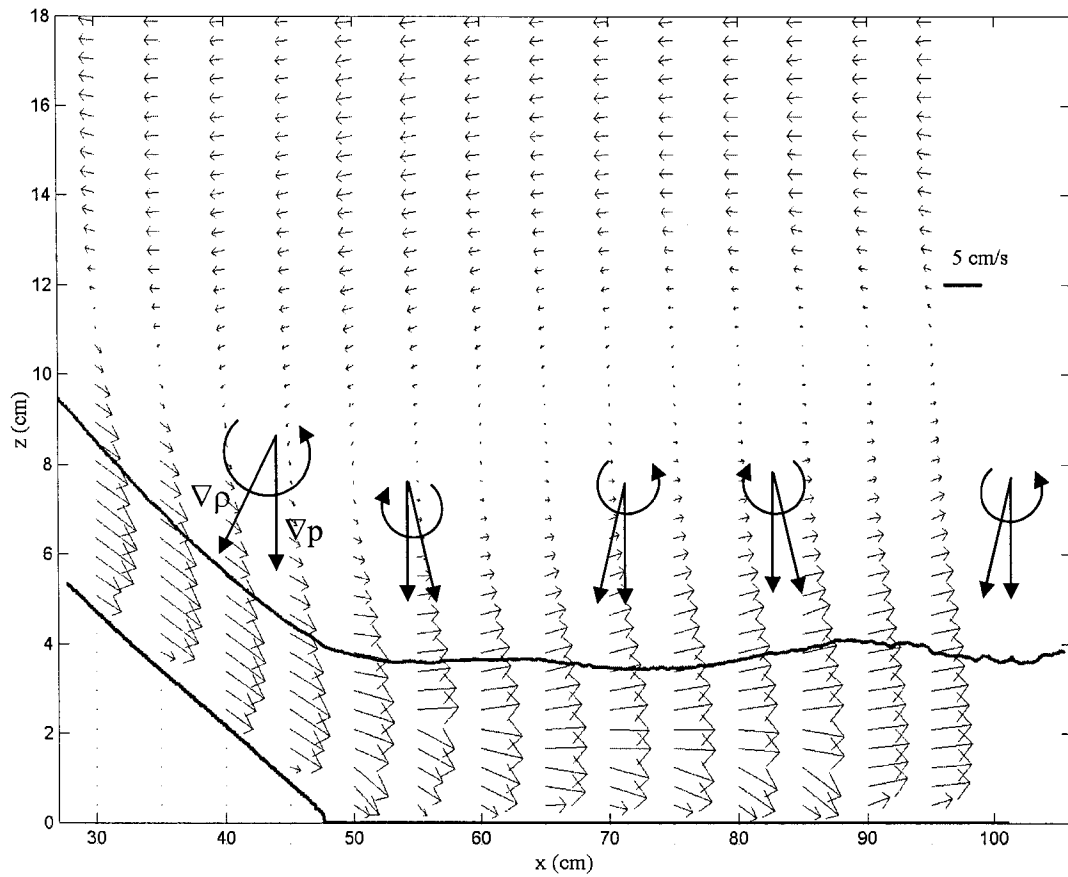
FIGURE 4-16. Time-averaged sample total velocity profiles at 14 locations over the maximal exchange regime in Exp 1. The corresponding time-averaged interface positions obtained after correcting for the horizontal non-uniformity of the laser sheet is over-plotted.

213

TABLE 4-1. List of experiments and their parameters. Fields of view are defined with reference to the sill crest being at x = 0.

Experiment	g' (cm/s^2)	Velocity data Resolution (cm/pixel)	Velocity data Field of view (cm)	Density data Resolution (cm/pixel)	Density data Field of view (cm)	Duration (min.)
1	1.62	0.053	28 : 101	0.075	15 : 106	14
2	6.47	0.053	28 : 101	0.075	15 : 106	9
3	18.03	0.043	33 : 92	0.076	-11 : 93	9

CHAPTER 5

CONCLUSIONS AND RECOMMENDATIONS

5.1 CONCLUSIONS

The current research has been focusing on experiments modeling two-layer exchange flows over smooth bottom sill in a channel connecting two reservoirs at slightly different densities (see figure 1-2). The experiments covered a range of reduced gravity, g', that varied between 1.6 and 18 cm/s^2 and provided a unique opportunity to study different flow phenomena in such flow setup during both maximal and sub-maximal exchange. Three major objectives have been considered, namely: a) the generation conditions of Kelvin-Helmholtz (K-H) instabilities in spatially accelerating flow field, in addition to exploring other interfacial wave activities due to the interplay between stratification and topography, b) the reservoir-channel interaction and how it affected the flow regime and the concurrent generated waves, together with investigating a low frequency mode that was observed at the sill crest herein and in previous studies, and c) the mean flow field and concentration properties in the lee of the topography. In the following the major findings are summarized.

For the flow along the topography, a new finite-amplitude mechanism through which frequent large-scale interfacial breaking waves occurred downwind the sill crest within the maximal regime has been observed. In this mechanism, interfacial shear causes K-H instabilities to develop around the sill crest. The growth of these instabilities at the crest, coupled with a low frequency oscillation of the density interface, results in the piling of lower layer fluid upstream of and at the sill crest. Once the interface attains a climax elevation, it starts dropping with the shallowness of the lower layer then resulting in a downstream shift of the instabilities and their subsequent remarkable growth into large scale waves due to the release of the lower layer accumulated fluid. The large scale interfacial waves attain steep fronts atop of which small amplitude K-H instabilities may form and the whole structure entrains big chunks of the upper fresh layer fluid into the lower higher momentum stream. The interfacial entrainment causes an increase in the flow rate of up to 40% of its value at the sill crest over a distance of about 30 cm. The entrainment coefficient, α_e, was estimated on average as equal to 0.1, which is significantly larger than 0.035 of plane turbulent wall jets.

215

High frequency K-H instabilities were generated at either side of the sill crest along the sharp interface in the wake of the down slope breaking waves during maximal exchange. Likewise, in the late sub-maximal regime, when subtle wave activities existed upstream of the sill crest, very organized and frequent K-H instabilities were generated down the slope. These provided ideal setting to study their generation conditions and properties including wavelength, growth patterns and rates, and speed of propagation. Their point of generation kept on shifting horizontally down the incline with time. Our measurements indicate that K-H instabilities are generated at bulk Richardson number, $J \cong 0.05 - 0.12$, which is significantly larger than the theoretical predictions by Haigh and Lawrence (1999) for parallel horizontal flows. A downward vertical shift of the density interface from the shear layer center, ε, was $\approx 0.14 \pm 0.06$. As time developed, the density interface dropped down further and ε measured 0.25 ± 0.11. At that stage, no more instability was observed. The effect of the shift is in line with the predictions of Haigh and Lawrence (1999), however, who reported that for parallel horizontal flows having $\varepsilon > 0.25$ K-H instabilities would not form. In their study, they had an upper limit for J of about 0.071 for the case of zero shift in order for K-H instabilities to be generated. However, for $0.0461 < J < 0.071$, they reported that Holmboe instabilities have faster growing rates.

During the maximal regime, K-H instabilities and the large breaking waves traveled at the mean flow speed, hence confirmed the current knowledge with horizontal flows that they have zero phase speed. Estimates based on parallel flow for the wavelengths were in line with our measurements. Our measurements for the growth rate were much smaller (a factor of 8) than predictions based on parallel flow assumption. Two growth patterns were observed for the late instabilities in the sub-maximal regime: pattern I in which the instability grows initially exponentially then levels off and experience stream wise vortex stretching until it is entrained into the lower layer, and pattern II in which the instability would grow continuously until it pinches off into the upper layer.

The reservoir-channel interaction has been explained to a first order in terms of the internal energy, E, for a two-layer flow model. In the early times within the maximal regime, the internal energy of the reservoir along the channel, E_{res}, is higher than its value dictated by the two hydraulic controls at the sill crest and the channel exit, E_{chan}. The difference in energy is dissipated through the generation and breaking of frequent large amplitude K-H instabilities that occur along the interface as the upper fresh water fluid leaves the channel into the reservoir. These instabilities are predominantly formed at the exit although some may have originated within the channel in the sub-critical flow reach bounded by the internal controls. They experience a sprout growth to almost ¼ of the total flow depth and the results from different

216

experiments at different reduced gravities indicate that Reynolds number has marginal effect on their mean height. Hilbert-Huang Transform (HHT) and Fast Fourier Transform (FFT) were both used to investigate the generation frequency of those K-H instabilities and how it changes with g'. The results indicated that as g' increased, the generation frequency increased yet no clear dependence could be found. During the maximal exchange, the discharge of the upper layer into the reservoir appears to behave as a surface plume with a densimetric Froude number, F_o, of about 0.24.

As time proceeds, the fresh water flux into the salt water reservoir causes the interface to drop which leads to smaller energy deficit between the reservoir and the channel, hence K-H instabilities become less frequent and smaller in height. The further drop in the interface level within the reservoir, due to continuous fresh water inflow, causes E_{res} to drop below E_{chan} at which time the maximal exchange energy can not be maintained any more and the exit control is lost, hence the flow becomes sub-maximal. During the sub-maximal regime, very subtle wave activities could be detected along the channel, yet signs of small amplitude K-H instabilities reflected from the wall of the tank could be observed incoming into the channel.

HHT and FFT were also used to examine a long low-frequency oscillation which was observed at the sill crest herein and in previous studies performed in the same tank. This long wave has been referred to internal basin seiching in those previous studies that reported its measurement close to the sill crest but did not investigate its origin (Zhu et al. (2002), Morin et al. (2004)). The HHT/FFT analyses of 15 time series of the interface positions within the channel and its alongside part of the reservoir indicated that it is likely being generated along the upstream face of the topography and propagate outwards. A recent study by Tedford et al. (2005) supports the idea that internal seiching could not propagate into the channel against the hydraulic controls. Our results show evidence that the long wave can only propagate into the channel in the sub-maximal regime once the exit hydraulic control is lost. It is not clear though why the observed wave within the channel is of the same period as the internal basin oscillation. Analysis of few time series of the interface positions within the reservoir (view B-B in figure 1-2c) indicated, however, the existence of the internal seiche period at all times.

In the lee of the topography, an intermediate dynamically passive layer at medium density formed between the upper and lower flowing layers. The layer extended within the maximal regime from $x \approx 30$ cm to about one meter downstream the sill crest. Further downstream, it appears that the flow acquired a two-layer structure and the intermediate layer ends. The down slope large scale interfacial waves caused the upper layer flow rate to constantly increase down the incline up to its toe, beyond which it remains almost constant at about 1.5 times its value at

217

the sill crest. The lower layer velocities provided much lower flow rates when integrated across depth and it seems it was not possible to correctly capture them given the large field of view. Cross sections at different locations revealed that the flow is highly three-dimensional. At the crest, the interface level at the outer wall was higher than at the inner wall due to possible horizontal curvature in the approach flow as it enters the channel. Differential elevations of up to about 2.5 cm were observed and periodic fluctuations of about 15 s were detected at g' of 1.64 cm/s^2. The cross sections within the intermediate layer showed very turbulent motions and non-uniform interfacial fluctuations across width, which could be another reason why the lower layer velocities were not correctly captured.

Within the intermediate layer zone, lee waves and undulations in the boundary velocity fields were observed concurrently and could be explained in view of the baroclinic generation of vorticity. Spectral analysis of the density interfacial fluctuations of the lower layer showed single peak at a periodic time of about 17 s for g' of 1.64 cm/s^2. PLIF indicated that a shallow bottommost layer of about one centimeter remained at 75% and higher of the maximum concentration. The concentration levels dropped remarkably at higher elevations from the bed but the concentration profiles showed self similarity as the velocity profiles did. Although the intermediate layer was observed to extend vertically up to about 12 cm of depth, its concentration was at 5% or less of the maximum concentration of the lower layer. This indicates that stable stratification suppresses the generated turbulence efficiently. In the experiment with reduced gravity of 18 cm/s^2, the thickness of the intermediate layer was remarkably bigger than in the other two experiments. It reached about 2/3 of the total depth and was more homogeneous due to larger mass and momentum transfer rates. In the late times of the experiment, an uprising plume-like structure, presumably driven convectively by the mean velocity of the upper layer flow, was observed up the slope at the tip of the intermediate layer.

5.2 RECOMMENDATIONS

The results presented in this thesis contribute a lot into exploring and understanding various flow phenomena in two layer exchange flow over bottom topography. Nevertheless, there are some issues that remain to be addressed. These are listed below in accordance with the relevant phenomena discussed previously in the conclusions and the respective chapters.

It appears from the results that the acceleration of the flow down the sloping topography causes K-H instabilities to form at conditions different from the case of parallel non-accelerating flow.

218

An analytical study using linear stability theory is required to predict the generation conditions of such instabilities in accelerating flow field. Similarly, the growth of such instabilities to large-amplitude billows that result in increased mixing on their break down proved to be non-linear. As such, their development is recommended to be studied numerically using recent computational fluid dynamics' models that would solve a set of non-linear stability equations. While for the linear stability analysis, the classic Taylor-Goldstein equation can be used, Landau equation can be used to study the non-linear amplitude development both in space and time.

A second recommended step is the modification of the internal hydraulic theory to include interfacial entrainment. While previous studies by Zhu and Lawrence (2000) included the streamline curvature and friction effects, interfacial entrainment is an equally important factor. Recently, Nielsen et al. (2004) studied mixing and entrainment in hydraulically driven stratified sill flows analytically and numerically. Their study included comparison between an approach based on shallow-water theory for reduced gravity flows with a cross-interface entrainment and another model with continuously varying stratification and velocity. They focused mainly on the effect of entrainment on the interface height and the location of the hydraulic control at the crest. They found poor agreement though between the two models for the location of the hydraulic control. They did not investigate how entrainment affects the flow rate along the sill. Further studies can address those issues.

Although the current HHT analysis for the field of view upstream to the sill crest within the maximal regime infers that the long wave that was observed within the channel is probably due to topography rather than internal seiching, a more detailed theoretical study is required to support that and investigate why its period matched that of the basin oscillation. Small amplitude surface waves might also contribute in communicating information between the two tanks. For that, both analytical studies on long wave generation due to topographic effects and experiments with a solid lid may be useful in fully resolving such issue.

Another important step would be to study the outflow dynamics in more detail. Similar experiments to the one described herein can be performed but focusing on the basin flow and the fate of the outflow into the reservoir. Also the reasons behind the sprout growth of the K-H instabilities as they leave the channel are equally important to investigate.

For the flow in the lee of the topography, the current study revealed interesting results for the mean concentration field in that the mixing between the lower and intermediate layer was limited to the top part of the lower layer. However, the large field of view had its difficulties with the non-uniformity of the laser sheet. Future experiments can be performed with smaller field of view to have higher resolution. The mass flux between the two layers is an essential component

that requires detailed analysis. Quantifying the mass flux and its dependence on density difference will help estimating the vertical transport of pollutants and heat.

220

REFERENCES

HAIGH, S. & LAWRENCE, G. A. 1999 Symmetric and non-symmetric Holmboe instabilities in an inviscid flow. *Phys. Fluids* **11**, 1459-1468.

MORIN, V. M., ZHU, D. Z., and LOEWEN, M. R. 2004 Super Critical Exchange Flow Down a Sill. *J. Hydraulic Engineering* **130** (6), 521-531.

NIELSEN, M. H., PRATT, L. & HELFRICH, K. 2004 Mixing and entrainment in hydraulically driven stratified flows. *J. Fluid Mech.* **515**, 415-443.

TEDFORD, E. W., LAWRENCE, G., and PIETERS, R. 2005 Interfacial Waves in a Laboratory Exchange Flow. *Proceedings of the 17th Canadian Hydrotechnical Conference,* CSCE, Edmonton, Canada.

ZHU, D. Z. & LAWRENCE, G. A. 2000 Hydraulics of exchange flows. *J. of Hydraulic Engineering,* ASCE, **126**(12), 921-928.

ZHU, D. Z., FOULI H. & OKYERE, Y. A. 2002 Exchange flow through an opening. *J. Hydraulic Research,* **40** (3), 341-350.

221

APPENDIX A

EXCHANGE FLOW THROUGH AN OPENING[1]

Exchange flow through an opening

Echange de fluide à travers une ouverture

DAVID Z. ZHU, *Associate Professor, Department of Civil and Environmental Engineering, University of Alberta, Edmonton, AB, T6G 2G7, CANADA. Tel: (780) 492-5813; Fax: (780) 492-0249, E-mail: dzhu@civil.ualberta.ca*

HESHAM FOULI, *Graduate student, Department of Civil and Environmental Engineering, University of Alberta, Edmonton, AB, T6G 2G7, CANADA. E-mail: hfouli@ualberta.ca*

YAW A. OKYERE, *Graduate student, Department of Civil and Environmental Engineering, University of Alberta, Edmonton, AB, T6G 2G7, CANADA.*

ABSTRACT

This paper presents a theoretical and experimental study of the exchange of fluids of different densities through an opening. Three types of openings are examined: a bottom opening (the opening is at the bottom of a gate), a middle opening (in the middle) and a window opening (the opening is in the middle but does not extend across the width). Simultaneous measurements of velocity field and interface position were obtained using flow visualization and image processing techniques. Experimental results confirm the predictions of the internal hydraulic theory that there are two internal hydraulic controls in the flow through bottom openings, but one control in the middle and window opening experiments. The neglect of non-hydrostatic forces and interfacial mixing in the theory, however, results in a significant underestimate of the exchange rate by more than 50 % in the middle and window opening experiments. The fluctuations in the interface position were caused by Kelvin-Helmholtz instabilities as well as basin-scale internal seiche, and the transition of internally supercritical flow to subcritical flow was caused by the mixing generated by these instabilities.

RÉSUMÉ

Cet article présente une étude théorique et expérimentale de l'échange de fluides de densités différentes à travers une ouverture. Trois types d'ouvertures sont examinés : une ouverture au fond (l'ouverture est située à la base d'une vanne), une ouverture médiane (au milieu), et une fenêtre (l'ouverture est au milieu mais n'occupe pas toute la largeur). Des mesures simultanées de champ de vitesse et de position d'interface ont été faites avec des techniques de visualisation d'écoulement et de traitement d'image. Les résultats expérimentaux confirment les prédictions théoriques de l'hydraulique interne, à savoir qu'il y a deux contrôles hydrauliques internes pour l'écoulement à travers les ouvertures de fond, mais un seul contrôle pour l'ouverture médiane et la fenêtre. Cependant, le fait de négliger dans la théorie les forces non hydrostatiques et le mélange à l'interface conduit à sous-estimer le taux d'échange de plus de 50% dans les cas d'ouverture médiane et en fenêtre. Les fluctuations de l'interface étaient dues à des instabilités de Kelvin-Helmholtz, ainsi qu'à une seiche à l'échelle du bassin, et le passage torrentiel fluvial de l'écoulement interne était causé par le mélange dû à ces instabilités.

Keywords: Exchange flows, internal hydraulics, hydraulic control, opening, non-hydrostatic effects, interfacial instability, mixing.

1. Introduction

When two bodies of fluids of slightly different densities are connected by a channel, fluids start to exchange. Such exchange flows are common in nature; for example, the exchange of more saline Mediterranean Sea water with less saline Atlantic Ocean water through the Strait of Gibraltar (Armi & Farmer, 1988), the exchange flow through the Bospherous (Oguz *et al.*, 1990), and the summertime exchange of warmer heavily polluted Hamilton Harbor water with cooler (more dense) Lake Ontario water through the Burlington ship canal (Hamblin & Lawrence, 1990). Two-layer exchange flows are commonly modeled as homogeneous layers of inviscid fluid with negligibly small vertical velocities. Consequently, the pressure distribution can be considered hydrostatic, and the hydraulic (or shallow water) equations can be applied to each layer. The extension of the hydraulic equations to two-layer flows is called the internal hydraulics; see for example, Armi (1986), Wood & Lai (1972). Previous studies on exchange flows have mostly focused on exchange flows through a channel where the change of channel geometry is gradual and the effect of non-hydrostatic forces can be neglected (Armi & Farmer,

1986). For such flows, Zhu (2002) developed a control curve approach to study exchange flows through complex geometry. Non-hydrostatic forces, however, could be important even for channels having smooth topography (Zhu & Lawrence 1998, 2000). Zhu & Lawrence (2000) showed that neglecting non-hydrostatic forces results in underestimating the flow rate even for exchange flows over a smooth topography.

Exchange flows through an opening are also common in nature. Examples of such flows include the exchange of cold and warm air through doorways and windows (Dalziel & Lane-Serff, 1991), the exchange of warm and cold water through a slot opening (Adams & Cosler, 1988) and in reservoir selective withdrawal (Harleman & Elder, 1965). Dalziel & Lane-Serff (1991) noted that the basic features of doorway exchange flow could be described by the internal hydraulics. By approximating the rapidly varying doorway geometry as a slowly varying channel, they neglected the effects of non-hydrostatic forces and assumed that the flow is critical at the doorways and window opening. Similarly, Adams & Cosler (1988) did not consider the effects of non-hydrostatic forces.

Given that exchange flows through a sharp opening tend to have

---

223

strong streamline curvature, as is evident in single-layer flow over a sharp-crested weir, it is questionable that the non-hydrostatic forces caused by streamline curvature can be neglected. Detailed experimental studies on these flows are needed in order to understand the hydraulics of the flows and to evaluate the effects of non-hydrostatic effects. Previous experimental studies by Adams & Cosler (1988) and Dalziel & Lane-Serff (1991) do not provide simultaneous measurements of the interface position and the flow rate, thus not sufficient for such study.

The objective of this study is to seek a better understanding of the hydraulics of exchange flows through various types of openings, and to examine the applicability of the internal hydraulics to these flows. Laboratory experiments were conducted and detailed flow measurements were taken using flow visualization and image processing techniques. The paper is structured as follows: Section 2 reviews the internal hydraulics and discusses the control mechanisms of exchange flows through various types of openings. Section 3 presents the experimental setup and apparatus. Sections 4 and 5 discuss experimental results and the comparison with theoretical predictions for exchange flows through an opening at the bottom and in the middle, respectively. Some interesting observations of the flow, such as interfacial instabilities and mixing mechanisms, are also discussed. The paper is concluded in Section 6.

2. Hydraulics of Exchange Flow Through an Opening

In this section, we will first briefly review the internal hydraulics for inviscid flow with a hydrostatic pressure distribution. We will then apply it to study exchange flows through various types of openings. To facilitate our discussion, we start by considering exchange flows through a combination of a bottom sill and a surface inverted sill in a rectangular channel, which connects two large reservoirs containing fluids of slightly different densities (Fig. 1). Provided the sills have gentle curvature, the pressure distribution will remain close to hydrostatic and thus the internal hydraulics is valid. The streamline curvature, however, increases when the sills become shorter. When the sills become infinitely short, this case becomes the flow through a sharp opening. It is the intent of this study to examine whether the internal hydraulics is still valid for such flows.

In the present study we focus on flows with small density difference, i.e. $\varepsilon = (\rho_2 - \rho_1)/\rho_2 << 1$, where ρ_1 and ρ_2 are the densities of the upper and lower layer, respectively. For such flows, the slope of the free surface is negligibly small, commonly referred to as the 'rigid lid' or horizontal free surface approximation. Thus the elevation of the free surface

$$H = y_1 + y_2 + h_1 + h_2 \qquad (1)$$

remains a constant, where y_1 and y_2 are the thickness of the upper and lower layer, and h_1 and h_2 are the thickness of the surface and bottom sill, respectively.

For shallow water flows, it is customary to assume that the pressure is hydrostatic, and that the horizontal velocity is uniform across depth in each layer. For steady, inviscid and irrotational

(a)

(b)
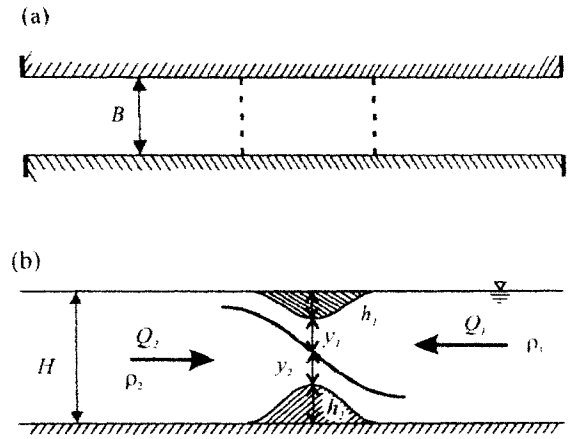
Fig. 1. Illustrating diagram showing two-layer exchange flows through a channel with sills. (a) Plan view, (b) side view.

flows, the energy head (or Bernoulli constant) E_i for layer i, ($i = 1, 2$), is conserved in the absence of hydraulic jumps or flow separation. Thus the internal energy E,

$$E \equiv (E_2 - E_1)/(\rho_2 - \rho_1)g = y_2 + h_2 + (U_2^2 - U_1^2)/2g' \qquad (2)$$

is also conserved along the channel. Here g is the gravitational acceleration, $g' = \varepsilon g$ is the reduced gravitational acceleration, and U is the mean horizontal velocity.

The conservation of the internal energy E together with the rigid-lid free surface condition (Eq. 1) gives the slope of the interface position,

$$\begin{aligned} d(y_2 + h_2)/dx = \\ \{F_1^2 h_{1_x} - F_2^2 h_{2_x} - (F_1^2 y_1 - F_2^2 y_2)b_x /b\}/(1 - G^2) \end{aligned} \qquad (3)$$

where $F_i^2 = U_i^2/g' y_i$ is the densimetric Froude number for layer i, $G^2 = F_1^2 + F_2^2$ is the composite (or internal) Froude number, and b is the width of the channel. Subscript x indicates the differentiation with respect to x.

The locations where $G = 1$ are known as internal hydraulic controls and the flow is said to be internally critical at these locations. The composite Froude number G acts in a similar manner to the Froude number F for single-layer flows with the flow being internally supercritical (or subcritical) when $G > 1$ (or $G < 1$). In subcritical flows, small interfacial disturbances can propagate towards both upstream and downstream, while they propagate only downstream in supercritical flows.

Possible locations of controls can be determined using Eq. (3) from the requirement that the numerator be zero. For flows where sills are separated from channel contractions, controls can only occur at sill crests or channel narrowest points. For each control, we can develop a relationship between the internal energy E and the flow rate Q using $G = 1$ together with Eq. (2). Such a relation, or a control curve (Zhu, 2002), represents all possible solutions of the flow with the control. Control curve technique is a power-

224

ful tool in analyzing two-layer flows and will be used in the following study.

It is convenient to normalize the flow variables with respect to the vertical scale H, the lateral scale B, the velocity scale $(g'H)^{1/2}$, and the flow rate scale $HB(g'H)^{1/2}$. The characteristic time scale, T, is equal to the total volume of water in the tank, AH, where A is the surface area of the tank, divided by the flow rate scale, i.e., $T = (A/B)/(g'H)^{1/2}$. With these scalings, we obtain the following set of dimensionless variables:

$$y_i^* = y_i/H; \quad h_i^* = h_i/H; \quad b^* = b/B; \quad E^* = E/H;$$

$$U_i^* = U_i/(g'H)^{1/2}; \quad Q_i^* = Q_i/(HB(g'H)^{1/2}); \quad t^* = t/T \tag{4}$$

where the parameters with an asterisk are dimensionless. For the remainder of this paper, dimensionless parameters will be used and the asterisks will be dropped.

2.1. Flow Through a Bottom Opening

Without the bottom sill, i.e. $h_2 = 0$ but $h_1 \neq 0$ in Fig. 1, the flow exchanges through an opening at the bottom that extends across the channel width B (Fig. 2a). Note that when the sill becomes very short, this case is similar to flow through a sharp opening. Here the sill crest control will also be called the opening control. The exchange flow through a bottom opening tends to be critical at the opening. A control curve for the opening control (or crest control) (Zhu, 2002) is plotted in Fig. 3, where $h_1 = 0.43$ and $h_2 = 0$ are used to simulate the conditions in Exp. B2 (discussed below). For the exchange flow shown in Fig. 1, a possible second control is located at the channel exit. The control curve for the exit control is also shown in Fig. 3. Clearly, with both the opening control and the exit control, the rate of exchange is determined by both controls and is obtained at the intersection point of the two control curves.

With two controls, the exchange flow is subcritical in the region bounded by the controls, but supercritical immediately outside. Given that interfacial disturbances cannot propagate against supercritical flows, the influence of the reservoirs is blocked by the controls. Exchange flow with two controls is called the maxi-
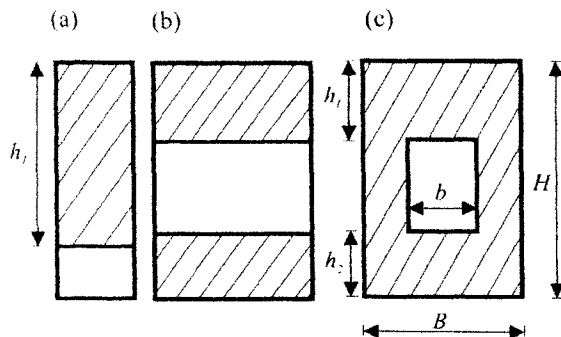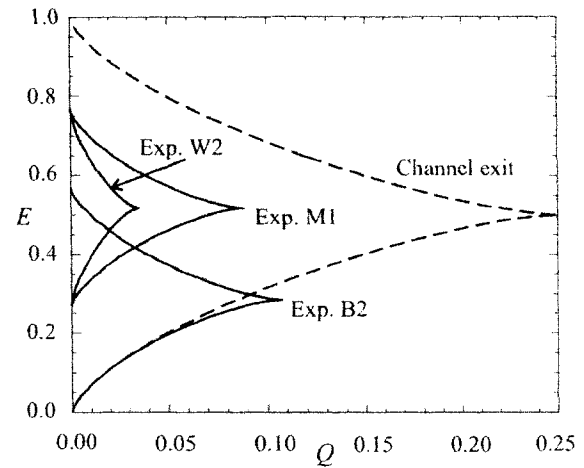

Fig. 3. Control curves showing solutions to the exchange flow through bottom, middle and window openings.
———— control curve for the opening control.
— — — control curve for the exit control.

mal exchange, as it gives the maximal flow rate for a given channel geometry and density difference. The maximal exchange flow is steady before one of the controls is flooded. When the exit control is lost due to the rise of the interface level in the right hand reservoir, the flow will then be subcritical all the way to that reservoir. Exchange flow with one control only is called the submaximal exchange, and is influenced by the variation in the reservoir condition. Submaximal exchange is determined by the remaining control together with the internal energy E specified by the reservoir condition.

2.2. Flow Through Middle and Window Openings

A middle opening (Fig. 2b) can be modeled by having finite values of h_1 and h_2. The case where an opening does not extend across the channel width (Fig. 2c) is called a window opening and is considered separately. The control curve for a middle opening is plotted in Fig. 3 with $h_1 = 0.23$ and $h_2 = 0.27$ to simulate Exp. M1. Noticeably different from a bottom opening, the control curve for a middle opening no longer intersects with the exit control curve, indicating that the flow cannot satisfy both controls. The flow is now controlled by the opening alone. The maximal flow rate $Q_{max} = \frac{1}{4} B (1 - h_1 - h_2)^{3/2}$ is obtained when $E = \frac{1}{2}(1 - h_1 - h_2)$ or $y_1 = y_2$ at the opening (see Zhu (2002) for details on control curves). The flow is critical at the opening and supercritical away from it. The single control in this flow is due to the increase in the bottom elevation at the opening such that the influence of the exit is blocked by the supercritical flow leaving the opening.

The case of a window opening (Fig. 2c) is similar to a middle opening, except for the additional lateral contraction. This lateral contraction will act to decrease the flow rate given $b < B$. The control curve for a window opening with $b = 0.4$ but the same h_1 and h_2 as in Exp. M1 is also plotted in Fig. 3. Similar to the mid-

Fig. 2. Types of openings: (a) bottom opening, (b) middle opening, (c) window opening.

dle opening, the exchange flow through a window opening is controlled solely by the opening where the flow is also symmetric with $y_1 = y_2$ at the opening.

3. Experiments

Experiments of exchange flows through an opening were conducted in a water tank of 245 cm long, 123.5 cm wide and 35 cm high (Fig. 4). The tank was divided into two reservoirs, which were connected by a rectangular channel of 150 cm long. The density difference was obtained by dissolving a known amount of salt (NaCl) into the left hand reservoir. Three types of openings were studied: a bottom opening, a middle opening and a window opening (Fig. 2). In experiments with a bottom opening, the height of the opening was varied (Exp. B1 - B4). In the middle opening experiments, the height of the opening was varied (Exp. M1 - M2), while the width of the opening was varied in the window opening experiments (Exp. W1 - W2). An additional experiment was conducted to study the effect of barotropic forcing by pumping fluid from one side of the reservoir to the other (Exp. F1). Detailed conditions for these experiments are summarized in Table 1.

Table 1. Table of experiments

Exp.	Opening	g' (cm/ s^2)	h_1/H	h_2/H	b/B opening width	Q^* flow rate	B channel width (cm)	L length scale (cm)	T time scale (s)
B1	Bottom	2.74	0.27	0	1	0.133	10	90	327
B2	Bottom	2.72	0.43	0	1	0.095	10	90	335
B3	Bottom	2.73	0.63	0	1	0.053	10	90	334
B4	Bottom	2.74	0.73	0	1	0.030	10	90	334
F1**	Bottom	2.72	0.67	0	1	0.087	10	90	335
M1	Middle	2.50	0.23	0.27	1	0.139	20	75	175
M2	Middle	3.19	0.40	0.27	1	0.080	20	75	155
W1	Window	2.50	0.23	0.27	0.7	0.101	20	75	175
W2	Window	2.50	0.23	0.27	0.4	0.071	20	75	175

Water depth $H = 30$ cm in all experiments, except in Exp. F1 where $H = 22.5$ cm.

* Flow rate was measured during the steady period of the experiments.

** Fluid was pumped from the right reservoir to the left, and the channel bed was raised by 7.5 cm.

A plate with an opening was fixed in the channel. The plate was located in the middle of the channel for the middle and window opening experiments. Thus the distance between the plate and the right-hand exit of the channel, L, is 75 cm. In the bottom opening experiments, the plate was moved towards left to give a larger L of 90 cm. Before the experiments, a barrier was inserted in the channel to separate the two reservoirs. Salt was added into the left hand reservoir, as well as sodium fluorescing dye to indicate the lower layer. Tiny neutrally buoyant tracer particles (Pliolite VT-L) were added into both reservoirs.

After removing the barrier, an exchange flow developed. Experiments were illuminated from above using a thin sheet of light generated by two 500-Watt halogen bulbs. Images of tracer particles and interface position were recorded separately using Sony Hi8 video cameras. The velocity field halfway between the opening and the channel right-hand exit was obtained by tracking the
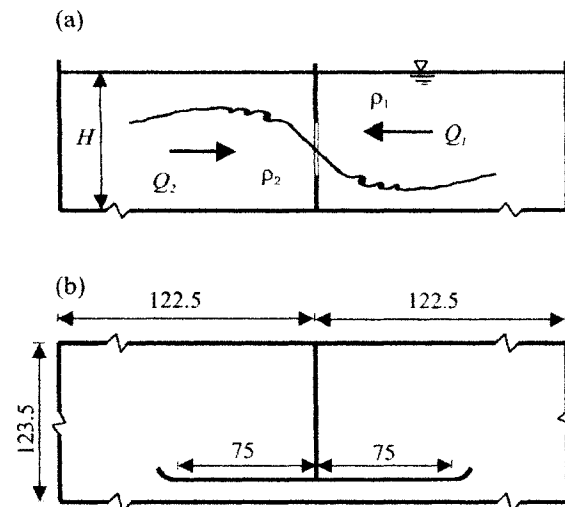
(a)

(b)

Fig. 4. Experimental setup: (a) side view, and (b) plan view. All dimensions are in centimeters

movements of tracer particles using a maximal cross-correlation technique (Steven & Coates, 1994). The location of the density interface was determined from the maximal gradient of light intensity between the transparent upper layer and the dyed lower layer. Using particles and dyes, simultaneous measurements of velocity field and interface positions were obtained.

Errors in the measurements of flow velocity field and flow rate are dependent on the resolution of the video images. Images of 640 x 480 pixels covered a flow area of 40 cm (horizontal) by 30 cm (vertical), giving a pixel resolution of 0.06 cm. In determining the velocity field the time interval between two images was chosen to ensure that particles had an average travel distance of approximately 10 pixels (0.6 cm), resulting in an error of approximately 10 % in velocity due to pixel resolution. This error was reduced to about 3 % by averaging 10 neighboring velocity profiles. Flow rate was then obtained by integrating velocity profiles over the depth. The errors in locating the free surface and the bottom positions (about 1 pixel) further increased the error in flow rate. This error was reduced by additional averaging over four flow rates obtained from four pairs of images taken within a second. We estimate a possible error of about 5 % in flow rate measurements.

Errors in the measurements of the interface position are mainly due to the relatively low resolution of the video images. In bottom opening experiments, the interface position from the opening to the channel right-hand exit is of interest. Images of 640 x 480 pixels covered a channel length of 120 cm. This gave a pixel resolution of about 0.2 cm. Errors of 1 - 2 pixels in the determination of the interface position correspond to relative errors of 1 - 3 %. In the middle and window opening experiments, the images centered around the opening and covered a channel length of 60 cm, yielding a pixel resolution of about 0.1 cm. This allows a more accurate measurement of the interface position. In all measurements, various averaging was performed on the data.

226

4. Exchange Flow Through a Bottom Opening

We start this section by discussing the evolution of the flow regimes. The experimental measurements are then compared with the predictions of the internal hydraulics. This is followed by the results of exchange flow with barotropic forcing.

4.1 Evolution of the Mean Flow

The exchange flow started when the barrier separating the two reservoirs was removed. After an initial unsteady period, the hydraulic control at the opening was first established. At a later time, the exit control was also established. With two controls the flow was steady maximal exchange (Fig. 5a). During the experiment, the interface level in the right-hand reservoir rose continuously as a result of the accumulation of the denser water. When it exceeded a certain level, the exit control was then flooded, and the flow was submaximal exchange (Fig. 5b). The flow rate in this submaximal exchange decreased continuously given the rise in the interface level in the right-hand reservoir. The following study focuses on the steady maximal flow regime.

The evolution of the flow regime is illustrated using the measurement of the flow rate in Exp. B2, as shown in Fig. 6. The steady maximal exchange started at $t \approx 0.3$ and lasted until $t \approx 1.3$. After that the flow rate decreased due to the loss of the exit control. During the steady maximal exchange, the flow rate remained constant. The small variation in the measurements is probably due to experimental errors. Errors in Exp. B2 have a standard deviation of about 2 %, consistent with our analysis of about 5 % error in flow rate measurement. Note that in this experiment, the water level is the same in both reservoirs, such that the flow in the up-

(a)

(b)
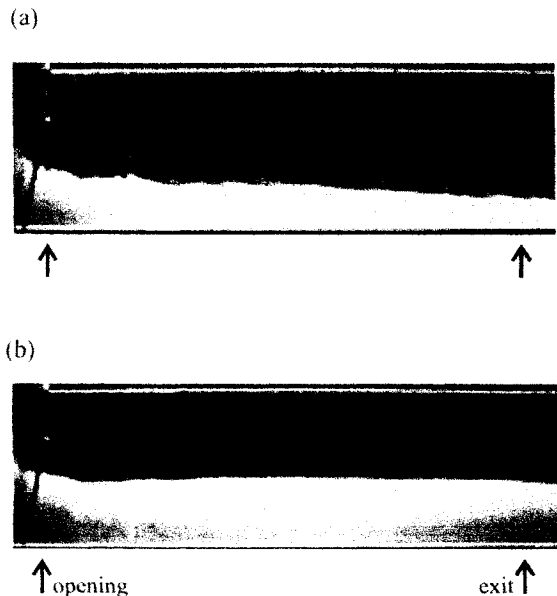

↑opening   exit↑

Fig. 5. Images showing the flow regimes in Exp. B1: (a) maximal exchange, (b) sub-maximal exchange.
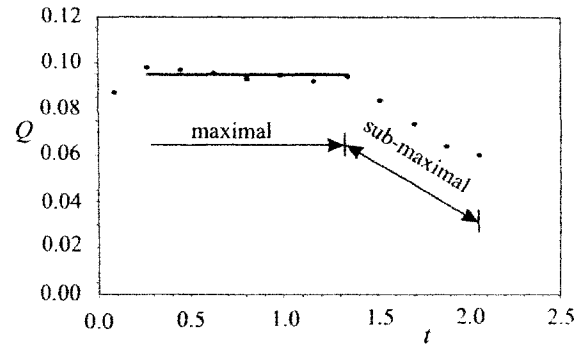

Fig. 6. Measurements of the flow rate with time in Exp. B2.
———— mean flow rate.

per layer must be balanced by the flow in the lower layer, i.e. $Q_1 = Q_2$.

4.2 Hydraulics of the Flow

Along-channel variation of the interface position was measured between the opening and the right-hand exit of the channel. A mean interface position was obtained by averaging out the interface fluctuations due to shear-generated instabilities, and is plotted in Fig. 7(a) for Exp. B2 during its maximal exchange regime. The upper layer converged when the flow moved from right to left. A circulating surface eddy formed upstream of the opening. This eddy effectively reduced the thickness of the upper layer, and was considered in determining the layer thickness. Unlike the interface position, the determination of the eddy size proves to be more difficult and has some uncertainty.

Using the measured flowrate and interface position, the along-channel variation of the composite Froude number G is obtained for Exp. B2 (Fig. 7b). It is obvious that this flow has two controls located at the opening and at the exit, as predicted by the internal hydraulics. Between the two controls, the flow is subcritical. Note that accurate determination of G at the opening is difficult as a small error in locating the horizontal position would result in a significant change in G. At the exit, the end effect also affects the G value. The G values at the opening and at the exit were found to be in the range of $0.9 - 1.2$ for Exp. B1 - B4. Recalling that the flow rate and the layer thickness could have a possible error of 5 % and 3 %, respectively, G could have a possible error of about 12 %. Thus the above measurements of G at the opening and the exit compare well with the prediction of the internal hydraulics. Variation of the internal energy E is plotted in Fig. 7(c). Instead of remaining constant as predicted by the internal hydraulics, E varies as a result of friction and non-hydrostatic forces. The friction at the interface, sidewalls and the bottom causes E_1 to increase and E_2 to decreases in the positive x-direction. Thus E, which is determined by subtracting E_1 from E_2 (Eq. 2), also decreases in the x-direction. The effect of friction is clearly seen in Fig. 7(c) where E decreases with x. Around the gate where streamline curvature is significant, the non-hydrostatic forces cause E to increase significantly with x. The internal energy E
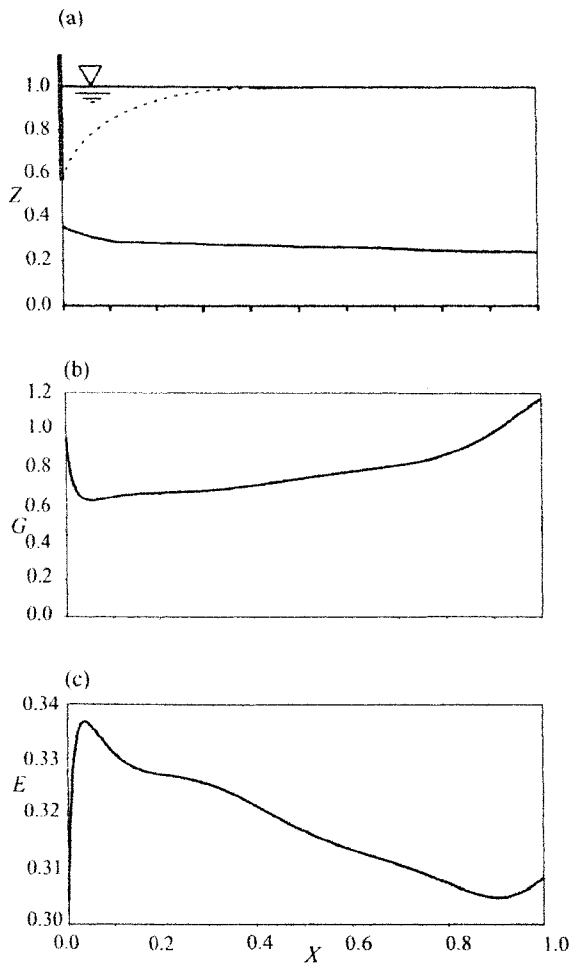
227

(a)

(b)

(c)

Fig. 7. Measurements of the along-channel variations of (a) the mean interface position, (b) the composite Froude number G, and (c) the internal energy in Exp. B2.

also increases at the channel exit but to a lesser extent. The non-hydrostatic effects are much smaller in the middle of the channel where friction is dominant. It is interesting to note that the effects of non-hydrostatic forces and friction tend to cancel each other in Exp. B2, and the internal energy E is very much the same at the gate and at the exit.

Measurements of the flow rate in Exp. B1 – B4 are compared with the predictions of the internal hydraulics for inviscid and hydrostatic flow in Fig. 8. With the controls at the gate and the channel exit, the internal hydraulics predicts the flow rate very well. Zhu & Lawrence (2000) showed that friction reduces the flow rate while non-hydrostatic forces tend to increase the flow rate. As these effects cancel each other as shown in Exp. B2, neglecting friction and non-hydrostatic forces does not cause major error in flowrate prediction. Note, however, that friction is more important in longer channels while non-hydrostatic forces depend on local streamline curvatures. In addition, accurate prediction of
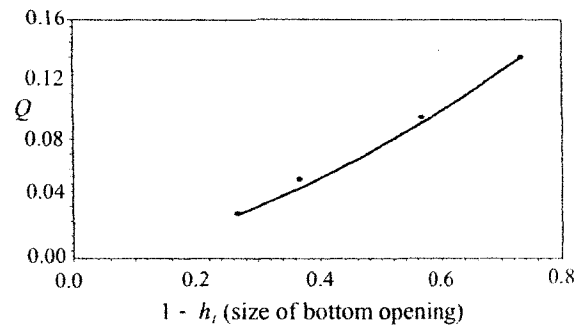

Fig. 8. Comparison of measured and predicted flow rates for exchange flows through a bottom opening of different sizes (Exp. B1 – B4). • measurements,————— prediction.

the interface position requires that both effects be considered (Zhu & Lawrence, 2000).

4.3 Exchange Flow with Barotropic Forcing

One experiment (Exp. F1) was conducted to study the effect of barotropic forcing on exchange flows. In the experiment, the denser fluid was pumped from the right to the left reservoir to maintain a net flow between the two layers, and the channel bottom was raised by 7.5 cm over the bottom of the reservoir in order to maintain the exit control for a longer period. When the net flow is strong enough it can arrest the upper layer and leave only the lower layer moving. Figure 9 shows the arrested flow observed in Exp. F1 where the upper layer was stagnant and only the lower layer was moving. At the interface of the two-layers, a special type of interfacial instability, namely, Holmboe instability (Zhu & Lawrence, 2001) is observed. Since the flow was almost parallel in a major section of the channel, this arrested flow provides an ideal condition to study Holmboe instability.

Given that only the lower layer was active, G was calculated based on the lower layer only. At the opening, G was 0.77 in Exp. F1, smaller than the measurements in the non-forcing cases. Harleman & Elder (1965) also reported smaller values with G ranging from 0.17 to 0.88 in their arrested flows. It is to be noted that there is some uncertainty in computing the G value at the opening. In Exp. F1, the contribution of the upper layer in G was neglected given the negligibly small flow rate in the upper layer. However, since the upper layer is significantly thinner (< 0.5 cm) than the lower layer (7.0 cm), an upper layer flow rate of only
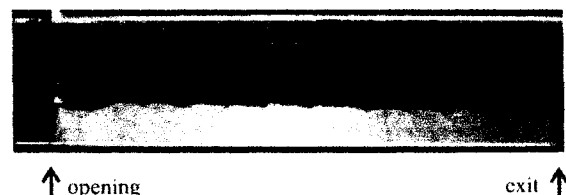

↑ opening   exit ↑

Fig. 9. Image showing an exchange flow with barotropic forcing in Exp. F1 where the upper layer is arrested.

228

2 % of the lower layer will yield the same Froude number in the upper layer as in the lower layer. The significant contribution in G by such a small flow rate in the upper layer makes the accurate determination of G difficult. This might be the reason that the reported G values vary significantly in the literature.

At the channel exit, G was measured at 1.82. This large G value is due to the fact that the channel bottom was raised. Thus after the exit, the lower layer falls over as in single-layer flow. Assuming that the brink depth is 0.715 of the critical depth as in single-layer flow (Henderson, 1966), this would yield a value of 1.65 for G at the exit, which is close to our measurement.

5. Exchange Flow Through Middle and Window Openings

In the middle and window opening experiments, the control at the opening was established shortly after the start of the experiments, and the flow became steady. Eventually the opening control was lost and the flow became unsteady. In this study, we will focus on the steady exchange. The hydraulics of the flows will first be examined and the measurements of flow rate will be compared with theoretical predictions. The results of the mean interface position and its fluctuations will then be discussed. Finally the transition from the supercritical to subcritical flow will be studied.

5.1. Flow Controls and Flow Rate

Images of the flow through a middle opening (Exp. M1) and a window opening (Exp. W1) are shown in Fig. 10. The interface fluctuated due to significant interfacial instabilities generated by the strong velocity gradient. In order to obtain a mean position of the interface, a time series of the interface position at the opening was obtained during the steady maximal regime in Fig. 11(a) for Exp. M1. The mean interface position was at 0.511, which is about the mid-depth of the opening of 0.517. The mean interface position was also measured to be at the mid-depth of the opening in Exp. W1.

For exchange flow through middle and window openings, the internal hydraulics predicts a maximal exchange rate of $Q_{max} = \frac{1}{4} b (1 - h_1 - h_2)^{3/2}$ based on $G = 1$ and $y_1 = y_2$ at the opening. The measurement of the interface position confirms the prediction that $y_1 = y_2$ at the opening. The flow rate measurements, however, are significantly larger than the predictions (Fig. 12). They are 57% and 69% larger than the predictions for the larger and smaller middle openings, respectively; and they are 63% and 100% larger than the predictions for the larger and smaller window openings, respectively. These flow rates were measured halfway between the opening and the channel right hand exit. At this location, the flow was parallel thus allowing an accurate measurement of the flow rate.

The above results are significantly different from the bottom opening experiments where the measured flow rates compared well with the predictions. The reason for this difference needs further study, but we hypothesize that it is due to the non-hydrostatic forces as well as the entrainment at the interface of the two layers. Zhu & Lawrence (2000) reported that the inclusion of non-hydrostatic forces results in an increase of 15% in flow rate
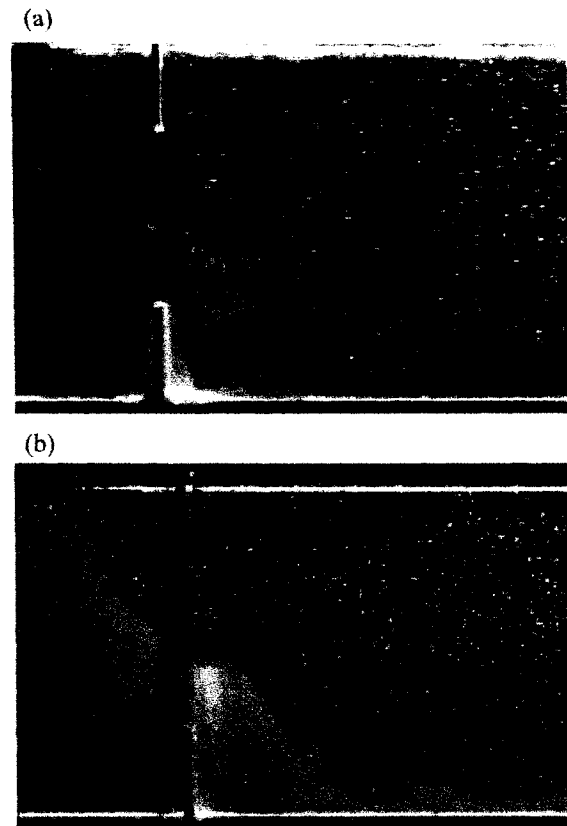
Fig. 10. Images showing the exchange flow through (a) a middle opening (Exp. M1), and (b) a window opening (Exp. W2).

in their flow over a smooth sill. In the bottom opening experiments, the friction between the two controls reduces the flow rate, and the effects of friction and non-hydrostatic forces cancel each other. Thus neglecting both effects in the prediction does not cause significant error. In the middle and window opening experiments, the flow is controlled at the opening only. Friction has minimal effect, whereas non-hydrostatic forces become even more important given strong streamline curvature. Neglecting non-hydrostatic forces results in significantly underestimating the flow rate. The fact that the error in the flow rate increases with decreasing opening size seems to further confirm the importance of non-hydrostatic forces.

Passing through the opening, the fast-moving lower layer entrains the fluid from the upper layer. This entrainment thus results in an increased flow rate in both the upper and lower layer. The rate of entrainment has been studied for some simple flows such as density currents (see, for example, Alavian et al, 1992). Recent study by Morin et al. (2002) showed that the flow rate is increased by 20% for the exchange flow over a smooth sill of 10 cm high and 50 cm long due to the interfacial entrainment. Detailed study is needed in order to quantify the amount of the flow rate increase due to the interfacial entrainment for the flows studied here.
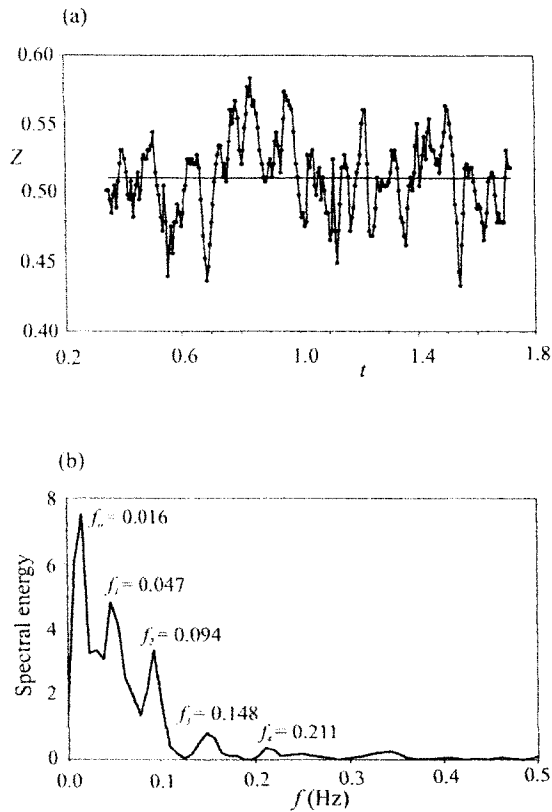
229

(a)

(b)

Fig. 11.   (a) Time series of the interface position at the opening in Exp. M1 (the time-averaged value is also indicated), and (b) its spectrum.

5.2. Interface Position

The interface of the exchange flows is subject to the fluctuations generated by interfacial instabilities as well as basin-scale oscillations (i.e. internal seiche). The processes responsible for the inter-
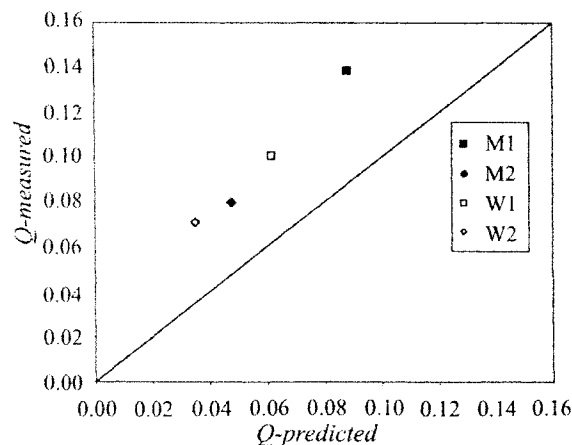

Fig. 12.   Comparison of measured and predicted flow rates for the exchange flow through middle and window openings.

face fluctuations will be first studied, followed by an examination of the mean position of the interface.

The time series of the interface position measured at the opening in Exp. M1 (Fig. 11a) was analyzed and its spectrum is shown in Fig. 11(b). Five spectral peaks can be identified. The most dominant peak has the lowest frequency f_0 of 0.016 Hz, corresponding to an oscillating period of 62.5 seconds. This low frequency oscillation is believed to be associated with the basin internal seiche. A quick estimate of the seiche period can be obtained by assuming the reservoir is a closed two-dimensional basin with a length $L_b = 123$ cm. The propagating speed of the interfacial wave is given by $C_i = \sqrt{g' y_1 y_2 /(y_1 + y_2)}$ (Zhu & Lawrence, 2000). Assuming the interface is at the mid-depth of the reservoir, i.e., $y_1 = y_2 = 15$ cm, the fundamental mode of the internal seiche has a period of $T_0 = 2L_b/C_i = 56.8$ seconds. This compares well with the measurement of 62.5 seconds. Note that the actual seiche period will be affected by some factors that are not considered in this simple model: the effect of the connecting channel and the fact that the basin is close to rectangular (i.e. three dimensional). Nevertheless these effects appear to be of secondary importance.

The next two spectral peaks have frequencies of $f_1 = 0.047$ Hz and $f_2 = 0.094$ Hz (or $T_1 = 21.3$ s and $T_2 = 10.6$ s). These frequencies are believed to be associated with the Kelvin-Helmholtz (K-H) instabilities generated at the interface. Detailed examination of the video images indeed revealed that the dominant periods of the K-H instabilities generated close to the opening are either 10 s or 20 s. Other spectral peaks have frequencies of $f_3 = 0.148$ Hz and $f_4 = 0.211$ Hz. It is clear that f_2 ($\approx 2.0f_1$), f_3 ($\approx 3.1f_1$), and f_4 ($\approx 4.5f_1$) are the first, second and third harmonics of the base frequency f_1. The existence of the third and fourth harmonics in interfacial instabilities has not been reported in the literature. Further study on these instabilities requires a detailed measurement of the flow field at the opening and is beyond the scope of this study.

The mean position of the interface will now be examined. The shape of the lower layer in the middle and window opening experiments is similar to a nappe in a single-layer flows over a sharp-crested weir, while the upper layer is like an inverted nappe (Fig. 10a). The mean position of the lower layer, also called 'nappe' here, was obtained by averaging its position over duration of 2 minutes at one second interval. Figure 13 shows the mean profile of the nappes in the middle and window opening experiments. The surface re-circulation zone is also plotted in Fig. 13. It is of interest to compare the trajectory of these nappes to that in a single-layer flow with its surface position at the weir the same as the interface position. Notice that the exchange flow here is significantly different from a single-layer flow. In particular, the flow at the opening has a much larger vertical acceleration.

Figure 13 clearly shows that the horizontal momentum of the nappe was killed much quicker and the nappe hit the bed closer to the opening in the exchange flows compared to a one-layer flow. This is because in the exchange flows, hydrostatic pressure increases down the nappe due to the increase in the upper layer thickness. In addition, there is significant friction along the nappe. These are significantly different from a single-layer flow where the pressure at both the upper and lower nappe remains atmo-
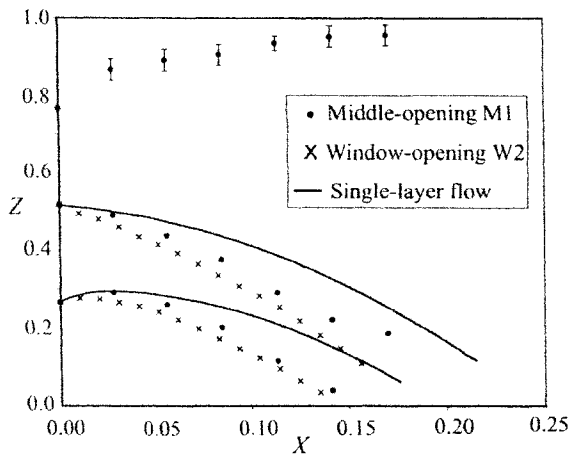
230

Fig. 13. Mean position of the lower layer in Exp. M1 and Exp. W2, compared with the nappe profile in single-layer flow over a sharp-crested weir.

spheric and the friction at the air-water surface is negligibly small. Furthermore, the significant vertical velocity in the exchange flows also helped to reduce the horizontal trajectory of the nappe. In the window experiments, the lateral expansion in the lower layer along the nappe further helped to reduce the horizontal trajectory of the nappe.

An interesting observation in Exp. W2 is that the lighter fluid was continuously being fed into the underneath of the lower nappe. This was seen as a pocket of clear fluid underneath the dyed lower layer (Fig. 10). Recall in single-layer flow over a weir, aeration is required under the lower nappe to maintain the pressure atmospheric. In window opening experiments, the under-pressure below the lower nappe was caused by the entrainment of the nappe, which resulted in the lighter fluid being fed there.

5.3. Transition to Subcritical Flow

The flow leaving the opening was internally supercritical in the experiments with middle and window openings. It is usually believed that this supercritical flow will go through an internal hydraulic jump to subcritical as prescribed by the downstream flow condition in the reservoirs. However, internal hydraulic jumps were not observed in any of the above experiments. Instead, the transition to the subcritical flow was completed through the expansion of the thin lower layer by the mixing caused by large K-H instabilities as is evident in Fig. 10. In the transition region, a mixed layer of intermediate density between the upper and lower layers was observed. This mixing zone eventually disappeared and the flow became two-layered again downstream.

Earlier studies have examined the velocity profile of a single-layer flow over a sharp-crested weir (Montes, 1998). Here we will examine the variation of G assuming that the flow rate is constant along the channel and velocity is uniform across the depth. Based on an averaged layer thickness, the variation of G downstream of the opening in Exp. M1 is shown in Fig. 14. The flow is internally supercritical at the opening with $G \approx 1.5$. This G value increases

to about 3.1 at $x \approx 0.3$ where the transition to subcritical flow starts. Though the lower layer thins continuously, G actually decreases at $x \approx 0.1$ as the upper layer thickens quickly due to the surface re-circulation eddy and its contribution in G reduces. The flow starts to approach uniform at $x \approx 0.5$ where $G \approx 1.3$, and becomes internally subcritical with $G \approx 0.8$ at $x \approx 0.65$. Note that the variation in the flow rate along the channel due to the entrainment and the uncertainty in determining the layer thickness can result in significant error in the estimates of G values, especially where mixing is appreciable.

6. Summary and Conclusions

Exchange flows through bottom, middle and window openings were studied theoretically and experimentally. Simultaneous measurements of the velocity field and the interface position were obtained using particle tracking and imaging processing techniques. Utilizing control curves, the internal hydraulic theory predicts the existence of two controls in the exchange flow through bottom openings. In the exchange flows through middle and window openings, the influence of the exit is blocked by the supercritical flow away from the opening. These flows thus have only one control located at the opening, with the interface located at the center of the opening. These predictions are confirmed in the experiments.

The internal hydraulic theory, however, could significantly underpredict the rate of exchange as it neglects the effects of friction, non-hydrostatic forces and interfacial entrainment. Inclusion of non-hydrostatic forces increases the prediction of the flow rate, whereas friction reduces the flow rate. In the bottom opening experiments, the friction between the two controls cancels out the effects of non-hydrostatic forces, and the predictions of the flow rate compare well with the measurements. In the middle and window opening experiments, on the other hand, the flow is controlled at the opening only. Thus friction has minimal effect in the flow rate, whereas non-hydrostatic forces become even more important given strong streamline curvature. Neglecting non-hydrostatic forces results in underestimating the flow rate. The effect of streamline curvature together with the interfacial entrainment causes an increase in flow rate by 50 – 100 % over the theoretical predictions.
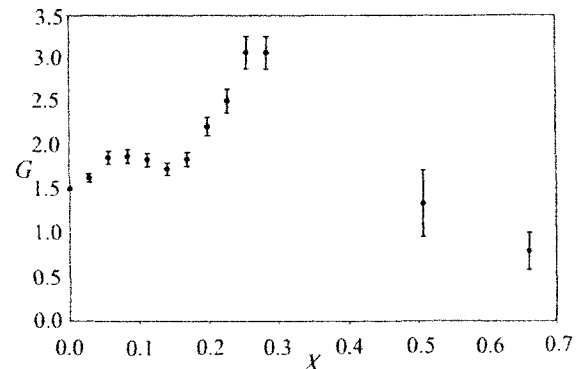

Fig. 14. Variation of G along the channel in Exp. M1 with error bars.

231

In the middle and window opening experiments, the interface of the two layers fluctuates due to the Kelvin-Helmholtz instabilities generated at the interface, as well as the low frequency basin-scale internal seiche. The observation of several modes of higher frequency oscillations is unexpected. These are believed to be higher harmonics of the fundamental mode of K-H instabilities. The mean position of the lower layer was measured and its horizontal trajectory is found to be much shorter compared to that in a single-layer flow. The transition of this supercritical flow to subcritical was completed through the expansion of the thin lower layer by the mixing caused by large K-H instabilities.

Exchange flow through a bottom opening with the upper layer arrested was also examined. A smaller G value was reported at the opening, consistent with earlier studies. This is due to the neglect of the upper layer in calculating G. Given the upper layer is significantly thinner than the lower layer at the opening, a very small flow rate in the upper layer could have significant contribution in G, thus there is some uncertainty in computing the G value at the opening.

References

ADAMS, E.E. and COSLER, D.J. (1988). Density exchange flow through a slotted curtain. *J. Hydr. Res.* 26, 261-273.

ALAVIAN, V., JIRKA, G.H., DENTON, R.A., JOHNSON, M.C. and STEFAN, H.G. (1992). Density currents entering lakes and reservoirs. *J. Hydr. Eng.*, ASCE, 118(11), 1464-1489.

ARMI, L. (1986). The hydraulics of two flowing layers with different densities. *J. Fluid Mech.*, 163, 27-58

ARMI, L. and FARMER, D.M. (1986). Maximum two layer exchange through a contraction with Barotropic net flow. *J. Fluid Mech.*, 164, 27-51.

ARMI, L. and FARMER, D.M. (1988). The flow of Mediterranean water through the Strait of Gibraltar. *Progress in Oceanography*, 21, 1-105.

DALZIEL, S.B. and LANE-SERFF, G.F. (1991). The hydraulics of doorway exchange flows. *Building and Environment*, 26, 121-135.

HAMBLIN, P.F. and LAWRENCE, G.A. (1990). Exchange flows between Hamilton Harbor and Lake Ontario. *Proc. of 1990 Annual Conf. of Canadian Society for Civil Eng.*, V: 140-148.

HARLEMAN, D.R.F. and ELDER, R.A. (1965). Withdrawal from two-layer stratified flows. *J. Hydr. Div.*, ASCE. 91(4), 43-58.

HENDERSON, F.M. (1966). *Open Channel Flow.* Macmillan Press.

MONTES, S. (1998). *Hydraulics of Open Channel Flow.* ASCE Press.

MORIN, V.M., ZHU, D.Z. and LOEWEN, M.R. (2002). Instability and entrainment in exchange flow over a smooth sill. *J. Hydr. Eng.*, ASCE, submitted.

OGUZ, T., OZSOY, E., LATIF, M.A., SUR, H.I. and UNLUATA, U. (1990). Modeling of hydraulically controlled exchange flow in the Bosphorus Strait. *J. Physical Oceanography*, 20, 945-965.

STEVEN, C. and COATES, M. (1994). Applications of maximized cross-correlation technique for resolving velocity fields in laboratory experiments. *J. Hydr. Res.*, 32, 195-212.

WOOD, I.R. and LAI, K.K. (1972). Flow of layered fluid over broad crested weir. *J. Hydr. Div.* ASCE, 98, 87-104.

ZHU, D.Z. (2002). Control curves for two-layer flows. *J. Hydr. Eng.*, ASCE, 128(1), 113-116.

ZHU, D.Z. and LAWRENCE, G.A. (1998). Non-hydrostatic effects in layered shallow water flows, *J. Fluid Mech.*, 355, 1-16.

ZHU, D.Z. and LAWRENCE, G.A. (2000). Hydraulics of exchange flows. *J. Hydr. Eng.*, ASCE, 126(12), 921-928.

ZHU, D.Z. and LAWRENCE, G.A. (2001). Holmboe's instability in exchange flows. *J. Fluid Mech.*, 429, 391-409.

232

APPENDIX B

Determining water density in laboratory experiments using NaCl - aqueous solution

The density of water can be obtained once the water temperature is measured and the weight concentration of the salt is computed. An optimized density (ρ) equation, which fits to the density data of NaCl aqueous solutions compiled by Lide (1998), can be used to predict $\rho(S, T)$. The new equation is a modified form of the seawater density equation given by Baddour (1994). It can be used for temperature (T) of 0 to 30 °C and salinity (S) of 0 to 0.25 mol/kg of NaCl. The equation is as follows with (T) in °C, (S) in ppt and (ρ) in kg/m^3:

$$\rho = 999.8426 + 0.0679 \times T - 0.0091 \times T^2 + 0.0001 \times T^3 - 1.1200 \times 10^{-6} \times T^4 + \\ 7.0000 \times 10^{-9} \times T^5 + S \times (0.7541 - 0.0029 \times T + 2.3780 \times 10^{-5} \times T^2)$$

(B.1)

with a maximum error of 6.1234x10^{-2} kg/m^3.

Temperatures were measured using a digital thermometer (Fisher Scientific) that provided accuracy to 0.1 °C, and the salt was weighed to 0.1 g using a digital scale. With the range of the quantities of salt used in the current study, the lowest amount was 1000 g which resulted in the minimum reduced gravity of g' of 1.64 cm/s^2. Consequently we estimate the error in g' to be less than 1%.

REFERENCES

BADDOUR. R. E. 1994. Thermal saline bubble plumes. Recent Advances in the Fluid Mech. of Turbulent Jets and Plumes. Kluwer Academic Publ., 117-129.

LIDE, D. R. 1998. CRC Handbook of Chemistry and Physics, 79th Edition, CRC, Boca Raton, Fla.

APPENDIX C

C.1 A brief account on planar laser induced fluorescence (PLIF)

Planar laser induced fluorescence (PLIF) is a relatively modern experimental technique for instantaneous concentration measurements in turbulent flows. The technique is non-intrusive and two-dimensional in character; hence it is convenient to use in studying turbulent mixing particularly in density stratified flows. For example, it was successfully used in describing the mixing process of a passive tracer in a stirred tank reactor (Houcine *et al.*, 1998). Cowen *et al.* (2001) used a single camera that provided coupled particle tracking velocimetry (PTV) and LIF measurements to study neutrally buoyant turbulent round jet. Roberts *et al.* (2001) used LIF and conductivity probes to study mixing in stratified jets. Webster *et al.* (2003) used LIF to study a neutrally buoyant chemical plume in turbulent open channel flow.

The method depends mainly on producing a coherent high power light sheet from a light source, commonly laser. The laser will illuminate the volume of fluid in the flow within the laser sheet during an experiment. A passive tracer dye, for example Rhodamine 6G, can be used where it absorbs part of the energy and emits the rest as fluorescence that can be recorded by a video camera. The technique can provide simultaneous measurements for concentration coupled with piv velocity field measurements to be used for mass flux measurements. For that two optical filters have to be used with two cameras for each technique. The filters have to be well chosen so that one would block the dye and the other would block the reflected light from the piv particles at the laser wavelength. There are many difficulties that may arise in the process due to variation of the laser power with time, but some devices can be used to stabilize it. Typical lasers used for research purposes are the Argon-ion and Nd:YAG lasers.

234

C.2 Calibration test for PLIF using a circular buoyant jet in quiescent fresh water

A sample calibration test for PLIF was performed in an aquarium using a circular buoyant jet emerging from a simple Pitot-tube. The laser sheet was aligned with the center line of the tube so that the central plane of the jet could be within the laser sheet. A syringe was used to inject NaCl solution of a known salinity and dye concentration. The tube was placed so that the jet would emerge horizontally in quiescent ambient fresh water. The different corrections stated in chapter 4 were performed except for the horizontal non-uniformity of the laser sheet, which was not an issue herein due to the much smaller field of view. The procedure adopted for the calibration was that of Grazzini (1999); for its simplicity and effectiveness. A TK-1280U JVC CCD camera was used with a high-pass optical filter in front of the lens to block the piv tracer particles. The particles were added to resolve their effect on the laser attenuation; hence simulating a real simultaneous experiment that has both piv particles and dye. The images were 640 x 480 pixels covering a field of view of about 40 x 30 cm. In what follows, sample results from this calibration test are presented. The reader is to refer to the details of each step in chapter 3. Figure C-1 shows the variation of the average gray scale arriving at the CCD from images of 18%-reflectance paper as the one used in chapter 3. Different aperture openings were used and the γ-correction factor was estimated as 0.315. In figure C-2, the variation of the dye fluorescence as a function in concentration is shown along with the verification of the power law (refer to: equation 4.2). Clearly the linear range of the luminescence-concentration is below about 0.1 g/m^3. This is much less the 0.5 limit reported earlier by Pawlak and Armi (1998).

Because the calibration tank used for the experiments in chapter 4 was placed within the channel, the effect of double glass was investigated in the aquarium by placing a second glass sheet in front of it. Figure C-3 shows that it has negligible effect on the gray scale value at different concentrations. All the corrections were performed following the procedure described in chapter 4 and a sample image of the jet is shown in figure C-4. Clearly the near, intermediate

235

and far fields of the jet can be seen. Rubin and Atkinson (2001) reported that the near field is valid within (6 – 10) times the nozzle diameter from the discharge point, whereas the far field, through which the turbulent stresses are in equilibrium and self-similarity of the concentration and velocity profiles can be assumed, starts from distances greater than 40 times the diameter. Although the image in figure C-4 is instantaneous, yet it clearly shows those fields with the region in between termed the intermediate field.

REFERENCES

COWEN, E. A., CHANG, K.-A. & LIAO, Q. 2001 A single-camera coupled PTV-LIF technique. *Exps. in Fluids* **31**, 63-73.

GRAZZINI, F. 1999 Etude expérimentale de la dispersion de polluants en présence d'obstacles. Doctoral thesis no. 1559 at the L'Institut National Polytechnique de Toulouse, France. Spécialité: Physique et Chimie de l'Environnement (in French).

PAWLAK G. & ARMI L. 1998 Vortex dynamics in a spatially accelerating shear layer. *J. Fluid Mech.* **376**, 1-35.

ROBERTS, P. J. W., MAILE, K. & DAVIERO, G. 2001 Mixing in Stratified Jets. *J. of Hydraulic Engineering*, ASCE, **127**, 194-200.

RUBIN, H. & ATKINSON, J. 2001 Environmental fluid mechanics. Marcel Dekker, Inc.

WEBSTER, D. R., RAHMAN, S. & DASI, L. P. 2003 Laser-induced fluorescence measurements of a turbulent plume. *J. of Engrg. Mech.*, ASCE, **129**, 1130-1137.
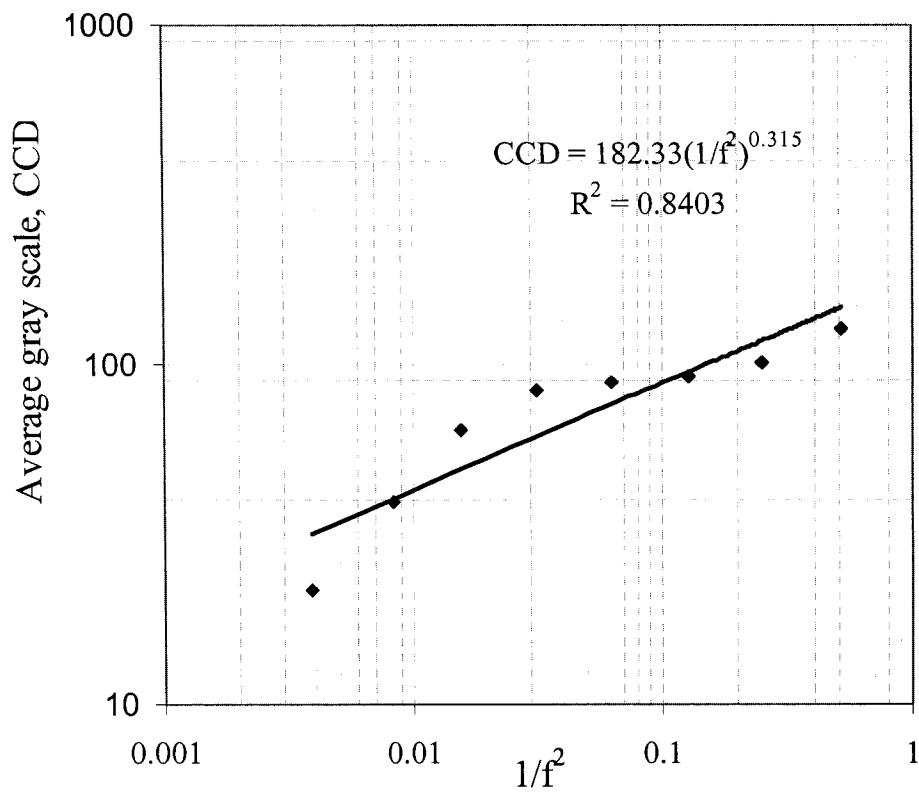
FIGURE C-1. Variation of the luminous intensity arriving at the CCD of the camera as a function of the aperture opening, f, on a logarithmic representation of the data showing the γ correction factor of the CCD ($\gamma = 0.315$).
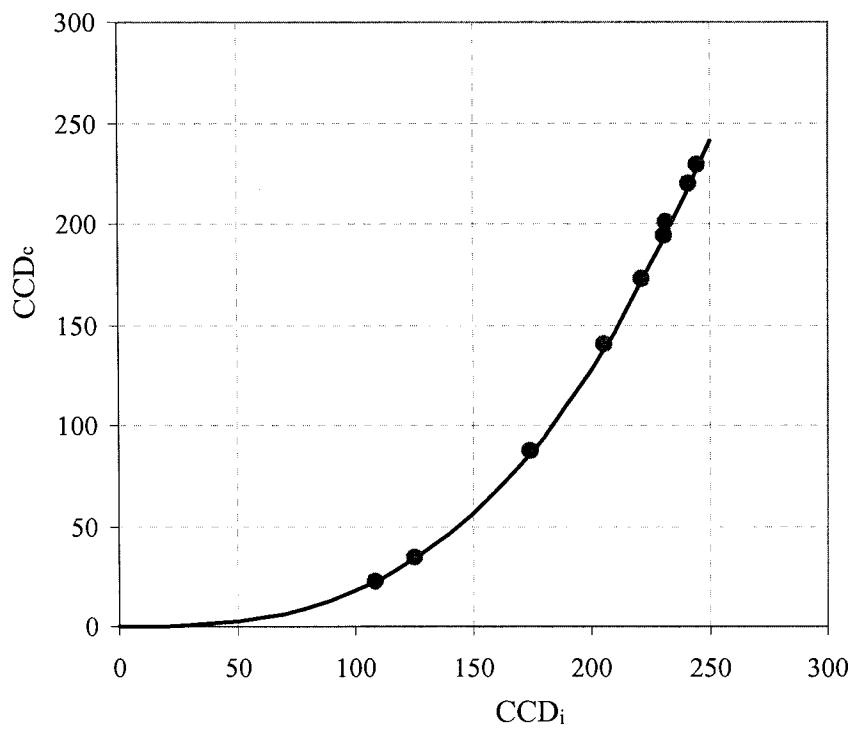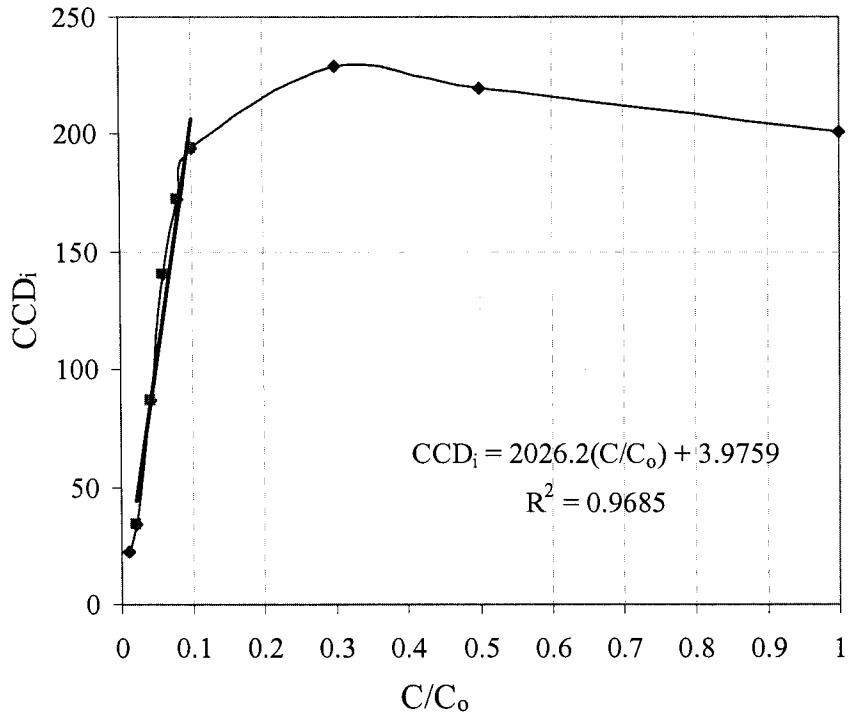
237

FIGURE C-2. a) Variation of fluorescence as a function in concentration C/C_o, with $C_o = 1$ g/m^3; and b) the transfer function of the camera for the different concentrations.
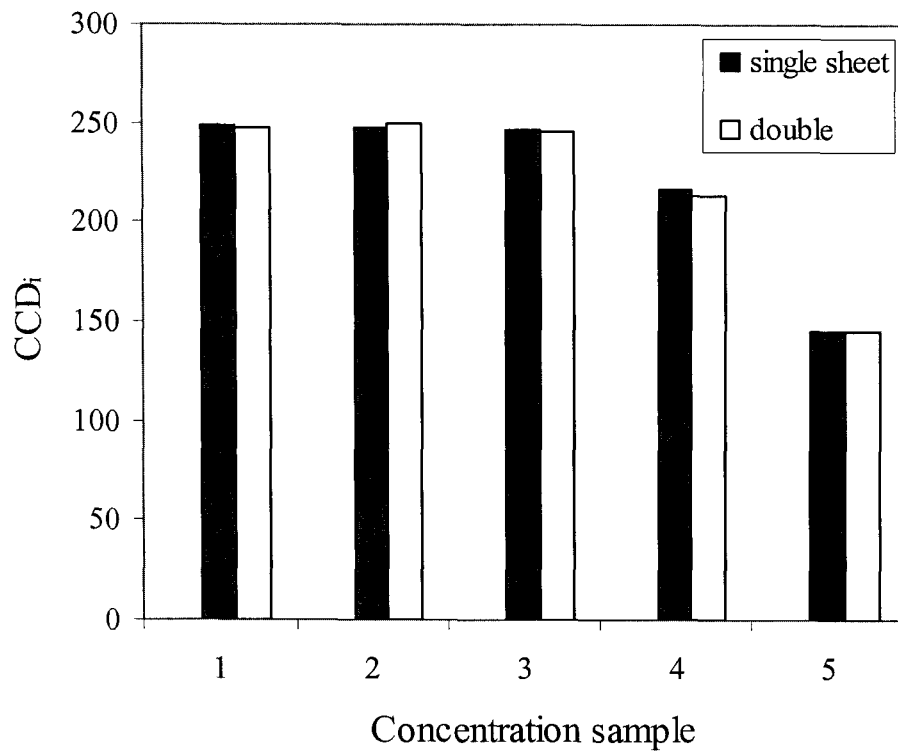
238

FIGURE C-3. Variation of fluorescence as a function in concentration for 5 samples at 0.02, 0.04, 0.06, 0.08 and 0.1 g/m^3 using single and double glass sheet.
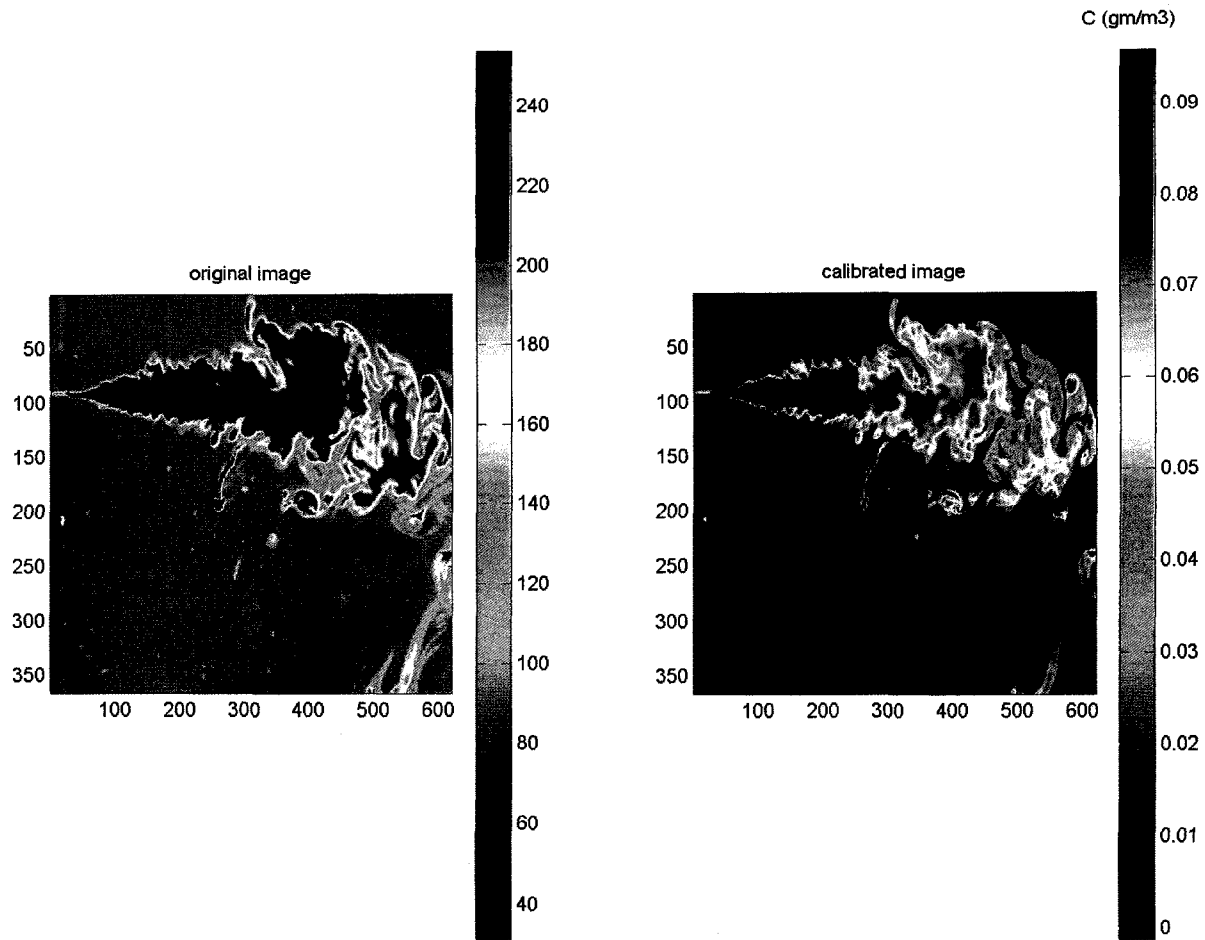
239

FIGURE C-4. Sample instantaneous image of the jet. To the left is the raw image, and to the right is its calibrated sister image. The macimum concentration used was about 0.08 g/m³.

APPENDIX D

ERROR ANALYSIS

For most of the quantities or parameters included in this thesis, two main quantities contributed in their computations. These two quantities are the velocity and interface positions data. In other words, the errors in any measured quantity would depend on the errors in the velocity and interface positions' measurements. The total error in DPIV measurements is the sum of errors due to velocity gradients, tracer particle density, out-of-plane motion, particle diameter, dynamic range, peak locking and AGW interpolation (Cowen and Monismith, 1997). Using their results to estimate these errors in the current experiments resulted in an average error in the instantaneous velocity field measurements of about 4%. For the instantaneous interface positions' measurements, the errors were estimated as 2 -3 pixels, which would translate to about 1% or less in the different experiments. Errors in the density estimates have been mentioned earlier in Appendix B and resulted in 1% or less as an error estimate for the reduced gravity g'. In the following, estimates of the errors in the main measured quantities are presented. Note that in computing time-averaged quantities, the random error is quite eliminated since the measurements are at relatively high frequency (10 Hz and up) and averaging was done for some quantities, such as the flow rate, over minutes.

D.1 The bulk Richardson, J

The bulk Richardson, J, is estimated using the relation:

$$J = \frac{g' \cdot \delta}{\Delta U^2}$$
D.1

By taking the natural logarithm of both sides, we obtain:

$$Ln\,(J) = Ln\,(g') + Ln\,(\delta) - 2 \times Ln\,(\Delta U)$$
D.2

and upon differentiating we get:

$$dJ/J = dg'/g' + d\delta/\delta - 2\left(d(\Delta U)/(\Delta U)\right)$$
D.3

By squaring and neglecting the cross terms, the percentage error in J can be obtained as:

$$\frac{\varepsilon_J}{J} = \sqrt{\left(\frac{\varepsilon_{g'}}{g'}\right)^2 + \left(\frac{\varepsilon_{\delta'}}{\delta}\right)^2 + \left(\frac{\varepsilon_{\Delta U}}{\Delta U}\right)^2}$$
D.4

The same procedure can be followed to estimate the percentage error in δ ($\delta = \Delta U/(\partial U/\partial z)$. Based on the results of Cowen and Monismith (1997), the error due to the velocity gradients was about 2%. With this value and those in the introductory part, the percentage error in δ was estimated as 10% and consequently that for J was estimated as about 12%.

D.2 The non-dimensional shift, $\mathcal{C}$

The non-dimensional shift, $\mathcal{C}$ ($\mathcal{C} = d / (\delta/2)$), in chapter 2 showed large scatter in the data. The error in $\mathcal{C}$ would be the square root of the sum of squares of the errors in the shift, d, and the shear layer thickness, δ. An estimate for the error in $\mathcal{C}$ is about 10%. The results reported in chapter 2 had values for $\mathcal{C}$ within 0.5. This shows that the shift is significant and confirms that K-H instabilities can be generated in accelerating flows at different conditions from parallel flows.

D.3 The flow rate, q

In computing the instantaneous flow rate, the instantaneous velocity profiles were integrated across depth. The closest velocity vectors to the free surface and the bed profile within the flow field were shifted by ½ the size of the search window. In integrating the upper layer velocity profiles, it was assumed that the velocity remained constant between the true free surface and the first velocity measurement below it. The first velocity measurement below the bed profile was set to zero. At the intersection of the laser sheet with both the free surface and the bed profile, the light showed some thickness (about 2 – 3 pixels). The profiles for the free surface and the bed used in the piv computations were shifted inwards not to include those effects (i.e. the flow field was considered within those shifted bed and free surface profiles). The areas outside this domain

242

were given median gray scale of the whole flow area. All these effects contribute into the errors in the flow rate. Surface tension may reduce the flow rate close to the free surface. However, its effect was assumed marginal. Because of the large number of measurements within the steady state in all experiments, the random error would be eliminated in the measurements when computing the time-averaged flow rate. Note that the steady maximal exchange lasted for minutes and our measurements were at least at 10 Hz (for 2 minutes, which is the shortest maximal exchange time, this result in 1200 measurements). Errors of about 3% were estimated for the flow rate.

D.4 The entrainment coefficient

The entrainment coefficient, E, was computed using the formula:

$$E = \frac{1}{V}\frac{dq}{dx}$$

D.5

in which V was either the depth averaged lower layer velocity over dx, or defined after Ellison and Turner (1959) by:

$$V = \frac{\int u^2(z)dz}{\int u(z)dz}$$

D.6

The error estimate in E would depend on errors in the velocity and interface positions' measurements. However, because E was estimated on a time-averaged basis over the period of maximal exchange (2400 and 2700 measurements in Exp 2 and 4), the random error in both quantities will reduce by a factor 50 and as such will be negligible. For example the errors in velocities will be approximately 0.1%. Based on the spatial resolution, this would be equivalent to errors of about 50% in the entrainment coefficient data due to local variable gradients in the flow rate data. For that, a nine-point moving average was used, which would reduce the error to about ±17%.

243

REFERENCES

COWEN, E. A. & MONISMITH, S. G. 1997 A hybrid digital particle tracking velocimetry technique. *Exp. Fluids* **22**, 199-211.

ELLISON, T. H. & TURNER, J. S. 1959 Turbulent entrainment in stratified flows. *J. Fluid Mech.* **6**, 423-448.